GL-TR-89-0259

The effects of structure and source complexity on waveforms: Crustal structure of Tibet and the recovery of complex seismic sources

Terry C. Wallace

University of Arizona
Department of Geosciences
Tucson, AZ 86721

7 September 1989

Final Report
May 1987-May 1989

GEOPHYSICS LABORATORY
AIR FORCE SYSTEMS COMMAND
UNITED STATES AIR FORCE
HANSCOM AIR FORCE BASE, MASSACHUSETTS 01731-5000

SPONSORED BY
Defense Advanced Research Projects Agency
Nuclear Monitoring Research Office
ARPA ORDER NO. 5299

MONITORED BY
Geophysics Laboratory
Contract No. F19628-87-K-0046

The views and conclusions contained in this document are those of the authors and should not be interpreted as representing the official policies, either expressed or implied, of the Defense Advanced Research Projects Agency or the U.S. Government.

This technical report has been reviewed and is approved for publication.

JAMES F. LEWKOWICZ
Contract Manager
Solid Earth Geophysics Branch
Earth Sciences Division

JAMES F. LEWKOWICZ
Branch Chief
Solid Earth Geophysics Branch
Earth Sciences Division

FOR THE COMMANDER

DONALD H. ECKHARDT, Director
Earth Sciences Division

This report has been reviewed by the ESD Public Affairs Office (PA) and is releasable to the National Technical Information Service (NTIS).

Qualified requestors may obtain additional copies from the Defense Technical Information Center. All others should apply to the National Technical Information Service.

If your address has changed, or if you wish to be removed from the mailing list, or if the addressee is no longer employed by your organization, please notify GL/IMA Hanscom AFB, MA 01731-5000. This will assist us in maintaining a current mailing list.

Do not return copies of this report unless contractual obligations or notices on a specific document requires that it be returned.

REPORT DOCUMENTATION PAGE

Form Approved OMB No. 0704-0188

1a. REPORT SECURITY CLASSIFICATION: Unclassified	1b. RESTRICTIVE MARKINGS
2a. SECURITY CLASSIFICATION AUTHORITY	3. DISTRIBUTION/AVAILABILITY OF REPORT: Approved for public release, distribution unlimited
2b. DECLASSIFICATION/DOWNGRADING SCHEDULE	
4. PERFORMING ORGANIZATION REPORT NUMBER(S)	5. MONITORING ORGANIZATION REPORT NUMBER(S): GL-TR-89-0259
6a. NAME OF PERFORMING ORGANIZATION: University of Arizona; 6b. OFFICE SYMBOL (If applicable)	7a. NAME OF MONITORING ORGANIZATION: Geophysics Laboratory
6c. ADDRESS (City, State, and ZIP Code): Department of Geosciences, Building #77, Tucson, AZ 85721	7b. ADDRESS (City, State, and ZIP Code): Hanscom Air Force Base, MA 01731-5000
8a. NAME OF FUNDING/SPONSORING ORGANIZATION: Defense Advanced Research Projects Agency; 8b. OFFICE SYMBOL (If applicable): NMRO	9. PROCUREMENT INSTRUMENT IDENTIFICATION NUMBER: F19628-87-K-0046
8c. ADDRESS (City, State, and ZIP Code): 1400 Wilson Boulevard, Arlington, VA 22209-2308	10. SOURCE OF FUNDING NUMBERS

PROGRAM ELEMENT NO.	PROJECT NO.	TASK NO.	WORK UNIT ACCESSION NO.
61102F	2309	G2	AV

11. TITLE (Include Security Classification): The effects of structure and source complexity on waveforms: Crustal structure of Tibet and the recovery of complex seismic sources

12. PERSONAL AUTHOR(S): Wallace, Terry C.

13a. TYPE OF REPORT	13b. TIME COVERED	14. DATE OF REPORT (Year, Month, Day)	15. PAGE COUNT
Final Report	FROM 5/87 TO 5/89	1989 September 7	198

16. SUPPLEMENTARY NOTATION

17. COSATI CODES			18. SUBJECT TERMS (Continue on reverse if necessary and identify by block number)
FIELD	GROUP	SUB-GROUP	Crustal thickness, Tibet, complex seismic sources

19. ABSTRACT (Continue on reverse if necessary and identify by block number)

In an attempt to better understand the effects of both source and path on regional distance waveforms, we have investigated the crustal structure of Eurasia and developed an algorithm for investigating complex seismic sources. Part I ~~of this report~~ is a study based on the inversion of 130 regional distance waveforms for average crustal thickness and upper mantle Pn velocity beneath Tibet. ~~The~~ results indicate an increase in Pn velocity, coincident with the increase in crustal thickness, of about 0.2 km/s beneath the Plateau. Impulsive Pn arrivals from paths that cross the Tibetan Plateau can be modeled with a positive upper mantle gradient, indicating an upper mantle lid approximately 100 km thick beneath southern Tibet. This "shield-like" structure has important consequences for the propagation of regional phases Pg, Pn and Sn. Part II ~~of~~ this report discusses an algorithm for time dependent moment tensor (TDMT) inversion. The algorithm was developed to investigate complex seismic sources, such as multiple earthquakes and, ultimately, explosions with tectonic release contamination. The TDMT inversion algorithm ~~has been~~ tested with ~~three~~ synthetic data examples with varying degrees of complexity. It ~~has~~ also ~~been~~ tested on the long-period body waves for ~~three~~ earthquakes: the 1982 Yemen earthquake, the 1971 San Fernando earthquake, and the 1952 Kern County earthquakes. Preliminary modeling in the nearfield of nuclear explosions ~~has~~ yielded mixed results.

20. DISTRIBUTION/AVAILABILITY OF ABSTRACT	21. ABSTRACT SECURITY CLASSIFICATION	
☒ UNCLASSIFIED/UNLIMITED ☒ SAME AS RPT. ☐ DTIC USERS	Unclassified	
22a. NAME OF RESPONSIBLE INDIVIDUAL: James Lewkowicz	22b. TELEPHONE (Include Area Code): (617) 377-3222	22c. OFFICE SYMBOL: GL/LWH

List of Contributing Scientists

Terry C. Wallace, William E. Holt, and Kim Junkyoung

Department of Geosciences
Building #77
University of Arizona
Tucson, AZ 85721

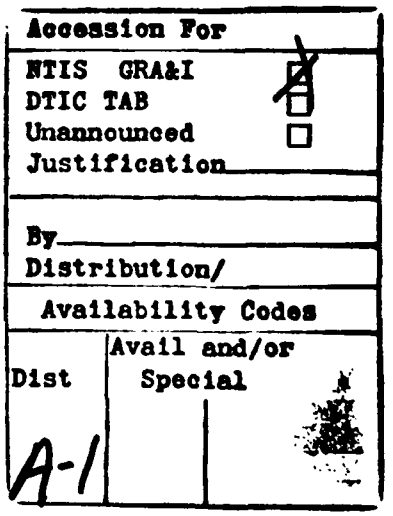

Table of Contents

I. Introduction

One of the main consequences of decreasing the yield limit in a threshold test ban treaty (TTB) or implementing a comprehensive test ban (CTB) is the increased reliance on regional distance seismograms for monitoring purposes. This requires a more complete understanding of short-period regional phases from both explosions and earthquakes. Most schemes for determining the yield of underground nuclear explosions are based on measuring the amplitude of phases such as Pn or Lg, on the coda of a particular phase. Unfortunately, these seismic signatures are a complex combination of both propagation and source effects, and any algorithm for accurate yield determination will require both empirical and analytical development. Here we report on our research efforts to calibrate Eurasian travel paths, and develop an algorithm to recover mixed seismic sources (complex earthquakes, explosions and tectonic release, or multiple explosions).

Regional phases Pg and Lg show a very strong dependence on travel path. In terms of rays it is possible to think of Pg and Lg as S or P waves trapped in a crustal waveguide. Although scattering is apparently a very important excitation mechanism (in the case of explosions the departure from plane-layered structure is thought to contribute significantly to the generation of Lg), the "continuity" of the waveguide is extremely important to the efficiency of Pg and Lg propagation. In Eurasian a number of investigators have noted path irregularities for Lg, in particular "blockage" due to mountain ranges. In Chapter II we discuss a study of Pn and Pg in western China and Tibet, which was used to produce a regionalized map of crustal thickness and Pn velocity.

Chapter III presents an algorithm for the recovery of time dependent moment tensors. The problem of mapping out the seismic source for complicated events such as explosions with tectonic release, or faulting events which have geometry which changes with time, has evolved through several stages: forward modeling and trial and error modeling, direct inversion and subtraction, and

finally time dependent moment tensor inversion. Stump and Johnson (1977) and Sipkin (1987) discuss procedures for inverting the time histories of moment tensor elements, and have shown it is possible to recover "mixed" seismic sources. We have developed a similar algorithm which we have used to recover faulting complexity from a number of moderate-to-large earthquakes. The next step is to use this algorithm on regional distance seismograms from explosions.

Chapter II

Crustal Thickness and Upper Mantle Velocities in the Tibetan Plateau Region From the Inversion of Regional P_{nl} Waveforms: Evidence for a Thick Upper Mantle Lid Beneath Southern Tibet

Paper in press in

Journal of Geophysical Research

William E. Holt

Terry C. Wallace

Abstract

The crustal thickness and upper mantle velocity variation in Tibet and surrounding regions was mapped through the inversion of 130 individual long-period P_{nl} waveforms. The 130 paths crisscross the Tibetan Plateau, Hindu Kush, Karakoram, southwest China, Burma, and northern India regions. We regionalized these areas on the basis of topographic and geologic expression and determined the average upper mantle velocity and crustal thickness value for each block or region through a linear least-squares inversion of the 130 parameter values. Crustal thicknesses in the Tibetan plateau, Karakoram, and Hindu Kush regions range from 63-72 km and Pn velocities are 0.10-0.20 km/s faster beneath these regions than those beneath northern India. We observed impulsive first arrivals (evidence for positive upper mantle gradients) on seismograms recorded at distances between 1000-1400 km. The paths of these waves crossed portions of Tibet, the Hindu Kush, and east India regions. Simple modeling of the long-period Pn waveform and amplitude requires fairly high upper mantle gradients of 0.18 km/s-0.25 km/s per 100 km beneath the Pamir-Hindu Kush region and requires an upper mantle lid in excess of 100 km thickness. The southern half of Tibet also requires a lid of about 100 km thickness. A thinner upper mantle lid (50 km) provided a poor match to the Tibetan observations, even with a very high gradient of 0.2 km/s per 100 km. The upper mantle structure of east India appears to be similar to the southern half of Tibet (100 km thick positive gradient zone). Both the increase in Pn velocity from India into Tibet, and the evidence for a thick upper mantle lid beneath Tibet are consistent with the model in which Indian lithosphere has underthrust southern Tibet. Due to poor path coverage, the structure beneath northern Tibet cannot be resolved, and thus, underthrusting beyond central Tibet cannot be constrained. The rapid increase in upper mantle velocity from northern India into Tibet can be explained by the pressure increase alone, produced by the double-thick crust, and indicates that the Indian lithosphere, which underlies Tibet, is out of thermal equilibrium.

Introduction and Background

The Tibetan Plateau has attracted the attention of several generations of geoscientists, and many mechanisms have been proposed to describe its evolution. There are two basic theories that describe the mechanism of uplift of the Tibetan plateau. In the first, uplift occurred by shallow underthrusting of the Indian lithosphere beneath Eurasia producing a crust of double thickness in Tibet [*Argand*, 1924; *Powell and Conaghan*, 1973, 1975]. The second hypothesis involves uniform crustal thickening and lithospheric shortening in response to compression [*Dewey and Burke*, 1973; *Toksöz and Bird*, 1977]. Both models account for the observation of a 60-70 km thick crust beneath the Tibetan Plateau, but differ in the nature of the upper mantle. The uniform thickening model has a mantle which is expected to be hot and weak in comparison with the underthrusting model, in which the mantle is more shield-like.

Numerous seismic investigations have shown that the Tibetan Plateau is underlain by a 55- to 85-km-thick crust [*Gupta and Narin*, 1967; *Bird and Toksöz*, 1977; *Chun and Yoshi*, 1977; *Pines et. al.*, 1980; *Patton*, 1980; *Chen and Molnar*, 1981], and most estimates agree upon an average thickness of 70 km. More enigmatic is the upper mantle velocity structure. Upper mantle velocities beneath Tibet and the Indian Shield are summarized in Figure 1. Using earthquake travel times, *Chen and Molnar* [1981] found high Pn and Sn velocities of 8.1 km/s and 4.7 km/s, respectively, beneath the Tibetan Plateau. Positive S-P residuals in north-central Tibet suggest that the high velocity upper mantle must be confined to a thin layer below the Tibetan crust [*Molnar and Chen*, 1984' Since these mean velocities within the upper mantle are not reflective of the expected velocity structure of a shield, they concluded that their seismic results are more compatible with the model of diffuse crustal thickening rather than continental underthrusting. *Barazangi and Ni* [1982] and *Ni and Barazangi* [1983] obtained high Pn and Sn velocities of 8.43 and 4.73 km/s, respectively, for the Tibetan Plateau region using earthquake travel times. They also found that high frequency Sn waves propagate efficiently in the upper mantle beneath Tibet and surrounding regions (see Figure 1)

with the exception of a region beneath the north-central part of the Plateau (the Chang Thang terrane). Ni and Barazangi concluded that the high Pn and Sn velocities and the efficient propagation of high frequency Sn waves were evidence that the Indian continental shield had underthrust Tibet.

Surface wave studies in northern Tibet [*Romanowicz*, 1982] and southern Tibet [*Jobert et al.*, 1985] also indicate high shear wave velocities in the uppermost mantle (4.65-4.7 km/s) and thin upper mantle lid (kid). Rayleigh wave phase velocities are low (4.4-4.5 km/s) beneath central Tibet [*Brandon and Romanowicz*, 1986], and the data seem to require that an upper mantle lid is absent in this region (see cross section, Figure 1). *Lyon-Caen* [1986] used travel times and modeled S and SS waveforms to constrain the upper mantle velocity beneath the Indian Shield and Tibet. She found high shear wave velocities of 4.7 km/s beneath both India and Tibet, but the upper mantle lid is apparently much thicker beneath the Indian Shield, and the mean upper mantle shear wave velocities are 4-5% lower beneath Tibet (between 70-250 km depth) relative to the mean velocity beneath the Indian Shield.

Although many of the seismic studies have produced contradictory models, it is generally agreed that Tibet has a thick crust, and is underlain by a mantle which has high velocities in the lid. The unresolved questions include exactly how thick is the lid, and what is the lateral heterogeneity of the structure.

In this paper we use the long-period P_{nl} waveforms to obtain both crustal thickness variations and upper mantle velocity variations beneath the Tibetan Plateau and surrounding regions (i.e., the Karakoram-Hindu Kush, southwest China, and Burma). This enables us to map the gross crustal structure of Tibet and to examine the transition in crustal thickness and upper mantle velocity along the margins of the plateau uplift and collision zone. The spatial change of crustal thickness and upper mantle velocity, from regions which have been intensely affected by the continental collision (Tibet), to regions less profoundly influenced (southwest

China, the Indian Shield), is important information that can provide additional constraints for the formation of the Tibetan plateau.

Data and Method of Analysis

The P_{nl} wavetrain is recorded at regional distances (2°-12°) and begins with a refracted arrival (Pn head wave) from the crust-mantle boundary. The head wave is followed by the P_L phase which can be described as the summation of the mode-converted and reflected P and SV wave energy that is trapped within the crust. The interference of mode converted and reflected phases within the crustal waveguide strongly influence the shape of the P_{nl} waveform. Changes in crustal thickness produce changes in the timing of different mode converted and reflected energy, and thus alter the waveform shape. If the source parameters are known, then P_{nl} synthetics can be parameterized in terms of the thickness of the crustal waveguide and upper mantle velocity. The average thickness of the crustal waveguide can then be computed by optimally matching the P_{nl} synthetic to the observed regional distance waveform. Upper mantle velocities can be determined if the absolute travel time, the crustal thickness, and distance from source are known.

A model consisting of a layer over a half-space was used to construct the synthetics for this study. *Helmberger and Engen* [1980] and *Wallace* [1986*b*] demonstrated that for periods greater than a few seconds, a single layer model is sufficient to construct accurate long-period P_{nl} synthetics for most continental paths. Therefore in matching our synthetic regional distance waveforms to the observed P_{nl} waves, we are looking at gross variations in crustal thickness, and not the fine details of crustal structure.

Our observations consist of long-period P_{nl} waveforms recorded at WWSSN stations. A total of 78 earthquakes with known source parameters in the Hindu Kush, Tibet, southwest China, and Burma, which were recorded at one or more WWSSN stations at regional distances, were used as a data base. This provided us with a total of 130 regional distance paths.

Figure 2 shows the location of the sources and paths superimposed on the smoothed topography of the collision zone. The smoothed topography was digitized from the map in *England and Houseman* [1986], and has a contour interval of 1 km. About twenty paths cross the Tibetan plateau proper. Table 1 lists the location and source parameters for the 78 earthquakes.

Each individual P_{nl} waveform was inverted for the average crustal thickness that the long-period energy sampled along the entire path. *Wallace* [1986*a*] showed that if the path has a laterally varying or dipping Moho, then the average crustal thickness between source and receiver can be obtained from the inversion of the P_{nl} waveform.

We chose a norm, defined as an error function, written as:

$$e = 1 - \left[\frac{\int fg}{\left[\int f^2 \right]^{1/2} \left[\int g^2 \right]^{1/2}} \right] \qquad (1)$$

where f is the observed P_{nl} seismogram and g is the synthetic seismogram. The limits of integration are equal to the time window over which the waveform was inverted. The time window usually varied for each record but generally ran from the beginning of the Pn pulse out to 70-90 seconds. If the observed and synthetic waveform shapes are identical, then the error function has a value of zero. If the waves are completely out of phase, then the error function has a maximum value of 2. The error function was minimized with respect to the average crustal thickness and upper mantle Pn velocity. The minimization of (1) involves the computation of numerical derivatives with respect to the crustal thickness:

$$\partial e / \partial Th_i = \frac{e(Th_i + \Delta Th_i) - e(Th_i)}{\Delta Th_i} \qquad (2)$$

Where Th_i is the crustal thickness for the ith iteration, and ΔTh_i is the perturbation of the model. The computation of numerical derivatives is simple and relatively time efficient. A change in crustal thickness or upper mantle velocity only alters the timing of the head wave and reflected wave arrivals for each ray, but does not change the shape of the single ray response. Rather than recompute the complete synthetic response for a new structure, it is only necessary to alter the timing of the head wave and reflected wave pulses of each ray [see *Wallace*, 1986*b*].

With an estimate of crustal thickness, the Pn velocity can be determined from the absolute travel time.

$$t = p\Delta + \left[\int_{r_t}^{r_s} r^{-1}(\gamma^2 - p^2)^{1/2} + \int_{r_t}^{r_o} r^{-1}(\gamma^2 - p^2)^{1/2} \right] dr \qquad (3)$$

where $p = r_t/Pn$, r_o is the radius of the earth, r_t is the radius to the refracting horizon (Moho), r_s is the radius to the assumed source depth, and $\gamma = r/v(r)$. The origin times were obtained from the ISC and PDE catalogues. Since the ISC and PDE depths are often different from the depths determined from body wave modeling, the origin time, and hence the absolute travel time, can be in error. We corrected for this by subtracting the travel time difference between the different source depths from the origin time (assuming a ray with a take-off angle of 24.5°, and using equation 3). ISC origin times are determined assuming a crustal thickness of 33 km, which is considerably thinner than the crust beneath most of our source regions. A crustal thickness of 70 km can lead to an origin time error of nearly 2 seconds. We thus applied a further correction to the origin time by estimating the crustal thickness beneath the source (Th_i) and subtracting the travel time difference (using equation 3) between a ray (take-off angle = 24.5°) traveling through the crust (6.2 km/s) and mantle (8.0 km/s) of thickness Th_i-33 km. Both of these corrections typically increased the absolute travel time and hence decreased the estimate for Pn velocity. We assume that epicenter location errors

are random and that errors in velocity due to event mislocation should average. Most of the source events are larger than 5.5 magnitude and typically had low station residuals.

In the inversion procedure, a starting model crustal thickness is first chosen. Using this starting model and absolute travel time, we determine a Pn velocity, and compute a synthetic P_{nl} response and error function. The procedure then involves the perturbation of the crustal thickness (ΔTh_i = 2 km), and the computation of a new synthetic and error function. The calculation of the partial, followed by inversion, yields the change in crustal thickness (δTh_i) necessary to drive the solution toward a minimum. The change in crustal thickness (δTh_i), added to the starting model thickness, constitutes the new crustal model. The computation of a new synthetic from the new structure follows, and the procedure is typically repeated automatically for 3-6 iterations until the convergence criteria are met. It is not uncommon to encounter local minima, and therefore we attempted the inversion from two or three different starting models.

Figure 3 shows an example for which the mechanism was a pure thrust on a shallow plane. The starting crustal thickness was 30 km. The match to the observed P_{nl} waveform (top), recorded at station Quetta at a distance of 1340 km, is poor with this starting model thickness. The waveforms for the following iterations are also shown, and demonstrate the increasingly better match with each iteration. For most of the waveform inversions, a constant value of 6.2 km/s was used to represent the average velocity of the crustal waveguide. Slightly lower average crustal velocities were used for paths that crossed western Burma and eastern India. The effects of average crustal velocities on model parameter estimates will be discussed later.

Testing the Method

Both the crustal thickness and the average crustal velocity influence the relative timing of multiple reflections and mode converted phases and thus influence the shape of the P_{nl}

waveform. A change in crustal thickness will affect the waveform much in the same manner as a change in average crustal velocity [*Wallace*, 1986*b*]. Because of this trade-off, the average crustal velocity is held constant in the inversion and we solved only for crustal thickness. *McConnell and McTaggart-Cowan* [1963] determined from available worldwide continental refraction results that the mean continental P wave velocity varied from 6.0-6.2 km/s down to a depth of 20 km. As a restriction on the number of unknowns, we assumed a constant mean velocity.

In order to examine the effects of changes in average crustal velocity on the inversion for crustal thickness and Pn velocity, we tested the inversion using a wide range of average crustal velocities. The results of the inversion are shown in Table 2, and Figure 4 shows a graph of crustal thickness versus the average crustal velocity used in the inversion. The source was a strike-slip mechanism in southwest China, recorded at Chaing Mai Thailand at a distance of 923 kilometers. Note that for low average velocities, a thinner crust is obtained. Higher values of average crustal velocity produce an estimate of a thicker crust. The results of this experiment indicate that uncertainties in average crustal velocity of ±0.1 km/s map into uncertainties in average crustal thickness of ±5% of the total thickness (±2 km; see Figure 4). Figure 4 also shows a plot of average crustal velocity versus the Pn value obtained in the inversion. Note that the Pn velocity when obtained with this inversion procedure is insensitive to changes in average crustal velocity. Thus, Pn velocity and crustal thickness are really independent parameters.

Average crustal velocities that have been obtained for Tibet range from 6.1-6.25 km/s [*Chen and Molnar*, 1975; *Gupta and Narin*, 1967; *Hirn et al.*, 1984*a*; and *Ma*, 1988], and P_L waveform modeling indicates that there are no siginficant low-velocity zones in the lower crust [*Shaw and Orcutt*, 1984]. Average shear wave velocities range from 3.4-3.5 km/s [*Chun and Yoshi*, 1977; *Romanowicz*, 1982]. Thus, the velocities for the thick Tibetan crust are comparable to normal continental average velocities. The test results for crustal velocity

versus crustal thickness presented above indicate that an uncertainty in average crustal velocity of ±0.1 km/s for P waves can lead to an error in crustal thickness estimates of ± 5% of the true crustal thickness. This leads to an uncertainty of approximately ±4 km for results from individual paths that transect the Tibetan plateau region.

Average velocities within the Indian Shield are higher than the velocities for the Tibetan plateau. *Bhattacharya* [1971] obtained an average crustal P wave velocity of 6.5 km/s for the Indian Peninsula. Average crustal velocities in the Gangetic Basin are lower (5.9 km/s) due to the effects of the low velocity sediments [*Chun and Yoshi*, 1977]. Observations recorded at Shillong, India from earthquake sources in Burma, required a low average crustal velocity of 5.8 km/s in order to fit the P_{nl} waveforms. This low velocity may be due to thick sedimentary basins along the path. *Brune and Singh* [1986] indicate that the region of the northern Bengal fan has normal crustal thicknesses of 35 km with approximately 13 km of low-velocity sediments. In addition, paths that cross the central lowlands of Burma encounter north-south trending sedimentary basins that are greater than 10 kilometers in thickness [*Curray et al.*, 1979]. Thus, the thick sediments in the Burma lowlands and the northern Bengal Fan produce the effects of a low average velocity crust for seismic energy traveling from Burma to Shillong. Crustal average velocities in some of the surrounding regions are 6.0-6.2 km/s in the Panxi rift of southwest China [*Zong-Ji*, 1987] and 6.1 km/s in the Hindu Kush and Pamir regions [*Roecker*, 1982].

The Effects of Source

Another possible origin for error in crustal thickness and Pn velocity is the seismic source parameters. In the inversion for crustal thickness and upper mantle velocity, the source is assumed to be known. Most of the sources for the moderate-sized earthquakes were obtained from body wave modeling and body wave inversion [*Chen and Molnar*, 1983; *Baranowski et al.*, 1984; *Nelson et al.*, 1987; *Holt et al.*, 1989]. The fault parameters from body wave modeling

and inversion can often be in error by 10 - 20° in strike, dip and rake. The source time function can have errors as well. The inversion procedure was tested for variability of the inversion parameters as a function of change in source. The same test example used in the previous section was employed in the source test. Table 3 shows the inversion parameters (crustal thickness and Pn velocity) obtained when the source parameters strike, dip and rake were all varied by increments of 5° beyond the best fit source (strike = 169.5°, rake = -17°, dip = 59.3°). Note from Table 3 that even when strike, dip and rake were varied as much as 35° beyond the optimal solution, the values for crustal thickness and Pn velocity are relatively unchanged. Thus, uncertainties in fault orientation in the range of ±20° should not cause a significant problem in the estimation of crustal thickness and Pn velocity from the inversion of long period P_{nl} waveforms. Figure 5 shows the waveform fit for several inversion tests with different values of strike, dip, and rake. This Figure indicates that the waveform matches and inversion results are all comparable, even for source orientations in which the strike, dip, and rake are 35° beyond the optimal source. We feel, therefore, that uncertainties of ±20° in strike, dip, and rake for dip-slip mechanisms, similarly pose no serious problems in the estimation of crustal thickness and Pn velocity from the inversion of P_{nl} waveforms.

In summary, regional distance P_{nl} waveforms have a characteristic signature which is dependent on the source [*Engen and Helmberger*, 1980; *Wallace et al.*, 1981]. However, smaller changes in source, within the bounds of uncertainty from body wave modeling or inversion, have little influence on the P_{nl} waveform, and accurate estimates of crustal thickness and Pn velocity can usually be obtained. Once the source is known, the long-period waveform can be fit fairly well by finding the optimal thickness of the crustal waveguide. The accuracy of the estimation of crustal thickness is dependent on the reliability of the average crustal velocity as demonstrated in Figure 4. Fortunately, the estimation of Pn velocity as an inversion parameter is nearly independent of the average crustal velocity (see Figure 4).

Another source parameter, the time function, also has an influence on the P_{nl} waveform, and thus, will have an effect on the estimation of crustal thickness and Pn velocity. Another inversion test was performed by varying only the trapezoidal source time function. Table 4 shows the inversion parameter values of crustal thickness and Pn velocity obtained as a function of different time functions. In general, an increase in time function length has the effect of spreading the Pn pulse out. An increase in time function length by about 50% changed the results very little (crustal thickness = 36.7 km, Pn = 7.93 km/s) and increased the waveform misfit or error only slightly. Doubling the time function length increased the error to 0.12 and changed the estimate for crustal thickness from 38 km to 35.2 km (7% decrease in thickness). Increasing the time function length by a factor of 3 provided the highest misfit (e=.208) and decreased the estimate for crustal thickness to 32 km. Thus, significant changes in time function length (factor of 2 or more) produce changes in crustal thickness on the order of 10%. Time functions obtained from body wave modeling are rarely off by as much as a factor of 2. Therefore, smaller inaccuracies in time function length (order 50%) should pose no problem in the estimation of crustal thickness from the inversion of long-period P_{nl} waveforms.

Average Path Parameters

A total of 130 individual P_{nl} waveforms were inverted for crustal thickness and upper mantle Pn velocity. Table 5 lists the results for each inversion. Figures 6 and 7 show ten sample paths along with the inversion results for different sections of the area of study. Differences in wave character, thickness, and Pn velocity can be noted according to different tectonic or geographic sectors that the travel paths crossed.

The area of study was divided up into a set of regionalized blocks. The blocks were partitioned on the basis of topography and geology. The size of the blocks was limited primarily by the path coverage. Figure 8a shows the regionalized block model superimposed

on the smoothed topography, while Figure 8b indicates the path coverage through the blocks. The five disperse paths in Block 1 traverse some fairly high topography in western Pakistan but also cover some lower elevation regions of southern U.S.S.R. and eastern Iran. Block 2 covers portions of the Tien Shan and Hindu Kush - Pamir. Blocks 4, 6, and 9 encompass the western Karakoram, central Tibet, and eastern Tibet regions respectively. Blocks 5, 7 and 10 cover the transition zone from low to high topography, or the Himalayan mountain front. Portions of northern and eastern India are within blocks 3 and 8, and block 11 includes the Indoburma ranges and northern Burma Arc. The Yunnan Grabens and Panxi Rift regions [*Zong-Ji*, 1987] are within blocks 12 and 13, and block 14 includes southern China.

The average crustal thickness and upper mantle velocity were determined for each block by performing a regionalized inversion of all the crustal thickness and Pn velocity results. It is assumed that the average thickness and slowness (1/Pn) of a given path are the sum of the fraction of the travel path in a given block multiplied by the thickness or slowness of that path. This can be expressed as

$$X_j = \sum_{i=1}^{n} X_i \, d_{ij}/D_j \qquad (4)$$

where X_j is the average parameter for each path j (crustal thickness or slowness obtained from the inversion of P_{nl} waveform that traveled path j), X_i is the same parameter for block i, d_{ij} is the distance traveled in block i by ray path j, and D_j is the total ray path length. Solving for X_i (the crustal thickness and slowness of each block) involves a linear weighted least squares inversion. The data variance covariance matrix was assumed to be a diagonal matrix of the variance for the parameters (crustal thickness and 1/Pn velocity obtained from the inversion of the individual waveforms) from each path. The assumed average standard deviations for crustal thickness and Pn velocity were ±4 km and ±0.1 km/s (or ±0.0015 s/km for slowness), respectively. The source of errors or uncertainties in crustal thickness have

already been discussed, and uncertainties in Pn velocity are largely due to errors in origin time or event location.

Figure 8b shows that some blocks are sampled well with ray paths crossing in more than one direction, whereas other blocks such as 7 are poorly sampled. The values obtained for each block are dependent on the density of paths which cross the block. A block is better resolved if there are paths which cross it from many different directions. Due to the limited coverage of stations and sources, this is rarely the case. Each block, however, offers some independent information. The dependence of a parameter, determined for block A, on the parameter determined for block B, can be checked by an examination of the model correlation coefficient matrix. If the diagonal terms are much larger than the off-diagonal terms, then the blocks are behaving independently. If there are significant off-diagonal terms, then the blocks are coupled. Blocks can be coupled if the paths travel in only one direction and if the paths must always travel through one or more other blocks.

Inversion Results From Regionalized Block Model

The inversion results for the regionalized block model are shown in Figures 9a and 9b. The standard deviation is a formal estimate obtained from the model variance covariance matrix after performing the weighted least squares inversion. The results for crustal thickness are shown in Figure 9a. Blocks 2 and 4 which include the Hindu Kush, Pamir, and Karakoram regions, have crustal thicknesses which varies from 63-67 km. Many workers have noted a 65- to 75-km-thick crust in the Pamir-Karakorum and Hindu Kush regions [*Roecker*, 1982; *Brandon and Romanowicz*, 1986; and *Mishra*, 1981], and there appears to be considerable Moho topography between the Karakoram and Hindu Kush [*Mishra*, 1981; *Finetti et al.*, 1979] where the Moho upwarps to shallower levels of 58 km. Since long-period regional distance (P_{nl}) energy essentially "averages" the structure along the travel path, the thickness values obtained for blocks 2 and 4 (67, and 63 km) are a reasonable average for the region.

The 65- to 72-km-thick crust for blocks 6 and 9 (central and eastern Tibet) agrees with results from numerous authors [*Gupta and Narin*, 1967; *Bird and Toksöz*, 1977; *Chun and Yoshi*, 1977; *Patton*, 1980; *Chen and Molnar*, 1981]. Blocks 5, 7 and 10 include portions of the Himalayan mountain front, up to the edge of the Tibetan plateau and have thicknesses that range from 43-49 km. *Kono* [1974] examined the Bouguer gravity in eastern Nepal and found that the crust under the Himalayas is much thinner than would be expected if the range was in isostatic compensation (see also Lyon-Caen and Molnar, 1984; Karner and Watts, 1983 for more information on gravity in the Himalaya). The model of *Kono* [1974] suggests that a smooth inclined north dipping Moho exists beneath the Himalayas. The value of crustal thicknesses for blocks 5, 7, and 10 are perhaps representative of the average thickness along the inclined Moho beneath the high topography of the Himalayas. Wide angle reflection work by *Hirn et al.* [1984*b*], however, does not support a smooth incline of the lithosphere beneath the Himalayas but rather is consistent with a 45-55 km deep, relatively flat, Moho underneath the ranges. This Moho takes a 15 km step just to the north of the High Himalayas. The crustal thickness values for blocks 3 and 8 are in agreement with other thicknesses observed for northern India and Pakistan [*Brune and Singh*, 1986; *Zong-Ji*, 1987].

Block 11 corresponds to the location of the Indoburman ranges, the eastern extent of the collision and mountain-building zone. Thickness values in the region just outside of block 11 to the east are around 30 km. The northern Indoburma reach elevations as high as 3 km. However, given the low average smoothed topography in this region (see Figure 8, block 11), the thick crust for this block (48 km) may indicate that the Indoburman ranges are overcompensated. *Le Dain et al.* [1984] noted the large negative gravity anomaly over the Indoburman ranges [*Verma et al.*, 1976; *Warsi and Molnar*, 1977] and suggested that the negative buoyancy of the subducting slab may be a mechanism that keeps the region out of isostatic balance. Other estimates of crustal thickness beneath the Indoburman ranges, inferred from gravity data, range from 35-45 km [*Zhang and Zang*, 1986], with a 10-km-thick

root [*Zong-Ji*, 1986]. The results from this study indicate a root around 13-18 km deep beneath the Indoburman ranges. The thickness values for blocks 12, 13, and 14 are all in agreement with crustal thicknesses computed from gravity and seismics [*Zong-Ji*, 1986; *Kan et al.*, 1986].

Upper Mantle Pn Velocities

In the inversion for block slowness, the number of blocks was reduced to 10 because of solution instability that was not encountered in the crustal thickness inversion. The inversion results for upper mantle Pn velocities (or block slowness) are shown in Figure 9b. Pn velocities in northern India are around 8.0 km/s, slightly lower than that expected for old continental lithosphere. The most interesting result shown in Figure 9b is the increase in Pn velocity coincident with the thicker crust of the Tibetan Plateau, Karakoram and Pamir-Hindu Kush (Blocks 5, 7, 4, and 2, respectively]. These Pn velocities are not as high as those obtained by *Menke and Jacob* [1976], *Barazangi and Ni* [1982], or *Ni and Barazangi* [1983] and are slightly higher than the Pn velocities obtained by *Chen and Molnar* [1981].

Upper mantle velocities in block 9 are lower than most of the adjacent blocks. Block 9 includes regions such as the Yunnan Grabens and Panxi Rift zones where both active strike-slip and normal faulting are prevalent. Low upper mantle velocities of 7.6-7.9 km/s have also been detected beneath the Yunnan region [*Kan et al.*, 1986; *Zong-Ji*, 1987]. *Kan et al.* [1986] noted considerable differences in Pn velocity of 7.75 and 8.1 km/s between northwest-trending and northeast-trending lines, respectively, and attributed it to anisotropy. The high Pn velocity obtained for block 8 probably reflects the presence of Indian lithosphere beneath the Indoburman ranges. Indian lithosphere (block 8) is cold and has high velocities in contrast to the Asian lithosphere to the east.

We performed another inversion for block slowness using a new set of travel times obtained by putting all source depths at a common datum of 33 km, the procedure used by

Chen and Molnar [1981]. The results for the 10 blocks are in Table 6. The relative velocity differences between adjacent blocks are approximately the same as the first set of parameters (Figure 9*b*), but the absolute values are shifted 0.04-0.08 km/s faster.

The Independence of the Model Parameter Estimates

Most of the blocks are relatively independent with a few exceptions. Three pairs of blocks have small trades-offs: blocks 4 and 5, blocks 7 and 8, and blocks 9 and 10 (14 block model, Fig. 10a). Thus, an increase in crustal thickness in block 4 causes a decrease in the crustal thickness estimate for block 5 and vise versa. Block pairs (7,8) and (9,10) have similar trade-off characteristics. Blocks 1, 2, 3, 6, 8, 13, and 14 are the best resolved blocks and are the least sensitive to noisy observations. Blocks 7, 9, and 10 are the poorest resolved and hence the parameter estimates for these blocks are the most sensitive to errors in the observations.

Singular value decomposition was used in the inversion for model parameters of the regionalized block model. Thus, the relationship between the influence of observations on model parameter estimates can be directly determined. The largest single values are linked with eigenvectors that point in the directions of blocks 13, 8, 3, 14, 2, and 6. These blocks are thus the most stable. Singular value decomposition is most useful in the determination of poorly resolved parameters. The eigenvector associated with the smallest single value points in the direction of blocks 9 and 10. The large components of the corresponding data eigenvector will certainly point in the directions of the observations, or rays, which cross these blocks. Observations of particular importance can be checked for reliability. If a particular observation is found to have a strong influence on a model parameter, and in addition, has a high noise factor (high uncertainty), then the effect of that observation on the model parameter estimate can be minimized by assigning it a larger than normal variance. As mentioned earlier, the primary cause for model parameter instability comes from either a low

number of rays, or block trade-off. In the inversion for block slowness, the combining of blocks 3 and 5, 7 and 8, and 9 and 10 significantly reduced the potential for block trade-off caused by noisy observations.

Investigation of Upper Mantle Velocity Gradients

The Pn velocities beneath Tibet and the Hindu Kush have important implications for the evolution of the Tibetan plateau. That is, Pn velocities in stable continental regions, which have high lithospheric strength, are generally higher (8.2 km/s) than tectonically active continental regions (low lithospheric strength) such as the Basin and Range of North America (7.8 km/s).

The thickness of the lithosphere is perhaps a more important indicator of mechanical strength, and perhaps flexural rigidity. In tectonically active regions, the lithosphere is generally thin relative to the size of stable continental lithosphere. A seismological indicator of lithospheric thickness is the thickness of the upper mantle lid zone. This upper mantle lid is defined by a gradual increase in velocity (or a constant velocity) down to a low-velocity zone, which is thought to represent the top of the asthenosphere. Tectonically active areas have a thin upper mantle lid, such as the 30-km-thick lid in *Burdick and Helmberger's* [1978] T7 model for the western United States. On the other hand, stable continental regions have a much thicker lid, such as the 100-km-thick lid model of *Given and Helmberger* [1980] for northwestern Eurasia. The top of the low velocity zone for stable continental regions occurs at around 140-170 km depth. Figure 10 [*Walck*, 1984] shows some velocity profiles that have been obtained for different tectonic regions. The lid thickness along with Pn velocity are thought to increase with time since the last tectonothermal event. Thus, the determination of the presence or absence of an upper mantle lid, along with its thickness, can provide constraints on the lithospheric thickness and strength of a region. If the thickening in Tibet

occurred through diffuse deformation, then the lithospheric strength of Tibet should probably be less than the lithospheric strength in a comparable stable continental region, such as India.

As long as Pn velocities are above 8.0 km/s (for normal continental thickness), then the existence of a positive upper mantle velocity gradient indicates that an upper mantle lid is probably present (see Figure 10). In this study, evidence was found for a positive upper mantle velocity gradient beneath portions of Tibet, the Hindu Kush, and India. Impulsive Pn arrivals were observed at distances beyond 1000 km for many paths which crossed the Tibet, Hindu Kush, and eastern India regions. *Hill* [1971] showed that a positive velocity gradient can profoundly influence the headwave arrival, increasing its amplitude with distance with respect to the zero gradient. He also showed that a negative gradient gives rise to an amplitude reduction of the Pn arrival relative to the zero gradient model. Using long-period WWSSN seismograms from nuclear explosions, *Given and Helmberger* [1980] determined that impulsive first arrivals observed on seismograms for distances between 9-13° was evidence for a smooth positive upper mantle velocity gradient between the depths of 60-150 km in northwestern Eurasia (see Figure 10). *Langston* [1982] examined the effects of upper mantle velocity increase on regional distance short period seismograms. He showed that the observed difference between regional distance seismograms in the eastern and western U.S. can be explained by the presence of a positive upper mantle velocity gradient in the eastern U.S. In the eastern U.S. high-amplitude turning rays produce a large first arrival with respect to the Pg phase. These large amplitude first arrivals thus conceal the later Pg phase.

Figure 11 shows three pairs of long-period seismograms from paths that traverse Tibet, the Hindu Kush, and Eastern India. The synthetics were generated for a zero gradient model. Note that there is a relative enhancement of the observed Pn amplitude in comparison with the synthetic Pn arrival from the zero gradient model. For this reason, we refer to these as impulsive first arrivals. For the observations, the Pn/P_L ratio is large whereas for the synthetic the ratio is smaller. The later P_L phase thus appears suppressed on the observed

waveform relative to the synthetic P_L amplitude. The impulsive first arrival is evidence for turning energy in the upper mantle (or a positive upper mantle velocity gradient). The most probable reason that the synthetic Pn relative amplitude and waveform shape fails to match the observed Pn is that a layer over a half-space model (constant velocity upper mantle), rather than a gradient model, was used to construct the synthetics.

The effects of an upper mantle velocity increase on regional distance long-period P_{nl} waveforms was investigated in order to model the observed, impulsive Pn arrivals. In regions of particular tectonic interest, such as the Tibetan Plateau and the Hindu Kush, all waveforms recorded at distances beyond 900-1000 km were modeled to determine if a layer over a half-space or an increasing mantle velocity (gradient) produced better matches to the observed P_{nl} waveforms. Waveforms from paths that crossed thinner continental crust, such as east India/West Burma, and south China regions, were also examined for upper mantle velocity characteristics.

In order to simulate a mantle gradient, an additional layer was placed below the crustal layer. The value of the velocity increase in the mantle was changed to represent different mantle gradients. Six velocity models were used to model waveforms from paths that crossed Tibet and the Hindu Kush and five models for observations in the east India/west Burma and south China regions. The models included a 65 km thick crust for the Tibet and Hindu Kush regions, and a 37 km thick crust in the East India and south China regions. Three models with a 100 km thick lid had gradients of 0.1 km/s, 0.18 km/s, and 0.25 km/s per 100 km. Two models with a 75 km and 50 km thick lid had gradients of 0.13 km/s and 0.20 km/s per 100 km respectively. For reference, the 100 km thick lid of *Given and Helmberger's* [1980] K8 model for northwestern Eurasia had a positive P-wave gradient of around 0.17 km/s per 100 kilometers. The synthetics were calculated using the full Cagniard solution [see *Helmberger and Malone*, 1975].

Green's functions for vertical strike-slip, vertical dip slip, and 45° dip slip faults were produced at distances between 800 and 1500 km in increments of 100 km. Figure 12 shows the amplitude of Pn from the six velocity models versus distance for the three different fault models. The increase in Pn amplitude (produced by the turning mantle rays), relative to the Pn amplitude from the zero gradient model, is most pronounced for the vertical dip-slip Green's functions (VDS) and least pronounced for the strike-slip radiation pattern (VSS), consistent with the results of *Langston* [1982].

The Pn amplitude is greatest for the steeper gradients. A gradient within a thin upper mantle lid has a more pronounced effect on Pn amplitude at shorter distances than does an equivalent gradient within a thicker upper mantle lid. At greater distances, however, the amplitudes from the thick mantle lid model exceed those from the thinner lid model. With the step velocity model, the bottom of the "lid" is considered the depth to the refracting horizon, since, below this depth, no "turning rays" exist. Thus a 100-km-thick upper mantle lid, with a gradient of 0.2 km/s per 100 km, is approximated by a velocity increase of 0.2 km/s at a depth of 100 km below the base of the crustal waveguide.

A step velocity increase is a gross approximation of an upper mantle gradient. To test the approximate gradient model, we generated Green's functions for a smooth, more realistic gradient (15-layer model, 0.18 km/s per 100 km) and compared them with the approximate gradient model. The same fundamental rays were used in the generation of both sets of amplitudes. These results are shown in Figure 13. In all cases, except at short distances, the two layer model predicts higher Pn amplitudes than the smooth gradient model. The amplitudes are closest for the vertical strike-slip case. With generalized ray theory and multilayered structures, it is difficult to determine all the rays that are important. Thus, we determined synthetic amplitudes for a smooth gradient (0.18 km/s per 100 km; vertical strike-slip case only) using reflectivity with a center frequency of 0.125 Hz. The amplitudes calculated from reflectivity, at distances of 1200-1500 km, are comparable to the amplitudes

from the approximate gradient model (Figure 13). These results indicate that the approximate gradient model is sufficiently accurate to simulate the effects of a gradient on the Pn waveforms.

The P_L phase is a leaky mode [*Oliver and Major*, 1960]. The ray theory description of the P_L phase is the combination of reflected and mode-converted P-SV energy that is trapped within the crustal waveguide. The term "leaky mode" is used because the waves are only partly trapped within the waveguide and thus some energy is lost into the underlying media, although the amount of energy lost is probably small [*Oliver and Major*, 1960]. Figure 14 shows the P_L amplitude versus distance for the three radiation patterns. The P_L amplitude is independent of the mantle gradient; however, not all of the rays that contribute to P_L were included in the lid structure. *Shaw and Orcutt* [1984] showed that P_L amplitudes actually increase slightly with increasing lid thickness for a given distance, which they attributed to a tunneling phenomenon. Other experiments with a dipping Moho [*Wallace*, 1986*b*] show that the P_L waveform will be more spread out and slightly diminished in amplitude. The P_L phase examined in this study consists of the first few long-period peaks and troughs that occur within a window of 30-60 seconds after the Pn arrival. From Figure 14 it can be noted that the amplitude decay is dependent on the radiation pattern, where the percentage of energy loss with distance is most pronounced for the 45° dip-slip case.

Modeling the Observations for Upper Mantle Gradient

Since the Pn amplitude is strongly dependent on the upper mantle gradient and lid thickness, the Pn portion of the observations can be modeled to constrain gross upper mantle structure. Absolute Pn amplitude can be modeled but uncertainties in seismic moment can produce ambiguities in constraining an optimal mantle velocity gradient and lid thickness. Since P_L amplitude is affected only slightly by the mantle gradient, it can be used as a normalizing factor. Thus, the Pn/P_L ratio can be matched to constrain gross upper mantle

structure. Normalizing the maximum Pn amplitude by the maximum P_L amplitude involves the assumption that the energy loss from leaking mode propagation is small. Significant energy loss from leaking modes can give Pn/P_L ratios that are consistent with those from an upper mantle positive velocity gradient. That is, if significant energy loss of the P_L phase is occurring, then the observed Pn/P_L ratio (relative amplitude) will increase relative to the synthetic Pn/P_L ratio (obtained from the zero gradient model), in which no leaking mode energy loss is accounted for. Although leaking mode energy loss may effect the relative amplitude, it will not effect the Pn pulse shape. The Pn pulse shape is affected by turning mantle rays in the upper mantle gradient zone.

The Pn pulse shape was modeled in addition to calculating Pn/P_L ratios to constrain gross upper mantle characteristics. For example, impulsive Pn first arrivals are poorly matched when a layer over a half space model is used to construct the synthetics (see Figure 11), whereas a mantle gradient model gives a better fit. Figure 15 shows an example of an observed waveform with a travel path that crossed the Tibetan Plateau. The synthetic from a layer over a half-space model provides a poor fit to the observed impulsive first arrival. A gradient of 0.18 or 0.25 km/s per 100 km appears to provide the best fit.

The modeling of P_{nl} waveforms for upper mantle structure is very non-unique. It is impossible to constrain both upper mantle lid thickness and velocity gradient. A 100 km thick lid with a gradient of 0.1 km/s per 100 km provides roughly the same response as a lid of 75 km thickness and gradient of 0.13 km/s per 100 km, although the distance decay is different for the two models. The purpose of our investigation is thus not to construct detailed models, but rather to determine if the observations are consistent with the presence of a positive upper mantle velocity gradient. Some bounds can be placed on lid thickness, however, since the upper mantle gradient has realistic limits, even if well constrained values for both gradient and thickness cannot be unequivocally determined. Given and *Helmberger* [1980] modeled seismograms recorded at distances beyond 9° by using a northwestern Eurasian upper

mantle gradient of 0.17 km/s per 100 kilometers. A positive upper mantle gradient of 0.20 to 0.25 km/s per 100 km might thus be considered an upper limit.

Figure 16 shows examples of observed regional distance seismograms from the four regions examined: the Hindu Kush, the Tibetan Plateau, eastern India/western Burma, and southern China. We modeled six observations from the Hindu Kush region, seven from the Tibetan plateau, four from eastern India/western Burma, and five from southern China. Figure 17 shows the paths that the modeled observations traveled. Both Pn waveform shape and Pn/P_L amplitudes, as a function of the gradient model, were determined for each region. Tables 7-10 indicate the Pn relative amplitude modeling results for each region. In every region except south China, the preferred model was an upper mantle gradient of 0.25 km/s per 100 km with a lid thickness of 100 km. The 0.18 km/s and 0.25 km/s per 100 km models did not provide significantly different results for the Tibetan Plateau and east India/west Burma regions. For south China, the zero gradient model is clearly the preferred structure. Here, even a slight gradient produced a poor fit.

The most obvious evidence for an upper mantle gradient exists in the observations from the Hindu Kush. Here, even a gradient of 0.25 km/s per 100 km appears too small to describe the observed Pn/P_L amplitude ratios. Figure 18 shows the Pn/P_L ratio versus distance for the observed data and four different gradient models. The Pn/P_L amplitude ratio varies with each observation because the Pn amplitude is strongly dependent on the source orientation and distance. The Pn/P_L amplitude ratios for the 0.25 km/s model, although the best match, are still less than the observed. One possible explanation is that the upper mantle lid is thicker than 100 km in the Hindu Kush region. Travel time studies by *Kaila* [1981] indicate that the gradient is positive in this region to depths greater than 240 km. *Brandon and Romanowicz* [1986] noted very high Rayleigh wave phase velocities of 5 km/s in this region as well.

The upper mantle structure in the southern half of Tibet is the best constrained in the Plateau region. The structure in the central and northern sections of the Tibetan Plateau are

not as well constrained. There are two reasons for this: 1) only a few paths cross this region and no one path travels exclusively through the region; and 2) those paths which do cross the region are from sources that are primarily strike-slip. The increase in Pn amplitude as a function of mantle gradient is the least pronounced for the strike-slip radiation pattern (see Figure 12). Thus, it is much easier to resolve upper mantle gradients using dip-slip sources since Pn amplitudes from this type of radiation pattern are much more sensitive to changes in mantle gradient.

Therefore, on the basis of the travel path coverage in the northern sector of the Tibetan Plateau, it is not possible to further constrain the upper mantle structure in the region of the Chang Thang platform where *Barazangi and Ni* [1982] noted a region of poor Sn propagation. Figure 17 has a dashed line which indicates the northern limit to the resolvable structure in Tibet. The lack of seismic coverage prevents us from concluding anything about the upper mantle structure beyond this line. For the southern half of the Tibetan Plateau, however, P_{nl} wave observations recorded at distances beyond 1000 km are most favorably matched with a 100 km thick zone of increasing mantle velocity. A 100-km-thick lid provides a good match to the observed impulsive Pn arrivals and Pn/P_L ratios when gradients of .18 - 0.25 km/s per 100 km are used. A lid with only a 50 km thickness was found to be inadequate in the Tibetan Plateau region. Even with a gradient as high as 0.2 km/s, the waveform shape (impulsive first arrival) and Pn/P_L amplitudes were found to be poorly matched with the 50-km-thick lid. With a gradient of 0.1 km/s per 100 km, a lid thickness of 100 km provided, for the most part, unacceptable matches as well. This indicates that if the gradient is as low as 0.1 km/s per 100 km, then a lid with a thickness greater than 100 km would be required. The layer over a half-space model produced the largest misfit between observed and predicted Pn/P_L amplitudes in the Tibetan Plateau region.

The best upper mantle model for the eastern India/western Burma regions, like the Tibet region, is a 100-km-thick zone of increasing velocity with gradients between 0.2 and 0.25 km/s

per 100 km. Again, the layer over a half-space model yielded the largest misfit between observed and predicted Pn/P_L. Roughly 80% of the travel path length for those observations in eastern India/western Burma was in the high velocity upper mantle sector of blocks 6 and 8 (see Figure 9b). The other 20% of the length of the travel paths cross beneath the low velocity upper mantle region of block 13. Thus, the greater percentage of the length of the turning mantle rays for the east India/west Burma observations are traveling within the Indian lithosphere.

Summary of the Velocity Structure in Tibet, Hindu Kush, India and South China

In summary, information from P_{nl} waveforms indicates that the upper mantle velocity beneath the southern half of the Tibetan Plateau is around 8.25 km/s. Directly beneath the thick crust of the Tibetan Plateau, our preferred model has a velocity increase to a depth of 170 km. With this thickness, the velocity gradient is 0.18 km/s-0.25 km/s per 100 km. Lower gradients, or a lid as thin as 50 km, yielded poorer fits to both impulsive Pn arrivals and Pn/P_L ratios (see example in Figure 15).

The mantle velocity beneath the thick crust of the Hindu Kush-Pamir region is around 8.2 km/s. Here, observations may require a steeper gradient than 0.25 km/s per 100 km (given a lid thickness of 100 km) or, more likely, a gradient with a much thicker lid. As suggested by *Kaila* [1981], there is a mantle gradient in this region which increases to depths of at least 240 km.

The region of east India/west Burma has an upper mantle velocity of 8.0-8.2 km/s beneath a normal crustal thickness of 35-45 km. The four observations that traverse the eastern India/western Burma regions are consistent with a mantle structure that is apparently similar to the mantle beneath Tibet. The southern China region has upper mantle velocities around 8.0 km/s beneath a 35-km-thick crust. Here, the mantle lid is either very thin (less than 50 km) or absent (zero gradient). The relative amplitudes of the Pn arrivals in the south China

region are matched extremely well by the zero gradient model. The construction of synthetics allows no provision for energy loss of the P_L phase through leaking modes. The fact that the Pn/P_L ratio for the south China observations are matched so well with the zero gradient model is evidence that energy loss of the P_L phase through leaking modes is negligible in this region. Although it cannot be directly proven, we assume for this study that P_L energy loss in the Hindu Kush, Tibet, and east India regions is also negligible. The fact that PL amplitudes increase slightly with increasing lid thickness [*Shaw and Orcutt*, 1984] adds to our confidence that P_L loss is negligible.

Discussion and Conclusions

An important result from this study is the apparent 0.2 km/s increase in upper mantle velocity from beneath northern India to beneath the Tibetan Plateau. The double crustal thickness in Tibet will produce a pressure increase at the base of the mantle of 10-12 kbars. With no corresponding rise in temperature, this pressure increase will produce a maximum velocity increase of 0.18 km/s using a velocity function of 0.15 km/s $kbar^{-1}$ [*Black and Braile*, 1982]. A temperature increase of 200-300°C will produce a decrease in velocity by approximately the same amount [*Black and Braile*, 1982]. Thus, the increase in velocity can be explained by the increase in pressure alone. The constraint that there be little or no temperature increase from the base of the Indian crust to the base of the Tibetan crust suggests that the upper mantle beneath Tibet may be out of thermal equilibrium. That is, crustal thickening (depression of the Moho) or continental underthrusting has occurred at a sufficiently rapid rate that temperature equilibration has not yet occurred. This inference seems to suggest that the upper mantle beneath Tibet is as strong or stronger than the upper mantle of the Indian lithosphere.

The seismic evidence from this study is consistent with the idea that the Indian lithosphere has underthrust Asia but does not rule out the possibility of diffuse deformation. The bases

for our conclusion are: 1) high Pn velocities beneath the Tibetan Plateau relative to the velocity beneath the Indian Shield; 2) positive upper mantle gradients beneath the southern half of Tibet; and 3) given reasonable velocity gradients of 0.18-0.25 km/s per 100 km, an upper mantle lid exists with a favorable thickness that is around 100 km. The results from this study indicate that lower gradients might require a thicker lid. Figure 19 is a summary cartoon of our conclusions.

The observations from travel paths that sampled Indian lithosphere were best modeled with an upper mantle gradient structure that was similar to the preferred Tibetan upper mantle structure. Given the paucity of data, however, constraints on differences between the two regions are poor. Nevertheless, the seismic evidence is consistent with the presence of an upper mantle "lid" beneath both eastern India and southern Tibet. With Pn velocities as high as 8.25 km/s, the positive gradient guarantees that a lid is present beneath Tibet. These seismic data, however, do not exclude the possibility of uniform thickening. The expected seismic velocity, temperature, and lithospheric strength behavior for the various models of the development of the Plateau remain uncertain, and a range of models might fit the geophysical data base. *England and Houseman* [1986] argue that high Pn velocities alone do not necessarily demand the presence of underthrust Indian lithosphere beneath Tibet. If thermal equilibrium is not obtained (after or during crustal thickening) then the upper mantle velocities beneath Tibet could still be high.

The results from this study are not sufficient to constrain the velocity and structure of the northern sector of the Tibetan Plateau. Therefore, the existence of underthrust Indian lithosphere beyond central Tibet cannot be constrained. If underthrusting beyond central Tibet is to be proposed, then the observations of a region of high Sn attenuation in the Chang Thang platform [*Barazangi and Ni*, 1982] and the positive S-P residuals in central Tibet [*Molnar and Chen*, 1984] must be explained.

The positive S-P residuals observed by *Molnar and Chen* [1984] are not necessarily inconsistent with the presence of underthrust Indian lithosphere. A 100-km-thick high velocity Indian lithospheric plate beneath Tibet would have a minor contribution to the observed S-P residuals. If the Asian mantle below 170 km is anomalously slow, then positive S-P residuals should still be observed, even with the presence of a high velocity lithosphere beneath Tibet. Even if the S-P residuals in central Tibet do indeed indicate that the upper 100 km of the mantle is slow relative to the upper mantle to the south (Himalayas), the underthrusting model can still be reconciled with the results of *Molnar and Chen* [1984]. If Indian lithosphere began to underthrust Asia about 25 million years ago by the mechanism proposed by *Bird* [1978], then with a rate of northward movement of 2-2.5 cm/yr [*Molnar*, 1984], the leading edge of the Indian lithosphere would be situated about 500-625 km north of the main boundary fault. This would correspond to the sector just to the south of where large S-P residuals have been observed [*Molnar and Chen*, 1984], and where high Sn attenuation has been noted [*Barazangi and Ni*, 1984]. Given the uncertainty of the rate of underthrusting and time of the initiation of intracontinental subduction [*Bird*, 1978], underthrusting could have proceeded further north if heating of the Indian lithosphere diminished the effect of a "lid" in the central and northern plateau. With India's present rate of northward movement of 5 cm/yr [*Minster and Jordan*, 1978], roughly half of India's northward movement is unaccounted for (assuming a rate of underthrusting of 2.0-2.5 cm/yr; Molnar, 1984]. The remaining amount of northward movement, therefore, is almost certainly taken up by shortening within Asia by the mechanism of crustal extrusion and thickening [*Molnar and Quidong*, 1984; *Tapponnier et al.*, 1986].

If underthrusting has not proceeded any further than 625 km north of the main boundary, it then becomes more difficult to explain the high topography and presumably thick crust in northern Tibet. The structure of central and northern Tibet thus needs to be better resolved before this problem can be unequivocally resolved.

Major strike-slip features in Tibet and China may have been developed in the early part of the continental collision as suggested by *Tapponnier et al.* [1986]. During this first phase of collision, northward movement of India was accommodated by shortening within Asia by mechanisms of both crustal thickening and strike-slip crustal extrusion [*Tapponnier et al.*, 1986]. This stage of the early collision was probably analogous to the present-day collision between Arabia and Eurasia [*Ni and Barazangi*, 1986]. Here mountain building, crustal thickening, and strike-slip movement on large features such as the northern Anatolian fault are observed. After considerable convergence and shortening within Asia, lithospheric delamination perhaps allowed the initiation of underthrusting of the Indian lithosphere [*Bird*, 1978]. The amount of lithospheric underthrusting is unresolved. The seismic evidence in this study, however, is most reasonably explained by the presence of Indian lithosphere below at least the southern half of Tibet. We feel that the present geophysical information is insufficient to determine if underthrusting has proceeded north of central Tibet. Perhaps due to strong coupling at the down-bending portion of the Indian lithosphere (along the seismically active portion of the Main Boundary Thrust), some component of the northward movement of India is still accommodated by shortening within Asia. This shortening is evidenced by the active strike-slip movement in Tibet, China, and Mongolia, and by the thrusting observed in the Tien Shan [*Molnar and Tapponnier*, 1975; *Tapponnier and Molnar*, 1976, 1977, 1979].

Acknowledgments

Partial funding for this work was provided by DARPA/AFGL grant F19628-87-K-0046. Two anonymous reviewers made suggestions which substantially improved the manuscript. We would like to thank Randy Richardson and Clem Chase for providing constructive comments. Norm Meader was most helpful in the typing of the manuscript.

References

Argand, E., La tecctonique de l'Asie, International Geological Congress 13th, Brussels, 1922 Reports, vol. 1, 170-372.

Baranowski, J., J. Armbruster, L. Seeber, and P. Molnar, Focal depths and fault plane solutions of earthquakes and active tectonics of the Himalaya, *J. Geophys. Res.*, *89*, 6918-6928.

Barazangi, M., and J. Ni, Velocities and propagation characteristics of Pn and Sn beneath the Himalayan arc and Tibetan Plateau: Possible evidence for underthrusting of Indian continental lithosphere beneath Tibet, *Geology*, *10*, 179-185, 1982.

Bhattacharya, S.N., Seismic surface-wave dispersion and crust-mantle structure of Indian Peninsula, *Indian J. Met. Geophys.*, *22*, 179-186, 1971.

Bird, P., Initiation of Intra-continental subduction in the Himalaya, *J. Geophys. Res.*, *83*, 4975-4987, 1978.

Bird, P., and M.N. Toksöz, Strong attenuation of Rayleigh waves in Tibet, *Nature*, *266*, 161-163, 1977.

Black, P.R., and L.W. Braile, Pn velocity and cooling of the continental lithosphere, *J. Geophys. Res.*, *87*,10557-10568, 1982.

Brandon, C., and B. Romanowicz, A "No-Lid" zone in the central Chang-Thang platform of Tibet: evidence from pure path phase velocity measurements of long-period Rayleigh waves, *J. Geophys. Res.*, *91*, 6547-6564, 1986.

Brune, J.N., and D.D. Singh, Continent-like crustal thickness beneath the Bay of Bengal sediments, *Bull. Seis. Soc. Am.*, *76*, 191-203, 1986.

Burdick, L.J., and D.V. Helmberger, The upper mantle P-velocity structure of the western United States, *J. Geophys. Res.*, *83*, 1699-1712, 1978.

Chen, W.P., and P. Molnar, Short-period Rayleigh wave dispersion across the Tibetan Plateau, *Bull. Seis. Soc. Am.*, *65*, 1051-1057, 1975.

Chen, W.P., and P. Molnar, Constraints on the seismic wave velocity structure beneath the Tibetan Plateau and their tectonic implications, *J. Geophys. Res.*, *86*, 5937-5962, 1981.

Chun, K.Y., and T. Yoshi, Crustal structure of the Tibetan Plateau: A surface-wave analysis, *Bull Seis. Soc. Am.*, *67*, 735-750, 1977.

Curray, J.R., D.G. Moore, L.A. Lawver, F.J. Emmel, R.W. Raitt, M. Henry, and R. Kieckhefer, Tectonics of the Andaman Sea and Burma: in Watkins, J.S., L. Montadert, and P. Dickerson, *eds.*, Geological and geophysical investigations of continental margins, *Am. Assoc. Petrol. Geol. Memoir 29*, 189-198, 1979.

Dewey, J., and K. Burke, Tebetan, Variscan and Precambrian basement reactivation: Products of continental collision, *J. Geology*, *81*, 683-692, 1973.

England, P., and G. Houseman, Finite strain calculations of continental deformation 2. Comparison with the India-Asia collision zone, *J. Geophys. Res.*, *91*, 3664-3676, 1986.

Finetti, I., F. Giorgetti, and G. Poretti, The Pakistani segment of the DSS profile Nanga Parbat-Karakul, *Boll. Geof. Teor. App.*, *21*, 159-171, 1979.

Fukao, Y., Upper mantle P structure on the ocean side of the Japan-Kurile arc, *J. Geophys. Res.*, *50*, 621-642, 1977.

Given, J.W., and D.V. Helmberger, Upper mantle structure of north-western Eurasia, *J. Geophys. Res.*, *85*, 7183-7194, 1980.

Guangxun, L., L. Fangquan, L. Guirong, Active tectonics and state of stress in seismic region of north-west Yunnan Province, China, *Seismology and Geology*, *8*, 12-14, 1986.

Gupta, H.K., and H. Narain, Crustal structure in the Himalayan and Tibet Plateau region from surface-wave dispersion, *Bull. Seis. Soc. Am.*, *57*, 235-248.

Helmberger, D.V., and G.R. Engen, Modeling the long-period body waves from shallow earthquakes at regional distances, *Bull. Seis. Soc. Am.*, *70*, 1699-1714, 1980.

Helmberger, D.V., and S.D. Malone, Modeling local earthquakes as dislocations in a layered half space *J. Geophys. Res.*, *80*, 4881-4888, 1975.

Hill, D.P., Velocity gradients and anelasticity for crustal body wave amplitudes, *J. Geophys. Res., 76*, 3309-3325, 1971.

Hirn, A.G., G. Jobert, G. Wittlinger, Z. Xu, and G. Yuan, Main features of the upper lithosphere in the unit between the high Himalayas and the Yarlung Tsangbo Jiang suture, *Ann. Geophys., 2*, 113-118, 1984*a*.

Hirn, A., J.C. Lepine, G. Jobert, M. Sapin, G. Wittlinger, X.Z. Xin, G. E. Yuan, W.X. Jing, T.J. Wen, X.S. Bai, M.R. Pandey and J.M. Tater, Crustal structure and variability of the Himalayan border of Tibet, *Nature, 307*, 23-25, 1984*b*.

Holt, W.E., T.C. Wallace, J.F. Ni, and M. Guzzman-Speziale, The active tectonics in the eastern Himalayan syntaxis and surrounding regions, in Prep., 1989.

Jackson, J., and D. McKenzie, Active tectonics of the Alpine-Himalayan belt between western Turkey and Pakistan, *Geophys. J. R. Astr. Soc., 77*, 185-264, 1984.

Jobert, N., B. Journet, G. Jobert, A. Hirn, and S. Ke Zhong, Deep structure of southern Tibet inferred form the dispersion of Rayleigh waves through a long-period seismic newark, *Nature, 313*, 386-388, 1985.

Kaila, K.L., Structure and seismotectonics of the Himalaya-Pamir Hindu Kush region and the Indian plate boundary, in *Zagros-Hindu Kush-Himalaya Geodynamid Evolution*, edited by H.K. Gupta, F.M. Delany, pp. 272-293, 1981.

Kaila, K.L., P.R. Reddy, and H. Narain, Crustal structure in the Himalayan foothills area of North India, from P-wave data of shallow earthquakes, *Bull. Seism. Soc. Am., 58*, 597-612, 1968.

Karner, G.D., and A.B. Watts, Gravity anomalies and flexure of the lithosphere at mountain ranges, *J. Geophys. Res., 88*, 10,449-10,477, 1983.

Kono, M., Gravity anomalies in east Nepal and their implications to the crustal structure of the Himalayas, *Geophys. J., 17*, 369-403, 1974.

Langston, C.A., Aspects of Pn and Pg propagation at regional distances, *Bull. Seis. Soc. Am.*, *72*, 457-471, 1982.

LeDain, A.Y., P. Tapponnier, and P. Molnar, Active faulting and Tectonics of Burma and surrounding regions, *J. Geophys. Res.*, *89*, 453-472, 1984.

Lyon-Caen, H. Comparison of the upper mantle shear wave velocity structure of the Indian Shield and the Tibetan Plateau and tectonic implications, *Geophys. J. R. Astr. Soc.*, *86*, 727-749, 1986.

Lyon-Caen, H. and Molnar P., Constraints on the structure of the Himalaya from an analysis of gravity anomalies and a Flexural model of the lithosphere, *J. Geophys. Res.*, *88*, 8171-8191, 1983.

Ma, X., Lithospheric dynamics of China, *Episodes*, *11*, 84-90, 1988.

McConnell, R.K. and G.H. McTaggart-Cowan, Crustal seismic refraction profiles, a compilation, *Scientific report*, *8*, Univ. of Toronto, 1963.

Menke, W.H., and K.H. Jacob, Seismicity Patterns in Pakistan and northwestern India associated with continental collision, *Bull. Seis. Soc. Am.*, *66*, 1695-1711, 1976.

Minster, B., and T. Jordan, The present-day plate motions, *J. Geophys. Res.*, *83*, 5331-5354, 1978.

Mishra, D.C., Crustal structure and dynamics under Himalaya and Pamir ranges, *Earth and Planetary Science Letters*, *57*, 415- 420, 1982.

Molnar, P., Structure and tectonics of the Himalaya: Constraints and implications of geophysical data, *Annu. Rev. Earth Planet. Sci.*, *12*, 489-518, 1984.

Molnar, P., and Q. Deng, Faulting associated with large earthquakes and the average rate of deformation in central and eastern Asia, *J. Geophys. Res.*, *89*, 6203-6228, 1984.

Molnar, P., and W.P. Chen, focal depths and fault plane solutions of earthquakes under the Tibetan plateau, *J. Geophys. Res.*, *88*, 1180-1196, 1983.

Molnar, P., and W.P. Chen, S-P wave travel time residuals and lateral inhomogeneity in the mantle beneath Tibet and the Himalaya, *J. Geophys. Res., 89*, 6911-6917, 1984.

Molnar, P., and P. Tapponier, Cenozoic tectonics of Asia: Effects of a continental collision, *Science, 189*, 419-425, 1975.

Nelson, M.R., R. McCaffrey, and P. Molnar, Source parameters for 11 earthquakes in the Tien Shan, Central Asia, determined by P and SH waveform inversion, *J. Geophys. Res., 92*, 12629-12648, 1987.

Ni, J., and M. Barazangi, High frequency seismic wave propagation beneath the Indian Shield, Himalayan Aarc, Tibetan Plateau and surrounding regions: High uppermost mantle velocities and efficient Sn propagation beneath Tibet, Geophys. *J. R. astr. Soc., 72*, 665-689, 1983.

Ni, J., and M. Barazangi, Seismotectonics of the Himalayan Collision zone: Geometry of the underthrusting Indian plate beneath the Himalaya, *J. Geophys. Res., 89*, 1147-1163, 1984.

Ni, J., and M. Barazangi, Seismotectonics of the Zagros continental collision zone and a comparison with the Himalayas, *J. Geophys. Res., 91*, 8205-8218, 1986.

Oliver, J., and Major, Leaking Modes and the Pl phase, *Bull. Seis. Soc. Amer., 50*, 165-180, 1960.

Patton, H., Crust and upper mantle structure of the Eurasian continent from the phase velocity measurements and Q of surface waves, *Rev. Geophys., 18*, 605-625, 1980.

Pines, I., T.L. Teng, R. Rosenthal, and S. Alexander, A surface wave dispersion study of the crustal and upper mantle structure of China, *J. Geophys. Res., 85*, 3829-3844, 1980.

Powell, C., and P. Conaghan, Plate tectonics and the Himalayas, *Earth Planet. Sci. Lett., 20*, 1-12, 1973.

Powell, C., and P. Conaghan, Tectonic models of the Tibetan Plateau, *Geology, 3*, 727-731, 1975.

Roecker, S.W., Velocity structure of the Pamir-Hindu Kush region: possible evidence of subducted crust, *J. Geophys. Res.*, *87*, 945-959, 1982.

Romanowicz, B.A., Constraints on the structure of the Tibet Plateau from pure path phase velocities of Love and Rayleigh waves, *J. Geophys. Res.*, *87*, 6865-6883, 1982.

Shaw, P., and J. Orcutt, Propagation of P_L and implications for the structure of Tibet, *J. Geophys. Res.*, *89*, 3135-3152, 1984.

Tapponnier, P., G. Peltzer, and R. Armijo, On the Mechanics of the Collision between India and Asia, *in* Coward M.P., and A.C. Ries, Collisional Tectonics, Geological Society Special Publication no. 19, 115-157, 1986.

Tapponnier, P, and P. Molnar, Slip-Line field theory and large scale continental tectonics *Nature*, *264*, 319-324, 1976.

Tapponnier, P., and P. Molnar, Active faulting and tectonics in China, *J. Geophys. Res.*, *82*, 2905-2930, 1977.

Tapponnier, P., and P. Molnar, Active faulting and Cenozoic tectonics of the Tien Shan, Mongolia, and Baykal regions, *J. Geophys. Res.*, *84*, 3425-3459, 1979.

Toksöz, M.N., and P. Bird, Formation and evolution of marginal basins and continental plateaus, in *Island Arc Basins*, *American Geophysical Union Maurice Ewing Series*, edited by C. Powell and P. Conaghan, pp. 379-393, AGU, Washington, D.C., 1977.

Verma, R.K., M. Mukhopadhyay, and M.S. Ahluwalia, Seismicity, gravity and tectonics of northeast India and northern Burma, *Bull. Seis. Soc. Amer.*, *66*, 1683-1694, 1976.

Walck, M.C., Teleseismic array analysis of upper mantle compressional velocity structure, Ph.D. thesis, California Institute of Technology, Pasadena, Calif., 1984.

Wallace, T.C., Inversion of long-period regional body waves for crustal structure, *Geophys. Res. Lett.*, *13*, 749-752, 1986a.

Wallace, T.C., Some useful approximations to generalized ray theory for regional distance seismograms, *Geophys. J. R. Astr. Soc.*, *85*, 349-363, 1986b.

Wallace, T.C., D.V. Helmberger, and G.R. Mellman, A technique for the inversion of regional data in source parameter studies, *J. Geophys. Res.*, *86*, 1679-1685, 1981.

Warsi, W.E.K., and P. Molnar, Gravity anomalies and plate tectonics in the Himalaya, Ecologie et geologie de l'Himalaya, Colloques internationaux du C.N.R.S., 268, 1977.

Zhang, J., and S. Zang, Characteristics of earthquake distribution and the mechanism of earthquakes in the boundary area between Burma, India, and China, *Acta Seismological sinica*, *8*, 1986.

Zong-Ji, C., Geodynamics and tectonic evolution of the Panxi rift, *Tectonophysics*, *133*, 287-304, 1987.

Figure Captions

Figure 1: Map of study area showing regions where efficient propagation of Sn, large S-P residuals, etc. have been found. Summary of mantle velocities (and average crustal thickness) beneath India and Tibet. Pn and Sn values from *Chen and Molnar* [1981] and *Barazangi and Ni* [1982] (Tibet), *Ni and Barazangi* [1983] (India and Tibet), *Kaila et al.* [1986] (northern India). Mantle shear wave velocities are from *Romanowicz* [1982] (northern Tibet), *Brandon and Romanowicz* [1986] (central Tibet), *Jobert et al.* [1985] (southern Tibet), and *Lyon-Caen* [1986] (India and Tibet).

Figure 2: 130 ray paths superimposed on the smoothed topography of the region.

Figure 3: Example inversion. Waveform match is shown for each iteration. The graph to the right indicates the error versus parameter thickness for the start and four following iterations. Note reduction of error from 0.97-0.107 in four iterations. Observed waveform = top, synthetic = bottom line. Graph is not intended to show solution minimum, but error for each iteration in inversion.

Figure 4: Crustal thickness values obtained in the inversion of single Pnl waveform as a function of different average crustal velocities. The error for each inversion is indicated as a vertical bar. Pn velocity obtained from inversion vs. average crustal velocity is also shown. The Pn velocity (obtained from inversion) is relatively independent of the average crustal velocity.

Figure 5: Final waveform match for four different inversion cases in which different source orientations are used. The strike, dip, and rake where varied +5°, +15°, +25°, and +35°

beyond the optimal source orientation. Cth = crustal thickness (inversion parameter), Pn = Moho head wave velocity (obtained from inversion of travel time). Observed waveform = top, synthetic waveform = bottom.

Figure 6: Ten sample paths superimposed on the smoothed topography. The path numbers do not correspond to the path numbers in Table 5, but correspond to path locations of observations in Figure 8.

Figure 7: Final waveform match from ten separate inversions of regional Pnl waveforms that traveled the ten different paths indicated in Figure 7. Path number is indicated next to waveform. Observed waveform = top, synthetic = bottom. Note that paths 2, 5, and 6 show impulsive second peaks relative to the synthetic (evidence of positive upper mantle velocity gradients).

Figure 8a: Regionalized block model superimposed on smoothed topography.

Figure 9b: Regionalized block model with path coverage.

Figure 9a: Model parameter estimates (crustal thickness for the 14 blocks. Standard deviation is a formal estimate from model variance-covariance matrix. Block numbers are also shown.

Figure 9b: Model parameter estimates (Pn velocity) for the 14 blocks. Standard deviation is a formal estimate from model variance-covariance matrix. Block numbers are also shown.

Figure 10: P-wave velocity structure for four different tectonic environments. T7 is for tectonically active continents [*Burdick and Helmberger*, 1978], ARC-TR is for island arcs

[*Fukao*, 1977], K8 is for stable shields [*Given and Helmberger*, 1980], and TGCA is for an oceanic spreading center [*Walck*, 1984]. After *Walck* [1984].

Figure 11: Three examples of final waveform match after inversion. Event 21 sampled east India/west Burma, event 27 sampled the Tibetan Plateau, and event 62 sampled the Pamir-Hindu Kush region. All three observations show strongly impulsive first arrivals (top) relative to the synthetic (bottom). This is evidence that the long-period energy is sampling positive upper mantle velocity gradients along these paths.

Figure 12: Maximum synthetic Pn amplitude versus distance for various gradient models. The zero gradient model (lhsp) is the lowest amplitude arrival (bottom curve). VSS = vertical strike-slip Green's function, VDS = vertical dip slip Green's function, 45D = 45° dip-slip Green's function. The vertical dip-slip Green's function is most sensitive to changes in upper-mantle gradient and lid thickness, and the vertical strike-slip is least sensitive to these changes.

Figure 13: Pn amplitude vs. distance for approximate gradient model and smooth gradient (15 layers) model for Green's functions VSS, VDS and 45D. VSS, Pn amplitudes for smooth gradient calculated using reflectivity is also shown.

Figure 14: Maximum synthetic P_L amplitude versus distance for various gradient models. The P_L amplitude is invariant to changes in upper mantle structure. The 45D dip-slip Green's function shows the greatest amplitude decrease with distance.

Figure 15: Waveform characteristics for event 27 recorded at NDI. The long-period energy sampled the Tibetan plateau. Observed waveform is on top. The zero gradient model = lhsp.

Note the impulsive first arrival is better matched by models with upper mantle lids of 100 km thickness and gradients of 0.18-0.25 km/s per 100 km. A thin lid (50 km) provides a poor match to the impulsive nature of the first arrival.

Figure 16: Four different waveforms (observed = top) for the four regions, (a) Hindu Kush-Pamir, (b) Tibet, (c) east India/west Burma, and (d) south China, examined for upper mantle structure. lhsp = the zero gradient model. Pn/P_L = ratio between maximum Pn amplitude and maximum P_L amplitude. The synthetics for various gradient models are shown below. Impulsive first arrival amplitudes, and relative amplitudes of the three waveforms that sampled the Hindu Kush, Tibet and east India regions are better matched with the 100 km thick lid models (gradient = 0.18-0.25 km/s per 100 km). South China (Event 15, HKC) is optimally matched by the zero gradient model.

Figure 17: The 24 paths, the waveforms from which, were modeled for upper mantle structure. The thick dashed line marks the northern limit of the resolvable upper mantle structure in the Hindu Kush - Pamir and Tibet regions.

Figure 18: Pn/P_L ratio versus distance for six observed waveforms which traversed the Hindu Kush-Pamir regions. The observed Pn/P_L ratio is the top line. Pn/P_L ratio for four gradient models is also shown. The ratio changes for each event because Pn amplitudes are sensitive to fault radiation pattern and distance from source. The largest misfit between observed and predicted relative amplitude occurs for the zero gradient model (lhsp - bottom curve). The gradient models all have 100-km-thick lids, and the steepest gradient (0.25 km/s per 100 km) provides the closest match to the relative amplitudes (rms error = 3.0). These results suggest that either a steeper gradient, or a thicker lid is required to completely match the relative Pn amplitude.

Figure 19: Cartoon showing Pn velocities and P-wave mantle velocities along with tectonic interpretation of an underthrust continental lithology. The structure beyond central Tibet is uncertain.

TABLE 1. List of the 78 Sources Recorded by Various WWSSN Stations to Provide 130 Regional Distance Paths in Tibet, Hindu Kush, Southwest China, Burma, and India

Event	Date	Origin Time	Lat (°N)	Long (°E)	Fault Orientation Strike	Rake	Dip	Time Function RT	TOP	FT	Assumed Depth (km)	ISC	PDE	Ref
1	06/24/83	07:18:22.3	21.77	103.31	47.6	45.7	58.7	1.0	2.0	1.0	10	18		1
2	02/05/66	15:12:33.0	26.20	103.10	169.6	-17.0	59.3	0.4	1.0	0.4	4	32		1
3	04/28/71	15:32:01.2	22.93	101.03	243.4	3.5	79.0	0.4	1.0	0.4	6	11		1
4	02/13/66	10:44:38.0	26.10	103.20	149.0	-70.0	67.0	0.4	1.0	0.4	4	6		1
5	11/28/84	10:29:21.0	26.70	97.08	248.6	12.8	53.8	0.4	3.0	0.4	6	4		1
6	12/21/79	06:31:52.0	27.10	97.04	116.7	96.9	48.5	0.4	2.2	0.4	10	32		1
7	02/06/70	22:10:42.4	23.10	100.78	241.5	-51.1	65.2	0.4	2.0	0.4	6	30		1
8	04/23/84	22:29:57.3	22.06	99.18	84.0	14.0	69.0	1.0	1.0	1.0	10	8		1
9	02/02/80	12:29:15.3	27.83	101.24	212.0	20.0	70.0	1.0	1.0	1.0	10	22		1
10	09/19/81	06:50:56.3	23.01	101.35	65.0	4.7	82.8	0.4	1.0	0.4	4	8		1
11	04/18/85	05:52:52.8	25.93	102.87	292.0	184.0	82.0	1.0	1.0	1.0	10	5		1
12	03/15/79	12:52:25.8	23.18	101.10	25.7	6.8	89.8	0.4	3.0	0.4	4	6		1
13	08/14/81	06:09:34.4	25.15	97.96	178.7	193.3	74.3	0.2	1.0	0.2	10	38		1
14	08/16/81	18:55:42.2	25.52	96.63	2.5	178.9	85.0	0.2	1.0	0.2	10	38		1
15	01/15/75	11:34:41.3	29.41	101.78	165.0	-75.0	45.3	0.6	1.6	0.6	10	29		1
16	09/28/66	14:00:21.0	27.53	100.08	-29.0	-86.2	43.0	0.6	2.2	0.6	10	12		1
17	08/30/67	04:22:05.1	31.61	100.26	238.3	-82.2	40.4	0.6	2.0	0.6	10	24		1
18	08/30/67	11:08:50.0	31.57	100.31	279.9	-54.8	55.6	0.6	1.4	0.6	8	35		1
19	02/07/73	16:06:25.8	31.50	100.33	225.6	-86.7	51.8	0.4	1.8	0.4	8	35		1
20	02/19/70	07:10:01.5	27.40	93.96	105.7	114.0	81.7	0.2	2.0	0.2	8	12		1
21	09/26/66	05:10:56.2	27.49	92.61	92.1	102.9	72.4	0.2	1.0	0.2	12	20		1
22	06/03/75	03:23:34.6	26.59	96.95	125.9	91.9	55.3	0.4	1.0	0.4	10	10		1
23	06/03/75	00:37:42.5	26.59	96.91	130.2	81.7	65.5	0.2	1.0	0.2	8	43		1
24	11/06/76	18:04:05.5	27.60	101.00	214.0	14.0	81.0	0.6	2.0	0.6	6	5		1
25	08/01/85	12:13:46.2	29.18	95.18	290.3	86.5	87.3	0.4	1.0	0.4	38	45		1
26	03/29/79	07:07:22.0	32.44	97.26	271.8	-9.7	83.1	0.2	1.6	0.2	10	45		1
27	06/09/81	22:08:18.6	34.51	91.42	171.0	187.9	69.8	0.4	1.4	0.4	10	10		1
28	10/21/64	23:09:19.0	28.04	93.75	92.7	100.5	77.2	0.6	2.6	0.6	14	37		1
29	12/13/76	06:36:55.9	27.33	101.01	209.3	4.5	76.1	0.2	1.4	0.2	2	2		1
30	09/01/64	13:22:37.3	27.12	92.26	79.9	89.8	71.0	0.2	1.2	0.2	6	33		1
31	03/14/67	06:58:04.6	28.40	94.30	74.2	87.5	90.0	0.2	1.0	0.2	15	20		1
32	05/29/76	19:36:52.7	24.54	98.93	50.0	-31.0	77.0	0.2	1.0	0.2	2	2		1
33	07/03/76	16:33:23.8	24.19	98.67	252.2	114.8	85.0	0.2	1.4	0.2	2	33		1
34	05/31/76	18:35:05.0	24.29	98.68	244.7	6.7	63.9	0.2	1.4	0.2	5	20		1
35	05/31/76	05:08:30.5	24.34	98.64	68.9	0.3	87.6	0.4	2.0	0.4	3	25		1
36	05/30/71	15:44:19.6	25.30	96.44	25.5	178.4	87.8	0.4	1.2	0.4	6	40		1
37	06/09/76	00:20:37.9	24.89	98.75	179.3	205.2	82.9	0.6	1.6	0.6	2	13		1
38	07/21/76	15:10:45.1	24.78	98.65	64.4	-7.2	88.2	0.4	2.6	0.4	6	4		1
39	05/31/71	05:13:58.6	25.19	96.51	193.0	173.9	90.0	0.2	1.0	0.2	10	22		1
40	09/14/71	03:11:06.3	22.97	100.71	191.1	-185.6	82.8	0.4	1.2	0.4	10	42		1
41	05/30/76	04:18:40.7	24.42	98.81	241.9	12.5	68.4	0.2	1.0	0.2	10	1		1
42	04/08/72	09:33:40.3	29.52	101.84	186.0	-81.4	46.3	0.2	1.0	0.2	10	40		1

(Continued)

TABLE 1 - Continued

Event	Date	Origin Time	Lat (°N)	Long (°E)	Fault Orientation Strike	Rake	Dip	Time Function RT	TOP	FT	Assumed Depth (km)	ISC	PDE	Ref
43	07/03/82	08:13:32.7	26.57	100.04	199.0	-90.0	49.9	0.2	1.0	0.2	10	12		1
44	10/23/81	03:44:44.5	29.89	94.93	-122.0	-172.0	17.4	0.2	1.0	0.2	10	0		1
45	05/22/71	20:03:31.9	32.36	92.11	250.8	-7.9	84.3	0.4	2.0	0.4	7	29		1
46	08/15/67	09:21:03.3	31.05	93.56	196.9	-38.3	74.9	0.2	1.0	0.2	10	36		1
47	05/05/75	05:18:46.3	33.13	92.84	256.3	-5.0	80.6	0.2	1.6	0.2	6	8		1
48	07/22/72	16:41:02.1	31.38	91.41	245.7	-1.8	59.4	0.2	1.6	0.2	7	17		1
49	04/03/71	04:49:03.1	32.16	94.99	181.3	-180.9	80.4	0.4	1.6	0.4	8	27		1
50	06/15/82	23:24:28.8	31.85	99.92	278.5	0.7	68.5	0.4	1.6	0.4	7	10		1
51	07/19/75	06:10:53.9	31.95	78.59	47.0	-56.0	51.0	1.0	1.0	1.0	9	31		2
52	07/29/75	02:40:51.2	32.57	78.49	210.0	-90.0	55.0	1.0	1.0	1.0	8	0		2
53	06/20/86	17:12:46.9	31.24	86.84	51.0	-4.0	78.0	1.0	1.0	1.0	15		33	3
54	10/03/75	05:14:23.0	30.25	66.31	26.0	2.0	88.0	1.0	1.0	1.0	11	11		4
55	10/03/75	17:31:36.0	30.41	66.35	28.0	2.0	88.0	1.0	1.0	1.0	10	33		4
56	02/13/83	01:40:10.9	39.90	75.13	228.0	-5.0	78.0	1.0	1.0	1.0	10		16	3
57	03/24/74	14:16:01.1	27.66	86.00	27.5	90.0	2.0	0.5	2.6	0.5	16	20		5
58	11/18/77	05:20:11.3	32.69	88.38	1.0	-91.0	71.0	1.0	1.0	1.0	10		33	3
59	07/14/73	04:51:20.0	35.18	86.48	190.0	215.0	60.0	0.6	1.6	0.6	6	22		6
60	07/14/73	13:39:29.4	35.26	86.60	37.0	304.0	68.0	0.6	1.6	0.6	7	29		6
61	09/03/72	16:48:29.5	35.98	73.42	341.0	105.0	55.0	0.5	2.0	0.5	12	45		5
62	01/31/77	14:26:14.8	40.11	70.86	81.0	100.0	40.0	0.4	1.8	0.4	12		20	7
63	07/13/77	08:09:15.7	29.69	67.13	109.0	166.0	75.0	1.0	1.0	1.0	15	10		3
64	02/11/69	22:08:51.0	41.20	79.24	65.0	83.0	41.0	1.0	1.0	1.0	10	3		7
65	06/27/66	10:41:08.1	29.62	80.83	277.0	70.0	27.0	1.5	2.0	1.5	15	33		5
66	12/16/66	20:52:16.3	29.62	80.79	290.0	90.0	24.0	1.5	0.5	1.5	12	19		5
67	03/06/66	02:10:52.0	31.51	80.55	0.0	270.0	45.0	1.0	1.0	1.0	8	5		6
68	03/24/75	05:33:47.0	29.55	68.60	244.0	58.3	38.0	1.0	1.0	1.0	10	26		4
69	04/28/75	11:06:43.5	35.82	79.92	169.0	211.0	62.0	1.0	1.0	1.0	7		33	6
70	06/04/75	02:24:32.9	35.87	79.85	180.0	239.0	62.0	0.4	1.4	0.4	9		31	6
71	03/23/71	20:47:15.5	41.42	79.20	73.0	93.0	46.0	0.4	1.4	0.4	11	14		7
72	05/10/71	14:51:45.0	42.85	71.29	37.0	57.0	48.0	0.4	1.4	0.4	15	14		7
73	02/20/67	15:18:38.8	33.63	75.33	341.0	105.0	55.0	0.2	2.6	0.2	10	18		5
74	06/19/79	16:29:11.6	26.74	87.48	245.0	-95.0	46.0	0.4	1.6	0.4	20	20		2
75	09/25/79	13:05:54.5	45.09	76.96	77.0	119.0	44.0	1.0	1.0	1.0	40		40	7
76	05/06/85	03:04:22.7	30.88	70.26	211.0	98.0	14.0	0.4	1.6	0.4	15		37	3
77	05/08/85	17:10:41.2	30.91	70.31	211.0	91.0	21.0	0.4	1.6	0.4	3		33	3
78	12/16/83	13:15:57.3	39.32	72.92	209.0	50.0	52.0	0.4	1.0	0.4	10		37	3

[1]Holt et al. [1989]
[2]Ni and Barazangi [1984]
[3]Harvard Solution
[4]Jackson and McKenzie [1984]
[5]Baranowski et al. [1984]
[6]Molnar and Chen [1983]
[7]Nelson et al. [1987]1

TABLE 2. Inversion Parameters CTH and Pn Obtained as a Function of Different Average Crustal Velocities

Average Crustal Velocity	CTH (km)	Pn Vel (km/s)	Error
5.5	26.9	7.89	0.130
5.6	27.5	7.89	0.130
5.7	29.0	7.90	0.132
5.8	30.4	7.89	0.121
5.9	31.6	7.91	0.107
6.0	34.0	7.92	0.103
6.1	36.2	7.94	0.080
6.2	37.7	7.94	0.084
6.3	38.4	7.93	0.101
6.4	40.7	7.94	0.140
6.5	42.0	7.93	0.174

TABLE 3. Inversion Parameters CTH and Pn Obtained as a Function of Different Source (Fault) Orientations.

Strike (t)	Rake (l)	Dip (d)	delta(θ,λ,δ)	CTH (km)	Pn (km/s)	Error
174.5	-12.0	64.3	$+5^{o}$	37.2	7.93	0.083
179.5	-7.0	69.3	$+10^{o}$	37.2	7.93	0.086
184.5	-2.0	74.3	$+15^{o}$	37.2	7.93	0.087
189.5	3.0	79.3	$+20^{o}$	38.7	7.96	0.079
194.5	8.0	84.3	$+25^{o}$	38.4	7.95	0.079
199.5	13.0	89.0	$+30^{0}$	38.5	7.96	0.078
204.5	18.0	90.0	$+35^{o}$	38.3	7.95	0.079

TABLE 4. Inversion Parameters CTH and Pn Obtained With Different Source Time Functions

Time Function			CTH (km)	Pn Vel	Error
RT	TOP	FT			
0.6	1.4	0.6	36.7	7.93	0.096
1.0	1.8	1.0	35.2	7.90	0.119
1.4	2.4	1.4	34.7	7.90	0.151
2.4	1.0	2.4	33.45	7.86	0.170
2.0	3.0	2.0	31.9	7.88	0.208

Optimal time function is RT = 0.4, TOP = 1.0, FT = 0.4.

TABLE 5. List of Paths, Event Number, Station, Inversion Results (CTH, Pn,) and the Final Error or Waveform Misfit

Path	Event	Station	Date	Distance (km)	Travel Time (sec)	CTH (km)	Pn (km/s)	CVEL	Error	T_d	T_h
1	68	MSH	03/24/75	1127.0	151.77	46.2	7.77	6.2	0.278	2.13	0.40
2	54	MSH	10/03/75	918.2	124.22	50.0	7.88	6.2	0.492	0.00	0.40
3	61	MSH	09/13/72	1244.2	161.22	54.0	8.15	6.2	0.364	4.40	0.67
4	72	MSH	05/10/71	1238.2	159.09	39.0	8.05	6.2	0.158	-0.13	0.40
5	62	MSH	01/31/77	1072.5	140.19	49.6	8.10	6.2	0.295	1.00	0.40
6	64	KBL	02/11/69	1175.6	156.10	61.6	8.05	6.2	0.400	-0.93	1.22
7	69	KBL	04/28/75	1000.3	132.01	62.3	8.28	6.2	0.128	3.46	1.22
8	70	KBL	06/04/75	994.5	133.60	59.9	8.05	6.2	0.289	2.93	1.22
9	71	KBL	03/23/71	1172.9	155.82	73.7	8.18	6.2	0.202	0.40	1.22
10	52	KBL	07/29/75	903.7	***	43.7	***	6.2	0.150	***	***
11	51	KBL	07/19/75	934.5	124.20	46.0	8.00	6.2	0.070	2.93	0.76
12	51	QUE	07/19/75	1127.3	147.16	42.9	8.03	6.2	0.190	2.93	0.76
13	67	QUE	03/16/66	1308.3	171.41	47.5	7.97	6.2	0.199	-0.40	0.40
14	69	QUE	04/28/75	1361.8	174.69	51.0	8.19	6.2	0.282	3.46	1.22
15	73	QUE	02/20/67	879.3	119.47	46.0	7.83	6.2	0.415	1.06	0.76
16	66	QUE	12/16/66	1337.1	172.09	40.5	8.04	6.2	0.132	0.93	0.40
17	78	QUE	12/16/83	1150.4	151.17	63.8	8.16	6.2	0.520	2.93	1.04
18	56	QUE	02/13/83	1312.8	172.12	75.1	8.24	6.2	0.460	0.80	1.22
19	51	NIL	07/19/75	534.0	78.04	55.0	7.74	6.2	0.690	2.93	0.54
20	52	NIL	07/29/75	503.3	***	47.3	***	6.2	0.204	***	***
21	59	NIL	07/14/73	1226.9	161.25	75.9	8.31	6.2	0.290	2.13	1.76
22	63	NIL	07/13/77	727.6	96.44	45.0	8.14	6.2	0.490	-0.66	0.31
23	69	NIL	04/28/75	656.0	92.25	42.3	7.66*	6.2	0.301	3.46	0.99
24	70	NIL	06/04/75	652.0	92.97	59.0	7.85	6.2	0.600	2.93	0.99
25	57	NIL	03/24/74	1389.1	176.90	46.5	8.15	6.2	0.327	0.53	0.40
26	65	LAH	06/27/66	658.7	90.43	41.5	7.80	6.2	0.247	2.40	0.40
27	66	LAH	12/16/66	655.0	90.39	46.8	7.90	6.2	0.236	0.93	0.40
28	27	NDI	06/09/81	1492.8	194.83	73.0	8.19	6.2	0.534	0.66	1.76
29	76	NDI	05/06/85	715.2	94.96	35.5	7.95	6.2	0.277	2.93	1.04
30	77	NDI	05/08/85	712.0	96.31	37.0	7.85	6.2	0.318	3.06	1.22
31	78	NDI	12/16/83	1244.4	167.00	57.0	7.86	6.2	0.568	3.60	1.22
32	69	NDI	04/28/75	831.2	113.30	57.5	8.05	6.2	0.282	3.46	1.22
33	70	NDI	06/04/75	834.5	114.30	65.4	8.11	6.2	0.364	2.93	1.22
34	71	NDI	03/23/71	1424.45	186.59	73.7	8.12	6.2	0.543	0.40	1.09
35	62	NDI	01/03/77	1394.8	179.54	58.2	8.19	6.2	0.317	1.06	1.00
36	64	NDI	02/11/69	1424.9	187.13	76.4	8.16	6.2	0.384	-0.93	1.22
37	59	NDI	07/14/73	1133.1	148.20	63.0	8.27	6.2	0.528	2.13	1.76
38	61	NDI	09/13/72	884.3	118.52	43.0	7.90	6.2	0.235	4.40	0.67
39	51	NDI	07/19/75	385.4	58.59	35.3	7.13*	6.2	0.686	2.93	1.00
40	53	NDI	06/20/86	953.7	127.26	66.7	8.21	6.2	0.349	2.40	1.76
41	54	NDI	10/03/75	1071.6	138.80	43.5	8.12	6.2	0.302	0.00	0.40

(Continued)

TABLE 5 - Continued

Path	Event	Station	Date	Distance (km)	Travel Time (sec)	CTH (km)	Pn (km/s)	CVEL	Error	T_d	T_h
42	55	NDI	10/03/75	1070.0	138.74	40.8	8.08	6.2	0.220	3.06	0.40
43	68	NDI	03/24/75	843.9	112.79	34.4	7.83	6.2	0.338	2.13	0.40
44	56	NDI	02/13/83	1258.9	164.12	73.7	8.32	6.2	0.267	0.80	1.22
45	58	NDI	11/18/77	1158.0	152.13	60.5	8.15	6.2	0.246	3.06	1.76
46	48	NDI	06/22/72	1400.2	182.73	70.6	8.20	6.2	0.370	1.33	1.76
47	16	HOW	09/28/66	1315.6	168.87	42.8	8.10	6.2	0.179	0.26	0.40
48	21	HOW	09/26/66	710.1	92.23	33.9	8.16	6.2	0.236	1.00	0.31
49	66	HOW	12/16/66	1096.3	142.36	41.5	8.05	6.2	0.273	0.93	0.40
50	28	HOW	10/21/64	829.55	112.23	38.0	7.75	6.2	0.131	3.06	0.23
51	30	HOW	09/01/64	656.45	87.71	31.0	7.95	6.2	0.192	3.60	0.40
52	8	SHL	04/23/84	838.6	109.91	39.9	8.10	5.8	0.291	-0.26	0.00
53	9	SHL	02/02/80	964.0	125.60	40.0	8.08	5.8	0.314	1.60	0.00
54	10	SHL	09/19/81	1001.6	132.80	39.0	7.93	5.8	0.234	0.53	0.00
55	11	SHL	04/18/85	1102.5	136.55	39.5	8.56*	6.2	0.278	-0.40	0.00
56	12	SHL	03/15/79	971.5	127.15	37.8	8.05	5.8	0.484	0.26	0.00
57	13	SHL	08/14/81	613.3	85.58	52.5	8.03	6.2	0.736	3.77	0.00
58	14	SHL	08/16/81	476.9	65.50	48.0	8.40*	6.2	0.584	4.00	0.27
59	27	SHL	06/09/81	992.4	132.63	55.0	8.06	6.2	0.436	0.66	1.76
60	16	SHL	09/28/66	845.0	113.56	52.0	8.05	6.2	0.269	0.26	0.40
61	15	SHL	01/15/75	1066.2	139.82	49.0	8.08	6.2	0.306	2.53	0.40
62	17	SHL	08/30/67	1057.6	139.51	58.7	8.17	6.2	0.345	1.36	0.76
63	37	SHL	06/09/76	695.9	92.93	37.0	8.08	5.8	0.291	1.46	0.00
64	38	SHL	07/21/76	691.6	93.76	43.6	8.03	5.8	0.714	-0.27	0.00
65	32	SHL	05/29/76	720.0	98.96	38.0	7.80	5.8	0.356	0.00	0.00
66	33	SHL	07/03/76	702.5	92.84	33.4	8.06	5.8	0.168	3.60	0.00
67	34	SHL	05/31/76	700.8	93.78	42.3	8.13	5.8	0.326	2.00	0.00
68	35	SHL	05/31/76	695.6	93.74	36.3	7.97	5.8	0.190	2.93	0.00
69	4	SHL	02/13/66	1135.8	150.26	43.8	7.94	6.2	0.275	0.27	0.00
70	22	SHL	06/03/75	519.4	73.24	47.9	7.97	5.8	0.106	0.00	0.40
71	23	SHL	06/03/75	515.0	76.80	47.9	7.47*	5.8	0.106	4.27	0.40
72	24	SHL	11/06/76	940.7	124.40	45.8	8.07	5.8	0.076	-0.13	0.40
73	6	SHL	12/21/79	542.0	81.80	33.2	7.16*	5.8	0.066	2.93	0.40
74	7	SHL	02/06/70	943.0	122.68	35.7	8.08	5.8	0.327	3.20	0.00
75	74	SHL	06/19/79	459.0	64.25	35.8	7.68*	6.2	0.361	0.00	0.31
76	57	SHL	03/24/74	630.0	84.45	40.2	8.03	6.2	0.330	0.53	0.31
77	65	SHL	06/27/66	1179.4	151.19	41.5	8.12	6.2	0.254	2.40	0.54
78	66	SHL	12/06/66	1183.0	153.03	44.2	8.08	6.2	0.194	0.93	0.54
79	59	SHL	07/14/73	1184.9	156.25	66.0	8.19	6.2	0.274	2.13	1.76
80	60	SHL	07/14/73	1187.9	155.30	70.9	8.33	6.2	0.436	2.93	1.76
81	58	SHL	11/18/77	859.5	117.76	56.0	7.91	6.2	0.430	3.06	1.76
82	39	SHL	05/31/71	467.5	66.50	44.9	7.96	6.2	0.413	1.86	0.40

(Continued)

TABLE 5 - Continued

Path	Event	Station	Date	Distance (km)	Travel Time (sec)	CTH (km)	Pn (km/s)	CVEL	Error	T_d	T_h
83	40	SHL	09/14/71	941.0	126.27	45.5	7.91	5.8	0.448	4.13	0.00
84	41	SHL	05/30/76	712.6	95.46	40.7	8.04	5.8	0.206	-0.93	0.00
85	42	SHL	04/08/72	1076.0	141.47	49.5	8.07	6.2	0.259	4.27	0.00
86	43	SHL	07/03/82	823.5	108.38	44.0	8.17	6.2	0.301	0.53	0.31
87	44	SHL	10/22/82	573.7	76.33	38.8	8.23	6.2	0.194	-1.33	0.54
88	20	SHL	02/19/70	290.0	42.67	38.0	8.08	6.2	0.677	0.53	0.31
89	48	SHL	06/22/72	645.9	91.48	55.0	7.87	6.2	0.542	1.33	1.44
90	49	SHL	04/03/71	791.0	104.16	51.0	8.33	6.2	0.268	2.53	0.72
91	50	SHL	06/15/82	1048.9	137.47	49.0	8.12	6.2	0.218	0.40	0.76
92	45	SHL	05/22/71	753.2	106.55	58.2	7.77	6.2	0.427	2.93	1.22
93	46	SHL	08/15/67	629.5	89.86	60.4	7.93	6.2	0.662	3.73	1.06
94	26	SHL	03/29/79	924.2	122.02	45.5	8.06	6.2	0.169	4.67	0.47
95	29	SHL	12/13/76	930.7	123.40	42.1	8.03	5.8	0.046	0.00	0.40
96	9	CHG	02/02/80	1027.5	138.27	40.0	7.76	6.2	0.314	1.86	0.40
97	10	CHG	09/19/81	528.6	77.66	29.0	7.66	6.2	0.202	0.53	0.00
98	11	CHG	04/18/85	886.3	119.43	38.5	7.81	6.2	0.363	-0.40	0.40
99	13	CHG	08/14/81	712.0	100.52	31.3	7.39*	6.2	0.268	4.00	0.18
100	14	CHG	08/16/81	783.5	106.14	30.4	7.70	6.2	0.199	4.00	0.18
101	16	CHG	09/28/66	974.5	132.67	35.0	7.61	6.2	0.400	0.26	0.40
102	15	CHG	01/15/75	1210.1	160.54	35.0	7.77	6.2	0.371	2.53	0.67
103	18	CHG	08/30/67	1422.0	187.70	41.0	7.82	6.2	0.000	3.60	0.90
104	37	CHG	06/09/76	675.8	90.38	27.9	7.90	6.2	0.183	1.46	0.00
105	38	CHG	07/21/76	663.9	90.95	30.0	7.69	6.2	0.305	-0.26	0.00
106	32	CHG	05/29/76	636.7	89.47	29.3	7.50*	6.2	0.356	0.00	0.00
107	33	CHG	07/03/76	598.7	82.78	25.5	7.57*	6.2	0.100	3.60	0.00
108	34	CHG	05/31/76	609.7	82.72	24.8	7.73	6.2	0.131	2.00	0.00
109	36	CHG	05/30/71	759.6	100.42	31.5	7.98	6.2	0.071	4.22	0.00
110	2	CHG	02/05/66	923.5	127.53	36.8	7.57*	6.2	0.077	3.73	0.31
111	4	CHG	02/13/66	918.6	125.78	35.0	7.63	6.2	0.409	0.26	0.31
112	21	CHG	09/26/66	1162.8	151.55	37.0	7.94	6.2	0.457	1.06	0.31
113	22	CHG	06/03/75	888.5	120.40	38.0	7.73	6.2	0.441	0.00	0.40
114	23	CHG	06/03/75	889.4	122.84	32.3	7.51*	6.2	0.096	4.62	0.00
115	6	CHG	12/21/79	941.4	126.34	36.6	7.77	6.2	0.227	2.93	0.40
116	39	CHG	05/31/71	753.0	102.18	37.9	7.82	6.2	0.141	1.86	0.31
117	40	CHG	09/14/71	496.6	67.86	32.0	7.93	6.2	0.300	4.13	0.00
118	41	CHG	05/30/76	633.0	85.86	29.4	7.77	6.2	0.157	-0.93	0.00
119	43	CHG	07/03/82	868.4	117.19	34.1	7.74	6.2	0.246	0.53	0.31
120	20	CHG	02/19/70	1082.8	143.09	35.5	7.86	6.2	0.400	0.53	0.31
121	25	CHG	08/01/85	1213.6	155.57	37.2	7.93	6.2	0.257	0.93	0.13
122	28	CHG	10/21/64	1154.9	149.88	34.1	7.94	6.2	0.190	3.06	0.13
123	29	CHG	12/13/76	968.4	132.64	32.0	7.58	6.2	0.200	0.00	0.40

(Continued)

TABLE 5 - Continued

Path	Event	Station	Date	Distance (km)	Travel Time (sec)	CTH (km)	Pn (km/s)	CVEL	Error	T_d	T_h
124	30	CHG	09/01/64	1150.7	148.43	44.7	8.17	6.2	0.223	3.60	0.40
125	3	HKC	04/28/71	1352.5	173.38	33.5	8.04	6.2	0.212	0.66	0.00
126	2	HKC	02/05/66	1203.8	155.92	29.8	7.96	6.2	0.181	3.73	0.31
127	4	HKC	02/13/66	1190.8	155.19	30.7	7.92	6.2	0.265	0.26	0.31
128	16	HKC	09/28/66	1535.4	194.17	33.0	8.10	6.2	0.396	0.26	0.31
129	15	HKC	01/15/75	1469.1	187.39	38.0	8.07	6.2	0.306	2.53	0.76
130	38	HKC	07/21/76	1603.5	207.03	32.0	7.92	6.2	0.420	2.13	0.00
131	12	HKC	03/15/79	1345.7	173.75	39.5	8.04	6.2	0.168	0.26	0.00

*Velocity omitted from inversion.

T_d is the correction to the origin time to account for differences between ISC depth and assumed depth. T_h is the correction for crustal material below 33 km. Both T_d and T_h were subtracted from the origin time to obtain the travel times listed in this table.

TABLE 6. Velocities from Inversion in Which All Source Depths Are Assumed to be 33 Km

Block	Pn
1	8.04 ± .05
2	8.19 ± .04
3	8.04 ± .03
4	8.23 ± .07
5	8.28 ± .04
6	8.08 ± .03
7	8.26 ± .06
8	8.26 ± .05
9	7.86 ± .02
10	8.07 ± .04

TABLE 7. Misfit Between Observed and Predicted Pn/Pl Ratios for Different Gradient Models

		Tibet	
# Obs.	Lid Thickness	Grad (km/s per 100 km)	RMS Error (Pn/P_L)
7	0.0 (LHSP)	0.00	7.54
7	50.0	0.20	6.19
7	75.0	0.13	6.85
7	100.0	0.10	5.53
7	100.0	0.18	3.99
7	100.0	0.25	3.09

Misfit is for all 7 paths that crossed Tibet.

TABLE 8. Misfit Between Observed and Predicted Pn/Pl for 6 Paths That Crossed the Hindu Kush Region

		Hindu Kush	
# Obs.	Lid Thickness	Grad (km/s per 100 km)	RMS Error (Pn/P_L)
6	0.0 (LHSP)	0.00	8.75
6	50.0	0.20	7.04
6	75.0	0.13	6.30
6	100.0	0.10	7.15
6	100.0	0.18	4.60
6	100.0	0.25	3.03

The misfit is indicated for 6 different gradient models.

TABLE 9. Misfit Between Observed and Predicted Pn/Pl Ratios for Various Upper Mantle Gradient Models

# Obs.	Lid Thickness	East India Grad (km/s per 100 km)	RMS Error (Pn/P_L)
4	0.0 (LHSP)	0.00	4.43
4	100.0	0.10	3.10
4	100.0	0.20	1.78
4	100.0	0.25	1.59

LHSP indicates a layer over a half space model. The 4 paths sampled the east India and west Burma regions.

TABLE 10. Misfit Between Observed and Predicted Pn/Pl Ratios for Various Models

# Obs.	Lid Thickness	China Grad (km/s per 100 km)	RMS Error (Pn/P_L)
6	0.0 (LHSP)	0.00	0.28
6	50.0	0.20	1.89
6	100.0	0.10	4.88
6	100.0	0.20	23.17

LHSP indicates a layer over a half space model. The 6 observations sampled the south China region.

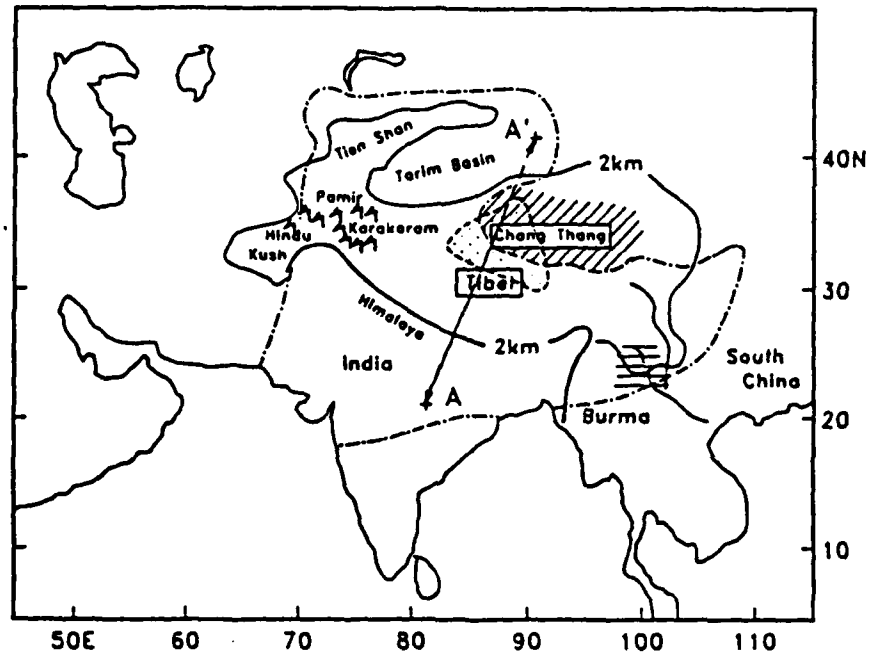
Tien Shan
A'
Tarim Basin
2km
40N
Pamir
Karakoram
Hindu
Kush
Chang Thang
Tibet
Himalaya
30
2km
India
South
China
A
Burma
20
10
50E
60
70
80
90
100
110

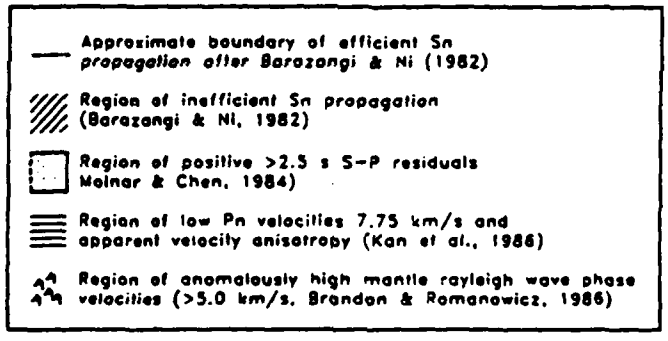
Approximate boundary of efficient Sn propagation after Barazangi & Ni (1982)
Region of inefficient Sn propagation (Barazangi & Ni, 1982)
Region of positive >2.5 s S-P residuals Molnar & Chen, 1984)
Region of low Pn velocities 7.75 km/s and apparent velocity anisotropy (Kan et al., 1986)
Region of anomalously high mantle rayleigh wave phase velocities (>5.0 km/s, Brandon & Romanowicz, 1986)

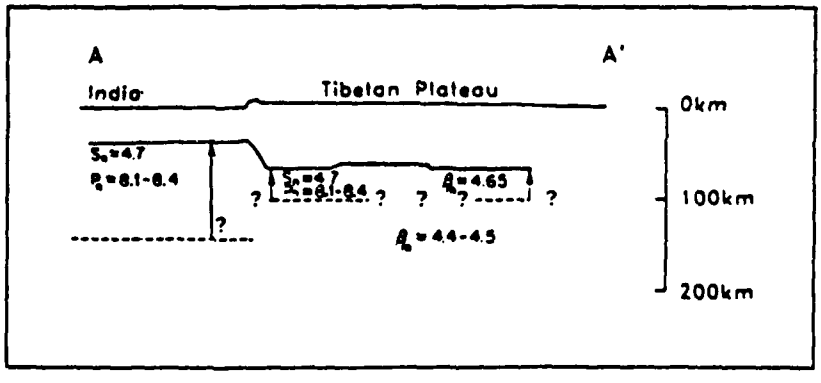
A
A'
India
Tibetan Plateau
0km
100km
200km
?
?
?
?
?
?
?

Figure 1

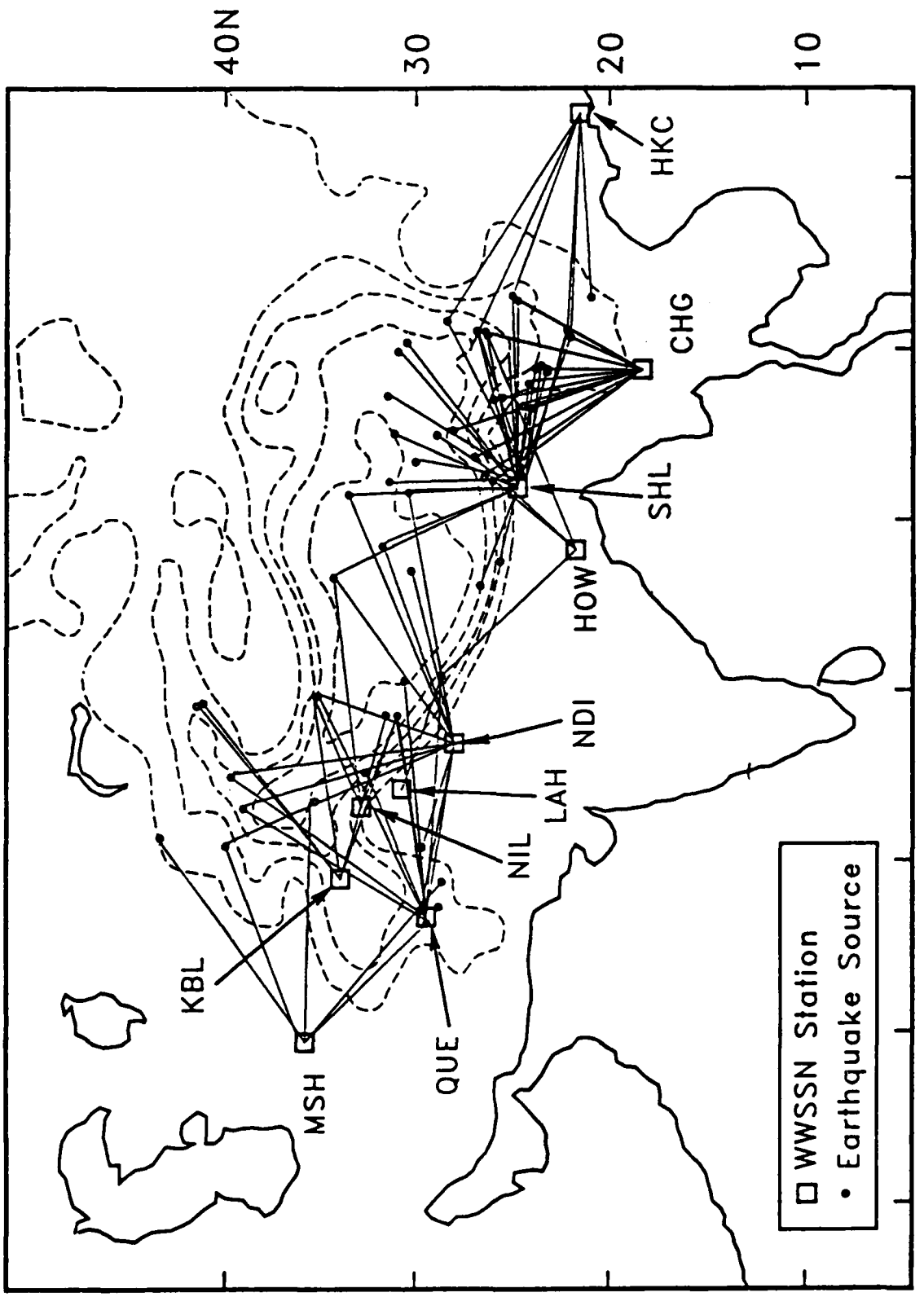
40N
30
20
10
50E
60
70
80
90
100
110
HKC
CHG
SHL
HOW
NDI
LAH
NIL
QUE
MSH
KBL
WWSSN Station
Earthquake Source

Figure 2

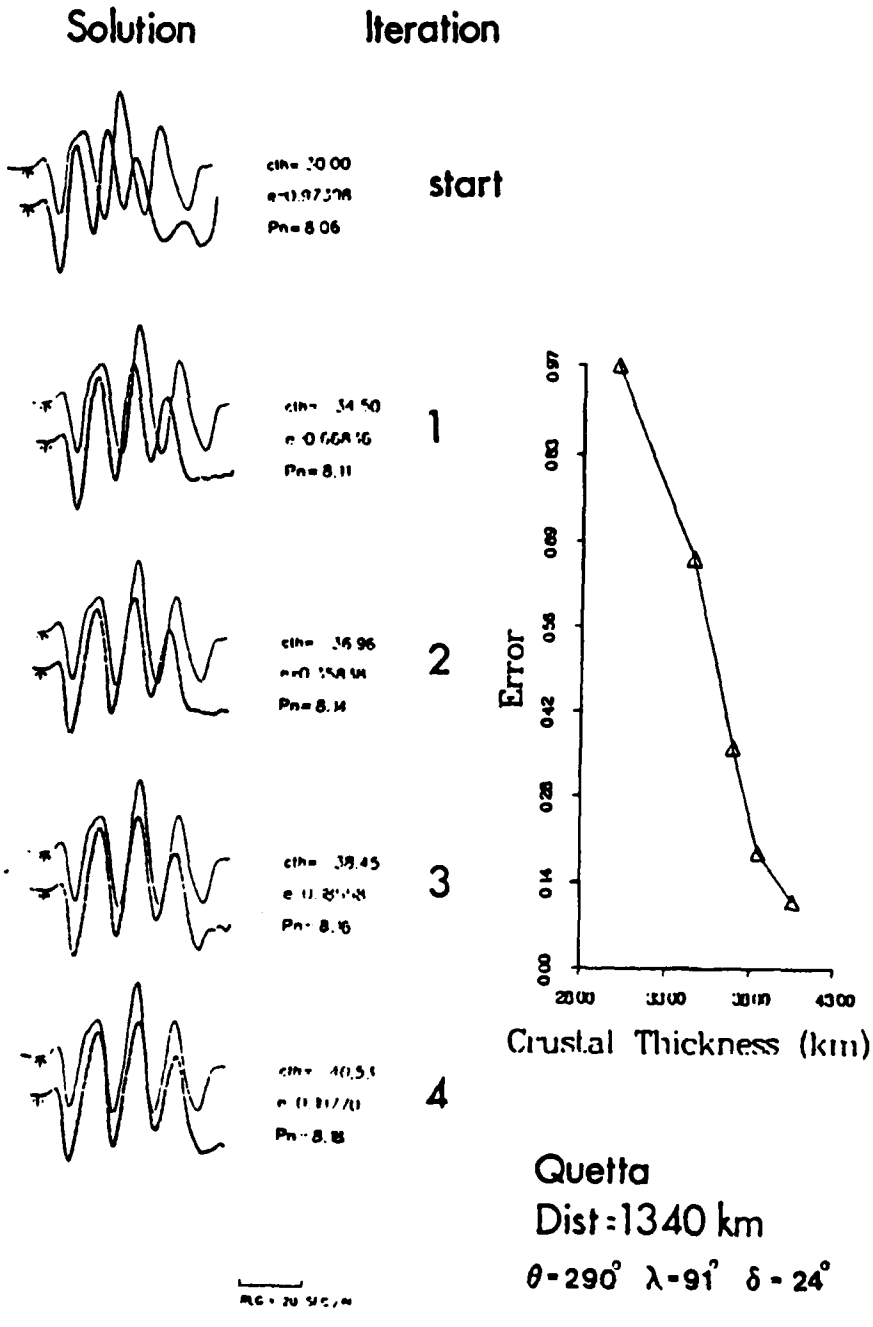

Fig. 3. Example inversion. Waveform match is shown for each iteration. The graph to the right indicates the error vs. parameter thickness for the start and four following iterations. Note reduction of error from 0.97-0.107 in four iterations. Observed waveform = top, synthetic = bottom line. Graph is not intended to show solution minimum, but error for each iteration in inversion.

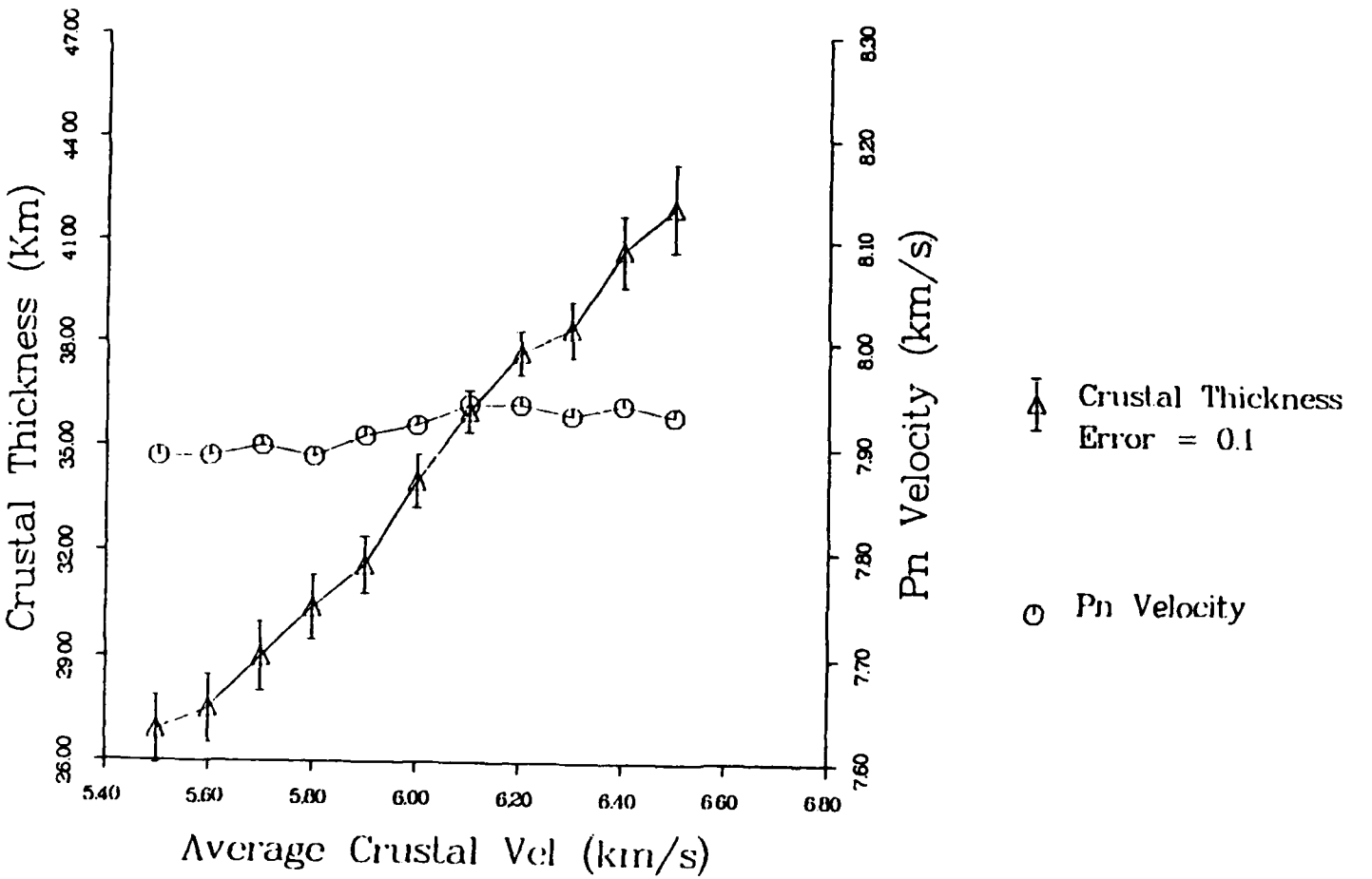
Crustal Thickness (Km)
26.00
29.00
32.00
35.00
38.00
41.00
44.00
47.00
Pn Velocity (km/s)
7.60
7.70
7.80
7.90
8.00
8.10
8.20
8.30
5.40
5.60
5.80
6.00
6.20
6.40
6.60
6.80
Average Crustal Vel (km/s)
Crustal Thickness
Error = 0.1
Pn Velocity

Figure 4

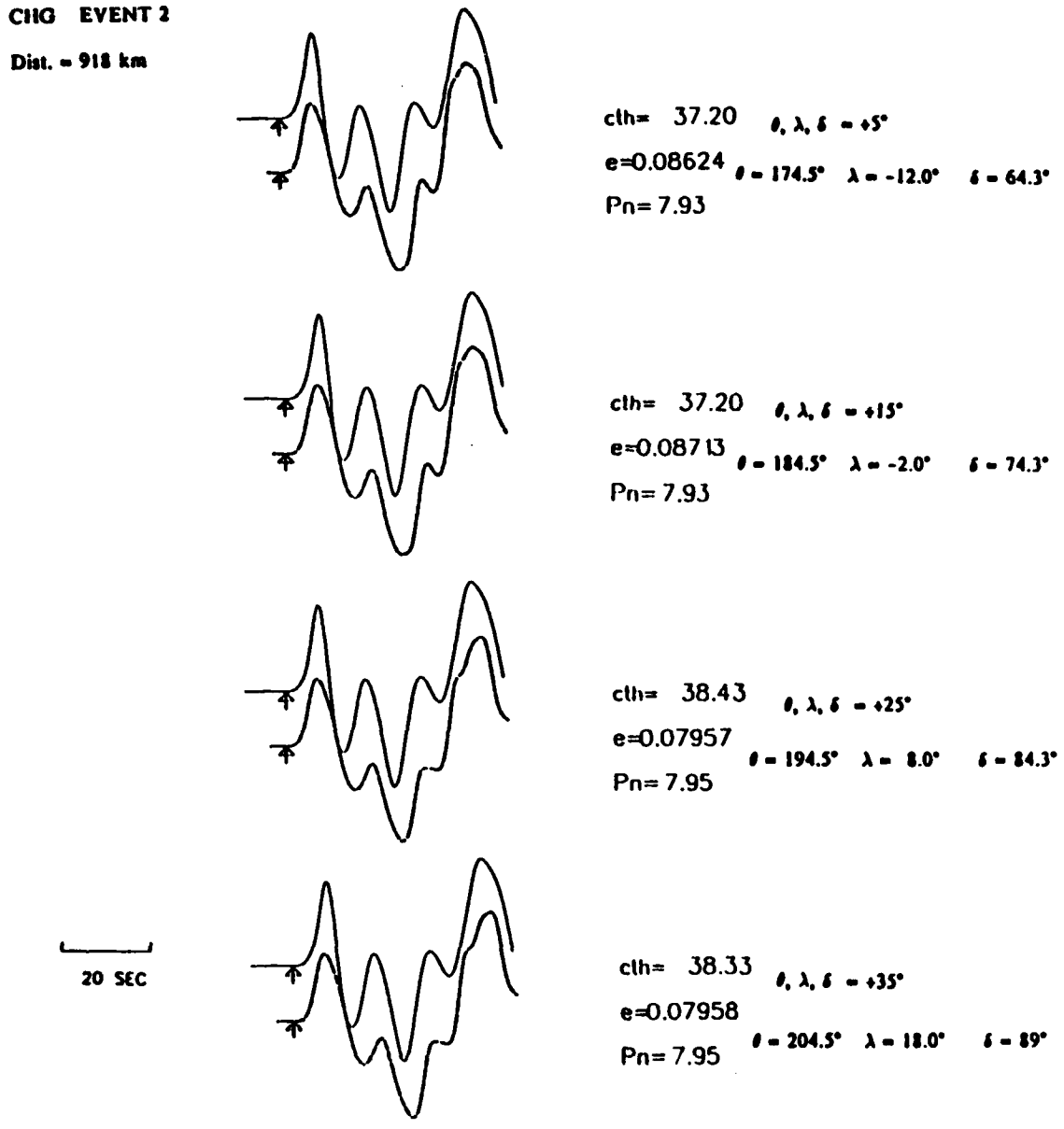
CHG EVENT 2
Dist. = 918 km
clh= 37.20 θ, λ, δ = +5°
e=0.08624 θ = 174.5° λ = -12.0° δ = 64.3°
Pn= 7.93
clh= 37.20 θ, λ, δ = +15°
e=0.08713 θ = 184.5° λ = -2.0° δ = 74.3°
Pn= 7.93
clh= 38.43 θ, λ, δ = +25°
e=0.07957 θ = 194.5° λ = 8.0° δ = 84.3°
Pn= 7.95
20 SEC
clh= 38.33 θ, λ, δ = +35°
e=0.07958 θ = 204.5° λ = 18.0° δ = 89°
Pn= 7.95

Figure 5

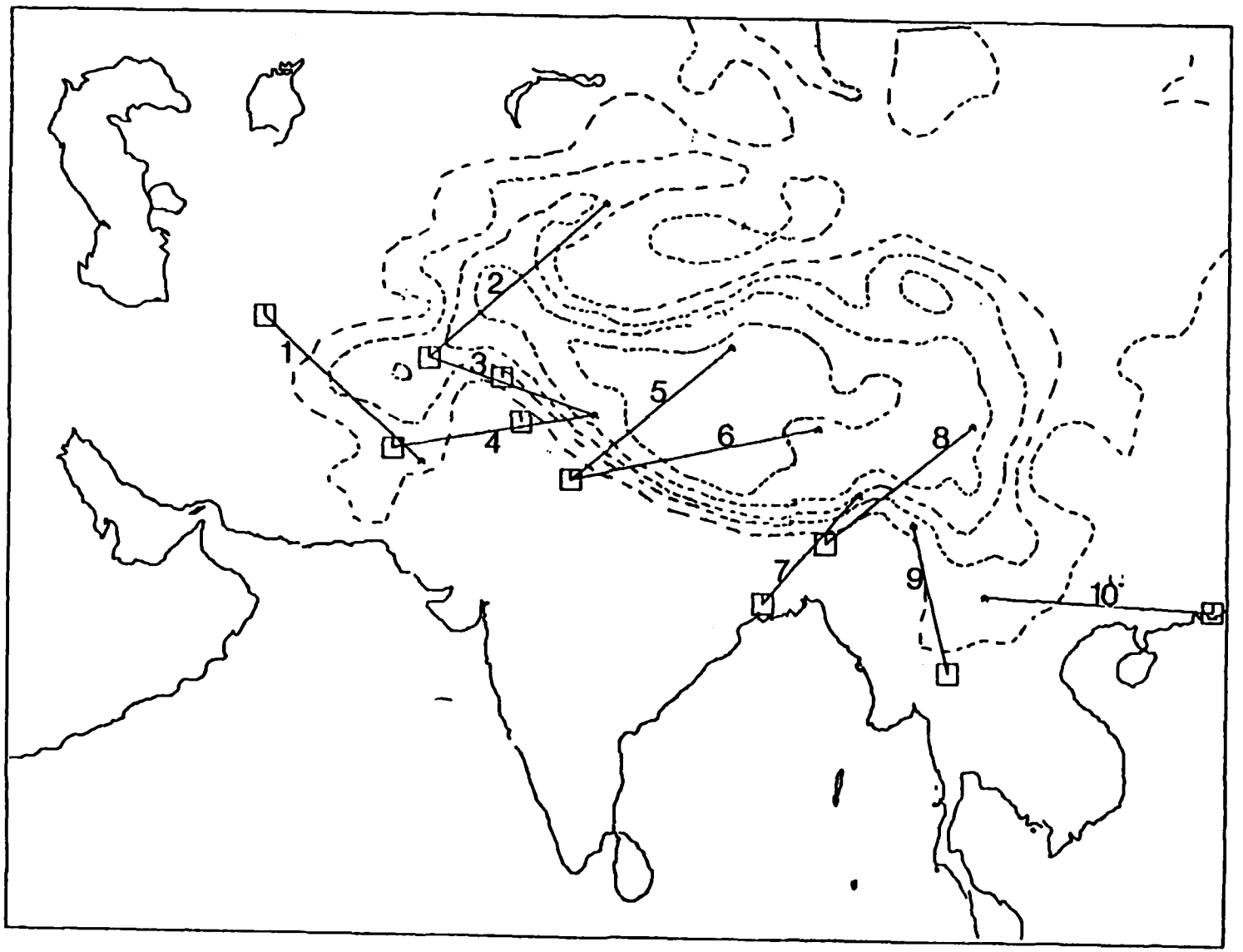

Figure 6

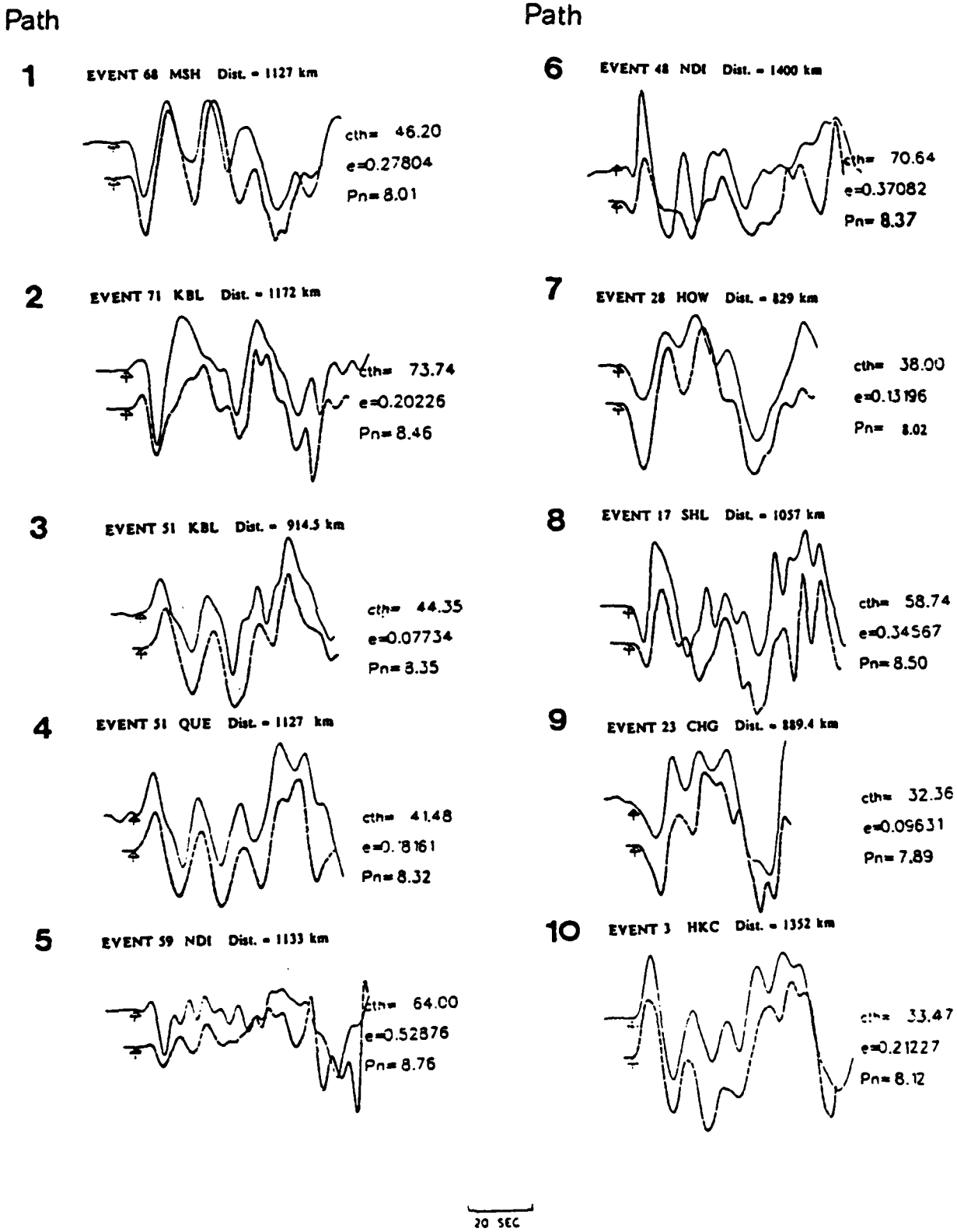
Path
1
EVENT 68 MSH Dist. = 1127 km
cth= 46.20
e=0.27804
Pn= 8.01
2
EVENT 71 KBL Dist. = 1172 km
cth= 73.74
e=0.20226
Pn= 8.46
3
EVENT 51 KBL Dist. = 914.5 km
cth= 44.35
e=0.07734
Pn= 8.35
4
EVENT 51 QUE Dist. = 1127 km
cth= 41.48
e=0.18161
Pn= 8.32
5
EVENT 59 NDI Dist. = 1133 km
cth= 64.00
e=0.52876
Pn= 8.76
Path
6
EVENT 48 NDI Dist. = 1400 km
cth= 70.64
e=0.37082
Pn= 8.37
7
EVENT 28 HOW Dist. = 829 km
cth= 38.00
e=0.13196
Pn= 8.02
8
EVENT 17 SHL Dist. = 1057 km
cth= 58.74
e=0.34567
Pn= 8.50
9
EVENT 23 CHG Dist. = 889.4 km
cth= 32.36
e=0.09631
Pn= 7.89
10
EVENT 3 HKC Dist. = 1352 km
cth= 33.47
e=0.21227
Pn= 8.12
20 SEC

Figure 7

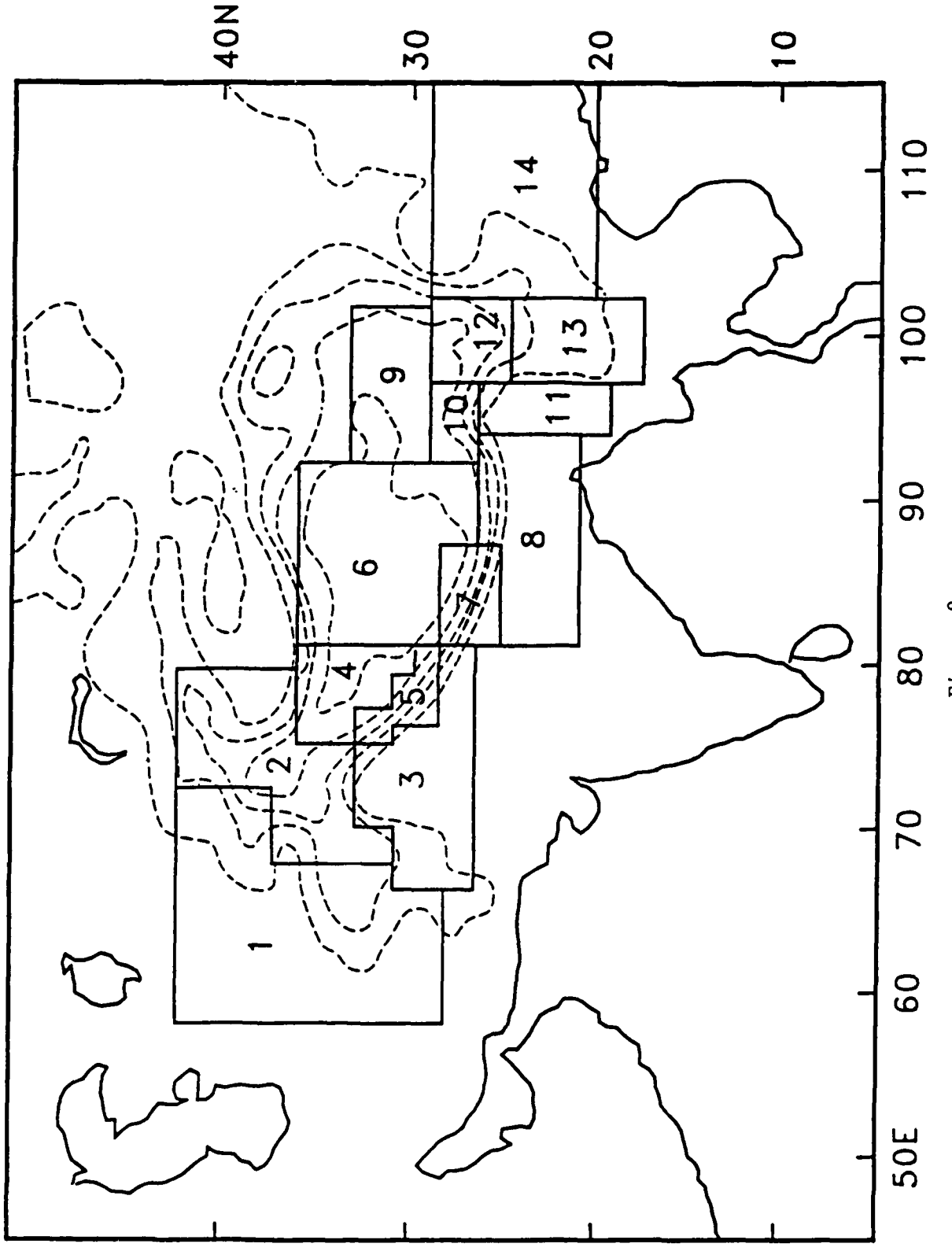

Figure 8a

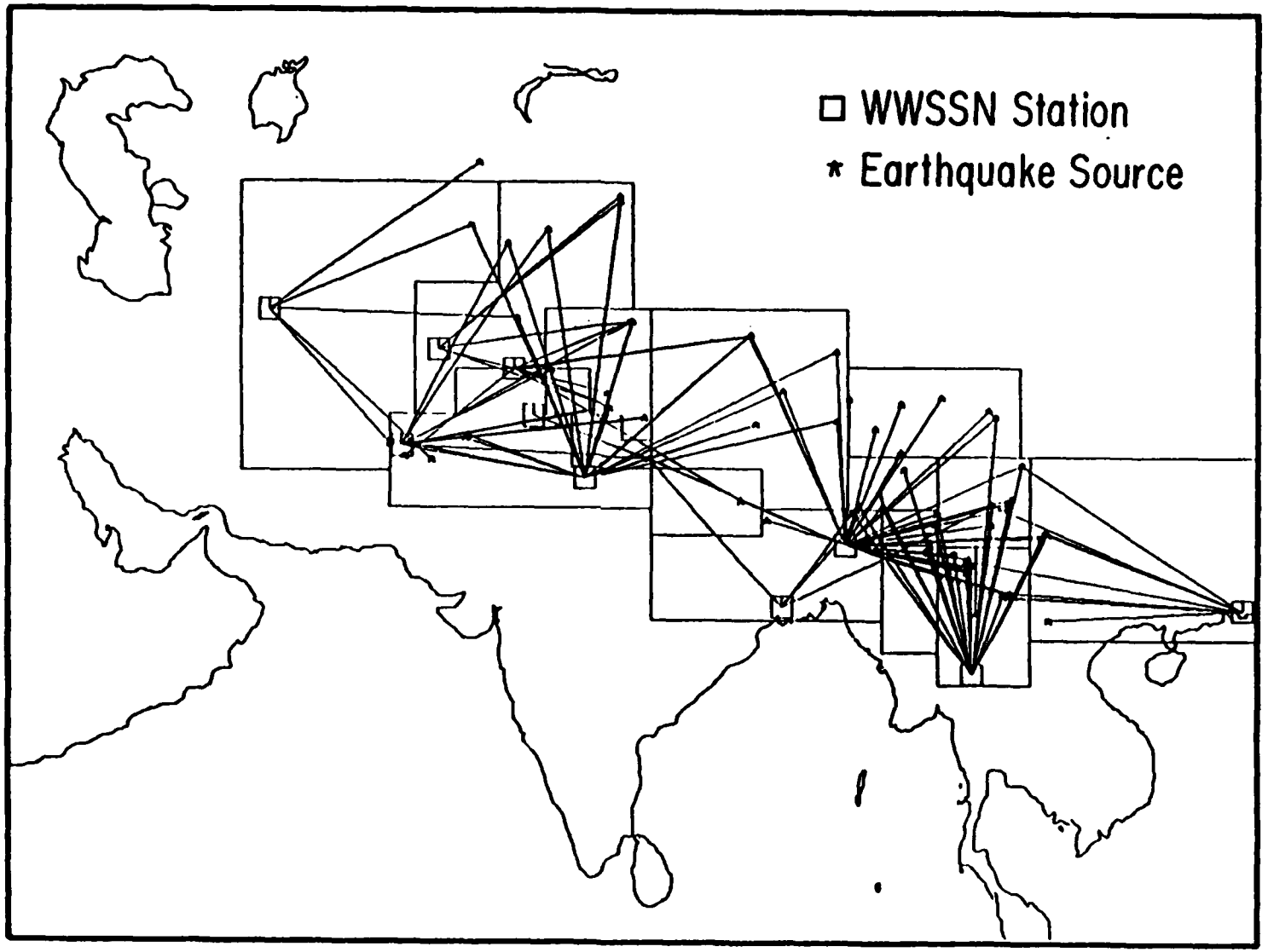

Figure 8b

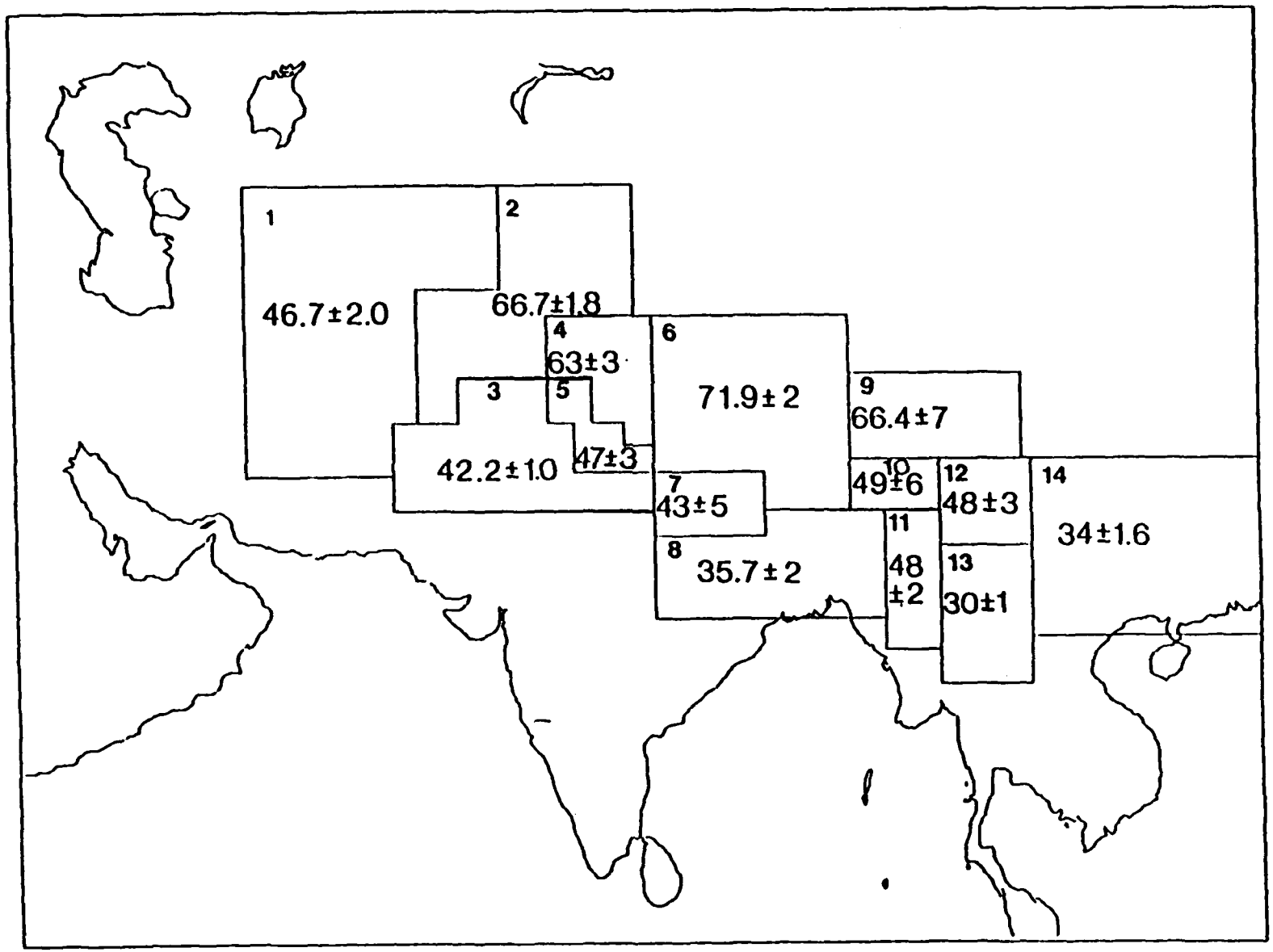
1
2
46.7±2.0
66.7±1.8
4
63±3
6
71.9±2
9
66.4±7
3
5
42.2±1.0
47±3
10
49±6
12
48±3
14
34±1.6
7
43±5
11
48
±2
8
35.7±2
13
30±1

Figure 9a

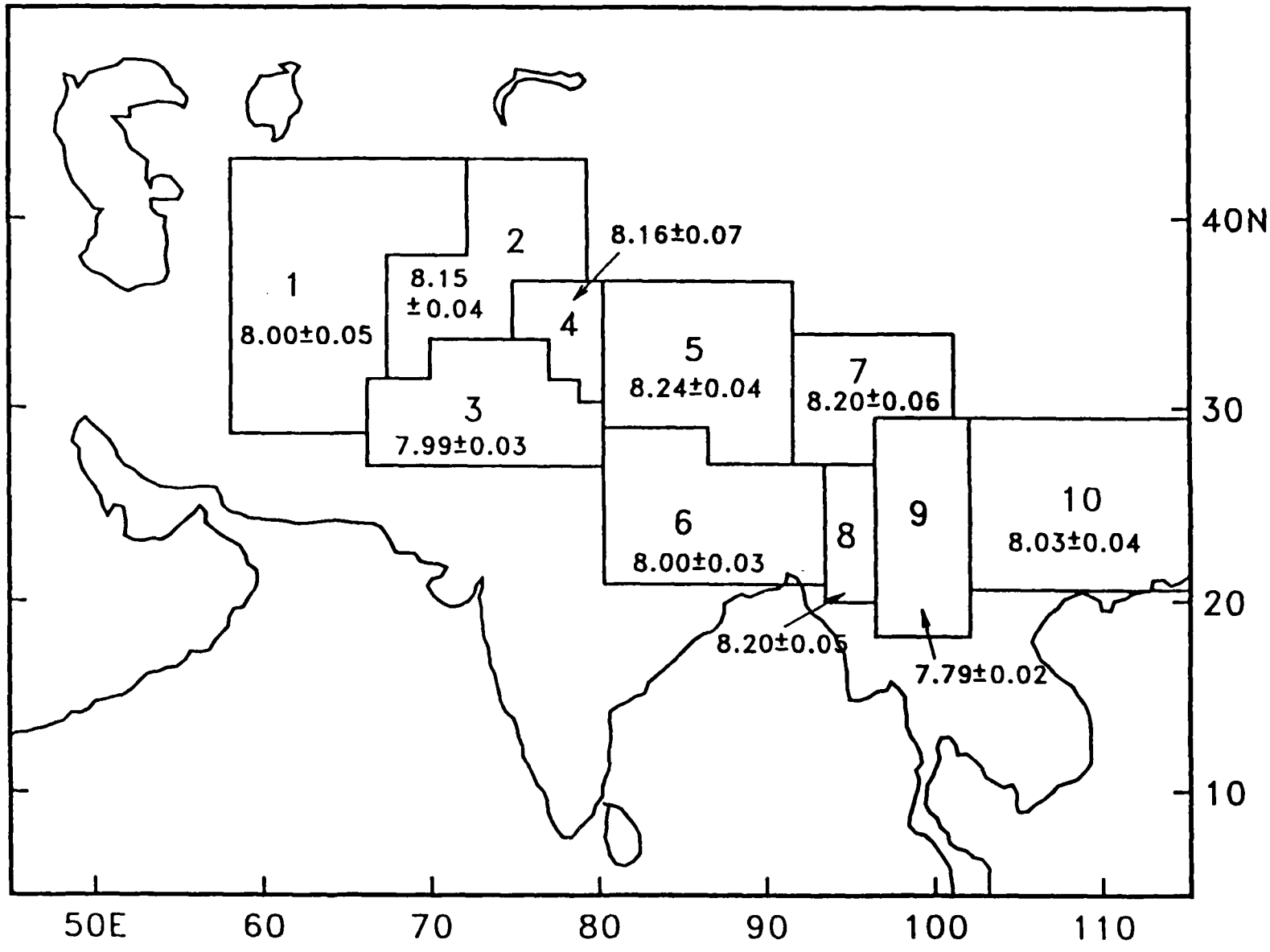
1
8.00±0.05
2
8.15
±0.04
3
7.99±0.03
4
8.16±0.07
5
8.24±0.04
6
8.00±0.03
7
8.20±0.06
8
8.20±0.05
9
7.79±0.02
10
8.03±0.04
40N
30
20
10
50E
60
70
80
90
100
110

Figure 9b

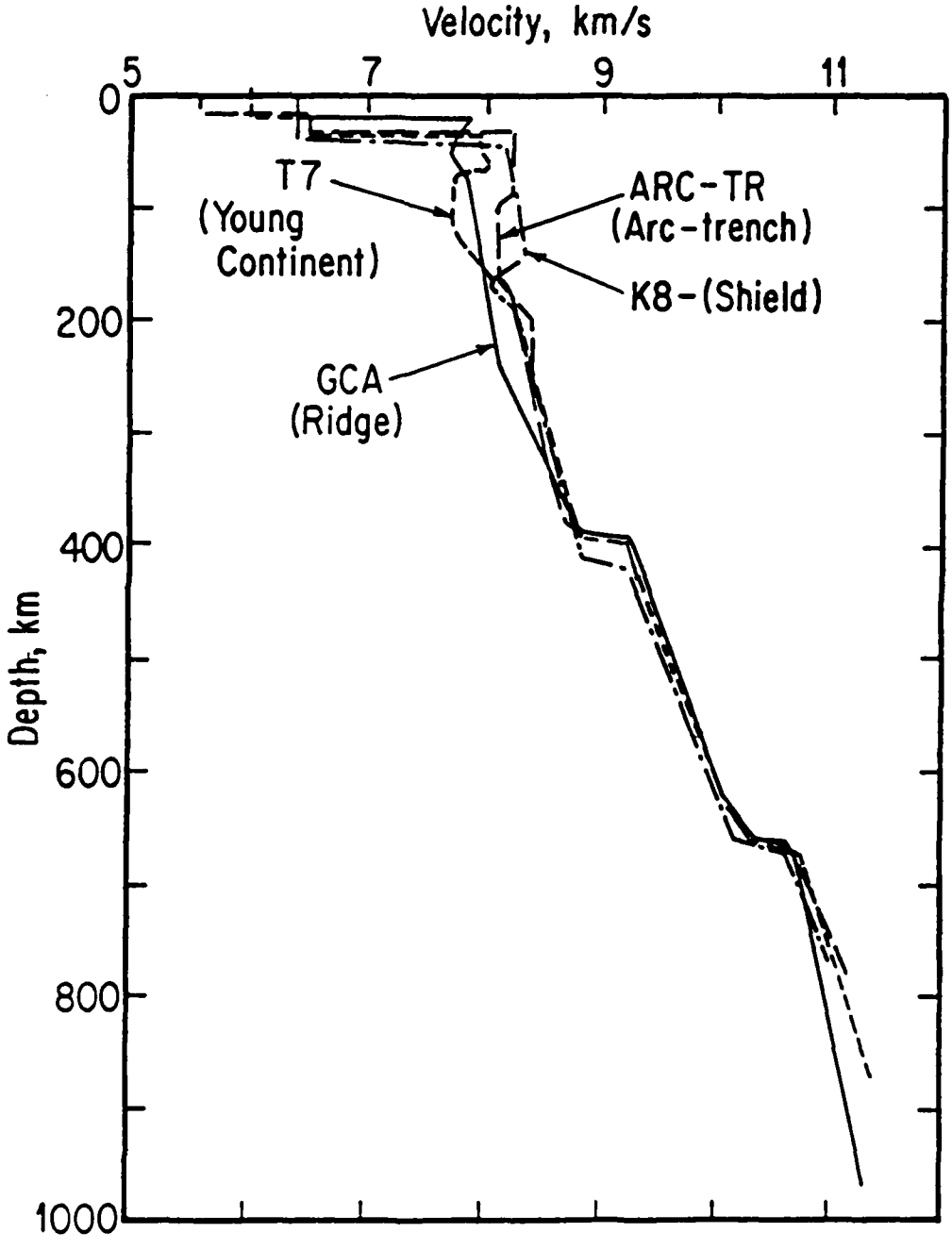
Velocity, km/s
5
7
9
11
0
200
400
600
800
1000
Depth, km
T7
(Young
Continent)
ARC-TR
(Arc-trench)
K8-(Shield)
GCA
(Ridge)

Figure 10

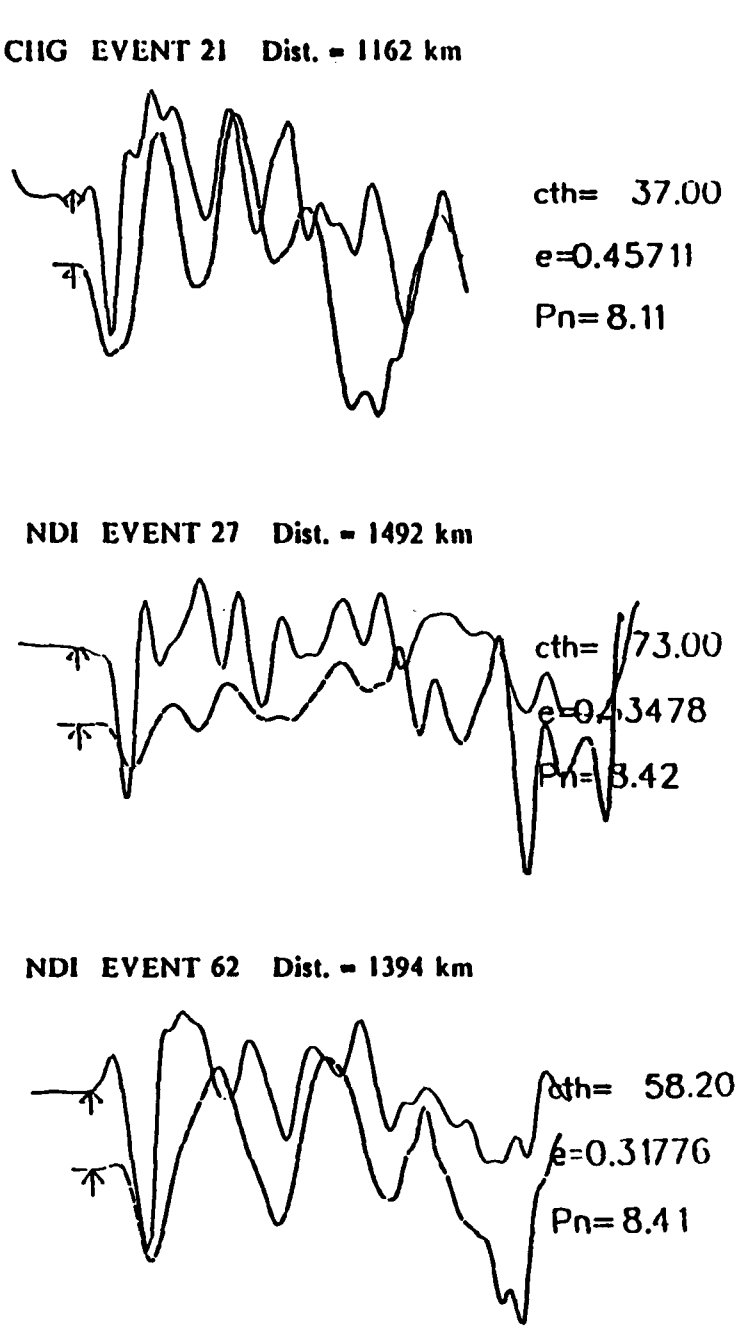
CHG EVENT 21 Dist. = 1162 km
cth= 37.00
e=0.45711
Pn=8.11
NDI EVENT 27 Dist. = 1492 km
cth= 73.00
e=0.43478
Pn=8.42
NDI EVENT 62 Dist. = 1394 km
cth= 58.20
e=0.31776
Pn=8.41
20 SEC

Figure 11

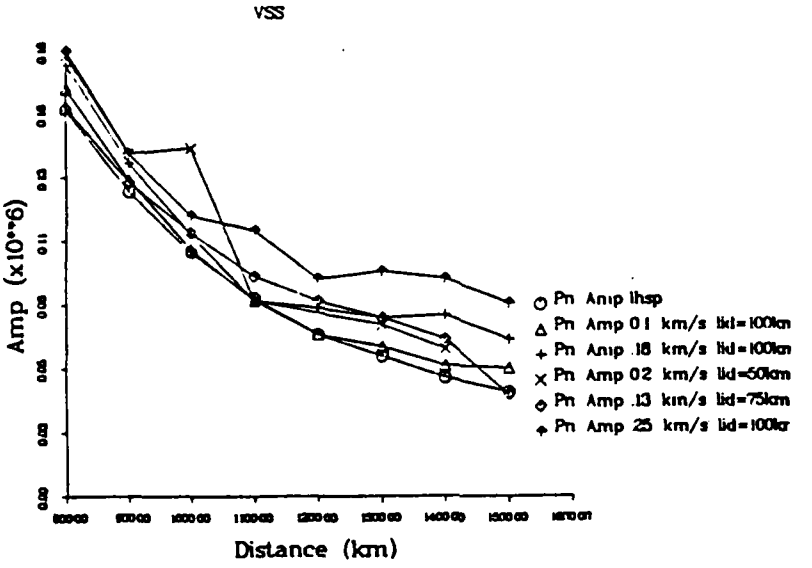
VSS
Amp (x10**6)
Distance (km)
Pn Amp lhsp
Pn Amp 0.1 km/s lid=100km
Pn Amp .18 km/s lid=100km
Pn Amp 0.2 km/s lid=50km
Pn Amp .13 km/s lid=75km
Pn Amp .25 km/s lid=100km

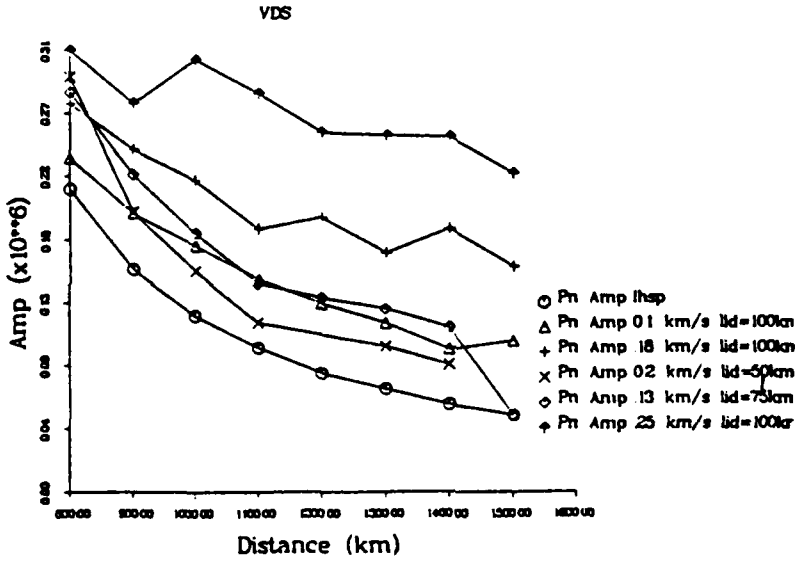
VDS
Amp (x10**6)
Distance (km)
Pn Amp lhsp
Pn Amp 0.1 km/s lid=100km
Pn Amp .18 km/s lid=100km
Pn Amp 0.2 km/s lid=50km
Pn Amp .13 km/s lid=75km
Pn Amp .25 km/s lid=100km

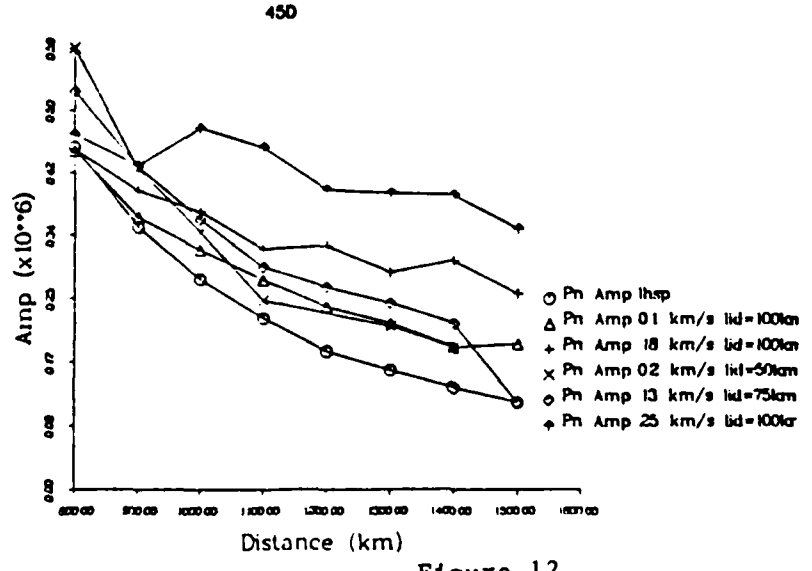
450
Amp (x10**6)
Distance (km)
Pn Amp lhsp
Pn Amp 0.1 km/s lid=100km
Pn Amp .18 km/s lid=100km
Pn Amp 0.2 km/s lid=50km
Pn Amp .13 km/s lid=75km
Pn Amp .25 km/s lid=100km

Figure 12

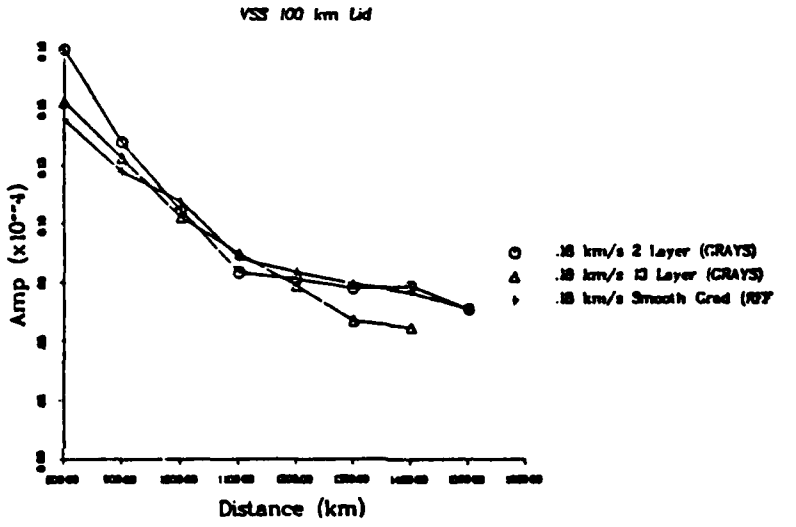
VSS 100 km Lid
Amp (x10**-4)
Distance (km)
.18 km/s 2 Layer (GRAYS)
.18 km/s 13 Layer (GRAYS)
.18 km/s Smooth Grad (REF

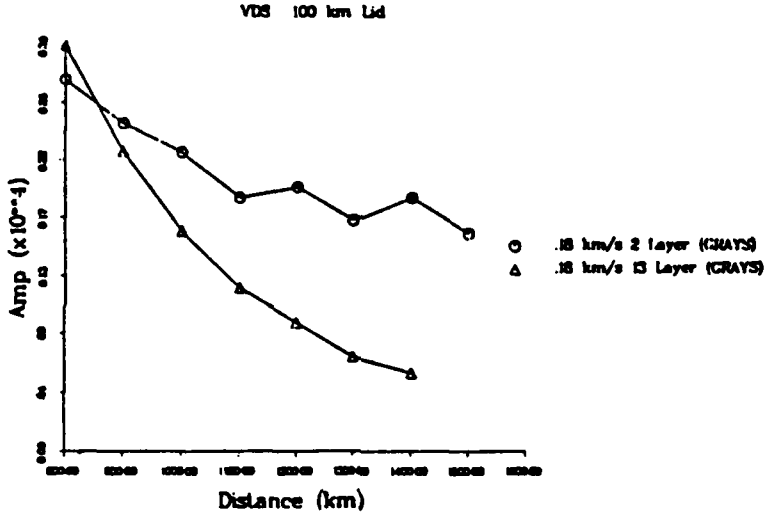
VDS 100 km Lid
Amp (x10**-4)
Distance (km)
.18 km/s 2 Layer (GRAYS)
.18 km/s 13 Layer (GRAYS)

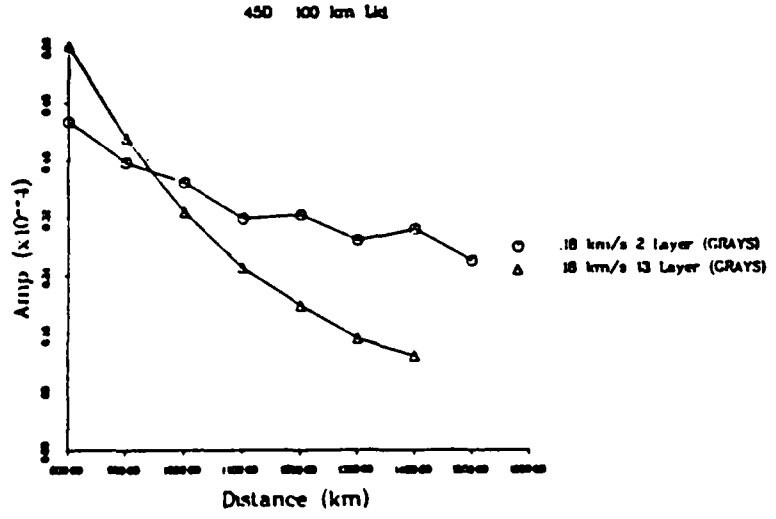
450 100 km Lid
Amp (x10**-4)
Distance (km)
.18 km/s 2 Layer (GRAYS)
.18 km/s 13 Layer (GRAYS)

Figure 13

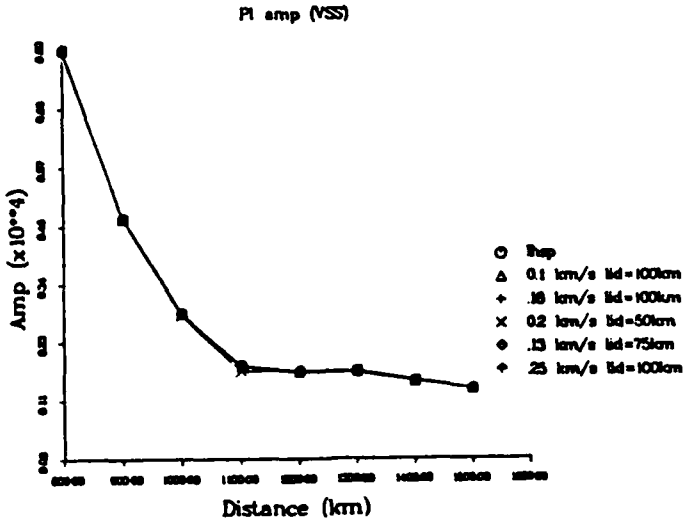
Pl amp (VSS)
Amp (x10**4)
Distance (km)
Thsp
0.1 km/s tld=100km
.18 km/s tld=100km
0.2 km/s tld=50km
.13 km/s tld=75km
.25 km/s tld=100km

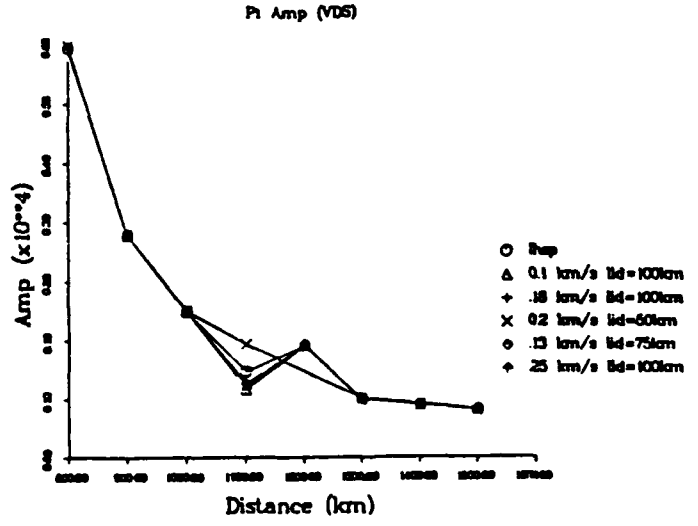
Pl Amp (VDS)
Amp (x10**4)
Distance (km)
Thsp
0.1 km/s tld=100km
.18 km/s tld=100km
0.2 km/s tld=50km
.13 km/s tld=75km
.25 km/s tld=100km

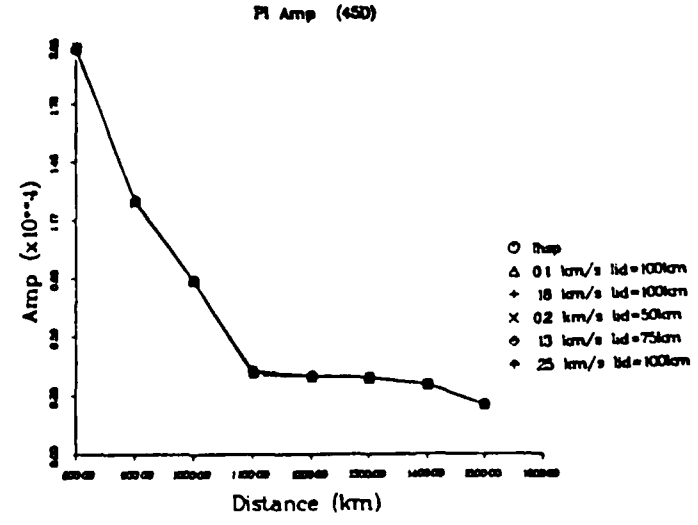
Pl Amp (4SD)
Amp (x10**4)
Distance (km)
Thsp
0.1 km/s tld=100km
.18 km/s tld=100km
0.2 km/s tld=50km
.13 km/s tld=75km
.25 km/s tld=100km

Figure 14

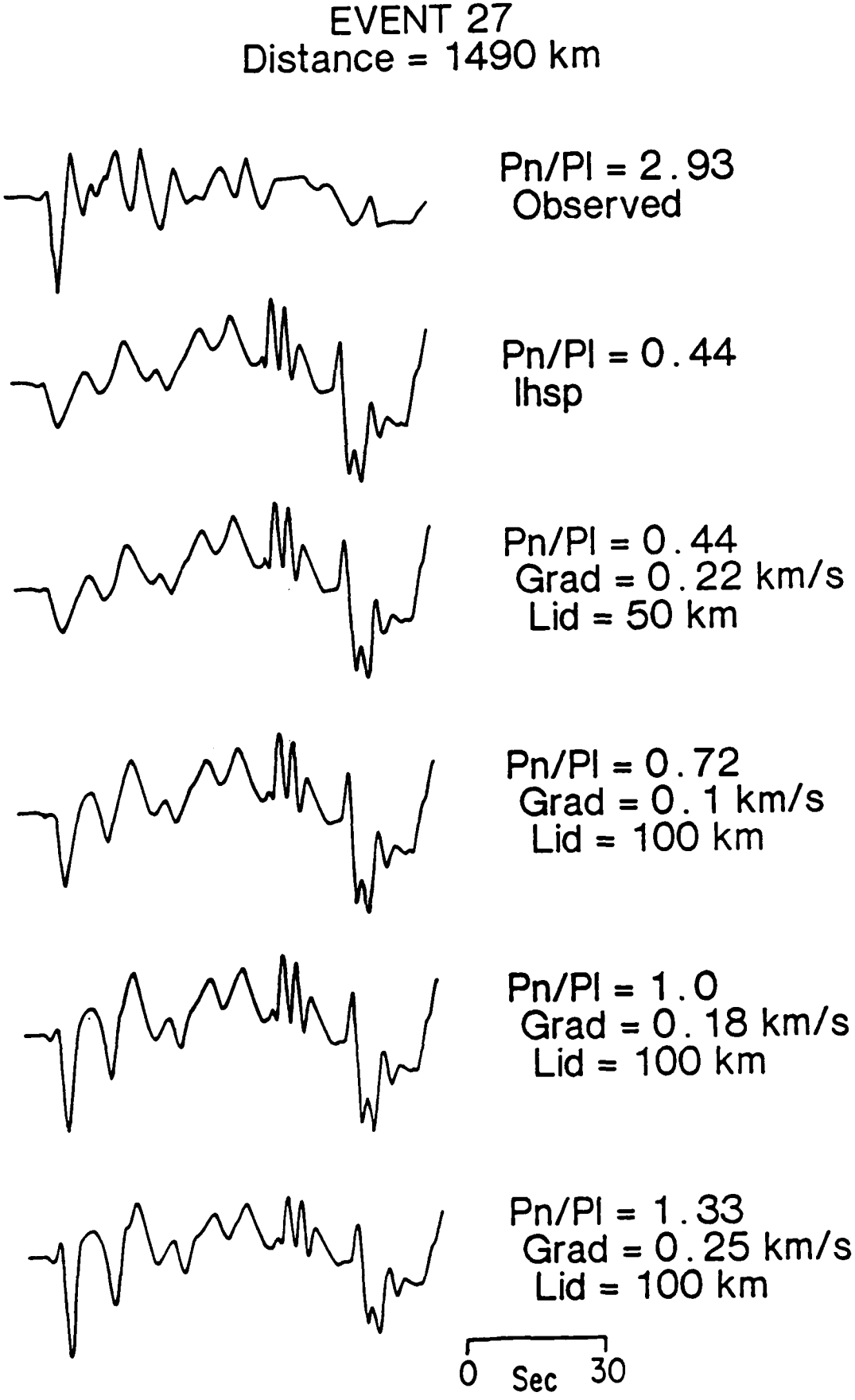
EVENT 27
Distance = 1490 km
Pn/Pl = 2.93
Observed
Pn/Pl = 0.44
lhsp
Pn/Pl = 0.44
Grad = 0.22 km/s
Lid = 50 km
Pn/Pl = 0.72
Grad = 0.1 km/s
Lid = 100 km
Pn/Pl = 1.0
Grad = 0.18 km/s
Lid = 100 km
Pn/Pl = 1.33
Grad = 0.25 km/s
Lid = 100 km
0 Sec 30

Figure 15

HINDU KUSH
EVENT 71 KBL
Distance = 1172 km

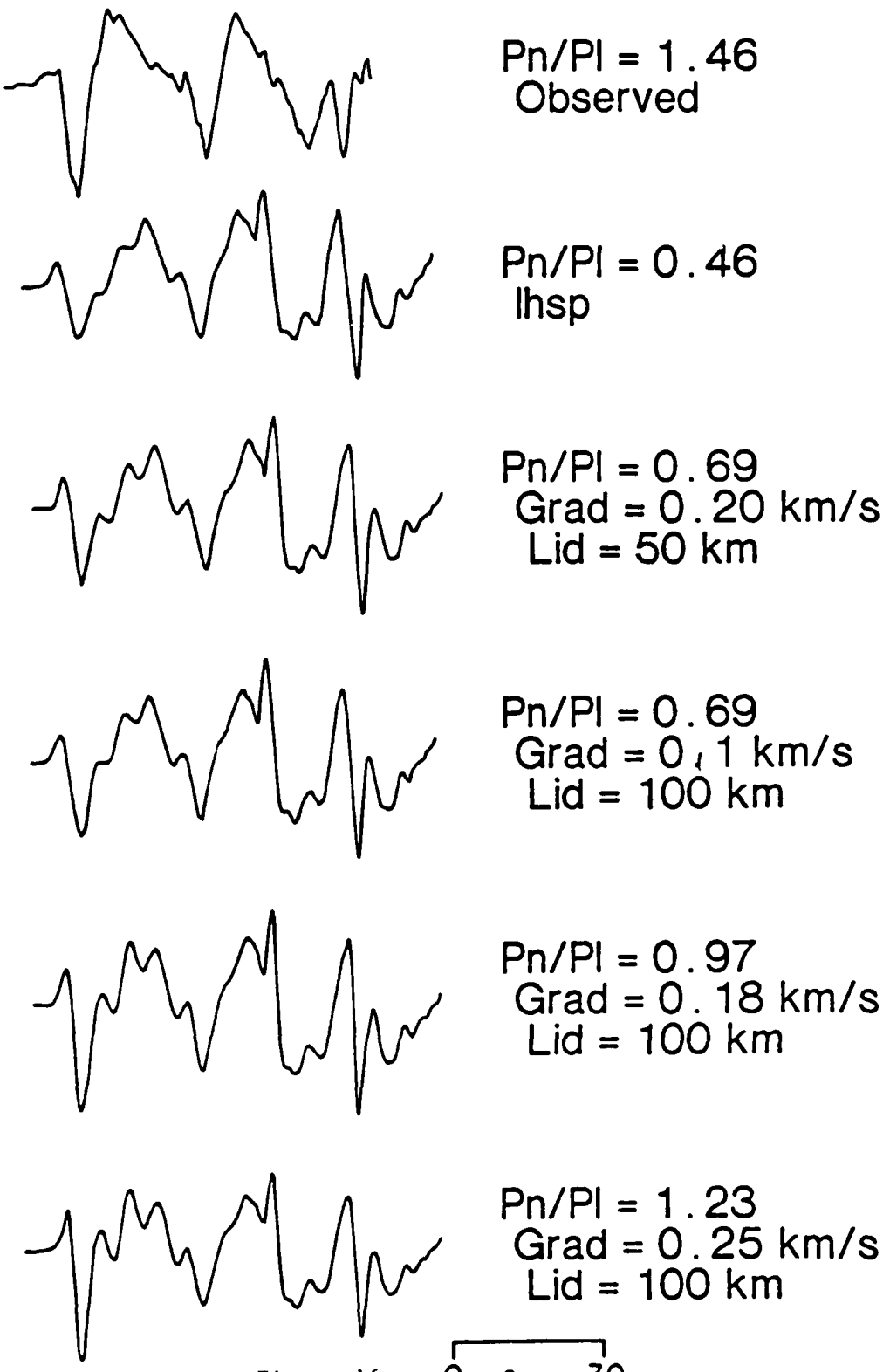

Figure 16a

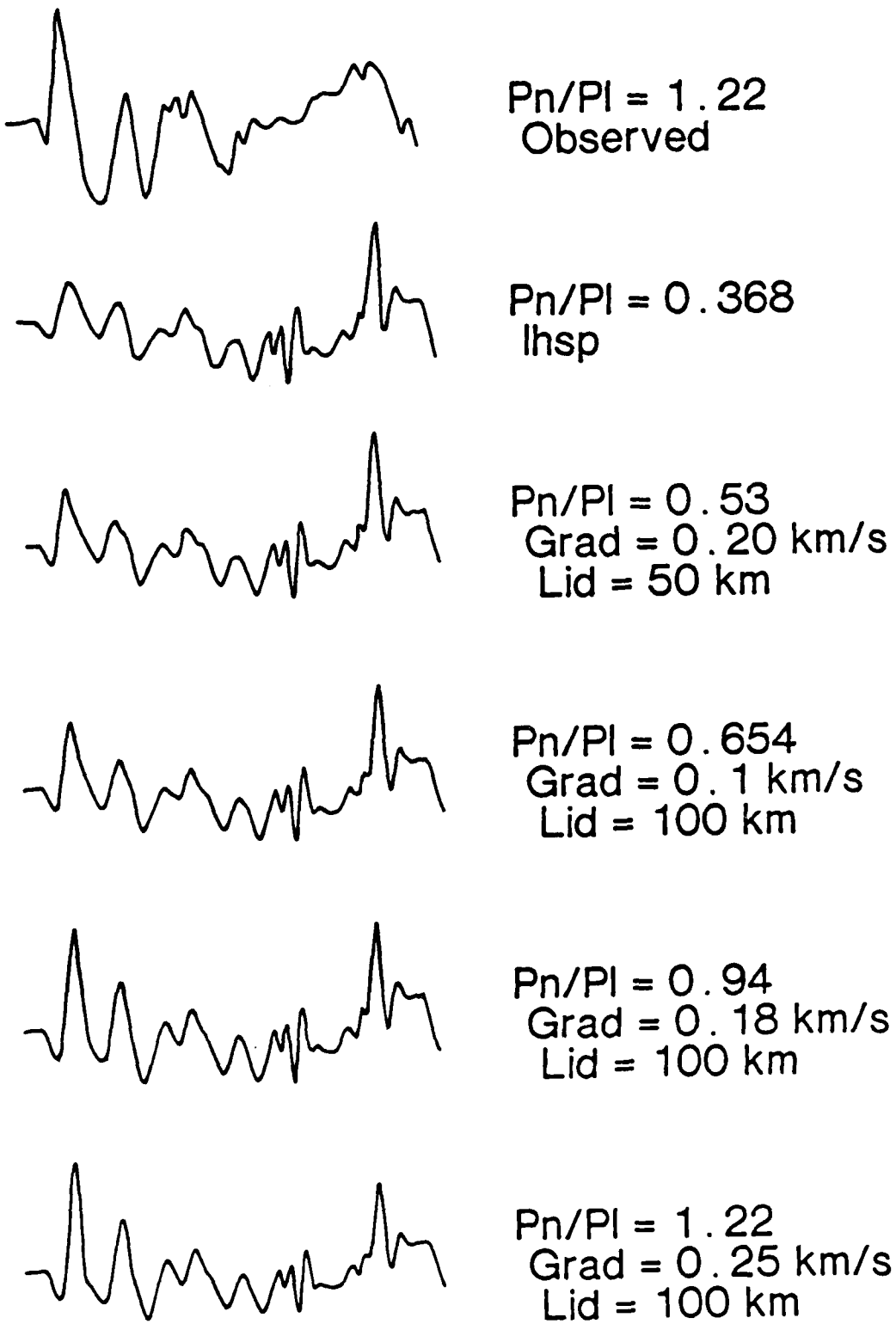
TIBET
EVENT 48 NDI
Distance = 1400 km
Pn/Pl = 1.22
Observed
Pn/Pl = 0.368
lhsp
Pn/Pl = 0.53
Grad = 0.20 km/s
Lid = 50 km
Pn/Pl = 0.654
Grad = 0.1 km/s
Lid = 100 km
Pn/Pl = 0.94
Grad = 0.18 km/s
Lid = 100 km
Pn/Pl = 1.22
Grad = 0.25 km/s
Lid = 100 km
0 Sec 30

Figure 16b

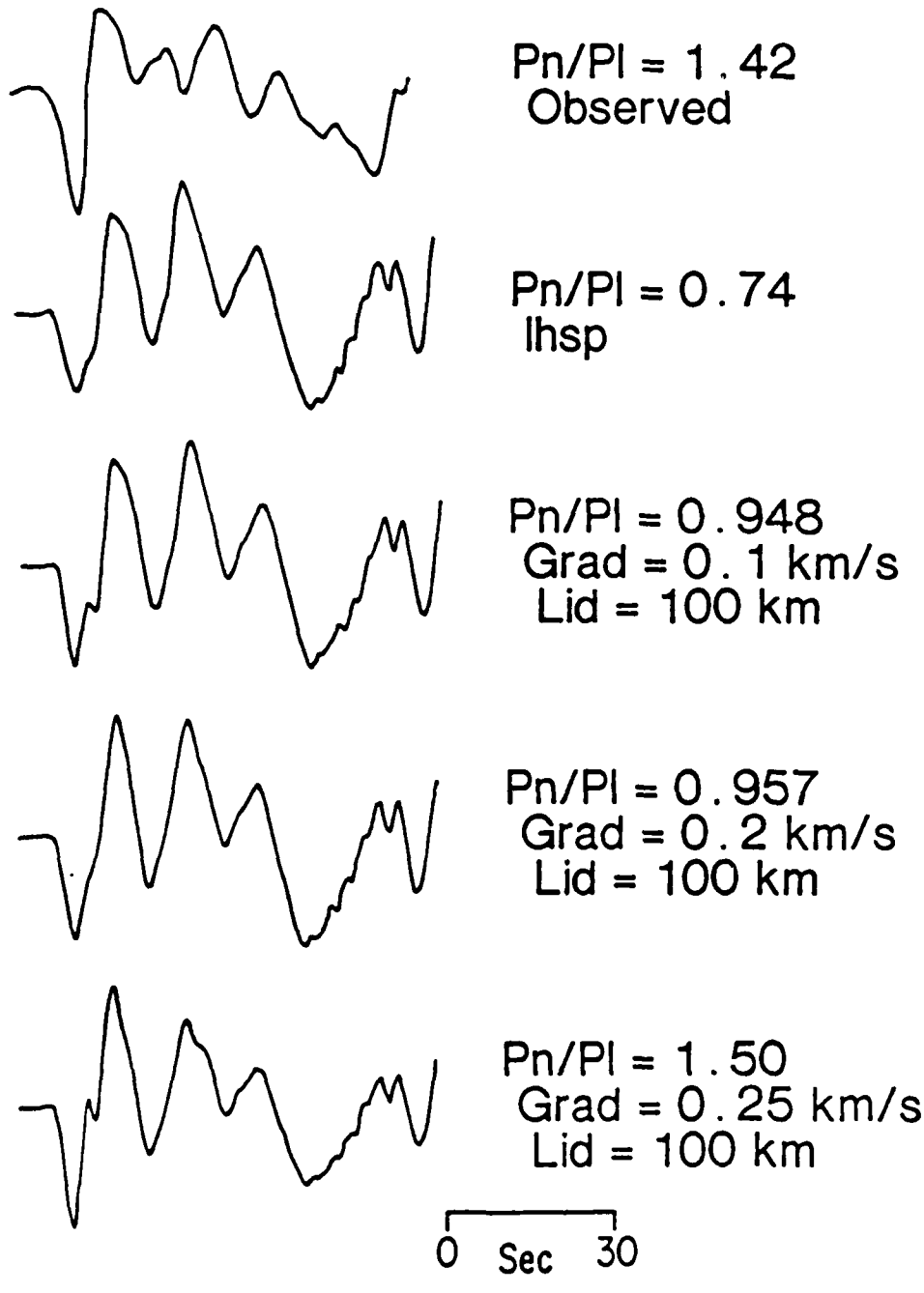
EAST INDIA
EVENT 30 CHG
Distance = 1150.7 km
Pn/Pl = 1.42
Observed
Pn/Pl = 0.74
lhsp
Pn/Pl = 0.948
Grad = 0.1 km/s
Lid = 100 km
Pn/Pl = 0.957
Grad = 0.2 km/s
Lid = 100 km
Pn/Pl = 1.50
Grad = 0.25 km/s
Lid = 100 km
0 Sec 30

Figure 16c

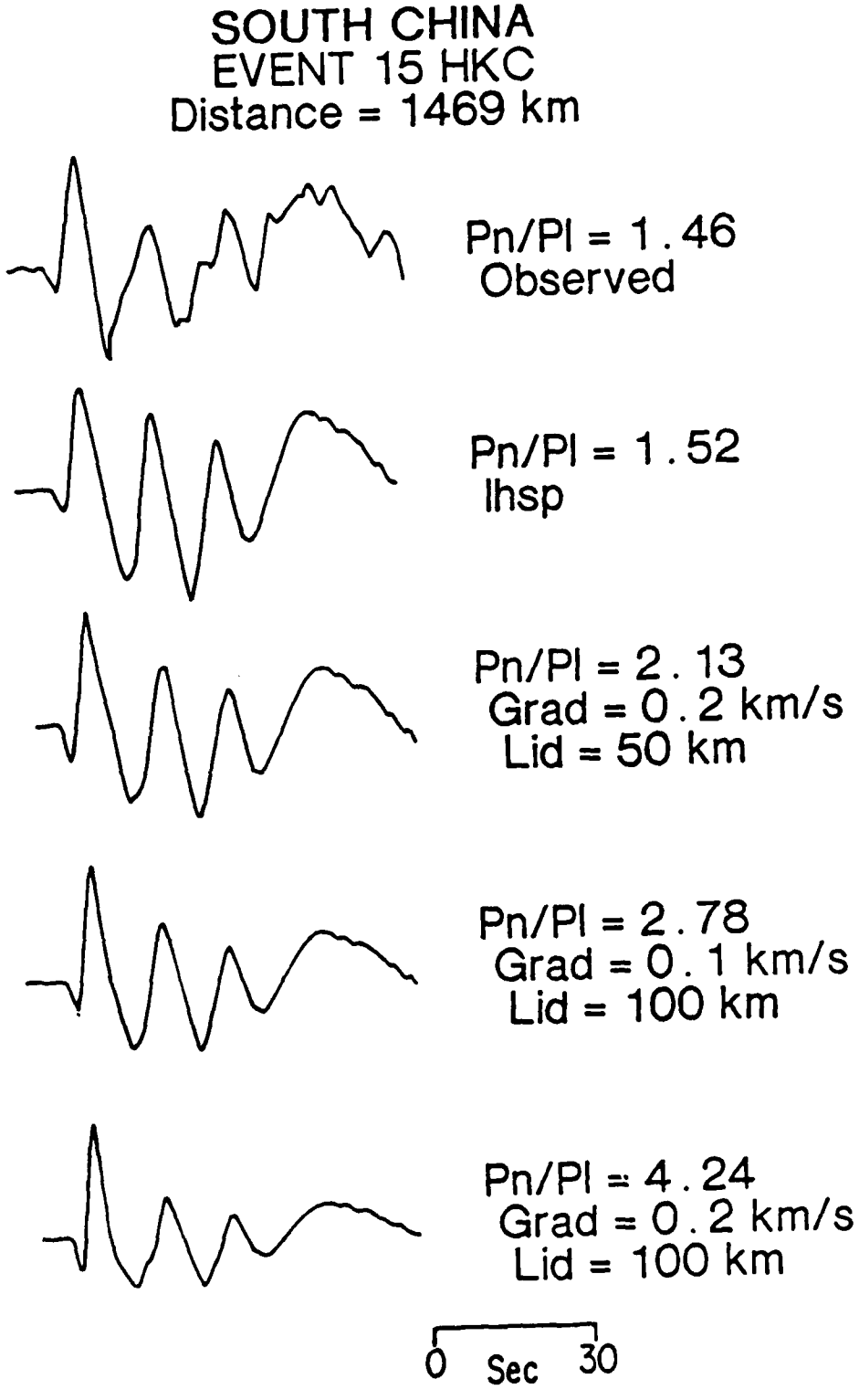
SOUTH CHINA
EVENT 15 HKC
Distance = 1469 km
Pn/Pl = 1.46
Observed
Pn/Pl = 1.52
lhsp
Pn/Pl = 2.13
Grad = 0.2 km/s
Lid = 50 km
Pn/Pl = 2.78
Grad = 0.1 km/s
Lid = 100 km
Pn/Pl = 4.24
Grad = 0.2 km/s
Lid = 100 km
0 Sec 30

Figure 16d

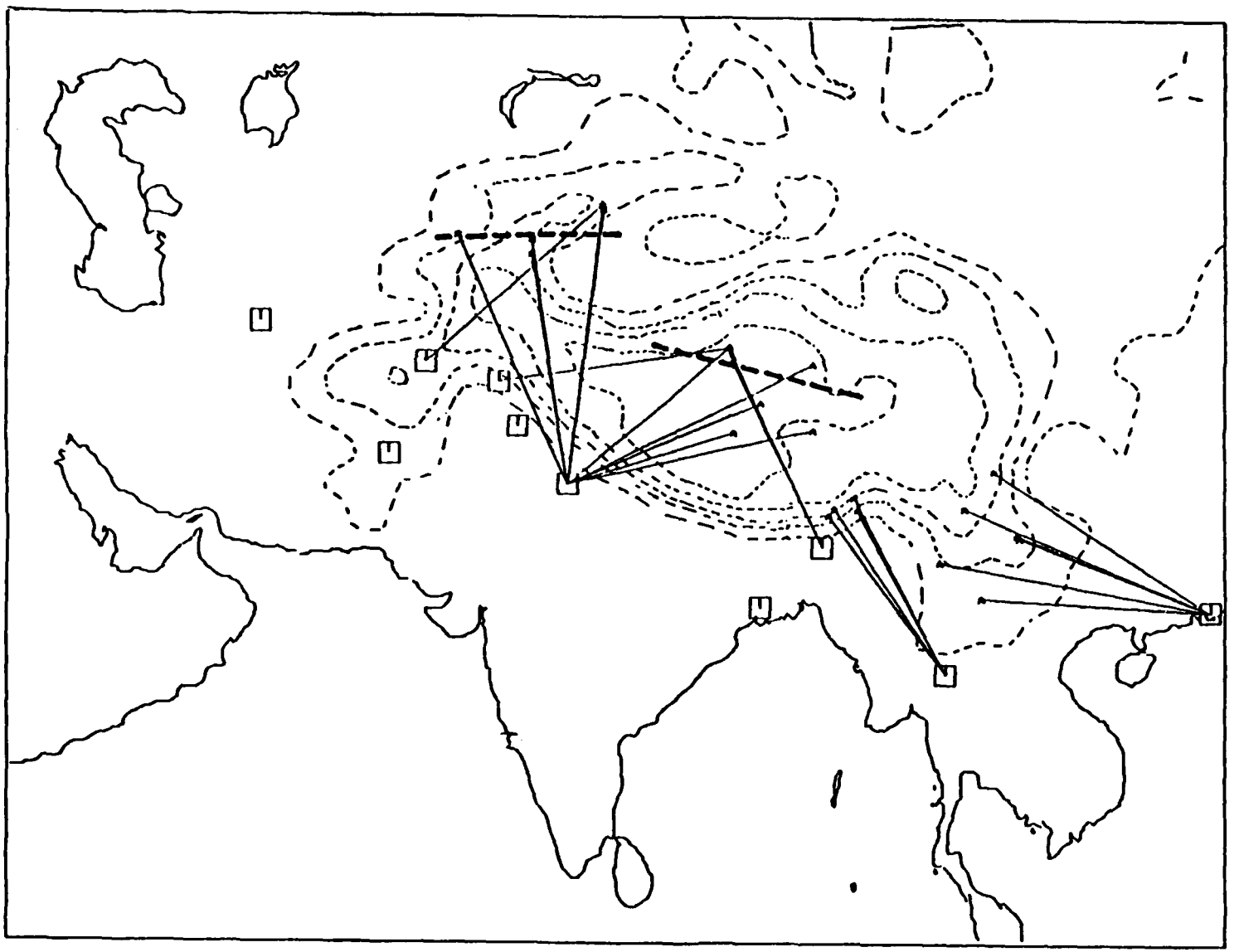

Figure 17

Figure 18

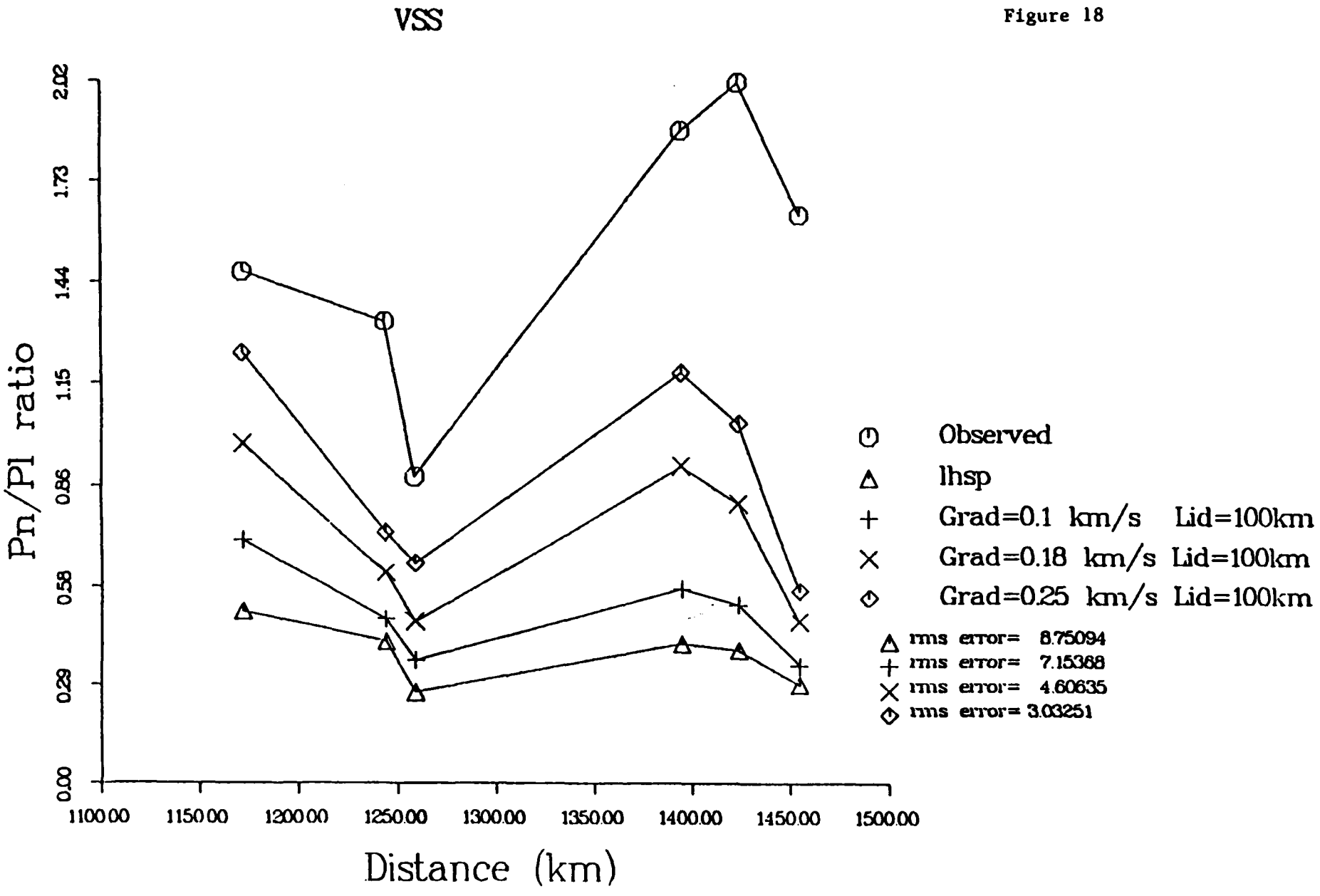
VSS
Pn/Pl ratio
0.00
0.29
0.58
0.86
1.15
1.44
1.73
2.02
1100.00
1150.00
1200.00
1250.00
1300.00
1350.00
1400.00
1450.00
1500.00
Distance (km)
Observed
lhsp
Grad=0.1 km/s Lid=100km
Grad=0.18 km/s Lid=100km
Grad=0.25 km/s Lid=100km
rms error= 8.75094
rms error= 7.15368
rms error= 4.60635
rms error= 3.03251

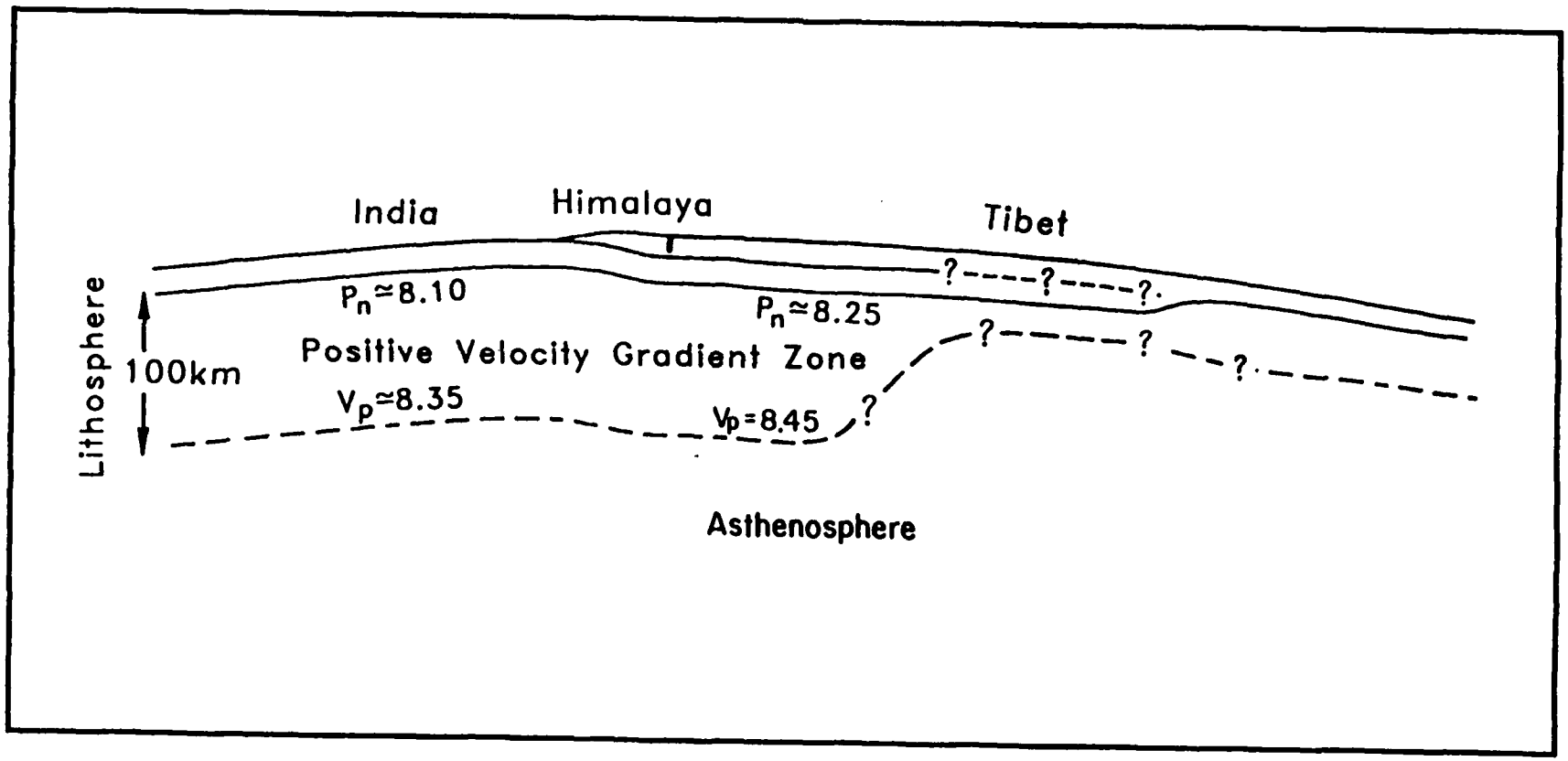
India
Himalaya
Tibet
Lithosphere
100km
$P_n \simeq 8.10$
$P_n \simeq 8.25$
Positive Velocity Gradient Zone
$V_p \simeq 8.35$
$V_p = 8.45$
Asthenosphere

Figure 19

Chapter III

Inversion of Complex Seismic Sources

Paper Submitted to

Journal of Geophysical Research

Kim Junkyoung

Terry C. Wallace

CHAPTER I

INTRODUCTION

Historically, there have been significant differences in the model of the rupture history of an earthquake as viewed by geologists and seismologists. There are many examples of earthquakes which show an apparent poor correlation of epicenter and focal mechanism with recognized Holocene surface faulting features. Further, the surface expressions of faulting are usually much more complicated than the seismologically derived source models. Recently, seismologists have begun to introduce source complexities and improved seismicity data have shown that rupture may occur on irregular or multiple surfaces. The results from the waveform inversion of shallow earthquakes using moment tensor source representation, with the constraint that the source be purely deviatoric (but not necessarily a pure double-couple) occasionally show substantial non-double-couple components (Sipkin, 1987). There are a variety of possible physical explanations for a complex seismic source, and these interpretations are very important for deciphering the active tectonics of any complex region. The detailed mapping of a seismic source requires a more sophisticated algorithm for determining earthquake source parameters than the standard moment tensor inversion. We have developed a time dependent moment tensor source representation to investigate the nature of complex seismic source mechanisms.

The problem of mapping out the seismic source parameters from the observed seismic waveform has evolved through several stages: from the traditional forward fitting of a synthetic waveforms to the observed seismograms by trial and error, to the

direct inversion of the observed seismogram. Inversion using the moment tensor source representation has become rather routine, and has been applied to normal mode data (Gilbert and Dziewonski,1971; Buland and Gilbert,1976), surface waves (Mendiguren,1977), and body waves (Stump and Johnson, 1977; Langston, 1981; Sipkin,1982). The advantage in using the moment tensor representation in the determination of the source parameters is that it can be posed as a linear inverse problem. Moreover, one of the characteristics of the moment tensor source representation is that it does not require **a priori** information of the seismic source model such as a double-couple or explosion source. Two main assumptions of the first-order moment tensor source representation are that of a point source, and that Green's functions can be constructed which will adequately model the effects of propagation.

When inverting the observed waveforms for the source parameters of an earthquake, it is usually assumed that the entire energy release can be modeled as a simple point source which involves rupture motion along one geometrically simple fault plane. While many earthquakes can be modeled using this conventional approach, the constant moment tensor assumption throughout the whole seismic energy release breaks down for complex sources where the fault orientation and the slip direction may change with time. In this thesis, the conventional algorithm for moment tensor inversion is referred to as the time independent moment tensor formulation (TIMT).

To simultaneously map both geometrical and temporal variations of the seismic sources for a complex rupture history from observed body waves, it is preferable to use a time dependent moment tensor inversion (TDMT). This removes the constraint of a constant moment tensor assumption throughout the episode of seismic energy release. The time dependent moment tensor inversion resolves six moment tensor elements independently as a function of a time by using linear formulations in the frequency domain. Although this algorithm allows more degrees of freedom in the inversion

process, in general we have determined that the moment tensor elements are resolved sufficiently well to map source complexity (source multiplicity, source time function of each source, and focal depth) by using additional physical constraints such as the degree of temporal consistency among six different moment tensor elements, causality of source time function, and the magnitude of CLVD (compensated-linear-vector-dipole) component.

Sipkin (1982) presented a similar algorithm, although the inverse problem is solved in the time domain. Sipkin uses a multichannel signal enhancement (MSE) algorithm, which determines source characteristics by solving directly the convolution equation in the time domain without losing time-dependency of moment tensor elements by the use of Claerbout's matrix formulation (1976) of the convolution equation.

The purpose of this dissertation is to develop and test a time-dependent moment tensor inversion technique. We consider three real examples; an earthquake doublet in Yemen (Dec. 13, 1983), the San Fernando (Feb. 9, 1972), and Kern County (July 21, 1952) earthquakes. Before applying the TDMT to data of the real earthquakes, the results of the conventional time independent moment tensor inversion are also compared to those of the time dependent moment tensor inversion technique for the synthetic waveform examples.

CHAPTER II

THEORY OF THE TIME DEPENDENT MOMENT TENSOR SOURCE REPRESENTATION

Introduction

It has long been known that the fault plane associated with most large earthquakes is not a simple planar surface. It is hard to imagine two large volumes of earth material moving past each other on a simple flat fault plane. However, most internal seismic source representations of earthquakes have been described in terms of simple discontinuities in displacement or strain across a rupture fault surface. The most common description of the seismic source which appears as surface displacement or strain is a moment tensor source representation. The moment tensor source representation describes the elastodynamic responses to a point seismic source in terms of a linear combination of Green's functions and it has been used widely for waveform inversion (Gilbert, 1970; Geller, 1976; Stump and Johnson, 1977; Langston, 1981; Barker and Langston, 1982). For example, a pure dislocation seismic source without volume change can be described as the linear sum of five body force couples, with the constraint that the trace of moment tensor equals zero. Volumetric sources, such as underground nuclear explosion, can be described as the linear sum of six body force couples. One of the most important characteristics of the moment tensor representation of the seismic source is that it does not require that a source model be specified, which can result in arguments about direct physical interpretation of the non-double-couple component of the moment tensor. A moment tensor is a symmetric

second order tensor which depends on both seismic source strength (seismic moment) and fault orientation by combination of the six moment tensor elements. It characterizes and contains all the information about the seismic source during the earthquake that can be learned from the observed seismic waveforms.

The two main assumptions of the conventional moment tensor source representation are that it can be approximated as a point source and that adequate Green's functions are available to describe the response of the earth structure. The point source assumption can be shown to be valid if the distance from source to receiver is large compared to the actual source volume and if the seismic waves of interest have wavelengths which are much longer than the linear dimensions of the associated fault. Both of these conditions are met when working with long period WWSSN body waves recorded at teleseismic distances.

Time Independent and Dependent Moment Tensor Approach

Assuming the seismic source can be represented by equivalent coupled body forces alone and constraining the moment tensor representation to be a second order tensor, the elastodynamic response of the earth to the seismic source becqmes

$$Uk(x',t') = Gki,j(x',t';0,0) * Mij(0,t') \quad (1)$$

where Uk is the displacement in the k-th direction, Gki,j is the elastodynamic Green's function, Mij is a set of time dependent moment tensors, and * denotes convolution (Stump and Johnson, 1977). k denotes vertical (k=1), radial (k=2), and tangential (k=3) motion. i denotes the direction of and j denotes the responding surface to the physical moment of given force system, respectively. The primed variables are defined in the receiver's coordinate system and the unprimed variables are defined in the seismic source's coordinate system.

In order to invert observed waveforms for seismic source parameters in terms of the seismic moment tensor, two avenues of approach are available. The first is the conventional time domain (time independent) approach, and the second is the frequency domain (time dependent) approach. The algorithm presented in this study is that of time dependent moment tensor, but for the completeness, the conventional time independent approach is covered first.

The time independent approach is useful when it is reasonable to assume that all the components of Mij(0,t) have the same time history, S(t), which is known **a priori**. If this is the case, equation (1) becomes

$$Uk(x',t') = [\ Gki,j(x',t';0,0)*S(t)\ ]\ Mij \qquad (2)$$

where Mij is now a set of constants (time independent moment tensor elements) and the only unknown in the equation. S(t) is the source time function, which has both information on duration of the seismic source and the history of seismic source excitation, (for example, rapid or slow rise time). Therefore, equation (2) becomes a linear formulation for application to the seismic waveform inversion. However, when the source time function is the principal object of the waveform inversion such that the fault orientation and the slip may change with time, the formulation becomes non-linear; waveform inversion must be parameterized in terms of both source time function, S(t), and **constant** moment tensor, Mij. Moreover, for complex seismic sources, Mij components are no longer constants throughout the seismic energy release since the fault orientation changes with time, making it much more complicated to do waveform inversion.

When the source time function S(t) can not be reasonably assumed, or when it is desirable to map out simultaneously both geometrical and temporal variations of the seismic source (complex rupture histories on multiple fault surfaces) from the observed

waveforms, Stump and Johnson (1977) suggested time dependent moment tensor inversion, which is a point-by-point linear inversion of Mij in the frequency domain. The inversion in the frequency domain is equivalent to the deconvolution process where the Green's functions are deconvolved from the observed waveforms in order to resolve moment tensor elements. They applied this algorithm mainly to the near field data for underground nuclear explosions. Taking the Fourier transforms of equation (2) reduces it to an equivalent form in the frequency domain,

$$Uk(x',f) = Gki,j(x',f;0,0)\ Mij(0,f) \tag{3}$$

where Gki,j is the Green's function in the frequency domain, and Mij is a set of time dependent moment tensor elements in the frequency domain. For this formulation, time dependent moment tensors Mij have all the information about the seismic source during the earthquake that can be learned from the observed seismic waveforms. This is because the time dependent moment tensor algorithm resolves six moment tensor elements independently as a function of time by using the formulation in the frequency domain.

Unfortunately, at every point of the inversion in the frequency domain, this algorithm allows 5 (for the assumption of purely deviatoric source) or 6 (volume change source or isotropic source) free parameters in contrast to the conventional time independent moment tensor algorithm. The inversion for the moment tensor in the frequency domain can also allow considerable trade-off of time function and the effects of unknown earth structure in the Green's functions, as suggested by Langston (1981). Even though there is considerable trade-off in determining Mij components using the time dependent moment tensor algorithm, inversions for various earth structure models and different source depths using corresponding Green's functions can mitigate the problem. Moreover, we have determined that time dependent moment tensor elements,

Mij(t), are resolved sufficiently well enough to map source complexity (source multiplicity, source time function of each source, and focal depth) in the presence of additional constraints such as the degree of temporal consistency among six different moment tensor elements, causality of source time function, and the size of CLVD component. Finally, though most actual data does not naturally and exactly constrain the appropriate physical source parameters which could then be clearly interpreted, using these possible physical constraints, we can resolve the most likely or most reasonable source parameters with given assumptions.

Inversion

The inversion procedure for the moment tensor elements can be described in matrix notation as follows:

$$U = G M. \tag{4}$$

In the time domain inversion as shown in Table 1, U is a N-dimensional vector composed of N-sampled values from any displacement component at a given station. The matrix G is composed of Green's functions for corresponding displacement components at stations corresponding to the U vector. The vector M is composed of the moment tensor elements. In principal, if U is sampled at every 0.25 second, typical for long period teleseismic body wave inversion, only 1.25 or 1.5 seconds of the observed seismograms are needed to resolve moment tensor elements, M. It is possible that only one component (vertical, radial or tangential) of the one given station with more than five or six sampled points is sufficient to determine the moment tensor elements M. Because of poor resolution of the waveform inversion process, more than one component of seismograms is usually inverted as well as more than 20 to 30

seconds of the seismogram. Therefore, waveform inversion of the linear matrix system of the moment tensor source representation is usually overdetermined.

Table 1. Simultaneous Equation of U = G M for Time Domain Inversion

		Gk1,1	Gk1,2	Gk1,3	Gk2,2	Gk2,3	
AT TIME=T1	U1	G1	G1	G1	G1	G1	M11
AT TIME=T2	U2	G2	G2	G2	G2	G2	M12
AT TIME=T3	U3	G3	G3	G3	G3	G3	M13
.	.	.	.	.	.	.	M22
.	.	.	.	.	.	.	M23
.	.	.	.	.	.	.	
.	.	.	.	.	.	.	
AT TIME=Tn	Un	Gn	Gn	Gn	Gn	Gn	

In the frequency domain, equation (4) is formed separately at each frequency point (Table 2). The vector U can be formulated as any combination of frequency responses of different kinds of the displacement components at the same station or the same kinds of the displacement components at different stations. At each frequency point, each two columns of G matrix are composed of the frequency responses and corresponding displacement components at the station (to U vector), and each two rows of G matrix are composed of the frequency responses to each moment tensor element. This matrix equation is equivalent to simultaneous linear equations with complex variables. Then the generalized linear inverse technique is used to solve this matrix form with appropriate Green's functions.

Green's Functions

Dislocation source theory (Helmberger, 1974; Langston and Helmberger, 1975) states that an arbitrarily oriented shear dislocation can be described as a combination of three fundamental dislocation sources, which we represent with our three Green's functions. These three Green's functions represent: (1) a vertical strike-slip

Table 2. Simultaneous Equation of U=G M at each Frequency Point, fn

	U1R	G1R	-G1I	G1R	-G1I	G1R	-G1I	G1R	-G1I	G1R	-G1I		M11R
sta1	U1I	G1I	G1R	G1I	G1R	G1I	G1R	G1I	G1R	G1I	G1R		M11I
	----	----	----	----	----	----	----	----	----	----	----		M12R
	U2R	G2R	-G2I	G2R	-G2I	G2R	-G2I	G2R	-G2I	G2R	-G2I		M12I
sta2	U2I	G2I	G2R	G2I	G2R	G2I	G2R	G2I	G2R	G2I	G2R		M23R
	----	----	----	----	----	----	----	----	----	----	----		M23I
	U3R												M22R
sta3	U3I												M22I
	----	----	----	----	----	----	----	----	----	----	----		M23R
	.												M23I
	.												
	.												
	----	----	----	----	----	----	----	----	----	----	----		
	UnR	GnR	-GnI	GnR	-GnI	GnR	-GnI	GnR	-GnI	GnR	-GnI		
stan	UnI	GnI	GnR	GnI	GnR	GnI	GnR	GnI	GnR	GnI	GnR		

(2) a vertical dip slip dislocation and (3) a dip slip dislocation on 45 degree dipping fault (observed at a 45 degree azimuth). *It is possible to represent any fault and its* corresponding waveforms as a weighted sum of the three Green's functions. The different weightings depends on strike, dip, and rake of the seismic dislocation source, and are transcendental functions (therefore of non-linear form). In contrast to this, the moment tensor source representation, which inherently has six fundamental unknowns, requires six Green's functions. These six Green's functions can be formed from the recombination of three fundamental Green's functions using a weighting of the receiver azimuth angle as shown in equations (5) and (6) (Barker, 1984). The Green's functions of vertical (k=1), and radial displacement (k=2) in the moment tensor formalism can be written:

$$G_{k1,1} = -0.5 H_{k1} \cos(2Az) + 0.5\, H_{k3}$$

$$G_{k2,2} = 0.5 H_{k1} \cos(2Az) + 0.5\, H_{k3}$$

$$G_{k1,2} = H_{k1} \sin(2Az) \qquad (5)$$

$$G_{k1,3} = H_{k2} \cos(Az)$$

$$G_{k2,3} = H_{k2} \sin(Az)$$

where $G_{ki,j}$ is a set of new Green's function for the moment tensor source representation and H_{ki} is i-th component of three fundamental Green's functions (i=1, vertical strike slip; i=2, vertical dip slip; i=3, 45 degree dip slip), and Az is the receiver azimuth angle. The Green's functions for a tangential displacement (k = 3) for the moment tensor formalism are given by

$$\begin{aligned} G_{31,1} &= 0.5\, H_{31} \sin(2Az) \\ G_{32,2} &= -0.5\, H_{31} \sin(2Az) \\ G_{31,2} &= -H_{31} \cos(2Az) \\ G_{31,3} &= -H_{32} \sin(Az) \\ G_{32,3} &= H_{32} \cos(Az). \end{aligned} \tag{6}$$

Green's functions for the moment tensor inversion in this study were calculated by the generalized ray theory technique, that is, summing responses for different rays from vertical strike slip, vertical dip slip, and 45 degree dip slip embedded at a particular depth for the assumed velocity structure of the source region. Sufficient numbers of rays which give significant responses such as the interferences between P, sP, and pP phases are included for the calculation of each Green's function but crustal reverberations under the receiver are neglected to avoid complexities in the source parameters. It is assumed that the velocity structure of the source region is a horizontally homogeneous and an isotropic planar medium. This assumption is, at least, reasonable in the long period, teleseismic data study. Green's functions are also convolved with an attenuation (t^*) operator, geometric spreading, and the instrument response (WWSSN long-period).

Generalized Inverse Technique and Analysis of Eigenvalue System

The solution of the matrix equation (4) in the frequency domain is overdetermined. The number of the observations (the total number of seismograms used for inversion) is usually much larger than the number of model parameters (the elements of the moment tensor) as in the case for most geophysical inverse problems. A linear least squares formulation for this problem, sometimes called the normal equations, can be written in matrix notation as follows:

$$G^T G\, M = G^T\, U \tag{7}$$

where $G^T G$ is a symmetric, positive definite matrix. The properties of the matrix $G^T G$ are very useful in the solution of equation (7). Even so, the matrix $G^T G$ can contain inaccuracies and present numerical difficulties. Such numerical problems in the inversion can be quite severe when the dimensions of $G^T G$ becomes large. Equation (7) above does not suggest any measure of quality for the system identification or solved model parameters. Instead of simply solving the square matrix system in equation (7) numerically, the generalized inverse technique (Wiggins, 1972) using single value decomposition (SVD) of the non-square matrix G is applied to solve the linear deconvolution problem in the least squares sense. The advantage of this is that it includes the quality estimates of the solved model parameters, and provides a measure of the tradeoff of resolution and stability. The eigenvalue problem of the square matrix can be modified to the single value decomposition problem for the non square general matrix. Following the single value decomposition the matrix G which maps the model parameters into the predicted data vectors can be written as

$$G = U_p\, \lambda_p\, V_p \tag{8}$$

where U_p are the p N-dimensional eigenvectors of GG^T, V_p are the p M- dimensional eigenvectors of G^TG, and λ_p is the p by p diagonal matrix with p single values (positive square roots of non-zero eigenvalues shared by GG^T or G^TG) along the diagonal. Then the generalized inverse operator is defined as:

$$G_g^{-1} = V_p \lambda_p^{-1} U_p. \tag{9}$$

Using single value decomposition for the non-square matrix G inherent in the generalized inverse technique, the eigenvalues and eigenvectors of the square matrix G^TG can give, before any actual inversion, information on both the stability and resolution of each inversion. Since the matrix G is actually composed of combined Green's functions of the receivers in the same order as the observed data, an adequacy of the station distribution in azimuth angle and epicentral distances for the selection of the receiving stations in the waveform inversion can also be tested using the eigenvalues and eigenvectors of the square matrix G^TG at each inversion point.

Experience indicates that some single values may become small, that is nearly singular, but rarely do they vanish completely. When a given matrix is nearly singular, the solution vector tends to grow without bound since a small single value can affect the solution adversely. In such an unstable eigenvalue system, any noise in observed data, even if small, can give rise to large changes in model parameter estimates. In order to reduce the difficulties when the matrix G^TG is nearly singular, we choose an alternate least squares problem which is known as the damped least squares method or ridge regression. This method is a hybrid because it combines the steepest descent method and simple unconstrained least squares method. For this damped least squares method, the model parameter vector can be described as

$$M = (G^TG + b\ I)^{-1}\ G^T\ U \tag{10}$$

where b is a damping factor and I is an identity matrix (*Lines and Treitel, 1984*). The principal difference between the unconstrained least squares method and the damped least squares method is that the damped least squares method produces a stable condition to avoid singularities or near singularities in the matrix G^TG. The damping factor b has the effect of adding a constant value to each diagonal term of G^TG. Hence, none of the eigenvalues of G^TG vanish. Also, terms that contain $1/\lambda$ for the small eigenvalues are damped.

In order to find a single optimal damping factor at each inversion point in the frequency domain, we investigated the trends of the trade-off between fitting the observed data and minimizing the deviation from the undamped solution. This produced a series of N independent damping factors, where N is the number of frequency points. At each frequency point, model parameter estimates were found for 41 different values of the damping factor, b, in equation (10), which ranged from zero to 10E-02. The number of b values to search for optimal damping value at each frequency domain inversion point was determined considering the size of minimum and maximum size of the single values and the shape of resultant tradeoff curves. In this manner, a trade-off curve was obtained at each frequency domain inversion point. A typical trade-off curve is shown Figure 1, where the x-axis represents the ratio of the damped model parameter estimate to the undamped model parameter estimate and the y-axis represents the ratio of the amount of misfit of the observed data in the frequency domain to the amplitude of the original observed data. From each trade-off curve at each frequency domain inversion point, the optimal damping value is based on finding the maximum curvature along the trade-off curve.

Using these optimal damping factors at the corresponding frequency domain inversion points, a set of damping factors was obtained. The procedure does, however, introduce a large number of degrees of freedom into this manner (the same number as

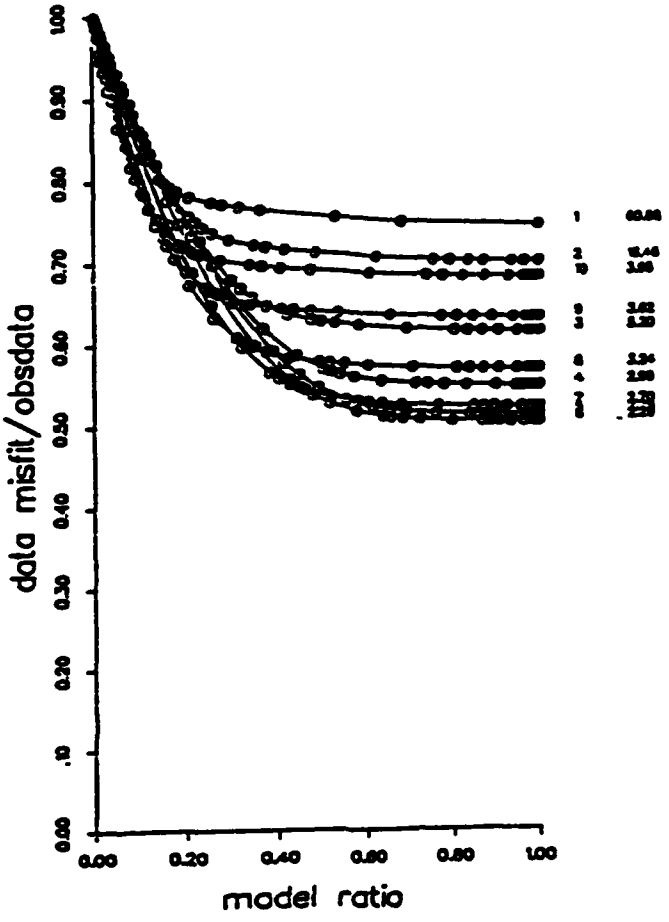

Figure 1. Trade-off curves to find optimal damping factors at each inversion point at frequency domain (from the first to 10th inversion point). Each trade-off curve is composed of 41 values of damping factors for trial. X-axis represents the ratio of the magnitude of damped model parameter estimation vector to that of the undamped model parameter estimation vector and Y-axis represents the ratio of the magnidtude of the misfit of the observed data vector to the magnitude of the observed data vector.

inversion points). It is possible to reduce the degrees of freedom introduced by replacing the set of independent damping factors by a lower order polynomial fit to the damping values. An orthogonal polynomial curve fit, in the least squares sense, was applied to the damping factor values and resulted in a 10th order polynomial. The resulting damping factors from this polynomial functions were, then, used for a damped least squares inversion.

Causality and Temporal Consistency

The time-dependent moment tensor technique will map all the effects of noise or inadequencies in the Green's functions into the resultant moment tensor elements. For this reason the quality of the moment tensor solution must be assessed on the basis of a series of subjective constraints. These constraints are causality and temporal consistency between different moment tensor elements. Procedurally, this amounts to comparing the shape of the moment release. To do this we pick an optimal time window and then estimate an adequate depth of each seismic source. The first condition is satisfied by finding a time window in which all six moment tensor elements vary with time in a reasonably consistent manner. Although each element is allowed to have an independent time history in the inversion process, it would be unphysical if three of the six components change rapidly with respect to time while the remaining three components change slowly with time. By fulfilling the requirement that the moment tensor elements show temporal consistency among six time dependent moment tensor elements, we fit the **a priori** assumption of a force-couple source. The second condition is the causality of source time function or the form of the moment tensor at onset. The first part of seismic energy release has to start at time zero, since the first motion of all waveforms for the waveform inversion are lined up and then deconvolved with corresponding Green's functions. This is especially important when

the seismic sources are composed of multiple subevents with different focal depths. A third condition of a quality solution is that the shape of all the time dependent solutions are robust with respect to filtering with the various combinations of frequency components as proved with the synthetic examples. The reason for the shape stability requirement is that the seismic energy release by actual physical displacement will be much more robust in contrast with the apparent seismic energy release with respect to the changes of frequency range. This also requires that there be a physical compatibility between subevents. Time windows which give nearly the same strike and dip angles but a rake which differs by 180 degrees compared to the focal mechanisms of the neighboring time windows are avoided. Occasionally, even though some time windows show a temporal consistency, this kind of overshoot or edge effect inherently caused by use of sinusoidal functions to synthesize time dependent moment tensor functions in the Fourier Transform maps into an unphysical seismic energy release process. This overshoot phenomena in the time dependent moment tensor inversion could be compared to the negative component of the source time function from inversions with the constant moment tensor assumption. Since each seismic event has finite amount of seismic energy release, time windows for a specific event can be constrained within a reasonable time boundary limits. The final condition of the quality of a solution is satisfied if the focal mechanism resolved for given time windows agrees to **a priori** geologic information such as surface rupture patterns and tectonic environment.

CHAPTER III.

SYNTHETIC EXAMPLES

Introduction

The time-dependent moment tensor inversion algorithm described in the last section has been tested with a set of experiments, using synthetic data generated for known shear dislocation seismic sources. These experiments are designed to test the feasibility and characteristics of the time-dependent moment tensor inversion algorithm, especially when analyzing time-dependent, complex seismic sources which contain source multiplicity, changing slip parameters, and interferences between subsources. One of these goals, specifically, is to investigate how well the source parameters such as source time function, scalar moments, focal depth and focal mechanisms can be resolved for different kinds of source complexity. At the same time, the trade-off between source depth and focal mechanism is investigated. The effect of using of Green's functions of inappropriate source depths on the causality and temporal consistency of source time function is also investigated. Finally, we investigated whether source complexity and inadequate Green's function will actually cause the inversion results to have significant non-double-couple components, as suggested by Barker and Langston (1982) and Sipkin (1986).

When the source depth is a critical source parameter in the study of earthquakes, it can be a difficult parameter to determine, since depth determination is an intrinsically non-linear process and may be biased by the trade-off with the source time function and focal mechanism in the moment tensor inversion. However, Sipkin

(1986) suggested in his MSE algorithm that the source depth can be found by maximizing variance reduction. In contrast to this constraint on determining source depth to fit the best of the observed waveforms, we suggest new physical constraints such as degree of temporal consistency and causality among six different moment tensor elements. The CLVD component which has been used as a measure of the inadequacy of the resolved source parameters is also considered in our study. Our synthetic experiments demonstrated that these new constraints can minimize trade-offs between source depth, focal mechanism, and source time function and can also improve significantly the confidence levels of the source parameters from moment tensor inversion. For moment tensor inversion these new constraints play a much more important role in the investigation of complex seismic sources. After the best source depth is determined, the focal mechanism is resolved solely from these moment tensor elements.

The evolving nature of the seismic source can be thought of a series of subevents, each with its own depth and fault geometry. It is difficult to isolate these subevents from one another. We do this through our constraint of temporal consistency. We pick an adequate time window where there is strong temporal consistency of all the moment tensor elements and calculate the area under each moment release function. Then these combinations of moment tensor elements are converted to the corresponding geometric fault orientation, using a focal mechanism with best-fit double-couple source.

The results for the time-dependent moment tensor inversion are compared to the results given by a conventional time-independent moment tensor inversion which assumes the constant moment tensor elements throughout the whole energy release. For this study, the experiments with synthetic data for source complexity are conducted for three kinds of different complex seismic source types. Three complex

sources considered here are; (1) a double event with change in orientation of the fault plane as a function of a time; (2) a double event with a difference in source depth between the two subevents; (3) a double event with temporal overlap and a change in orientation between the first and the second subevents. For all three synthetic examples, the relative seismic moments of the first subevent is twice that of the second subevent.

The interpretation of the resulting five time-dependent moment tensor elements is constrained by requiring a non-volumetric, or a purely deviatoric source, M33=-(M11+M22). The eigenvalues of the resultant moment tensor can be decomposed in many ways. One possibility is that the moment tensor is decomposed into two double-couples: a major and minor double- couple. This could represent simultaneous displacements on two orthogonal fault planes having two orientations. Both the major and minor double-couple source have the same source time history and the principal axes (P, T, and B axes) have different directions between two simultaneous events at the same place. This type of seismic source is fairly unphysical. The minor double-couple mechanism in the two double-couple decomposition could be interpreted as noise due to laterally varying structure (Wallace, 1985). A decomposition of the moment tensor into a best-fit major double couple component and minor compensated-linear-vector-dipole (CLVD) component which shares the same principal stress system seems to be the most reasonable assumption for these synthetic data examples. When the moment tensor is decomposed into major double-couple (DC) components and minor compensated-linear-vector-dipole (CLVD) components, the CLVD component simply indicates a measure of an inadequacy of the waveform fit to observed seismograms or a measure of complexity of the moment tensor. Time-dependent moment tensors inherently have a larger CLVD than time independent moment tensor inversion. The main reason for higher CLVD component for the TDMT inversion algorithm is due to

introduction of the more freedom in the inversion process of the waveform in the frequency domain. We will explore the constraint minimizing the CLVD including the other constraints in the following three examples.

First Example

The first example is a double event with change in slip orientation and scalar moment, and no change in source depth between the two subevents. The purpose of this example is to simply show the effectiveness of the time dependent moment tensor inversion, and its utility in resolving the time dependent source parameters of a double events with changes of shear fault geometry as a function of a time. The observed data for this synthetic example were generated using focal mechanisms, source time functions, and focal depths in Table 3.

Table 3. Source Parameters for Observed Seismogram for Example #1

	Subevent 1	Subevent 2
Source depth	9 km	9_1 km
Focal mechanism(degree)		
Strike	0	345
Dip	75	75
Rake	90	90
Trapezoidal source-time function(second)		
Rise time	1	1
Duration	2	2
Falloff	1	1
Delay time(second)	0	6
Relative seismic moment	1.0	0.5

The synthetic seismograms were made with a P wave which contains P, pP, and sP. A attenuation factor $t^* = 1.0$ second was used to approximate realistic effects, and an instrument (WWSSN long period, 15-100) was used as a band pass filter. The time

independent moment tensor inversion with Green's function (9 km), which is the depth for both subevents, gives a little different single focal mechanism from two synthetic focal mechanisms as shown in Table 4. The assumption of a single source time function (6 seconds) for time independent or constant moment tensor inversion will be discussed later in the discussion section.

The CLVD component from the conventional moment tensor inversion is as large as 35% of the major double couple. This is very high for double-couple dominated synthetic data inversion. This large value of the CLVD for the noise free synthetic data comes from the source complexity, forcing the complex source (two subevents with change in fault orientation) into an assumption of a single double couple. One more possible reason seems to be the assumption of constant moment tensor throughout the whole energy release which is inherent in time-independent moment tensor inversion. Therefore, both assumptions of a fixed single source time function and constant moment tensor source for the complex seismic source of fault orientation change are mapped into a different focal mechanism from two given ones and significantly high CLVD component (35 %).

Of course, the resolution of the source parameters and CLVD component could be improved if the restriction for the length of a single source time function is allowed to be a non-linear process. Even in this case, it is inherently difficult to resolve the source complexity of fault orientation, which changes with time, since time-independent moment tensor inversion uses the assumption of constant moment tensor, allowing only one possibility of fault geometry throughout the seismic energy release.

Table 4. TIMT Results for Example #1

Subevent	Strike	Dip	Rake	CLVD%
0-6 sec	12	73	112	35

For the TDMT or time dependent moment tensor inversion, each moment tensor element is transformed to the time domain independently from the equivalent moment tensor solution in the frequency domain. Figure 2 shows time dependent moment tensor elements. Considering the constraints of temporal consistency and causality, the inversion resolves the source multiplicity into two subevents very well. Even the relative magnitude of the scalar moment which is proportional to the area under the source time function, and the shape of each source time function (two trapezoids) which is equivalent to the simultaneous change for all the time-dependent moment tensor elements appear to be resolved very well.

Mapping the resultant moment tensor elements to the corresponding focal mechanism shows that focal mechanisms of the two subevents are also resolved very well as shown in Table 5. Moreover, the difference in shear fault orientation between the two subevents could be easily identified through the figure itself by apparently different combination of relative amplitudes of time dependent moment tensor elements between two subevents.

Compared to the CLVD component (35 %) of TIMT inversion, the TDMT inversion yields a much smaller non-double-couple component: less than 1 %. This indicates that the source parameters for the complex source are well resolved, and fit the synthetic data. The waveform matches, as shown in Figure 3, are also very good throughout the entire waveform at all stations.

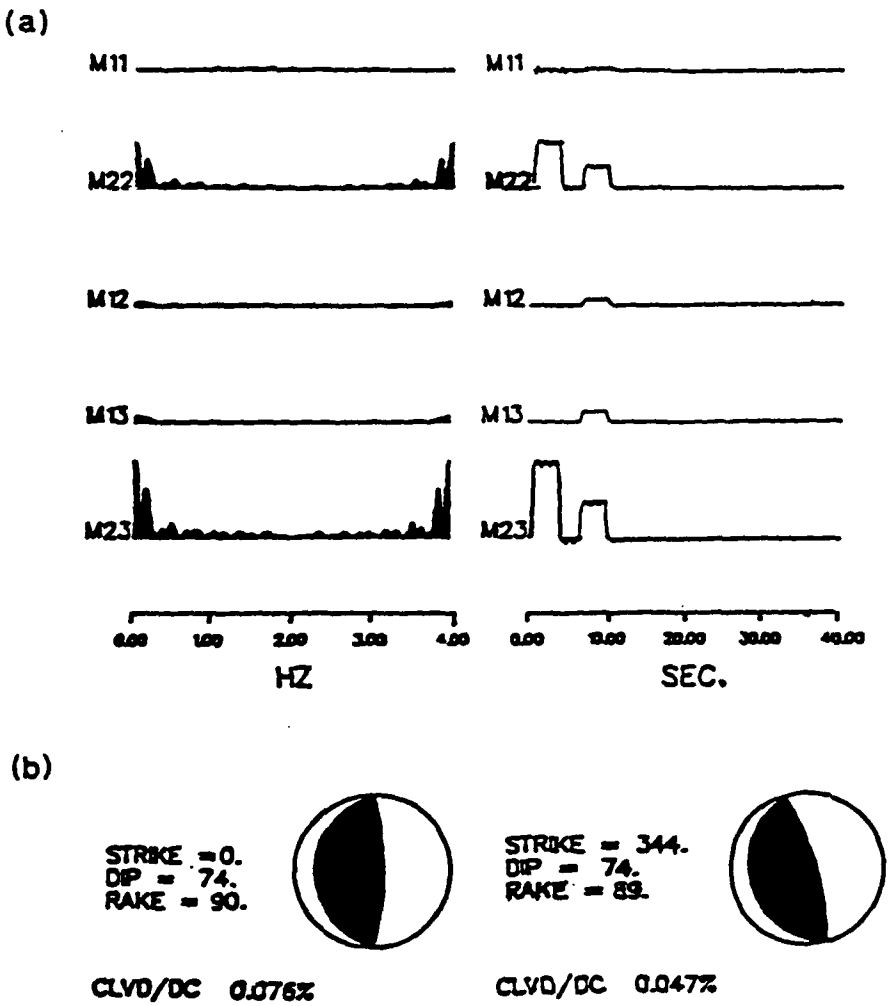

Figure 2. (a) Resultant time dependent moment tensor elements from the waveform inversion of the first synthetic example with Green's function of 9 km focal depth. (b) Resultant focal mechanisms with the assumption of two subevents. Both time dependent moment tensor elements and focal mechanisms are resolved very well with CLVD component much less than 1%.

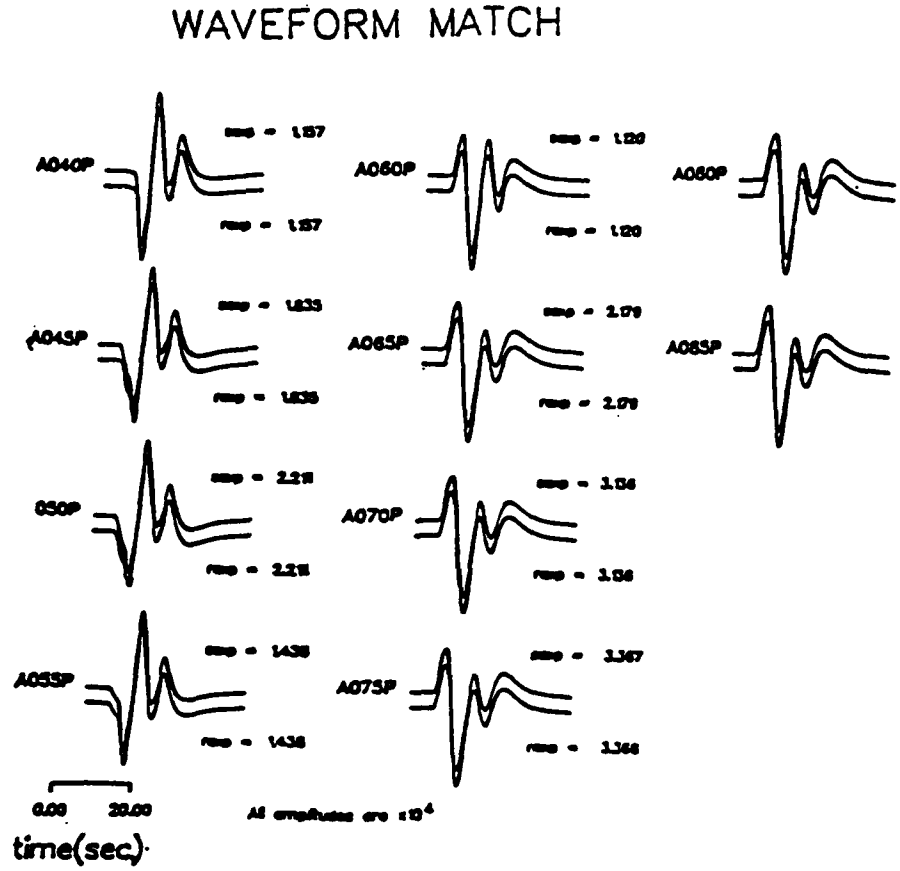

Figure 3. Teleseismic waveform comparisons of the original complex source data set with synthetic seismograms obtained from time dependent moment tensor inversion of the first example. The waveform matches are very well throughout the entire waveform at all the stations.

Table 5. TDMT Results for Example #1

Subevent	Strike	Dip	Rake	CLVD%
0-4 sec	0	74	90	0.08
6-10 sec	344	74	89	0.05

This synthetic example shows that we can resolve source multiplicity and changing seismic source parameters for subevents (such as two focal mechanisms), the shape of each source time function, and even relative magnitudes of scalar moment in a linear process. Adequate Green's functions are essential to the interpretation. We can test the source depth by doing multiple inversions with Green's functions of different source depth. Using the same data, inversions with inadequate Green's functions (7 km which is shallower than and 13 km which is deeper than the 9 km "true" depth) as shown in Figure 4 indicates that there seems to have been seismic energy release before time zero for both cases. The fact that the result from inversion with Green's functions (13 km) shows more non-causality can be used as a measure of the inadequacy of Green's functions, and correct the source depth (9 km). A series of inversions with different depths can be used to find the best source depth.

Second Example

The second example has two subevents at different depths. In other words, it is a test for resolving a complex earthquake source which has a change in focal depth as a function of time. The result is compared to that with the assumption of TIMT throughout the entire rupture process. The synthetic data example corresponds to a typical example of many earthquakes sequences in the Intermountain region of the western U. S. which propagates upward or downward with evolving complex rupture history on multiple dislocation surfaces, as some of the improved seismic mapping

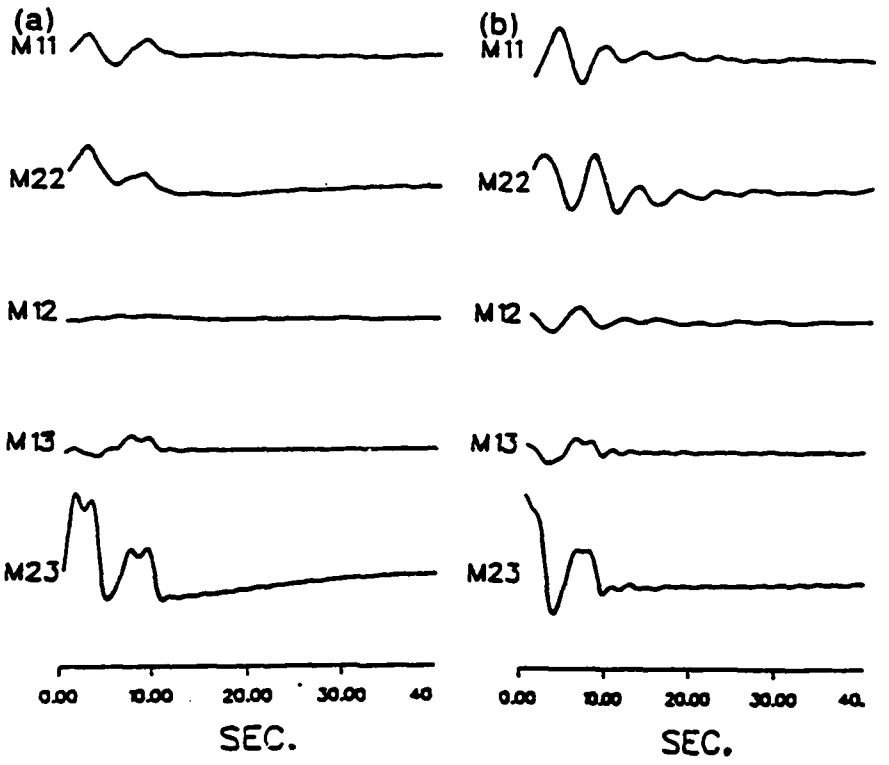

Figure 4. Resultant time dependent moment tensor elements of the first synthetic example with Green's functions of (a)7 km and (b)13 km which are not true focal depths. Two moment tensor functions show well-developed non- causality for the first part of energy release.

techniques have shown currently (Wallace 1985; Doser and Smith 1983; Lide and Ryall 1986). Observed seismograms for this example are generated using the source parameters in Table 6.

Table 6. Source Parameters for Synthetic Seismogram for Example #2

	Subevent 1	Subevent 2
Source depth	9 km	13 km
Focal mechanism(degree)		
Strike	0	0
Dip	75	75
Rake	90	90
Trapezoidal source-time function(second)		
Rise time	1	1
Duration	2	2
Falloff	1	1
Delay time(second)	0	6
Relative seismic moment	1.0	0.5

Using the TIMT inversion with a smooth single source time function (6 seconds) and Green's function of 9 km, a single focal mechanism slightly different from the two assumed focal mechanisms is resolved, as shown in Table 7. A single focal mechanism is resolved fairly well even though CLVD component is 37%, when the length of a single source time function is limited to the 6 seconds. The assumption of the single source time function for time-independent moment tensor inversion will be discussed in a later section.

In contrast to the good resolution of the focal mechanism, the CLVD component is 37%, which is very high considering this is a noise-free synthetic waveform inversion. The high CLVD from the moment tensor inversion for real earthquakes could represent many possibilities: for example, source complexity, ruptures on non-planar fault plane, inadequate Green's function for the inversion, or different

physics of seismic source (tensile fracture) as summarized by Sipkin (1986). Obviously, for this case where there is no **a priori** information about source complexity, the high CLVD is a measure of the inadequacy of the assumption of a constant time function. Though a single focal mechanism for two subevents is resolved well, the high CLVD component indicates inadequate inversion of multiple subevents.

Table 7. TIMT Results for Example #2

Subevent	Strike	Dip	Rake	CLVD%
0-6 sec	1	70	91	35

The results using the TDMT inversion with Green's function of 9 km source depth, which is the first subevent's source depth are shown in Figure 5. All the five time dependent moment tensor elements show that there are apparently two time windows of energy release. Comparing these two time windows of energy release, the first subevent has apparently more temporal consistency than the second subevent. This is connected with the incorrect source depth for the second subevent. Both focal mechanisms, with the assumption of two subevents, are resolved very well. Moreover, the causality constraint is met for the first subevent.

Table 8. TDMT Results for Example #2 with Focal Depth of 9 km

Subevent	Strike	Dip	Rake	CLVD%
0-4 sec	360	73	91	11
6-10 sec	2	75	86	28

The CLVD components are 11% and 28% for the two sources (see Table 8) respectively. The high CLVD component (28 %) for the second subevent, though less

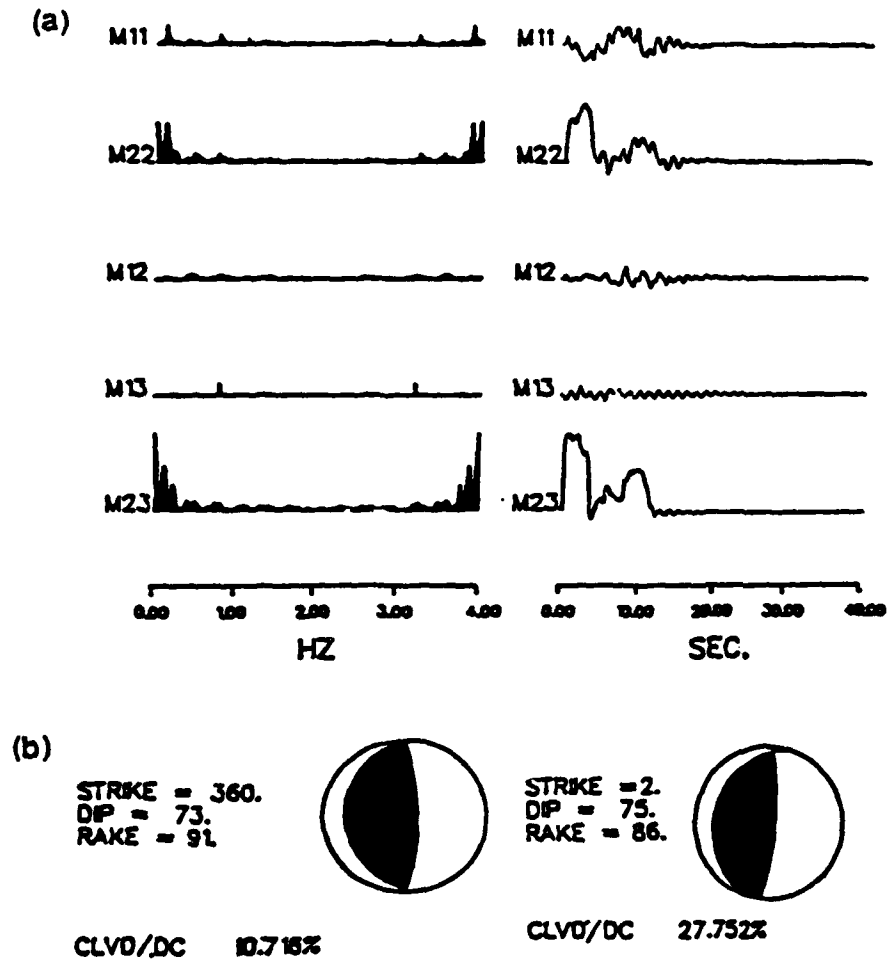

Figure 5. (a) Resultant time dependent moment tensor elements from the waveform inversion of the second synthetic example with Green's function of 9 km focal depth which is focal depth of the first subevent. (b) Focal mechanisms of two subevents with the assumption of two temporal consistencies and corresponding CLVD components.

than that (37%) determined by the TIMT inversion, is caused by using Green's functions of inadequate focal depth. The CLVD component (11%) for the first subevent is also somewhat high.

Therefore, the inverse operator in the time dependent moment tensor formulation has characteristics that relative areas under the curves among five elements are preserved well, though inadequate Green's functions for the second subevent introduce "noise". The inadequacy of Green's functions for the second subevent is mapped to the less developed temporal consistency, shape complexity of source time function, and relatively higher CLVD component (28%).

Using Green's functions of 13 km source depth, which is the second subevent's source depth, the resultant five time dependent moment tensor elements show that the second subevent is resolved apparently better, with more temporal consistencies, than the first subevent compared to the previous case (see Figure 6). For the second period of energy release, the largest amplitude of moment tensor element (M23) can give an idea about the source time function. Note the non-causality for the first window of energy release. This apparent non-casualty problem seems to be caused by inverting waveforms using the Green's functions for incorrect source depth. Other examples of inversion with shallower Green's function (7 km) for the same data are shown Figure 7, and also demonstrate that the non-causality problem is mainly due to inverting using Green's functions with inappropriate source depth.

Table 9. TDMT Results for Example #2 with Focal Depth of 13 km

Subevent	Strike	Dip	Rake	CLVD%
0-4 sec	3	70	89	4
6-10 sec	1	73	86	4

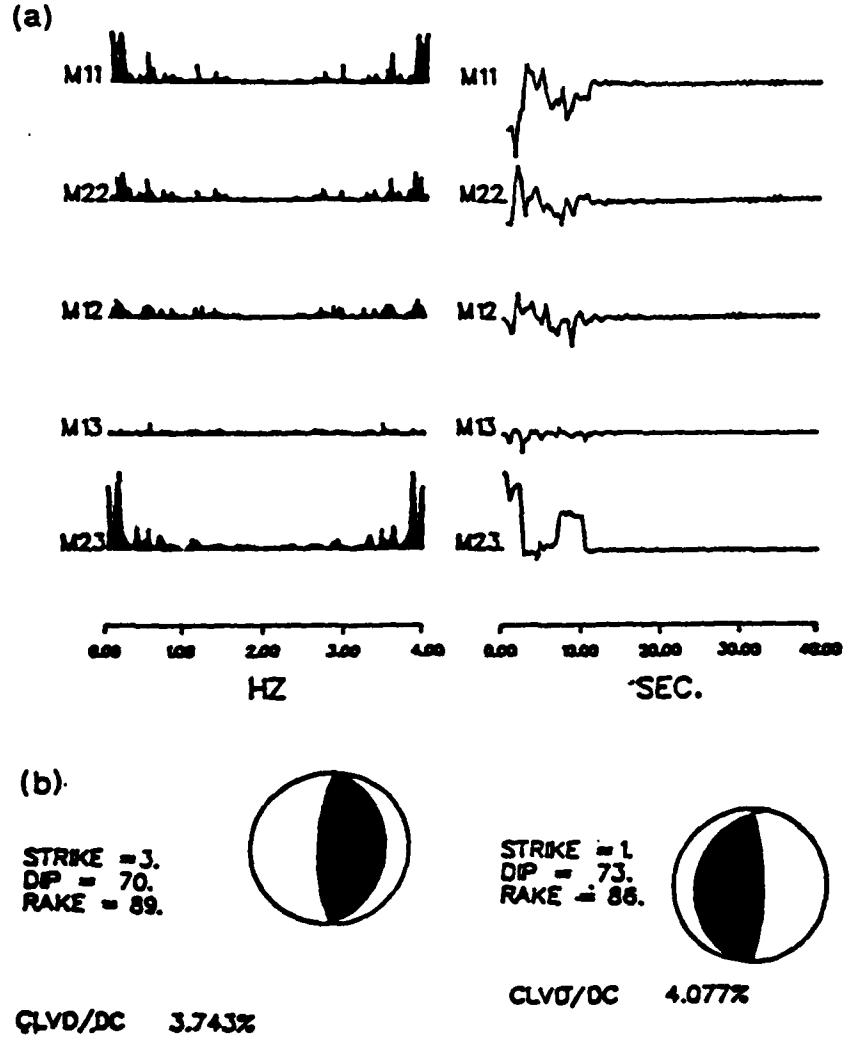

Figure 6. (a) Resultant time dependent moment tensor elements from the waveform inversion of the second synthetic example with Green's function of 13 km focal depth which is focal depth of the second subevent. (b) Focal mechanisms of two subevents with the assumption of two temporal consistencies and corresponding CLVD components.

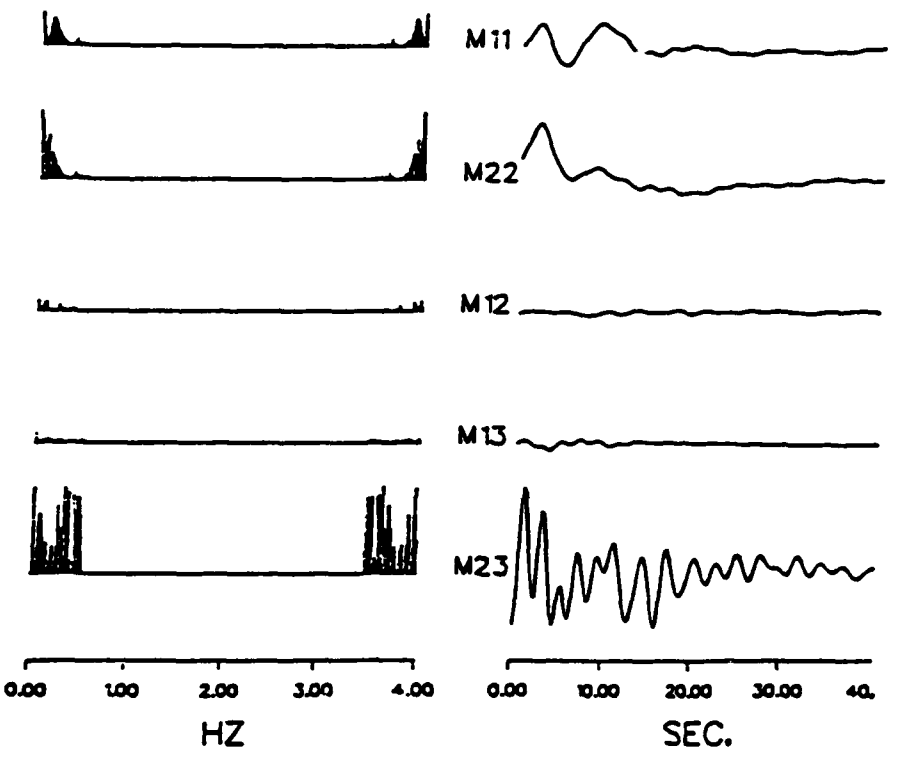

Figure 7. Resultant time dependent moment tensor elements from the waveform inversion of the second synthetic example with Green's function of 7 km focal depth which is not compatible with depths of both subevents. Moment tensor functions show well-developed non-causality for the first part of seismic energy release.

The TDMT solution, using Green's functions for a 13 km focal depth, gives two focal mechanisms that are resolved well and with CLVD/DC of about 4% (see Table 7). Although the CLVD component (4%) from the first subevent inversion is less than for a source depth of 9 km, the non-causality and less well developed temporal consistency of all the time dependent moment tensor clearly indicates insufficient resolution of the first part of energy release.

The determination of source multiplicity has been usually considered as a non-linear process and also requires **a priori** information about multiplicity by conventional time independent moment tensor inversion. As shown in this synthetic example, however, determination of source multiplicity is a simple linear process when using a time-dependent moment tensor inversion. This synthetic data example also shows that source parameters of two subevents with change in source depth as a function of a time can be resolved using time dependent moment tensor inversion. Additionally, the constraints of temporal consistency and causality between five time dependent moment tensor curves, and the size of the CLVD component can be used to investigate source complexity as a function of depth.

Third Example

The third synthetic example is a double event with overlapping (from 5 to 7 seconds) source time functions and fault geometry which differs between the two subevents. This example is designed to investigate how much the temporal consistency, or interference in the time from the two sources, will affect the inversion process. It is also designed to investigate how well source parameters of each subevent (source time function, seismic moment, and focal mechanism) can be resolved from the resultant time dependent moment tensors. Synthetic seismograms for this example are

generated using the focal mechanism, source time functions, and focal depths in Table 10.

Table 10. Source Parameters for Observed Seismogram for Example #3

	Subevent 1	Subevent 2
Source depth	9 km	9 km
Focal mechanism(degree)		
Strike	0	345
Dip	75	75
Rake	90	90
Trapezoidal source-time function(second)		
Rise time	2	2
Duration	3	3
Falloff	0	2
Delay time(second)	0	5
Relative seismic moment	1.0	0.5

The results by a TIMT inversion with the assumption of smooth single source time function using Green's function of 9 km source depth are shown in Table 11. A much different single focal mechanism than either subevent is obtained and the value of CLVD/DC is 50%. The high value of CLVD could mislead the interpretation of the seismic source, implying a source such as magma injection, which is physically very different from two evolving double-couple dominated shear dislocations.

Table 11. TIMT Results for Example #3

Subevent	Strike	Dip	Rake	CLVD%
0-6 sec	27	79	139	50

The TDMT in the Figure 8 shows evidence that this event may be composed of two subevents with boundary at 5-7 second since there are unusually abrupt changes

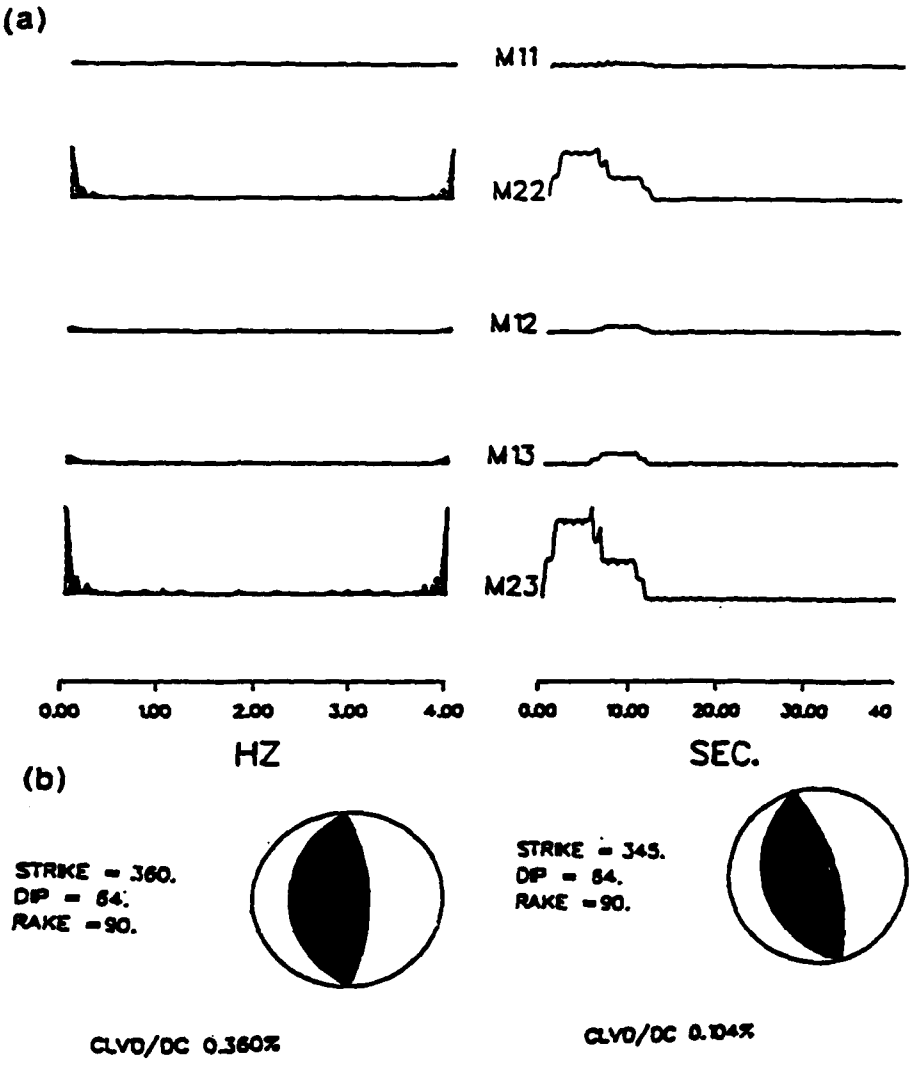

Figure 8. (a) Resultant time dependent moment tensor elements from the waveform inversion of the third synthetic example with Green's function of 9km focal depth. (b) Focal mechanisms of two subevents with the assumption of two temporal consistencies and corresponding CLVD components.

in the shape at the same time point for all five moment tensor elements. Though the time interval between 5 to 7 seconds is designed to be overlapped, with the assumption of two subevents (0-6 seconds and 6-12 seconds, respectively), focal mechanisms of the two subevents are resolved very well. Compared to the 50% of CLVD component in the TIMT, the CLVD component for each subevent in the TDMT inversion is less than 1% as shown in Table 12.

Table 12. TDMT Results for Example #3

Subevent	Strike	Dip	Rake	CLVD%
0-6 sec	360	74	90	0.1
6-12 sec	345	73	90	0.4

Even assuming a single event with 12 seconds duration, an averaged focal mechanism in strike angle is resolved; strike 355^{o}, dip 74^{o}, rake 90^{o}. The CLVD/DC is about 1%. Compared to the source parameters with the assumptions of a single source and constant moment tensor, time dependent moment tensor inversion resolves at least an averaged focal mechanism. The much smaller CLVD component (than 50%) also indicates that physical characteristics of two subevents are typical double-couple dominated source which means pure shear dislocation on the fault plane.

Unfortunately, total seismic moment from 0 to 12 seconds is not well conserved. The total seismic moment is not fully mapped into the time dependent moment tensor domain, due to the interference between time functions for each event. Though it is somewhat difficult to resolve total seismic moment of overlapped source complexity, unusually robust, abrupt change of shape at the same time point for all the time dependent moment tensor could indicate that there is interference between two subsources.

As shown at this example, using temporal consistency without any **a priori** information about source multiplicity, it is possible to determine the source parameters and source multiplicity even with source interference. Note that the CLVD component from the time independent algorithm (>50%) is much higher than that (about 1%) from the time dependent algorithm. This is extremely important since high CLVD components (as much as 50%) may otherwise indicate intrinsically different physics of the seismic source.

Discussion

Based on these three synthetic examples, the algorithm of TDMT inversion is proposed to be a good way to analyze complex sources. The algorithm presented here gives very satisfying results in synthetic data tests for various source complexity. The first step in resolving source complexity is to identify the source multiplicity. The most important condition for significant seismic energy releases is temporal consistency, or apparent simultaneous shape changes, for all the time dependent moment tensor elements. Secondly, the causality and the size of CLVD component constrain the parameters of the multiple sources. The first synthetic example shows that a multiple source with no focal depth change could be mapped clearly into the two sources in the domain of time dependent elements and then separated into two subevents easily. The TDMT inversion of the second example (with Green's functions of 9 km and 13 km source depth, respectively) shows two subevents can be identified on the basis of simultaneous shape-change of the moment tensor elements. The non-causality criteria required a source depth of 9 km, as does the high CLVD component. From the third synthetic example, the source complexity caused by the interference between two subevents is mapped into the time dependent elements as a form of unusually abrupt changes for all the elements during the interval of overlap between

the two subevents. Therefore each source is mapped into time-dependent moment tensor elements with characteristic temporal consistency, causality, and CLVD component.

The resolution of the depth of source initiation and propagation, which is an intrinsically non-linear process, can be accomplished with time-dependent moment tensors since Green's functions for incorrect source depths show non-causality, increased shape complication for all the elements, and a considerably higher CLVD component. As shown from all the results with Green's functions with inappropriate source depth, when the first part of the energy release is inverted by inadequate source depth, the time-dependent moment tensor shows apparently well-developed non-causality. The second example shows that when the second part of energy release is inverted with Green's functions of incorrect source depth, time-dependent moment tensor shows not only unusually complicated shapes but also considerably higher CLVD component.

The three synthetic examples demonstrate that the focal mechanism is the most robust source parameter even using inadequate Green's functions with this algorithm. This is consistent with Sipkin's observation. This shows that the inverse operator of TDMT conserves the relative areas between all the moment tensor elements even for slightly inadequate Green's functions. This property is an advantage when inverting for seismic source with no **a priori** information.

Some of the proposed physical explanations for non-double-couple component of earthquakes include source multiplicity, rupture on non-planar fault planes, and intrinsic source mechanisms. Three synthetic experiments with a single smooth source time function demonstrate that substantially high non-double-couple component is always caused by forcing multiple sources into a single source representation. Synthetic experiments also suggest that moment tensor inversion with inadequate

Green's function for source depth, and sources which overlap can cause a high CLVD component.

As shown from the three synthetic examples, the TDMT inversion technique has a clear advantage over the TIMT inversion techniques in order to map out seismic source complexity. Since TDMT inversion does not need any **a priori** information on the source time history, that is, source multiplicity and finiteness of each source, it is a simple and straightforward linear deconvolution process in order to resolve these source parameters. For the TIMT inversion, simultaneous inversion of source time function (length, shape and multiplicity) and constant moment tensor elements in the time domain suffers from a non-linear inversion process. For the simple shear dislocation source, there may be not much difference in ability to resolve source parameters between TDMT and TIMT inversion process, though the TIMT inversion is still non-linear. For complex seismic sources, however, the assumption of constant moment tensor can not be justified. That is, the physics of the evolving source complexity, (for example, change of fault plane geometry and focal depth with time) could be mapped into both constant moment tensors and source time function (finiteness and shape) simultaneously. This inadequate mapping of source complexity into the moment tensor and source time function, suggests that the solutions from TIMT inversions could be biased.

As pointed out earlier at the previous section, the assumption of a fixed single source time function (6 seconds for all the synthetic data example inversion) for TIMT inversions is restrictive, since changing the length of source time function, for example, extending it to 8-10 seconds in a constant moment tensor inversion, could improve the fit to the waveforms. However, since information on length of source time function itself is an intrinsically unknown parameter, opening the assumption of the length of source time function by non-linear process does not improve the results

much. For the multiple source, using the constant moment tensor assumption, it becomes even harder to resolve finiteness and other source parameters of each subevent by non-linear process since the number of unknowns is increased as a product of the subevents.

Sipkin (1986) tried to place further constraints such as a 'similarity restriction', on the moment tensor elements in the MSE inversion algorithm, which uses the same moment tensor formulation of the source as that of this study, except in the time domain. More constraints such as minimizing complexity and length of the source time history as **a priori** information necessary to fit the data are applied to the inversion process for source time function. Langston (1981) also suggested that a source inversion method has to give the smoothest answer as **a priori** information possible in the face of probable unknowns in earth structure. Such smoothness can be applied as a form of constraining the duration of possible source time functions, smoothing the shape of source time history, and minimizing the number of variables. Instead of having "smoothness" as **a priori** information, we suggest that solutions could be allowed to map into the time dependent moment tensor domain. Then the resultant time dependent moment tensor elements can be interpreted using various physical constraints such as temporal consistency and non-causality between all the moment tensor elements as shown in this study. Time dependent moment tensor inversion without an **a priori** constraint seems to be the best option since this process will preserve characteristics of the inherent source process itself. Moreover, in order to resolve source multiplicity, which is one of the most important goals in this study, the constraints for the smoothness themselves are unknowns in the deconvolution process.

Unmodeled parameters such as sufficient numbers of rays, source and receiver structure, and attenuation have effects on the inversion results of time dependent moment tensor elements. Namely, unmodeled phenomena are mapped onto the moment

tensor elements. However, if we repeat the time dependent inversions by changing the source structure and Green's function for different depths and choose adequate time windows using physical constraints as introduced earlier, then it is possible, within reasonable limits, to separate out the more significant subevents for evolving source complexity. This can then be used to resolve scalar moments, focal mechanisms, and source time functions for each subevent. Therefore, if the degree of adequacy of Green's function for the source structure which is one of the most important assumptions in the moment tensor inversion is also a problem in any other moment tensor inversion algorithm, and the time dependent moment tensor inversion algorithm can give a better solution for a complex source.

CHAPTER 4

COMPLEX EARTHQUAKES

The 1982 Yemen Earthquake

Introduction

The destructive December 13, 1982 Yemen earthquake is of considerable interest because it is historically the first earthquake in the southwestern Arabian Peninsula which was accompanied by well-developed surface ruptures, and extensional ground cracks. It was also followed by extensive aftershock seismicity. The southwest boundary of the Arabian Peninsula, which is relatively seismically inactive, has been characterized by Ambraseys and Meiville (1983) as couple of moderate magnitude of earthquakes on the basis of historical seismicity. It has been suggested that the main event shows multiple rupture histories (Sipkin 1986; Choy and Kind 1987), with displacements dominated by normal-slip. The earthquake is apparently related to the development of the tensional tectonics along the western margin of the Arabian Peninsula. Sipkin (1986) suggested a fault model of two double-couple point sources, approximately equal in size and separated by 12 seconds, on the basis of analysis of long-period data from the Global Digital Seismograph Network. Choy and Kind (1987) model the event as two faults model separated by 3.0 seconds in time with the second event dominant, (three times larger in seismic moment), using the broadband data by combining short- and long-period data from Global Digital Seismograph Network. Langer et el. (1987) suggested the model of conjugate normal-slip faulting between the first and the second subevent in an extensional tectonic setting to explain geometrical

distribution of the 12-days aftershocks. All the interpretations suggested that this event is a complex earthquake whose rupture process consisted of at least two subevents, even though there still remains disagreement over which of these fault models best explains the entire rupture history of the earthquake.

The purpose of this study is to investigate the first-order mapping of geometric and temporal source complexity of the Yemen earthquake (Figure 9) using the moment tenser source representation and then, to resolve the disagreement between fault models. We studied the source complexity of the Yemen earthquake by performing a time dependent moment tensor inversion in the frequency domain using the observed WWSSN teleseismic waveforms. Since the conventional constant-moment-tensor assumption breaks down for complex seismic sources that have complex rupture histories on multiple surfaces, it is preferable to use time-dependent moment tensor inversion instead of TIMT.

For the time-dependent moment tensor inversion, seventeen long-period teleseismic P-waves records (see Figure 10) recorded on WWSSN instruments are inverted. The data are chosen for azimuthal and distance coverage within the teleseismic range. The length of time window for the inversion of the observed seismograms was 25 seconds after the first P wave arrival. The Green's functions used in this inversion were generated using the method of Langston and Helmberger (1975) and included direct P, pP and sP along with attenuation effects ($t^* = 1.0$ second for P waves) and geometric spreading. A simple layered source model consisting of a 30 km ($V_p = 6.2$ km/sec) crust overlying a semi-infinite half space mantle ($V_p = 8.2$ km/sec) was used in generating the Green's functions. The main reason to assume a simple structure and small numbers of contributing rays, is to decrease the unknown effects of structure. In order to overcome the problems of determining the focal depth, a separate sets of Green's functions were generated for depths between 3 km and 15 km

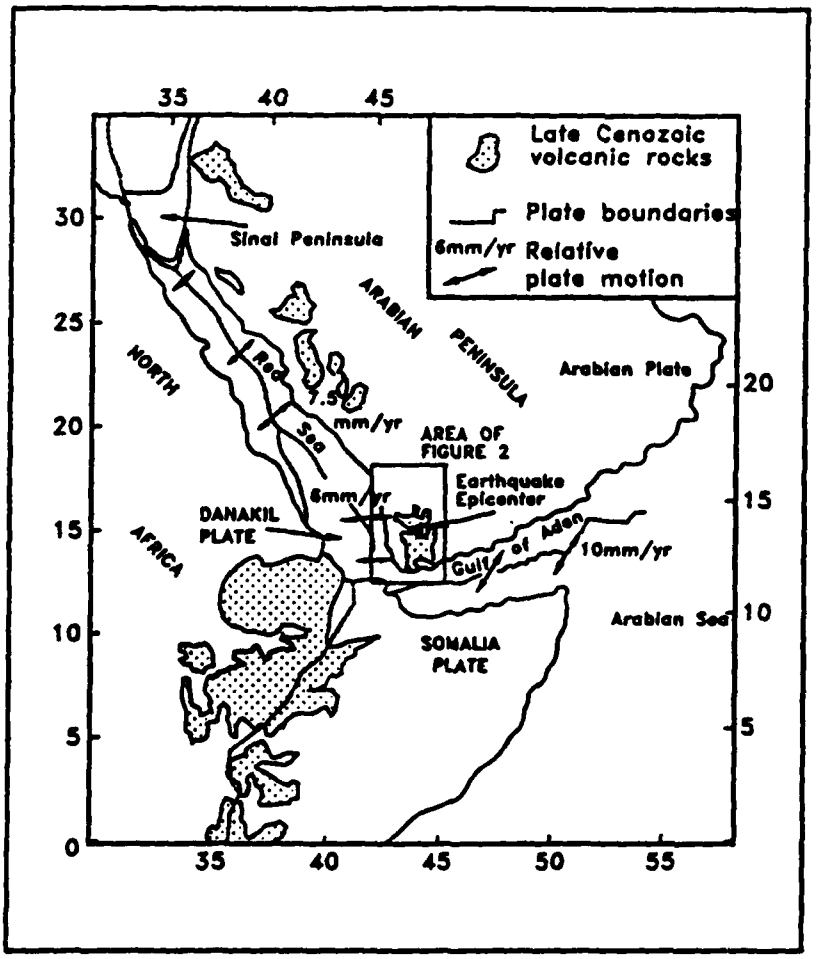

Figure 9. Tectonic map of the major Cenozoic volcanic fields, the epicenter associated with the December 13, 1982 Yemen earthquake (from Plafker et al., 1987).

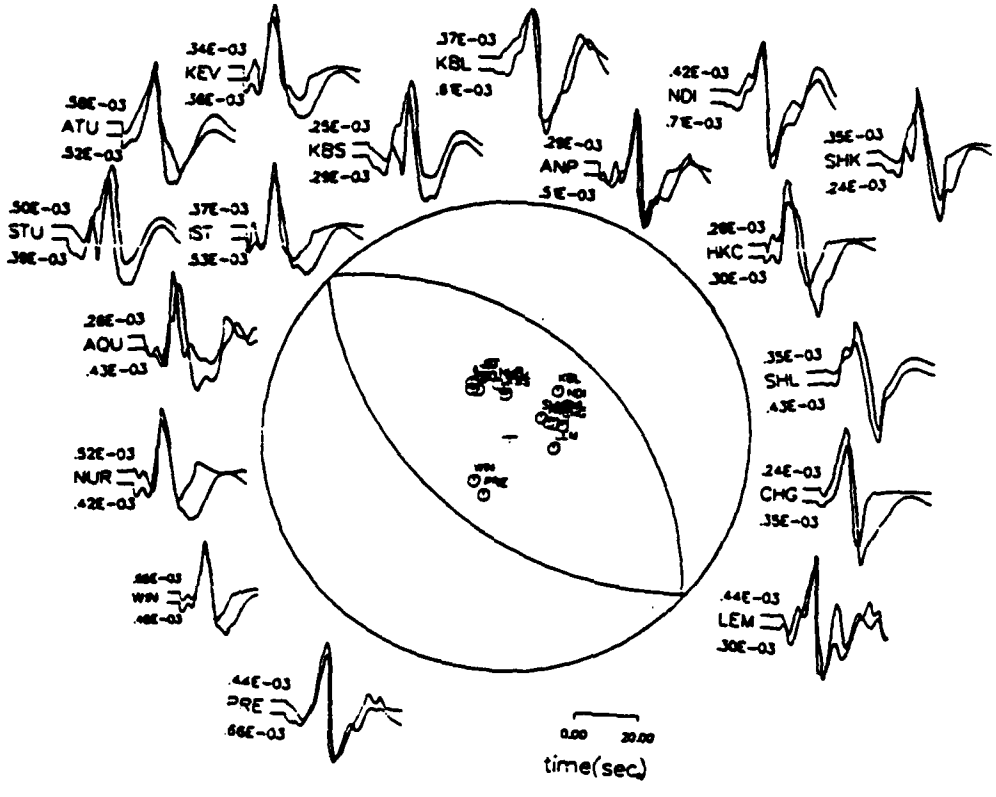

Figure 10. Seventeen teleseismic station distribution and corresponding long-period teleseismic P waveforms (upper waveforms are observed and lower ones are synthetic waveforms). This figure also shows waveform matches between observed and synthetic results from the time dependent moment tensor inversion.

at two km intervals. A separate inversion was then done for each set of Green's functions for the different source depth in order to differentiate subevents in time sequence and their corresponding depths.

Data Analysis and Results

The generalized inverse technique used in the frequency domain inversion revealed a near-singular condition of the coefficient matrix for most of the inversion points in the frequency domain. To overcome near-singularity effects in the inversion process, a damped least squares method was used instead of a simple least squares algorithm. To find a single optimal damping factor at each inversion point in the frequency domain, we investigated the trends of the trade-off between fitting observed data, minimizing the change of magnitude of model parameters without significantly affecting the fit to the observed data.

At each inversion point in the frequency domain, estimates of the model parameters were found for 41 different values of the damping factor, which ranges from zero (no damping in the inversion) to 0.01 depending on the size of the eigenvalues of the coefficient matrix of all the inversion points. In this manner, a trade-off curve was obtained at each inversion point in the frequency domain. A set of typical trade-off curves for the first ten inversion points is shown in Figure 1, where the X-axis represents the ratio of the magnitude of damped model parameter vector to that of undamped model parameter vector, and Y-axis represents the ratio of the amount of misfit of the observed data to the magnitude of the observed data vector. From each trade-off curve at each point in the frequency domain, the optimal damping factor, which was one of the 41 values, is determined based on finding the maximum geometrical curvature along the trade-off curve. This process produced a

series of N independent damping factors, where N is the number of the inversion points in the frequency domain.

Using these optimal damping factors for the corresponding frequency domain inversion points introduces a large increase in the degrees of freedom (equal to the number of inversion points). It is possible to reduce the degrees of freedom by replacing the set of independent damping factors with a lower-order polynomial fit to the curves of damping values. An orthogonal polynomial curve fit, in the least square sense, as shown in Figure 11 was applied to the damping values and resulted in a 10th-order polynomial. The resulting damping factors from this polynomial functions were, then, used for a damped least squares inversion. Compared to the results from the simple least squares inversion, the inversion using damped least squares sense gave a much more stable solution and improved significantly the resolution of the seismic source parameters.

To invert source parameters from the observed waveforms using time-dependent moment tensor source representation, we minimized the RMS fit to the observed waveforms, or inverted in the least square sense, and then isolated the best-fit double-couple mechanism for the earthquake from the whole moment tensor elements. To interpret the resultant time dependent moment tensor elements, we employ the constraint that the source be purely deviatoric during the inversion process (M33=-M11-M22), and then decomposed the result into a pure main double-couple mechanism plus minor non-double-couple components. Since no previous study has suggested that the origin of the Yemen earthquake had significantly different source physics from a dislocation slip mechanism, decomposition of the resultant moment tensor matrix into major double-couple and minor CLVD seems reasonable.

The moment tensors and corresponding time functions are much more complicated than those of the synthetic example discussed in the previous chapter. The moment

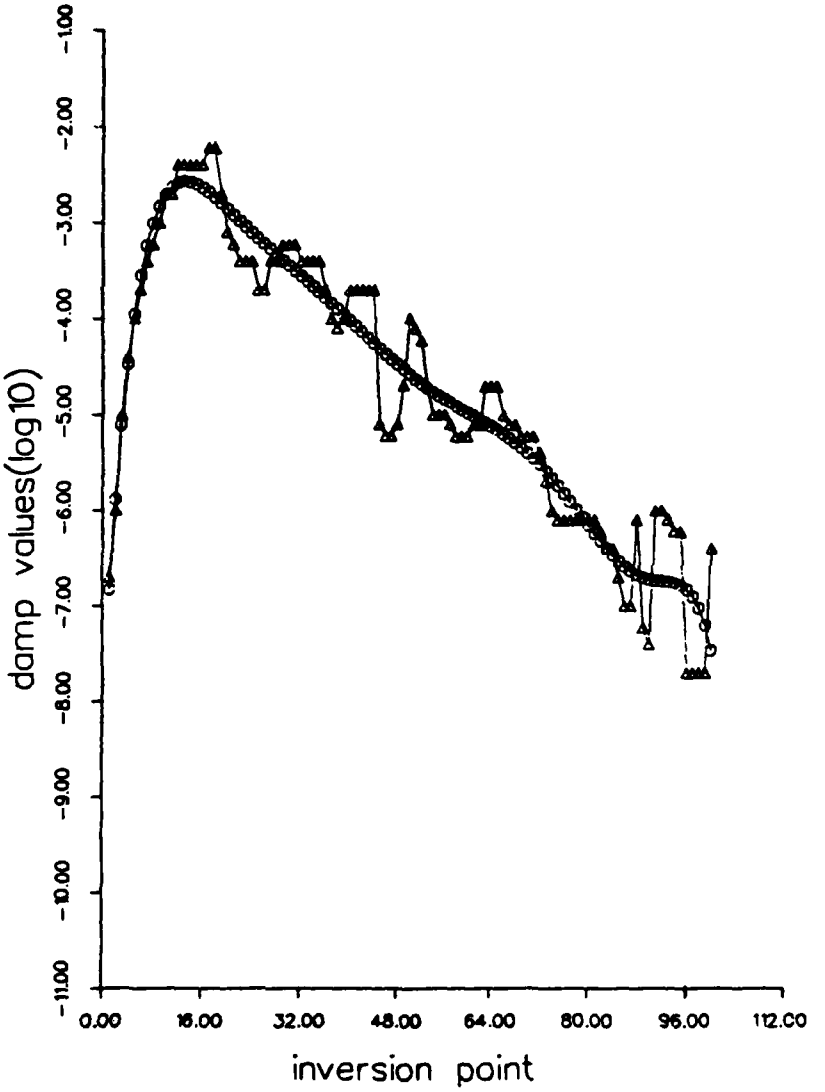

Figure 11. An orthogonal polynomial curve fit (10th order), in the least square sense, to the set of the optimal damping values from the trade-off curves of the first to the 100th inversion point. The degree of freedom of the inversion introduced by independent damping values at each inversion point can be reduced for the waveform inversion.

tensors are shown in Figure 12. The optimal time windows for differentiating subevents of significant energy release and estimating an adequate source depth for the subevents was determined by satisfying five criteria. The first was to pick an adequate time window such that all five moment tensor elements vary with time in a reasonably consistent manner (temporal consistency). The second criteria is that the shape of all five time functions be robust with respect to filtering, and various combinations of damping. The reason for this requirement of stability is that the energy release associated with displacements will be much more robust than noise-like energy. The change of frequency content for various time domains is strongly influenced by the noise level. A **priori** information about the frequency characteristics of noise and signal would be useful in satisfying this condition. The third criteria is a physical compatibility between subevents. We avoid the time windows which give mechanisms which have nearly the same strike and dip angle as adjacent windows but have a rake which differs by 180 degree, "ringing". Even though some such time windows have good temporal consistency, this kind of phenomena, "ringing", is unphysical. The overshoot, or edge effect between adjacent time windows seems to be inherent since the Fourier Transform represents a time dependent function as weighted sums of sine or cosine periodic functions. This is especially bad when the noise level is large. The negative component of the source time functions is also caused by inadequate Green's functions, specifically the wrong source depth, and has no physical meaning. The fourth criteria is that energy release occurs over a finite length in time. Since the total energy of a given event is always limited, the time windows for a specific event must be constrained within reasonable time limit. The final criteria to be satisfied is the focal mechanisms resolved for the time windows should agree with the **a priori** geologic constraints, surface rupture patterns and tectonics.

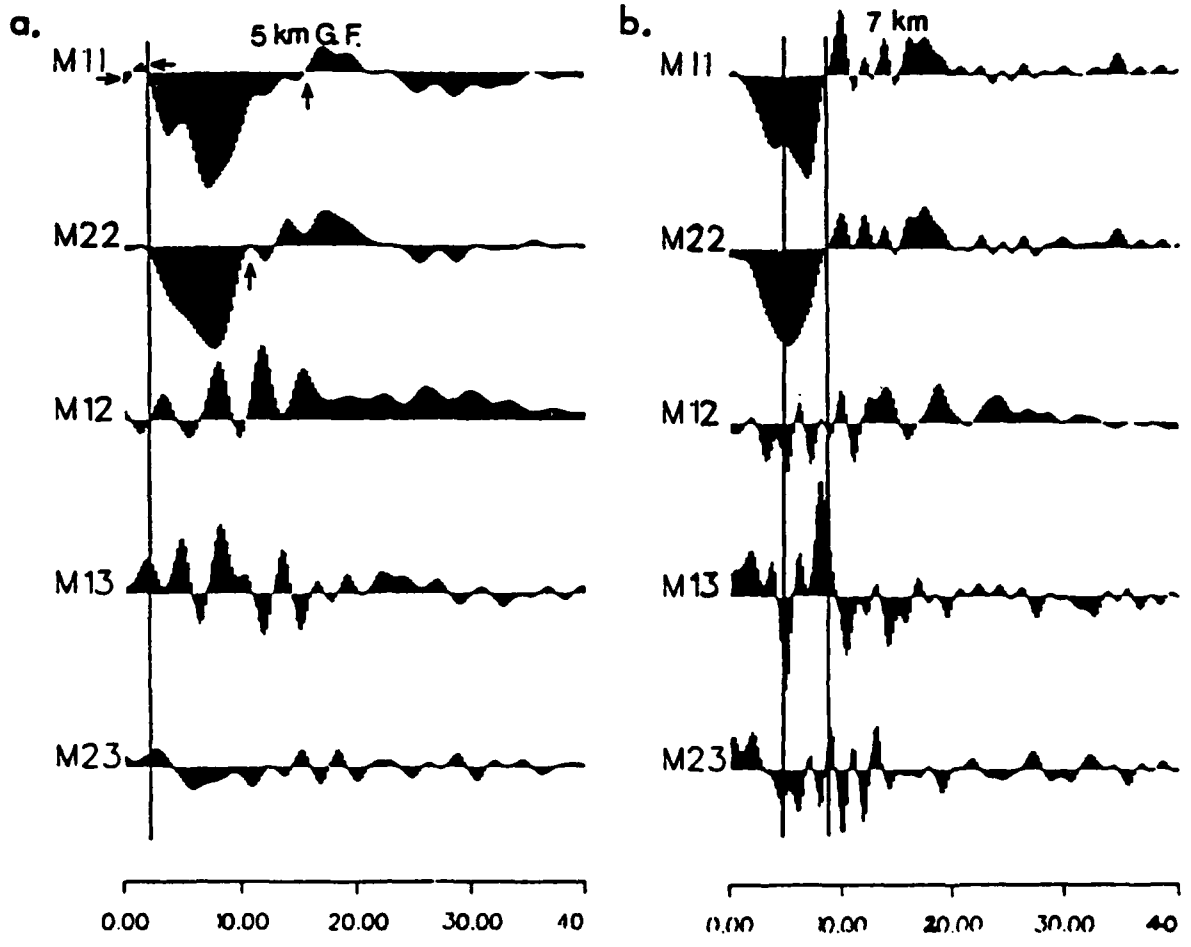

Figure 12. Resultant time dependent moment tensor elements or moment tensor functions from the waveform inversion of the 1982, Yemen earthquake with Green's functions of 5-km, 7-km, 9-km, and 11-km focal depths. The lines of temporal consistency for the first portion apparently show backward moving of temporal consistency as focal depth of the Green's functions increases.

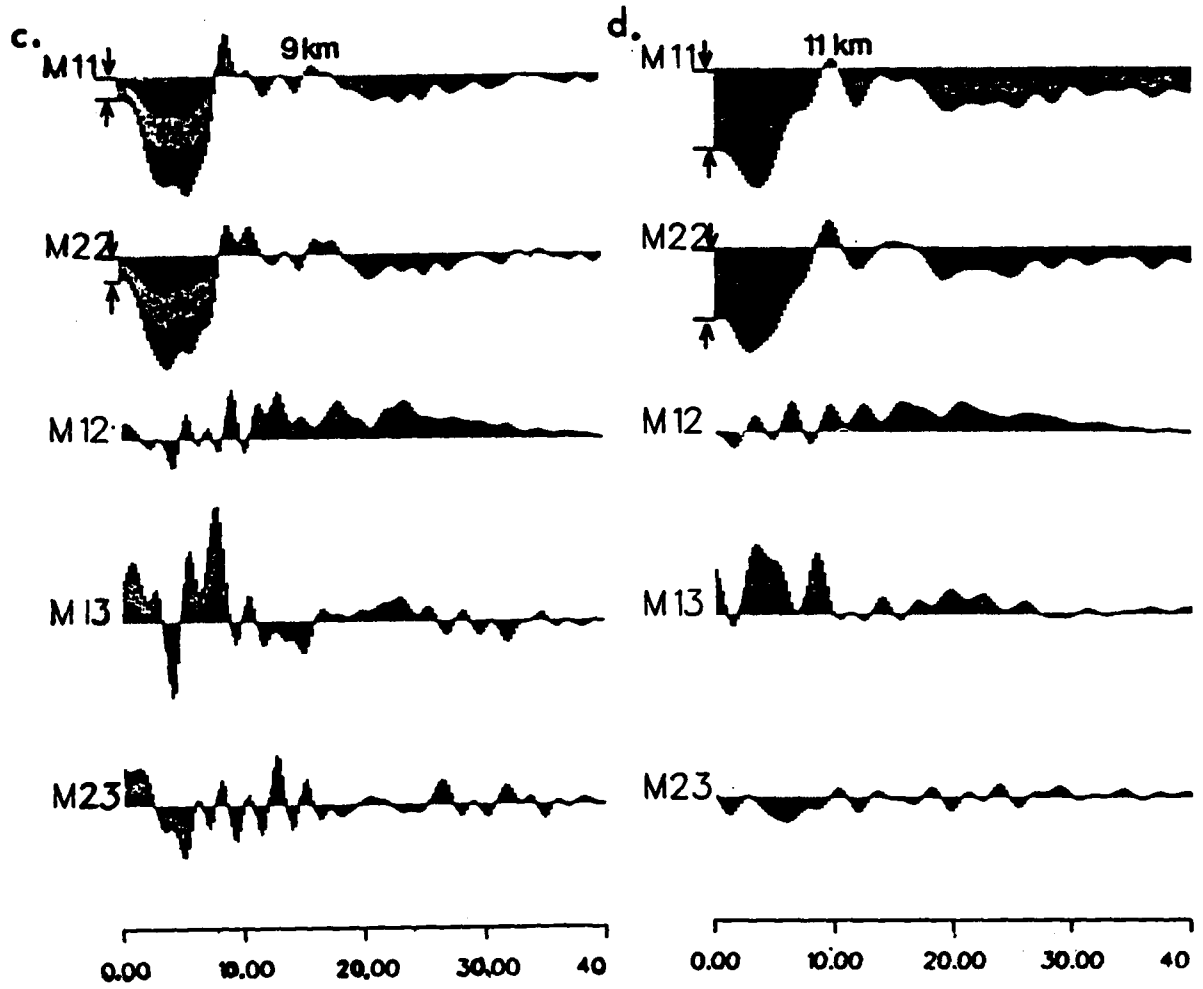

Figure 12. Resultant time dependent moment tensor elements or moment tensor functions from the waveform inversion of the 1982, Yemen earthquake with Green's functions of 5-km, 7-km, 9-km, and 11-km focal depths. The lines of temporal consistency for the first portion apparently show backward moving of temporal consistency as focal depth of the Green's functions increases.

It is interesting to note that the resultant time dependent moment tensor functions in Figure 12 show an apparent similarity or temporal consistency for the whole ranges of focal depths (5 km to 11 km). That is, these moment tensor functions appears to be composed of a broad energy release from 0 to 5 seconds followed by a second pulse with a total duration of about 10 seconds for the entire ranges of focal depths tried in the inversion. However, the "zero crossing" or end of the first source changes for the four depths: 5, 7, 9, and 11 km. Considering the causality of the moment tensor functions, the solution associated with the Green's function of 5 km focal depth has the seismic energy release starting 3-4 seconds after onset of signal arrival. The moment tensor solutions for the depths of 9, 11 km focal depths show that the seismic energy releases started 3-4 seconds before the onset of the P wave arrival, as shown offset arrows. Therefore, the degree of temporal consistency and causality of the resultant five moment tensor functions is greatest when inverting with Green's functions of 7 km focal depth, and the first seismic energy release was determined to have this focal depth.

There is a significant change in shape in the moment tensor functions around 4-5 seconds, which is indicated by an abrupt change in slope. This is most easily seen on the M11, M22 and M13 in Figure 12. These observations are consistent for all the focal depths and robust after filtering over a variety of ranges of frequency.

We derive a corresponding focal mechanism from the resultant moment tensor functions with Green's function for 7-km focal depth by calculating the area under each moment tensor element for an assigned time window. These values are used for M11 through M23 and used to construct a moment tensor matrix which is then decomposed, and used to find the best-fit double-couple. The focal mechanism associated with the best fit double-couple for the first time window (strike=315, dip=43, and rake=-89) is shown in Figure 13a. One of the nodal planes defines a normal fault

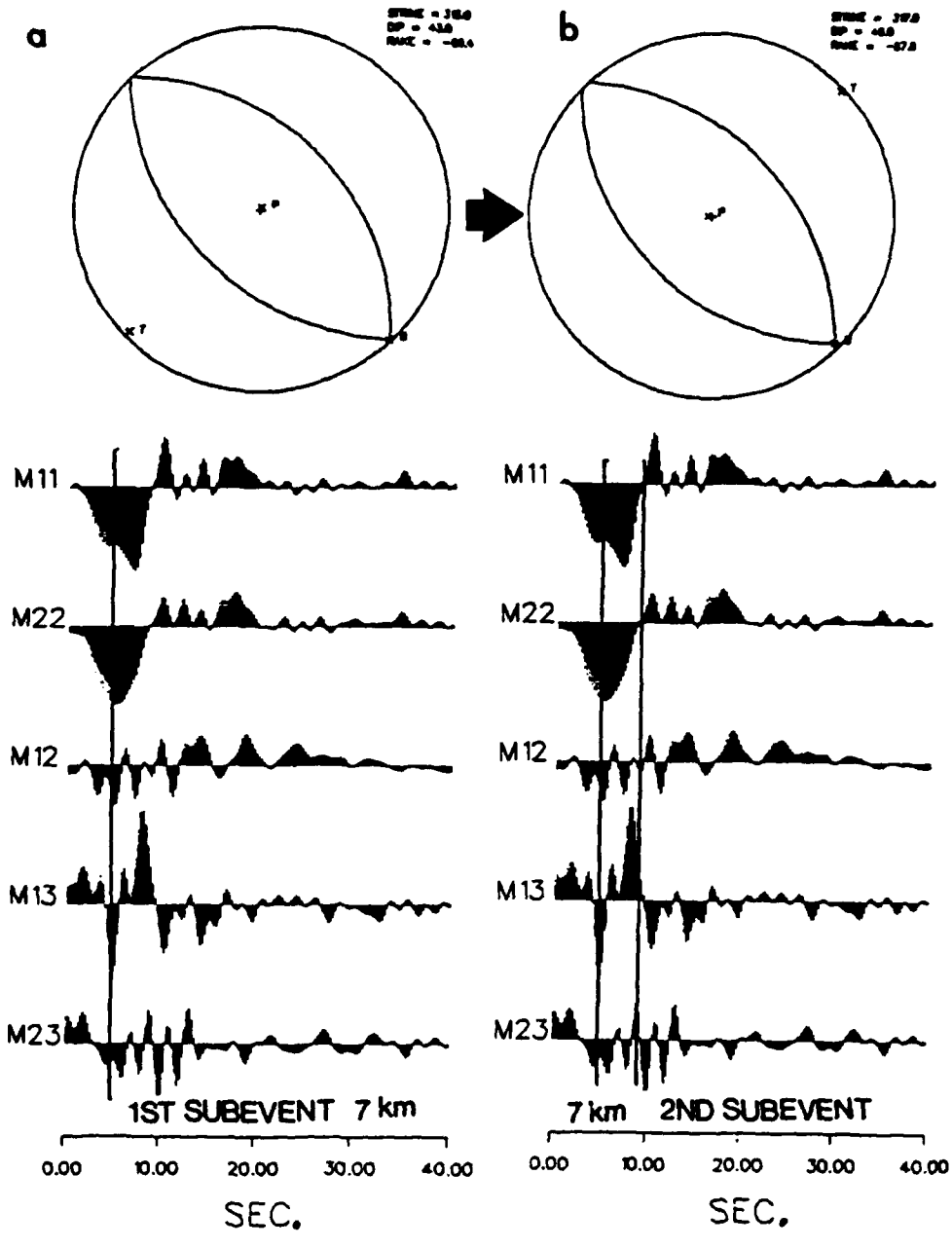

Figure 13. Two focal mechanisms and corresponding moment tensor functions determined for two subevents from the waveform inversion of the 1982, Yemen earthquake. The focal depths are resolved as 7-km for both subevents.

which is consistent with the linear surface rupture of extension cracks observed from this earthquake (NW direction). The moment for this event is 1.88 x 10^{25} dyne-cm which accounts for nearly 42 % of the seismic moment which Sipkin (1986) found for the Yemen event. The CLVD component is about 28%, which is high.

The next window of significant energy release was determined by taking different combinations of time windows with different starting time and lengths. Inverting with Green's function for the 5-km focal depth, there is relatively little temporal consistency for the second portion of the seismic energy release as shown by the offset arrows. Resultant moment tensor functions with Green's functions for 9 km and 11 km focal depths show relatively little temporal consistency for the start of the second seismic energy release episode. For the time dependent moment tensor elements with Green's functions of 7 km focal depth, the time window 5-9 seconds shows a good temporal consistency for the second seismic energy release. Performing the same kind of focal mechanism calculation for this time window yields the focal mechanism labeled subevent two in Figure 13b. The fault plane of the second subevent is nearly identical to the first subevent (strike=317, dip=45, and rake=-88). The moment for this subevent is 1.48 x 10^{25} dyne-cm which accounts for 33 % of the seismic moment which Sipkin (1986) found and the CLVD component is about 22%.

Trying to resolve any other significant seismic energy release in the moment tensor functions further back at greater times in the records yields a double-couple mechanism with relatively small moment, and a large non-double-couple component. This fact, along with the observation that there are no more well-developed windows of temporal consistency for the moment tensor functions for any of the inversion focal depths, suggests that all the significant subevents associated with the Yemen earthquake are resolved.

As a test of the overall consistency of the rupture process the P, B, and T axes as well as the fault planes were traced sequentially in time. This is done by determining the moment tensor for short time windows, from first onset of the event up to 9 seconds (see Figure 14). Each focal mechanism and the corresponding principal axis for each one-second time window were matched very well to the corresponding focal mechanisms of two main subevents. No abrupt change in focal mechanism within each subevent duration implies that, at least, within time windows of two main subevents there is not extreme source complexity. If there is a significant change in focal mechanism or overlapped sources within the time window, it would be expected that there would be fluctuations of focal mechanism between each short time window, or at least an increasing CLVD component. If the source process for the time window of 0 to 9 seconds is forced to a single event, the focal mechanism was similar to that of the two subevents but it has a significantly higher CLVD (58 %) component. The high value of the CLVD component associated with a single point source assumption as compared to those of two subevents obviously indicates that resultant moment tensor functions maps this event into a double event.

The waveform fits obtained using the time dependent moment tensor solutions are shown in Figure 10. The waveform fit is very good not only for the first or two swings, but for the entire waveform of body waves with a few exceptions.

As shown in the rake angles of two subevents (-89 and -88 degrees for the first and second subevent respectively), our fault model of a double source is nearly pure normal-slip for both subevents. Choy and Kind (1987) have significant amount of both right-(230 degrees of rake angle) and left-lateral (300 degrees of rake angle) strike-slip components for two subevents. The crack zones at the surface around the epicenter which are dominated by tensional features show no significant component of left-or right-lateral displacement (Plafker et al., 1987), and are much more consistent with the

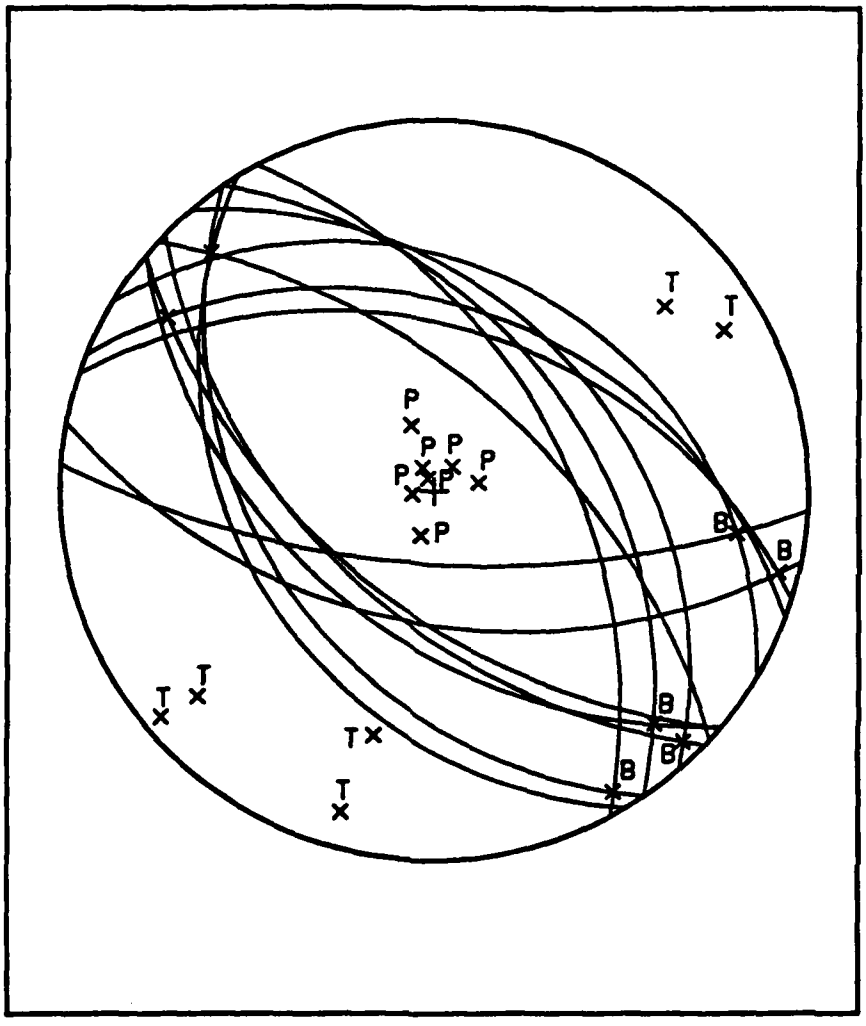

Figure 14. The evolving focal mechanisms and corresponding P, T, and B axes with shorter time windows from 0 to 9 seconds of the seismic energy release. All the P, T, and B axes from the waveform inversion show typical normal-slip motion and well stabilized for given time interval.

fault model of pure normal-slip. The change for left to right lateral slip is very difficult to explain in Choy and Kind's solution. This sort of "overshoot" in the faulting process is unphysical, unless pre-existing, weak fault planes which are geometrically favorable for both forward and backward directions of slip, but not necessary aligned with the planes of maximum shear stress caused by the regional stress caused the event. Our model of two normal slip subevents is the simplest interpretation.

Our fault model apparently does not match the onset of the second subevent (5 seconds) for Sipkin's (1986) model which has the second subevent at 12 seconds from the beginning of the seismic energy release. There are two possible explanations for this: (1) Sipkin used GDSN which is much longer period, or, (2) our analysis missed an event. Note that resultant moment tensor functions in Figure 12b show some seismic energy release after 12 seconds which could be a shear dislocation. However, performing the focal mechanism calculation for this time window yields a best-fit double-couple with the plane whose strike, dip angles are not much different from the two subevents, but a slip-direction which is about 180 degrees different from the first part of the record (thrust-slip motion vs. normal-slip motion). Since shear dislocation should not overshoot, the apparent energy release for this time window is probably due to numerical overshoot at the boundary of the inversion. It also gives a significantly higher non-double-couple component (>50 %) for this time window as compared to the first part of the record. These observations from the TDMT analysis suggests that all of the significant seismic energy releases occurred within 9 seconds.

Table 13. Total Seismic Moments for Various Source Models

	Total Seismic Moment
Sipkin (1986)	4.5×10^{25} dyne-cm
Choy and Kind (1987)	3.0×10^{25} dyne-cm
This study	3.4×10^{25} dyne-cm

The total seismic moment of the Yemen event from the TDMT analysis is smaller than the estimate by Sipkin (1986) as shown Table 13. Since Sipkin (1986) also used a time dependent moment tensor inversion algorithm in the time domain with long-period teleseismic data, the difference of the total seismic moment between ours and Sipkin's is puzzling. Even though Sipkin (1986) suggested the fault model where the second subevent starts after 12 seconds, we suggest that the difference of the total seismic moment may be due to the unresolved subevents or overlapping between two subevents. Experience with synthetic data shows that it is difficult to resolve overlapping subevents in time and that total seismic moments using only the constraints of temporal consistency and causality is underpredicted. Since the synthetic examples also showed that a high non-double-couple component can be caused by overlap between subevents, the high non-double-couple components (28 %, 22 % for the first and second subevent, respectively) for both subevents of our modeling, as compared to those by Sipkin (1986) (15 % and 8 % for the first and second subevent respectively) could be evidence for a overlapping between sources. Therefore, it is possible that the seismic energy release of two subevents which were within the first 9 seconds had a time overlap between them.

Another problem which may introduce error into the time dependent solutions is that of inadequate Green's functions. This problem is common to all moment tensor

inversion techniques. To incorporate all of the source structure information into the Green's function model requires precise knowledge of the source velocity structure as well as the inclusion of a great many generalized rays. Because the velocity structure for the long-period response in southwestern Arabian peninsula is not known precisely, we have used the simple source structure and attenuation model outlined earlier to avoid mapping structural artifacts into the time function.

The 1971 San Fernando Earthquake

Introduction

The nature of the fault geometry of the San Fernando earthquake of February 9, 1971, California has been controversial, and yet it is a very important problem in terms of deciphering the active tectonics of the west-central Transverse Ranges region. There are models to match either the local or teleseismic observations, or both of them simultaneously, and all these are different. Because of the abundance of geophysical data, and the importance of this earthquake, much effort has been expended to model the various aspects of the San Fernando earthquake. Each data set, such as near-field, static displacement and dynamic strong ground motion and far-field body waves, provides constraints to the faulting mechanism. Langston (1978) suggested a variable-dip, single-fault model to best fit the teleseismic body wave data while Heaton (1982) claimed a model consisting of two steep, constant-dip, subparallel thrust faults to best fit the combined data sets of strong ground motion, teleseismic P and SH waveforms, and static offsets of the ground. Barker and Langston (1982) also performed moment tensor inversion of teleseismic long-period body-waves for this event with a constant-moment-tensor assumption throughout the entire rupture process. Nonetheless, there still remains considerable controversy over the faulting history of this earthquake.

The San Fernando earthquake of February 9, 1971, is consistent with other events in the Transverse Ranges, and is an oblique thrust. This is distant from the adjacent strike-slip systems such as the San Andreas and the Garlock faults. From a geologic hazard point of view, the proximity of the surface expression of the San Fernando fault to the highly populated Los Angeles area makes it an extremely important. The tectonic setting of epicenter, and aftershock region is quite complex: the area is characterized by the predominate northwest trending grain of much of southern California disrupted by the east-west trending Transverse Ranges (Hadley and Kanamori, 1978). This region is also considered to be a part of the southern boundary of the southern California uplift, which is mapped as several north-dipping thrust faults. In contrast to the San Fernando fault, which is considered to be the surface rupture of the 1972 seismic event, the San Gabriel fault system, which has not experienced significant movement since the Pliocene (Crowell, 1954), also passes through the aftershock region to the northwest (see Figure 15).

The purpose of this study is to investigate the first-order mapping of geometric and temporal source complexity of the San Fernando earthquake and then, possibly to relate this result to the tectonics of the San Fernando region. As with the previous studies we model the source complexity of the San Fernando earthquake with the time dependent moment tensor inversion of the observed teleseismic body wave.

The data set we use contains seventeen long-period teleseismic P waves records on WWSS and Canadian Network taken from Langston (1978). The Green's functions used in this inversion are generated using the method of Langston and Helmberger (1975) and include only three important rays; direct P, pP and sP. Attenuation effects (t^* =1.0 second for P waves) and geometric spreading are added. A single layer-over-half space source structure model, which is the same as the model A in Table 1 of the Langston (1978) was used in generating the Green's functions. In order

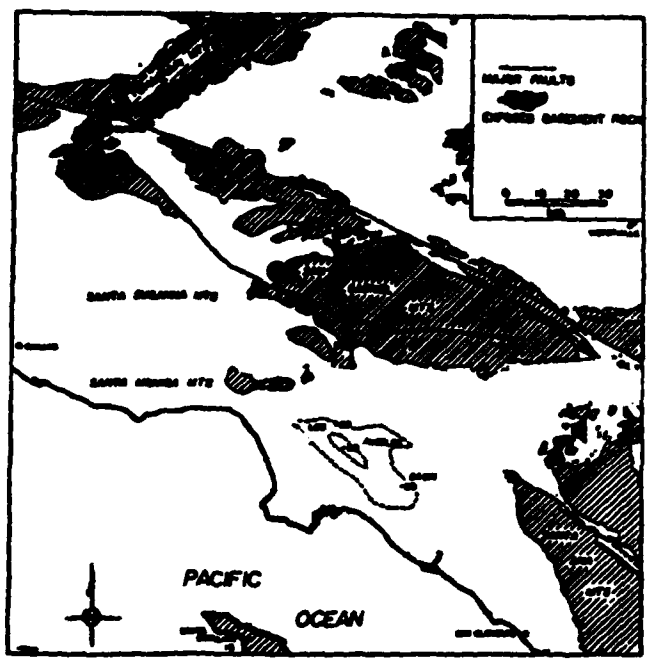

Figure 15. Map of the major faults (the San Andreas, Garlock and San Gabriel), the epicenter and exposed bedrock associated with the 1971 San Fernando earthquake (modified from Hanks, 1975)

to determine the focal depth, the waveform inversion was performed for different Green's functions generated at depths between 3 km and 15 km (two km intervals).

Results

We performed the TDMT inversion for the San Fernando earthquake using the teleseismic body waves, and the results are shown in Figure 16. To invert for source parameters from the observed waveforms, we minimized the RMS misfit of the observed waveforms, or inverted in the least square sense, and then isolated the best-fit double-couple mechanism for the earthquake from the whole moment tensor elements. Again the source is assumed to be purely deviatoric. Since no study has suggested that the origin of the San Fernando earthquake has significantly different source physics from a double-couple mechanism, decomposition of resultant moment tensor matrix into major double-couple and minor CLVD component is reasonable.

The resultant time dependent moment tensor functions (Figure 17) show a similar degree of temporal consistency over the entire ranges of the focal depths (3 km to 15 km) with a slight shift in the offset of the time function. That is, these time dependent functions appears to represent energy release from 0 to 5 seconds followed by a second energy pulse with a total duration of 10-13 seconds over the entire ranges of focal depths. The resultant time dependent moment tensor elements has significant shape change around 4-5 seconds after the onset, which is seen most easily on the M11 and M22 components. This is consistent for all the focal depths and robust for filtering of various ranges of frequency domain moment tensor elements, which suggest two sources.

In addition to investigating the physical constraints such as temporal consistency and causality among time dependent moment tensor elements, the constraint of minimum size of non-double-couple component for resolution of the double-couple

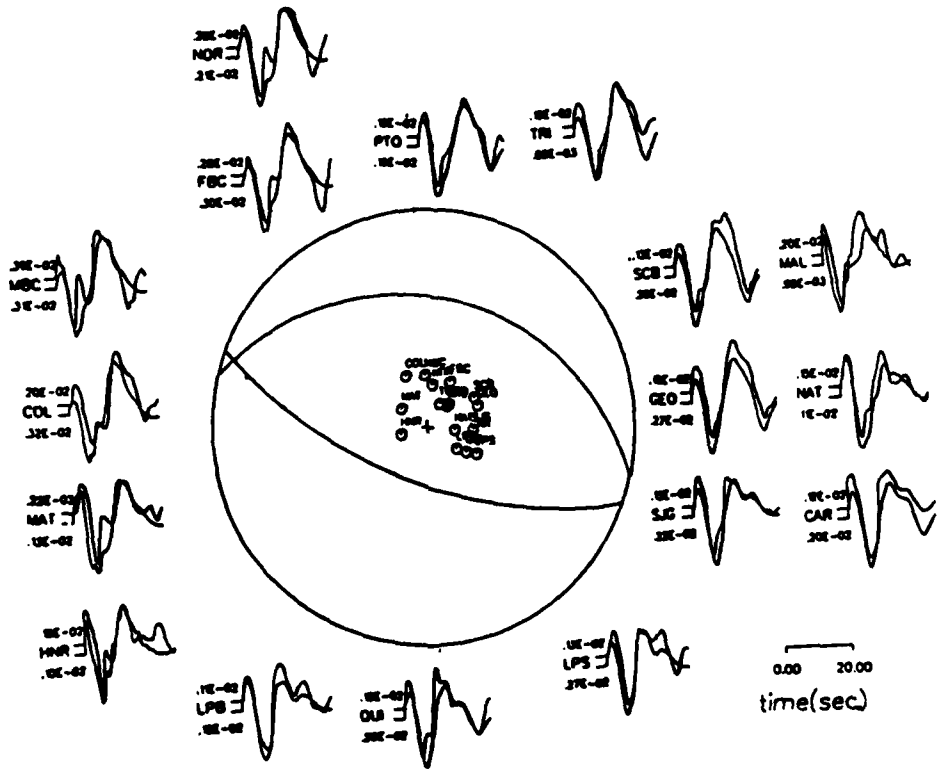

Figure 16. Seventeen teleseismic station distribution and corresponding long-period teleseismic P waveforms (upper waveforms are observed and lower ones are synthetic) for the moment tensor inversion. This figure also shows waveform matches between observed and synthetic results from the time dependent moment tensor inversion.

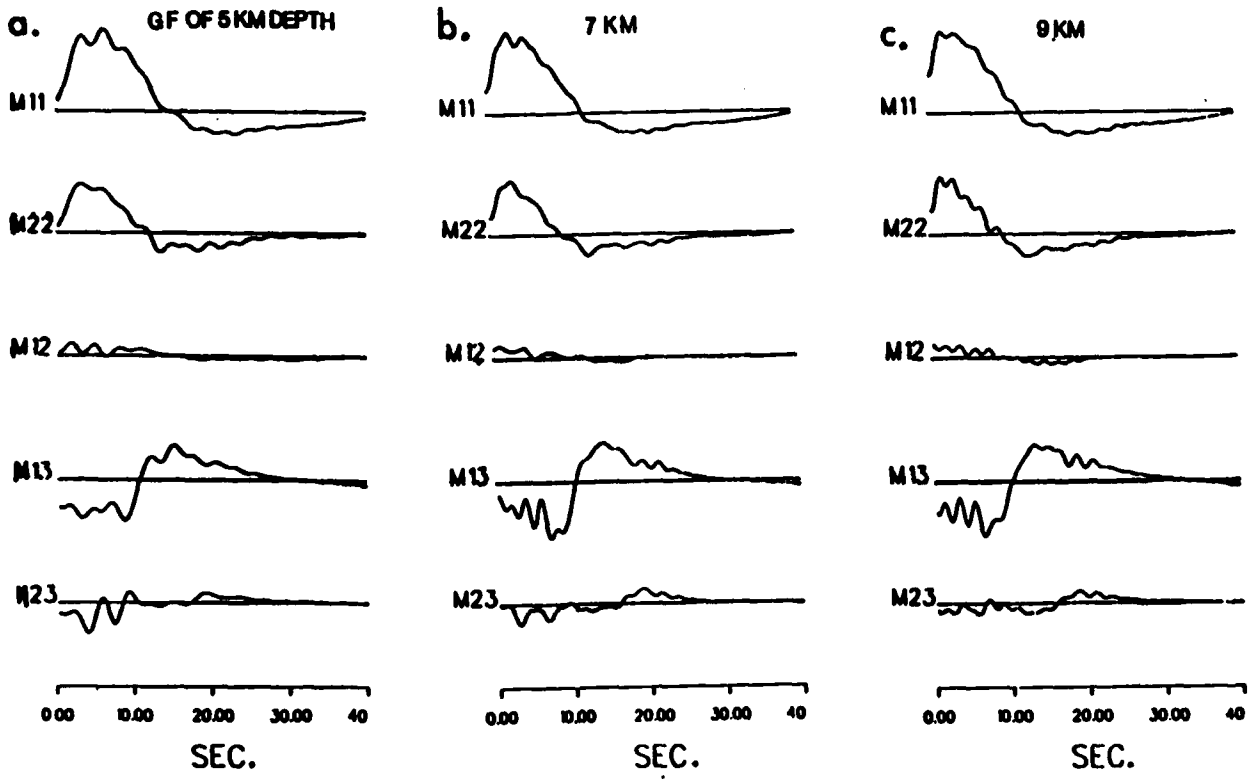

Figure 17. Resultant time dependent moment tensor elements or moment tensor functions from the waveform inversion of the 1971 San Fernando earthquake with Green's functions of 5-km, 7-km, 9- km, 11-km, 13-km, 15-km focal depths. Considering the causality, the five moment tensor functions for 13-km focal depth show the best-developed causality.

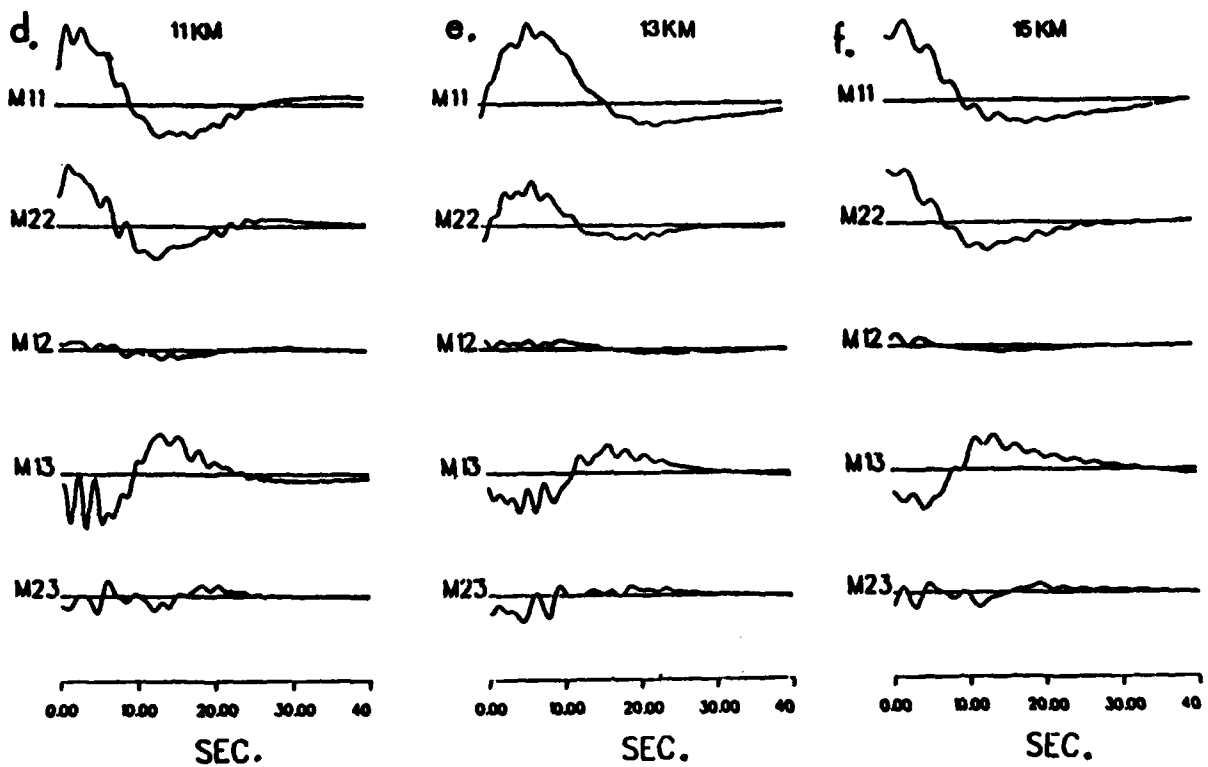

Figure 17. Resultant time dependent moment tensor elements or moment tensor functions from the waveform inversion of the 1971 San Fernando earthquake with Green's functions of 5-km, 7-km, 9- km, 11-km, 13-km, 15-km focal depths. Considering the causality, the five moment tensor functions for 13-km focal depth show the best-developed causality.

seismic energy release was tested from 3 km to 15 km using three different time windows as shown in Table 14.

Table 14. CLVD Components for Different Focal Depth

	CLVD component (%)	
Focal Depth	0-5	5-12 (second)
15 km	39	34
13 km	16	21
11 km	38	34
9 km	36	24
7 km	32	14
5 km	33	34
3 km	29	35

The first part and second part of the time dependent moment tensor functions obtained using a Green's function for a focal depths of 13 km and 7 km respectively, shows the smallest value of the CLVD component (16 %, 14% for the first and second subevent, respectively).

Barker and Langston (1982) suggested that any double-couple parameters for this event with assumption of a constant moment tensor representation for the entire faulting process are not reliable since the non-double-couple component is expected to be high for such an apparent complex event. However, using time-dependent moment tensor inversion, each non-double-couple component for the double point source assumption shows fairly low values such as 14-17 % as shown in Table 14. A single point source assumption for 0-10 seconds yields much higher values (>50 %). Much lower values for the CLVD in the TDMT as opposed to the TIMT inversion could be explained partially by simply allowing an evolving complex seismic source.

Determining the depth of each subevent, which is an inherently a non-linear process in the moment tensor source representation, was done by the causality constraint discussed earlier. The depth of 13 km fits the observations best for the first subevent. The temporal consistency of the first portion of the five moment tensor functions is also good when using the Green's function of 13 km source depth for the inversion. However, resultant time dependent moment tensor elements using the Green's functions of 13 km focal depth shows a much less-developed temporal consistency between all the five moment tensor functions at the end of main energy release, around 10 seconds as shown by several offset arrows in Figure 17. The physical constraints, combined with the minimum size of the none-double-couple component thus allow us to differentiate the significant seismic energy release from the resultant moment tensor functions. Therefore this first subevent was determined to have focal depth of 13 km.

To derive a focal mechanism from the resultant moment tensor functions, we calculated the area under each moment tensor element and assigned the values to M11 through M23. The focal mechanism associated with the best-fit double couple for this time window (0-5 seconds) is shown in Figure 18a and labeled subevent one. For the first time window of temporal consistency, taking the nodal plane whose strike, dip, and rake are 286°, 29°, and 84° respectively, yields a thrust fault that agrees with the general trends of the surface faulting of the San Fernando earthquake. The relatively small CLVD component of 16 % suggests that the slip occurred mainly along a simple fault plane during the first time window.

In an attempt to resolve a second subevent further back in the time record, the time dependent moment tensor functions obtained were tested with the condition of consistency for different depths. The best fit is with a focal depth of 7 km which shows a minimum CLVD component (16 %) in the time window of 5 to 12 seconds. The

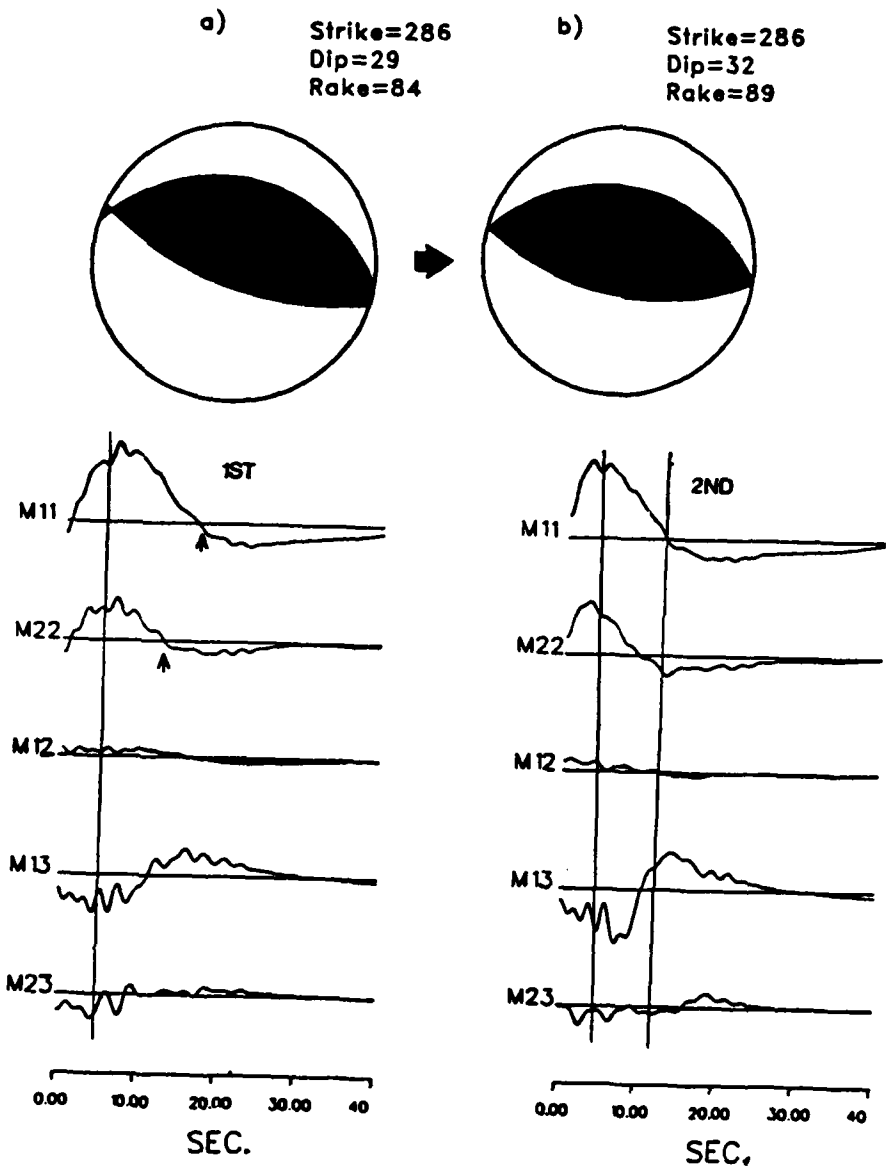

Figure 18. Two focal mechanisms and corresponding moment tensor functions for two subevents from the waveform inversion of the 1972 San Fernando earthquake. The focal depths are resolved as 13-km and 7-km for the first and second subevent, respectively.

inversion results with either 5 km or 9 km focal depths have nearly the same degree of temporal consistency for the second time window. Calculation of the best-fit double couple for this subevent gives the focal mechanism shown in Figure 18b labeled subevent two. The fault plane shows a thrust fault which is similar to the first fault plane; strike = 286°, dip = 32°, and rake = 89°). The small CLVD component (14-16 %) for this time window again suggests that there is no source complexity within this time window. The main difference of our focal mechanism and that of Heaton (1982) (54° and 45°, dip angle of the first and second subevent, respectively) or Langston (1978) (53° and 29°) is significantly shallower dip angles. This will be discussed in a later section.

To investigate the source complexity within the two subevents, (such as focal mechanism changes or source interference), the possibility of the focal mechanisms and the CLVD components for both 13 km and 7 km focal depth were traced using time windows of two seconds length. Figure 19 shows these focal mechanisms between 0 and 12 seconds, and are nearly identical to those of the two subevents (for 13 km the first subevent and 7 km for the second event). The CLVD components for the short-period time windows (>20 %) for all the time windows for the different focal depths (13 km and 7 km) are larger than those of the two subevents (14-17 %).

Note that all five components of the moment tensor for all inversion depths (3 km to 15 km) show significant energy release even after 12 seconds. There are two possible explanations for this apparent energy release. Either unmodeled shear dislocation or numerical noise caused by inversion process of the overdetermined linear simultaneous equations was mapped into the moment tensor. Performing a focal mechanism calculation for this time window yields a best-fit double-couple with the plane whose strike, dip angle are similar to subevent one or two, but a rake which differs by about 180° (for example, thrust fault vs. normal fault). Since this

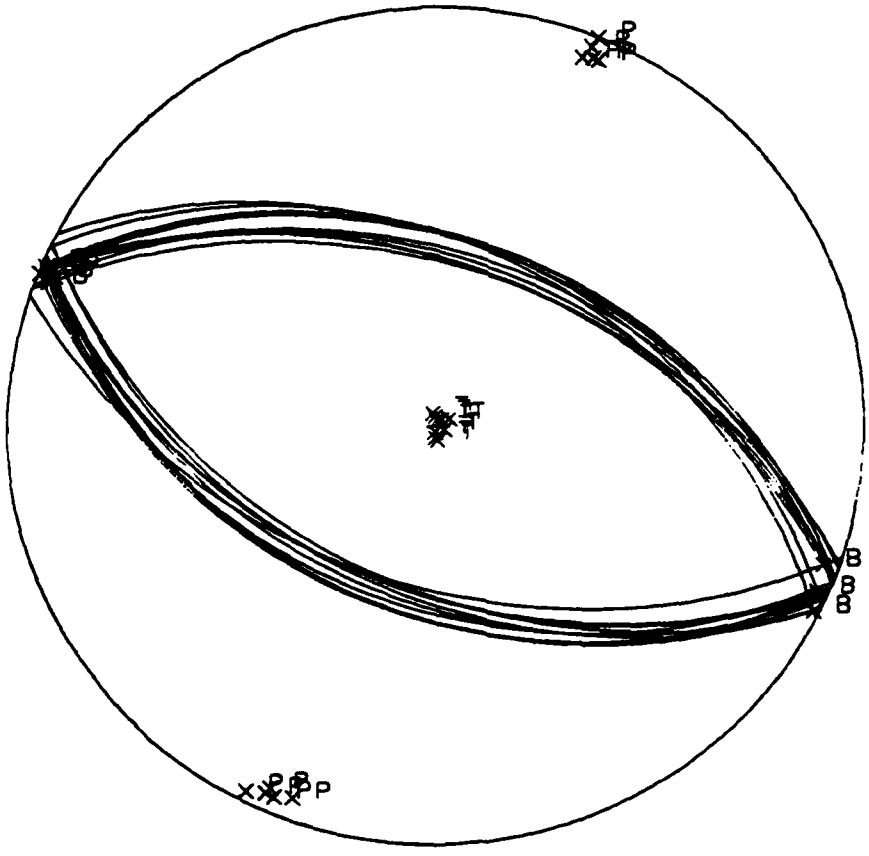

Figure 19. The evolving focal mechanisms and corresponding P, T, and B axes with 1-second time window from 0 to 10 seconds of the seismic energy release. All the P, T, and B axes from the waveform inversion are well stabilized for this time interval.

contradicts the accepted theory that shear slip motion does not overshoot, the energy release is probably due to numerical noise. Trying to resolve any other subevents further in the time record, moreover, yields double couple mechanisms with very small seismic moments (small area) and large CLVD components (>40%). Further, the inversion results do not show the robustness of the source time function shape for different values of filtering nor show much temporal consistency. These observations suggest that all of the important subevents associated with this event have been resolved within the first 12 seconds.

The waveform fits obtained using the time dependent moment tensor solution are shown in Figure 16. It is important to point out that these synthetic waveforms were generated by convolving one of the time-dependent moment tensor solutions with a Green's functions for the appropriate focal depth. The stated interpretation of each earthquake as two subevents does not enter into the generation of the synthetic waveforms. The synthetic waveforms generated using either time dependent moment tensor solution (i.e., the 13 km or 7 km solution) are of the same quality. Although the 13 km time dependent moment tensor solution does not physically describe the entire rupture process of the San Fernando event, it still models over the entire earthquake mathematically. This attests to the robustness of the time dependent moment tensor solutions. Note that the waveform fit is very good throughout the entire waveform.

Discussion

The inversion results, based on teleseismic WWSSN long-period body waves (P and SH waves) indicate that the San Fernando earthquake can be modeled as two double-couple sources. This interpretation of our study is consistent with the results by many previous workers such as Langston (1978) and Heaton (1982), who modeled this

event as a double event. Barker and Langston (1982) also suggested that the finite source time function obtained from the long-period-pass-filtered data, using the constant-moment-tensor assumption over entire faulting process, implies that at least a two source model is necessary for modeling WWSSN long-period body waves (see Figure 20). However, they considered any double-couple parameters derived from the teleseismic waveform inversion using TIMT inversions to be unreliable due to the high CLVD component.

Our study also supports that the San Fernando earthquake is composed of two evolving subevents. Both the large shape change at around 5 seconds, and loss of the temporal consistency at the end of the seismic energy release episode (Figure 17) suggest that it is unreasonable to consider the San Fernando earthquake as a single point double-couple source with a single source depth (13 km). Moreover, resultant moment tensor functions derived for a depth of 7 km show a greater degree of temporal consistency at the end of the seismic energy release. The resultant moment tensor functions derived for a depth of 7 km also shows a well-developed non-causality at the beginning of the seismic energy release, which implies that the ruptures did not origin there, but at 13km. The two source model also has a smaller non-double-couple components as compared to that of one point source (> 50 %), and supports the hypothesis that the San Fernando earthquake must be considered as a two source fault with changing source depths, possibly with upward rupture propagation.

The observation that the time boundary between the two subevents is around 5 seconds, although it does not go to zero displacement and it does not separate sharply as that from synthetic data inversion implying that the San Fernando earthquake ruptured with a little overlap between the first and second subevents. Our previous synthetic data example for the overlapping between two subevents also showed that

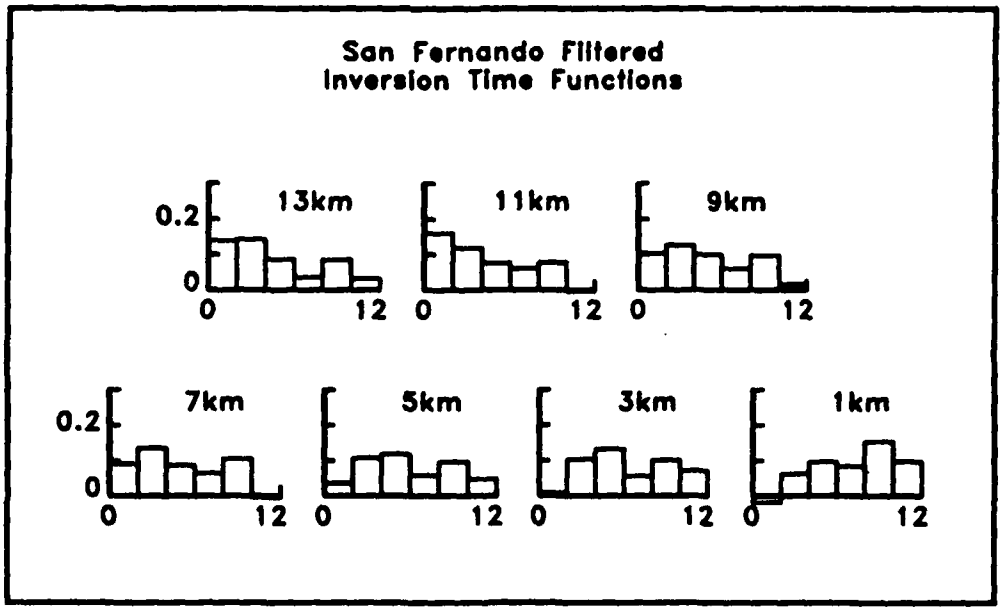

Figure 20. Source time functions for the filtered data at several different depths from 1-km to 13-km. This figure apparently shows consistency between source time functions, indicating the broader energy pulse followed by a narrower pulse of 2-4 seconds (from Figure 10b of Barker and Langston, 1982).

moment tensor functions do not cross the zero amplitude line at the boundary between two subevents.

As was pointed out earlier in the last section, our solution has considerably shallower dip angles for both subevents (29° for the first subevent and 31° for the second subevent) compared to the fault models suggested by Langston (1978) in Figure 21a (53° and 29° for the first and second subevent respectively) and Heaton (1982) (54° and 45° for the first and second subevent respectively). The two-source, steep dip-angle-faults model, suggested by Heaton (1982) is shown in Figure 21b, and matches the surface expression of the San Fernando fault (the second subevent) and to the Sierra Madre fault (the first subevent). Since there is little constraint on the dip of the San Fernando fault still makes it difficult to resolve geometry of the rupture process of the main event, approach to long-term aftershock seismicity could be an approach to constraining the geometry of the main event.

We find that the tectonics of the study region is much more consistent with our proposed model of fault geometry than the Heaton and Langston model. Hadley and Kanamori (1978) showed that even the shallowest aftershock earthquakes are consistently 3 to 5 km below the inferred main shock fault plane of Langston (1978) (Figure 22a). They infer from the observation of temporal and spatial distribution of the aftershocks that either the fault surface could be downstepped to the west or these aftershock events are occurring along a deeper, subparallel fracture. We believe that the aftershock distribution is consistent with our model. When projecting only the events denoted by square signs, which are located mainly in the central areas and most likely represent the geometry of the San Fernando aftershock fault zone, two shallow-dip, subparallel fault planes, can be seen. Figure 22b shows this interpretation. We hope that this long-term observation of the aftershock seismic activity represents

a.

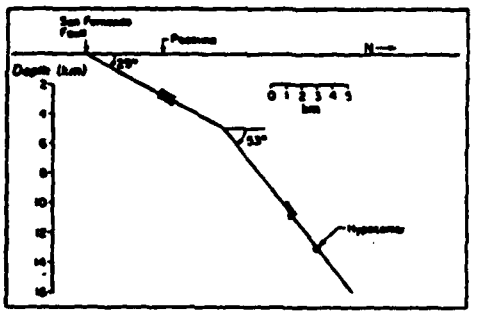

b.

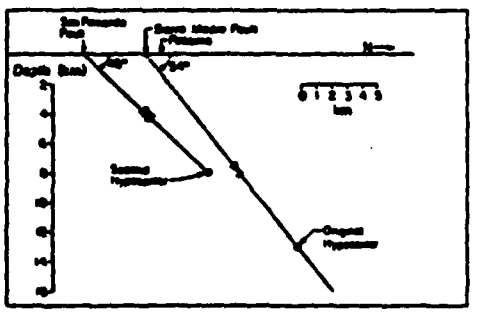

Figure 21. (a) The cross-sectional view of fault geometry which consists of a single fault whose dip shallows as depth decreases (from Figure 2 of Heaton, 1982). (b) The cross-sectional view of fault geometry which consists of two parallel thrust faults (b) (from Figure 5 of Heaton, 1982)

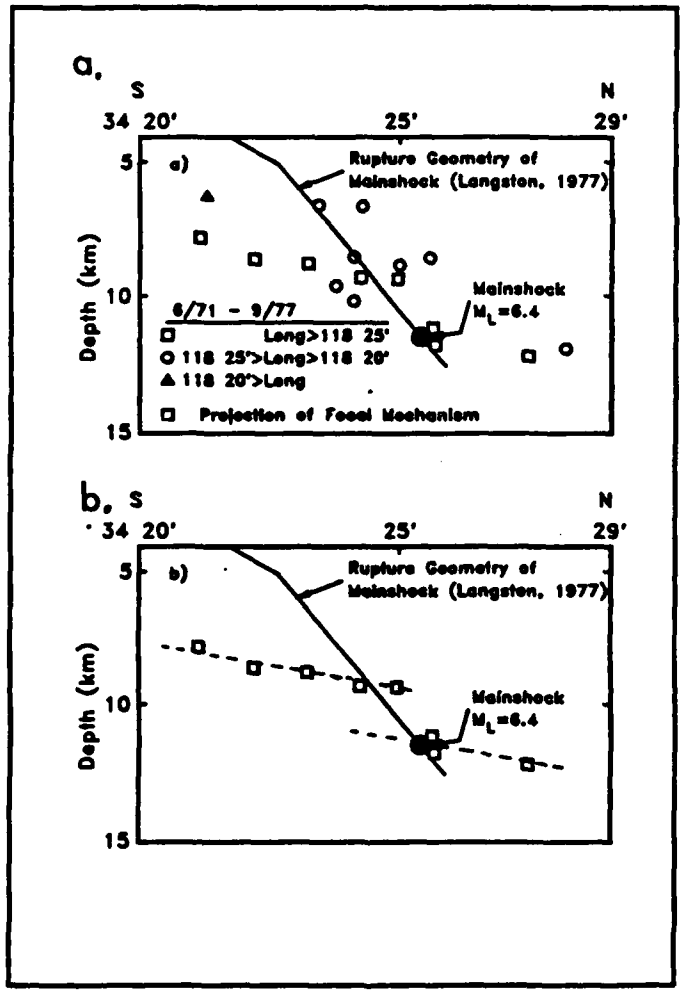

Figure 22. Cross-sectional view of the aftershock seismicity through the main event. (a) aftershock earthquakes for the whole aftershock region (b) aftershock earthquakes for the aftershock region which is greater than 118° 25' in longitude (modified from Hadley and Kanamori,1978).

the fault geometry of the San Fernando region, and thus implies two shallow-dip-angle fault geometry.

In addition to this general trend of the seismic activity in the San Fernando region, there are two specific example of earthquakes, one of which was an aftershock of the San Fernando event and have the very shallow, almost flat fault plane. Hadley and Kanamori (1978) suggested that one of the aftershock earthquakes (10/17/1976) located slightly deeper, and several kilometers north of the main event could represent the shear rupture along a flat plane. Another deep, M_L=4.5 earthquake (4/8/1976), located about 30 km west of San Fernando, also shows a rupture plane with shallow-dip-angle. These two observations demonstrate that shallow-dip-angle fault geometry of the main seismic event is consistent with this tectonic environment. The difference between previous works by Heaton (1982) and Langston (1978) and our resolution seems to be not only from the inversion method and but also partly from data set of the inversion or forward waveform matching (Langston and Heaton).

The first seismic energy release, 5 seconds long, can be represented by a point source of 13 km depth, but after 5 seconds the faulting can not represented by a point source with the same focal depth (13 km). The second part of the energy release is represented by the point source at 7 km depth. Therefore our fault model, which is consistent with regional tectonics, indicates that the San Fernando earthquake ruptured along two shallow- dip fault planes which are upstepped to the south with a little overlap of rupture timing between the two subevents.

Our fault model apparently does not match the conventional interpretation of the San Fernando fault, which is believed to be the main surface rupture of the San Fernando earthquake. Instead, our two subparallel shallower-dip-angle fault model has a more extensive fault plane to the south, and the movement on that fault plane never reached the surface. The possible extension of the fault plane to the southward is

apparently more consistent with the fault that most of the aftershock activity within San Fernando zone has been thrust faulting at depths shallower than, and to the south, of the main shock. Therefore our fault model suggests that the San Fernando fault is believed to be the surface mapping of the pre-existing weak fault planes which are geometrically favorable for slip but not necessarily aligned with the planes of maximum shear stress such as strike slip motion of the San Andreas fault.

1952 Kern County Earthquake

Introduction

The July 21, 1952, Kern County Earthquake is of considerable interest because of its large size (M_L = 7.2) and characteristic surface rupture pattern, which shows a remarkable contrast between the areas where the fault crosses sediments of the San Joaquin Valley and where it crosses exposed Sierra Nevada bedrock (Figure 23). The White Wolf fault shows multiple rupture histories (Dunbar et al., 1980, Stein and Thatcher, 1981) and apparently has a very complex fault plane. As improved seismic mapping techniques have been developed, many earthquake sequences in the Intermountain region of the western U.S. have been found to involve complex rupture histories on multiple dislocation surfaces. The White Wolf fault is apparently not a typical strike-slip fault like the San Andreas and Garlock faults but shows complicated rupture surfaces that have experienced large vertical components of displacement. From a geologic hazard point of view, the proximity of the White Wolf fault to the Big Bend of the San Andreas fault is extremely important. Castle (1978) has suggested the White Wolf fault is the result of rapid uplift associated with the northwest-bounding tectonic flexure of southern California.

Considering the importance of the earthquake and the abundance of seismic waveform data, it is somewhat surprising that there is very little documentation of

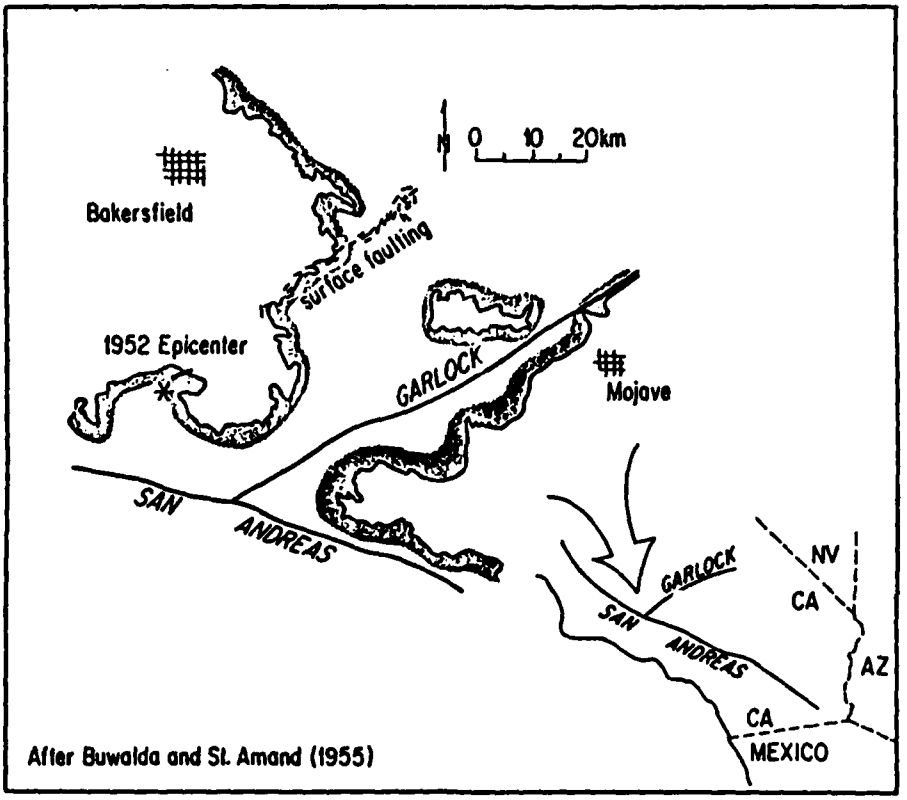

Figure 23. Map of the major faults (the San Andreas and Garlock) and epicenter and surface faulting trends on the White Wolf fault associated with the 1952 Kern County Earthquake (from Buwaldo and St. Amand, 1955). Also shown the boundaries among Sierra Nevada bedrock, the San Joaquin Valley, and the Mojave desert.

seismic waveform modeling using recently improved seismic techniques, although Dunbar et al. (1980) and Stein and Thatcher (1981) have interpreted the complexity of this seismic source using geodetic data. To understand the source complexity of the Kern County earthquake as suggested by previous studies, we performed the moment tensor inversion of the observed seismic waveforms. Unfortunately, the conventional constant-moment-tensor assumption breaks down for complex seismic sources for which the fault orientation and slip change with time. To map out seismic sources that have complex rupture histories on multiple fault surfaces, or to map out both geometrical and temporal variation of the complex earthquake source simultaneously from the observed waveforms, it is preferable to use a time dependent moment tensor inversion instead of one that assumes a constant moment tensor throughout seismic energy release. This is because the time dependent moment tensor inversion resolves six moment tensor elements independently as a function of time by using a linear formulation in the frequency domain. Although this algorithm allows more degrees of freedom in the inversion process, in general we have determined that the moment tensor elements are resolved sufficiently to map source complexity (source multiplicity, source time function of each subevent, and focal depth). We do this by adding additional physical constraints, such as the degree of temporal consistency among six different moment tensor elements, causality of source time function, and the size of the CLVD component. The resulting time dependent moment tensor elements can be used to describe seismic source kinematics and even to infer seismic source dynamics.

As predicted by the geodetic analysis of the source complexities (Dunbar et al. 1980; Stein and Thatcher 1981), the moment tensor inversion of the teleseismic body waveforms of the Kern County earthquake gave a moment tensor which had a large non-double-couple component. Assuming a moment tensor eigenvalue system with no volume change, the CLVD is one of the most important characteristics of the seismic

source used to decipher the tectonic phenomena of a given region. A variety of seismic source mechanisms have been proposed to explain these non-double-couple force systems using the moment tensor inversion of the teleseismic waveforms: source multiplicity, rupture on nonplanar fault surfaces, effects of near-source structure, and inherent source characteristics such as tensile failure under high fluid pressure. Based on this information, we have investigated the high non-double-couple result obtained for the Kern County Earthquake. This study suggests that the high CLVD could be caused not only by inadequate waveform data but also by source complexity.

The data set we use is the long-period teleseismic body waveforms (seven P-waves and three SH-waves). Although all the waveforms for moment tensor inversion are recorded on a variety of historic receiver instruments, normalizing all the waveforms with reasonable assumptions makes it possible to minimize the uncertainties of waveform inversion. The purpose of this report is to map out the time dependent complexity of the Kern County seismic source and then to relate this result to the tectonics of the White Wolf fault using the time-dependent moment tensor inversion of ten teleseismic waveforms.

Analysis of Data and Results

Before discussing the details of the time-dependent moment tensor inversion results, we want to introduce results of two previous studies. Figure 24 shows two inferred focal mechanisms of the Kern County earthquake suggested by Dunbar et al. (1980) from the modeling results of pre-, co-, and post-seismic strain changes. These two inferred focal mechanisms show a fixed angle in both strike to the NE and dip between the first and the second part of the seismic energy release. Next, Figure 25 shows three inferred focal mechanisms of the Kern County earthquake in a study by Stein and Thatcher (1981). They used geodetic data to model observed displacement

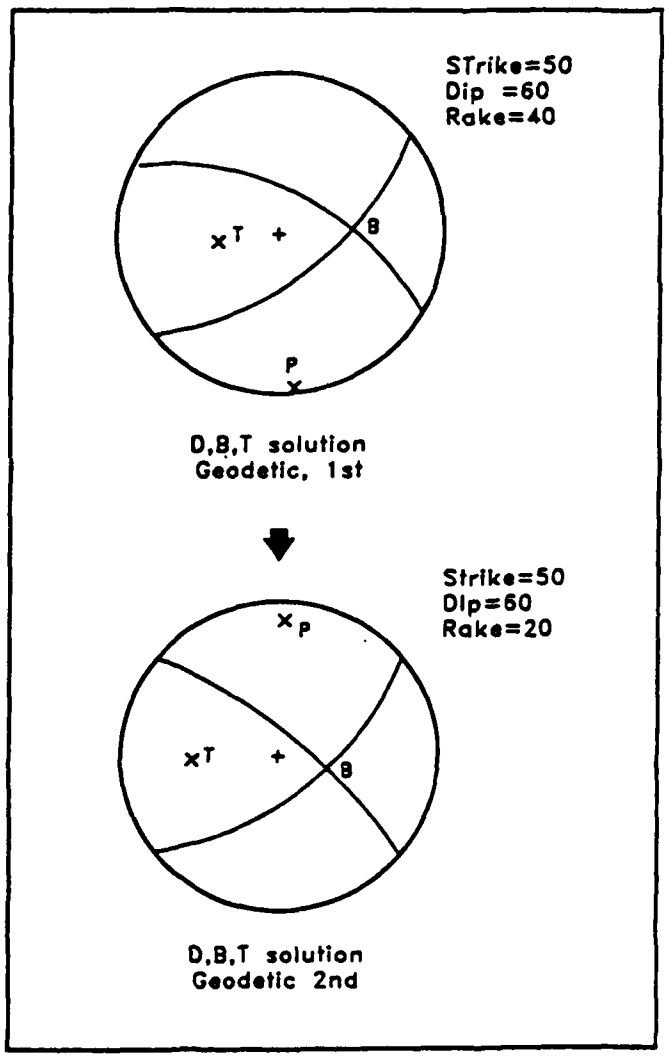

Figure 24. Two inferred focal mechanisms of 1952 Kern County earthquake from Dunbar et al.'s (1980) results using geodetic survey data (pre-, co-, and postseismic strain changes). The upper one is for the first subevent, and the lower is for the second subevent. Two focal mechanisms show fixed strike (N50°E) and dip angle 60°SE) and also show slightly more strike-slip component during the later part of the seismic energy release.

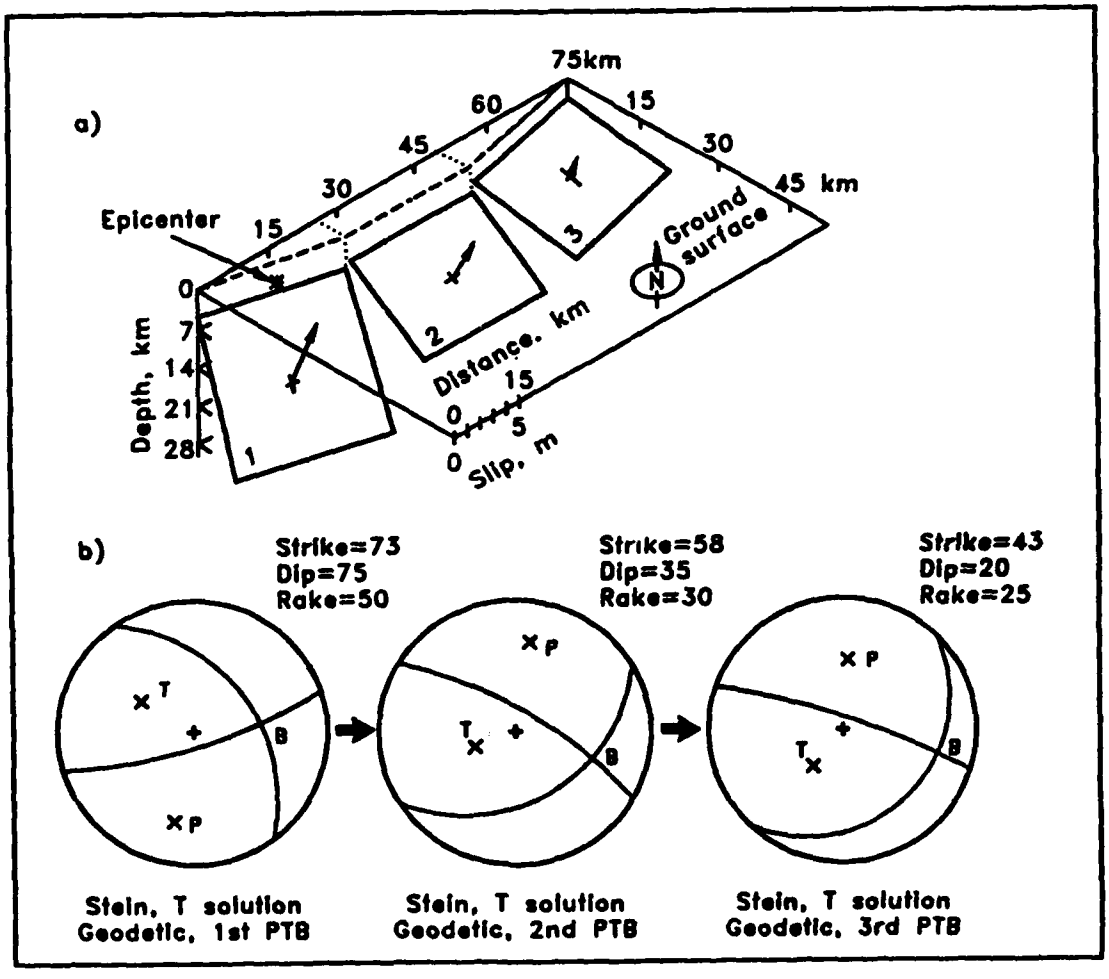

Figure 25. Three planar fault surfaces and corresponding inferred focal mechanisms of the 1952 Kern County Earthquake from Stein and Thatcher's (1981) interpretation using geodetic data. Three evolving focal mechanisms show counterclockwise rotation in strike, shallower in dip angle, and more left lateral strike slip at later part of seismic energy release.

and strains on the free surface caused by multiple subsurface rupture planes. Their three focal mechanisms suggest a counterclockwise rotation of strike angle, shallowing of dip angle, and more left-lateral strike-slip motion associated with later seismic energy release along the northeastern part of the White Wolf fault. These two previous studies of geodetic data modeling strongly suggest that the Kern County earthquake occurred not on a single fault plane but on multiple rupture planes along the White Wolf fault.

We performed time dependent moment tensor inversion for the Kern County earthquake using ten long-period teleseismic body waves, as shown in Figure 26. To invert source parameters from the data, we minimized the RMS fit to the waveform data, or inverted in the least squares sense, and then isolated the best-fit double-couple for the earthquake from the whole moment tensor solution. The best-fit double-couple mechanism results from averaging the intermediate and largest (in absolute value) eigenvalues of the diagonalized moment tensor. This value is taken as the double-couple portion of the earthquake, and the remainder is the compensated-linear-vector-dipole (CLVD) component.

When interpreting time-dependent moment tensor results, we considered several constraints to differentiate significant seismic energy release from background noise. To do this, we picked the optimal time window and then estimated an adequate depth for each seismic source. The constraints used to map out the seismic source parameters from the resultant time dependent moment tensor elements are much more important when considering the time dependent moment tensor inversion algorithm, which allows more freedom in the resultant moment tensor elements. The first condition is satisfied by finding the time window in which all six moment tensor elements vary with time in a reasonably consistent manner. Although each element is allowed to have an independent time history in the inversion process, it would be

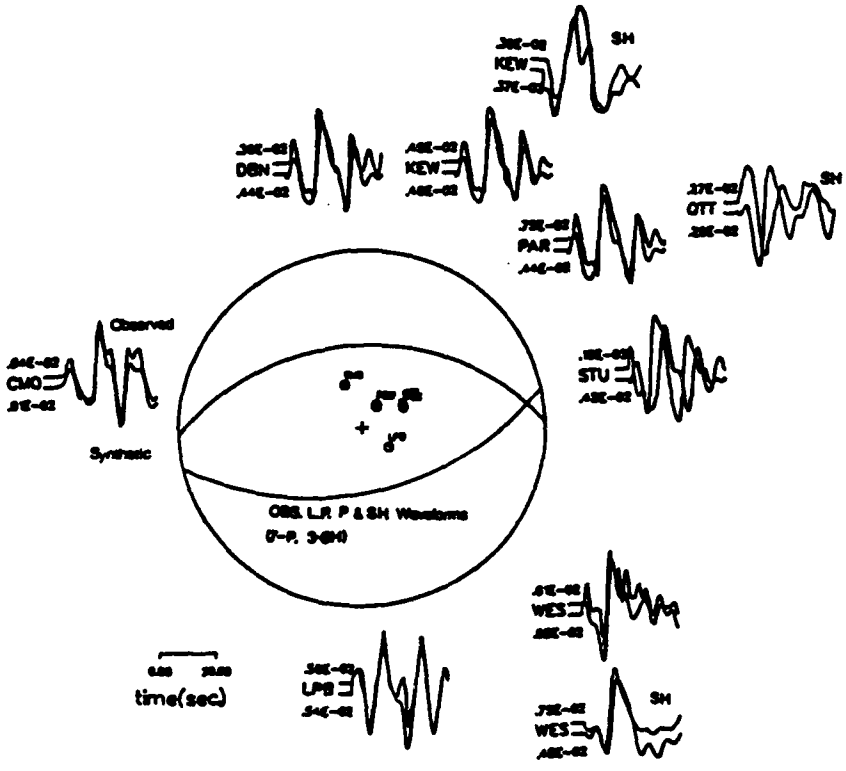

Figure 26. Teleseismic station distribution and corresponding long period teleseismic P and SH waveforms (upper ones are observed and lower ones are synthetic) for the moment tensor inversion. 7 P waveforms and 3 SH waveforms are used for the waveform inversion which are recorded on a variety of historic instruments. This figure also shows waveform matches between observed and synthetic results from the time dependent moment tensor inversion.

physically unrealistic if three of the components changed rapidly with time while the other three changed slowly. By fulfilling the requirement that the moment tensor elements show temporal consistency among six time dependent moment tensor elements, we are likely to have a "seismic source." The second condition is the causality of the source time function, which is more important, especially when the seismic sources are composed of multiple subevents with different focal depths. The third condition is that the shapes of all the time dependent solutions are robust with respect to filtering with the various combinations of frequency components derived from the synthetic examples. The reason for shape stability is that the seismic energy release is a genuine physical displacement that will be much more robust in comparison with the apparent seismic energy release associated with changes in frequency range. The final constraint is a physical compatibility between subevents. We avoid time windows which give us nearly the same strike and dip angles but a rake which differs by 180° compared with rakes of focal mechanisms of neighboring time windows. Even though some time windows show a good temporal consistency, this kind of overshoot or edge effect, inherently caused by using sinusoidal functions to synthesize time dependent moment tensor functions in the Fourier Transform, seems to be physically unrealistic in the seismic energy release process. This overshoot phenomena in the time dependent moment tensor inversion could be compared with the negative component of the source time function from an inversion that assumes a constant moment tensor. Since each seismic event has a finite amount of seismic energy release, time windows for a specific event can be constrained within a reasonable time boundary. This condition is satisfied if the focal mechanism resolved for a given time window agrees with geologic information, such as surface rupture patterns and tectonic environment.

In studying the resultant time dependent moment tensor from the waveform inversion of the Kern County earthquake, we noted that the line of temporal

consistency of the first portion of the moment tensor functions for three different Green's functions of 25-km, 20-km, and 15-km depth apparently shows clockwise rotation (Figure 27). The temporal consistency of the first portion of the five moment tensor functions is greatest when inverting with a Green's function of 20-km source depth. When inverting with a Green's function of 15-km focal depth, a time dependent moment tensor function shows the worst case of causality of the source time function. These constraints thus allow us to differentiate the significant seismic energy release using the resultant moment tensor functions. Therefore this first source was determined to have focal depth for this time window of 20 km. Another interesting feature is that the moment tensor functions for a 20-km focal depth apparently show significant seismic energy release until 20 to 25 s, although there is no well-developed temporal consistency, as indicated by two offset arrows (Figure 27b). To derive a focal mechanism from the *resultant moment tensor functions* with a Green's function of 20-km focal depth, we calculated the area under each moment tensor element for this time window, and then assigned these values to M11 through M23. Using these values, we calculated a moment tensor matrix and determined the best-fit double-couple. This yields the focal mechanism in Figure 28a labeled subevent one. One of the nodal planes with NE of strike and SE dip from this result is consistent with the surface faulting of the White Wolf fault observed for this earthquake.

Performing the same kind of focal mechanism calculation for the next time window (8 to 15 seconds) of the resultant moment tensor functions with a Green's function of 20-km focal depth (although not well developed in terms of temporal consistency) yields a best-fit double-couple with nearly the same strike and dip as subevent one, but a rake which differs by 180°. This fact, along with a much higher CLVD component for this time window, suggests that the seismic energy release after the first energy release is mapped out through incorrect Green's functions

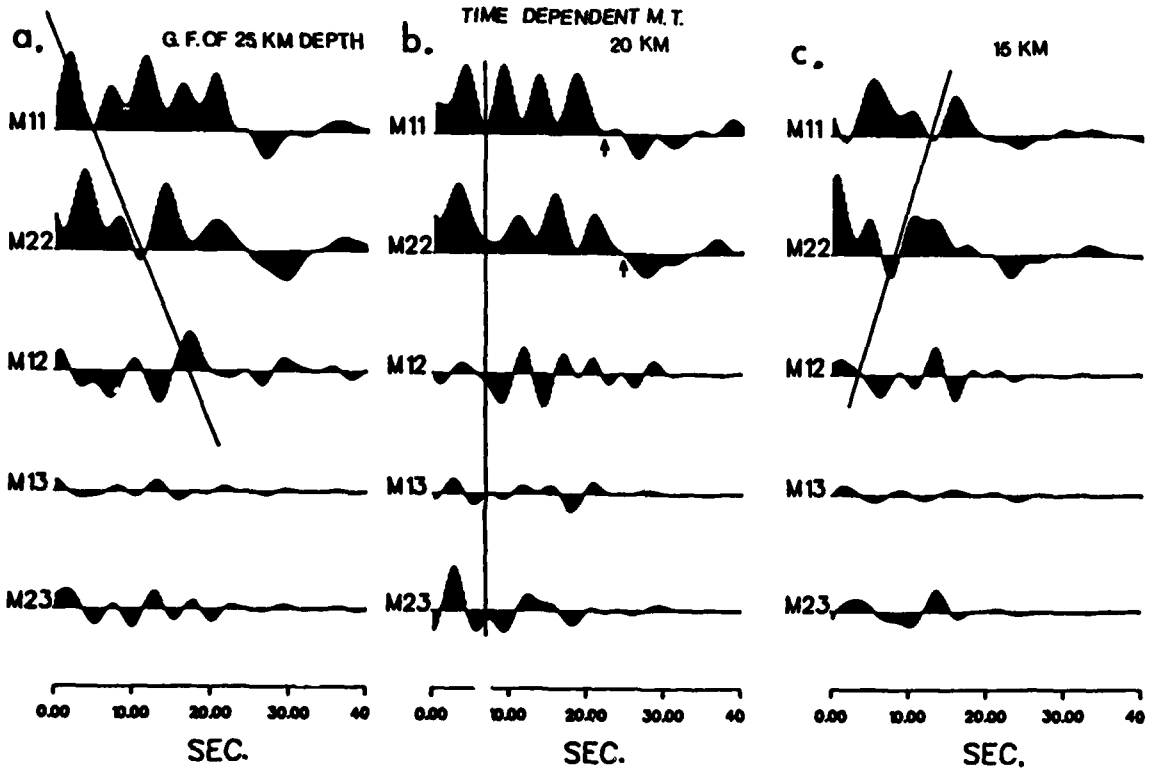

Figure 27. Resultant time dependent moment tensor elements or moment tensor functions from the waveform inversion of the 1952 Kern County Earthquake with Green's functions of 25 km, 20km, and 15 km focal depths. Considering the temporal consistency, resultant moment tensor functions for three different focal depths show clockwise rotation of temporal lines for 25 km, 20 km, and 15 km focal depths. Time dependent moment tensor elements for 20 km focal depth show most well developed temporal consistency and those for 15 km focal depth show worst.

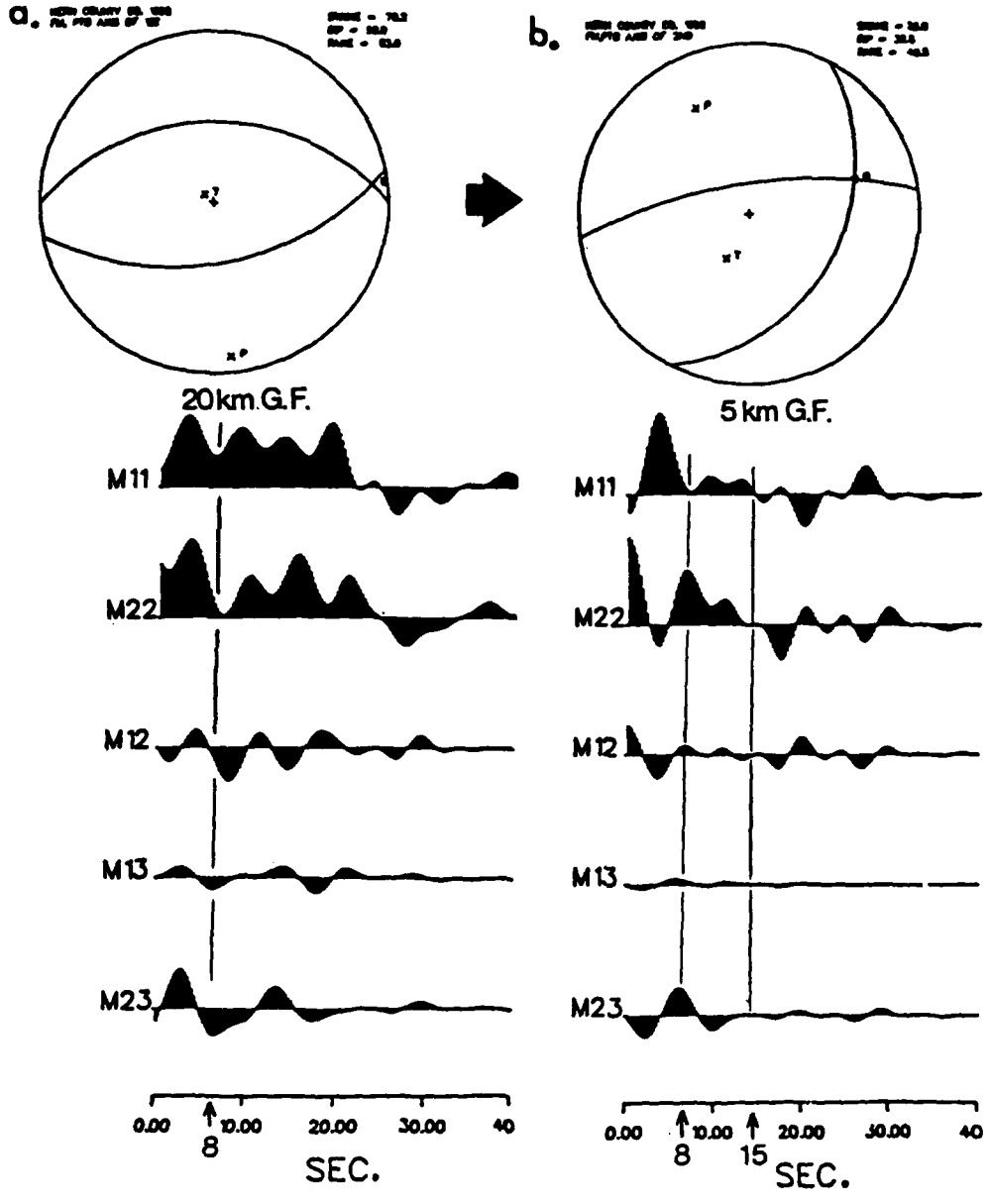

Figure 28. Two focal mechanisms and corresponding moment tensor functions for two subevents from the waveform inversion of the 1952 Kern County Earthquake. The focal depths are resolved as 20 km and 5 km for the first and second subevent, respectively.

(inappropriate depth). This suggestion is consistent with inversion with a constant moment tensor assumption in which the time function changes from positive to negative if a Green's function of the wrong depth is used. We must, therefore, examine the time dependent moment function results using Green's functions with other focal depths to determine which moment tensor functions show good temporal consistency and satisfy the other constraints after the first time window.

The time dependent moment tensor which shows the best temporal consistency around the next stage of significant seismic energy release for all the moment tensor elements is obtained for Green's functions for a 5-km focal depth, as shown in Figure 28b. Note that there is neither development of temporal consistency nor causality of the source time function at the start of the source time function (time equals zero) for the moment tensor functions. This is because the inversion assumes that the first significant seismic energy release originates from a 5-km focal depth, which of course it does not. After the time window (8-15 seconds) which has the largest temporal consistency, the moment tensor elements are random and the amplitudes becomes much smaller. Trying to resolve any other subevents further back in the record yields a double-couple mechanism with small moments and large CLVD components. This observation, along with the fact that there are no more temporal consistencies for moment tensor functions with other Green's functions of different source depths, suggests that all the significant subevents associated with the Kern County event seem to be resolved by searching for time windows of significant seismic energy release. Therefore, the focal depth of the second significant seismic energy release is 5 km. The double-couple calculation for this time window yields the focal mechanism labeled subevent 2 in Figure 28b. The nodal plane with roughly a NE direction and SE dip seems to be the actual fault plane, considering the geological surface rupture trend of the NE part of the White Wolf fault. Therefore, the interpretation of the time

dependent moment tensor inversion mapped the Kern County earthquake as a double point source which propagates upward from 20 km to 5 km, as shown in Figure 29. The strike angle of the second subevent's actual fault plane is rotated counterclockwise. The second rupture plane also requires a change of fault plane dip (shallower), and a change in rake from primarily thrust to relatively more strike-slip motion at the NE part, or shallower depth, of the White Wolf fault.

In order to investigate more source complexity or abrupt fault geometry change within these time windows of the two subevents, moment tensor functions are traced using the 3-s time window from 0 to 15 s. Figure 30 shows that there is counterclockwise rotation of strike angle and P, T, and B axes. The P, T, and B axes change smoothly for 15 s of seismic energy release. This suggests a smoothly changing focal mechanism; the corresponding P, T, and B axes suggest no more abrupt changes in fault geometry until 15 s. Even though focal mechanisms or the derived P, T, and B axes resulting from tracing the moment tensor function *with* a 3-s time window do not exactly match those of the two-subevent assumption, this technique allows us to investigate greater source complexity even within the given subevent or the stability of the given focal mechanism solutions.

Since maximum and minimum principal axes derived from earthquake focal mechanisms are some of the most commonly used indicators of tectonic processes, we inverted for the corresponding P, T, and B axes from the focal mechanisms of the 1952 Kern County earthquake as shown in Figure 30. The mainly thrust motion (about 85° of rake angle) of the first subevent with an epicenter near the SW corner of the White Wolf fault requires a vertical minimum principal axis (T) and a N-S direction of the maximum principal axis (P), as opposed to the regional stress field around the San Andreas fault (N-S direction of P axis and E-W or WNW-ESE direction of T). This apparent rotation or exchange of two principal stresses (T and B axis while P remains

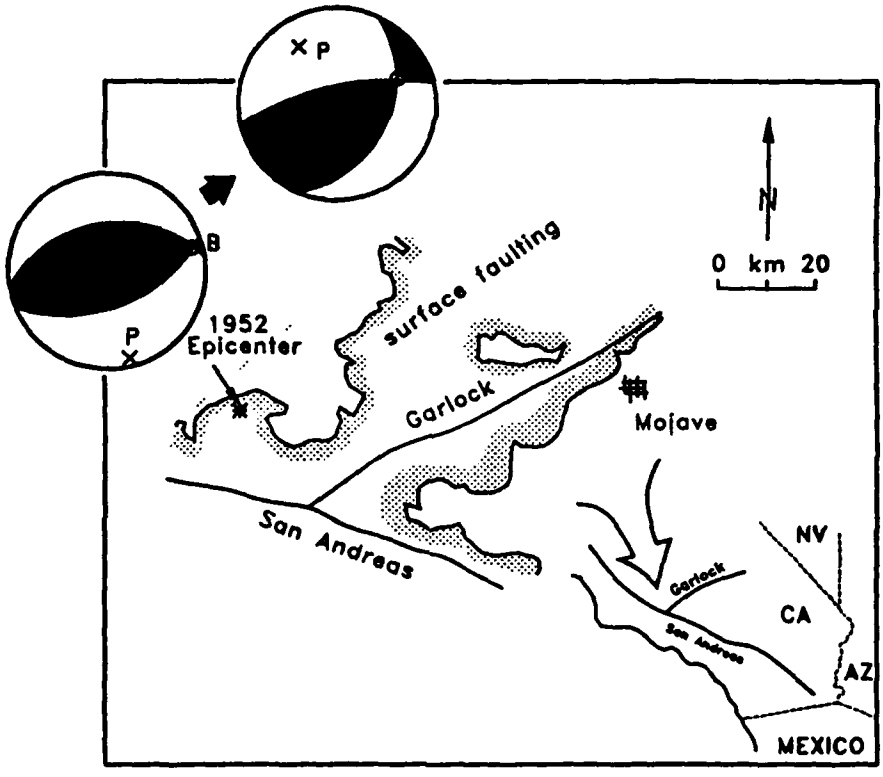

Figure 29. Two focal mechanisms with the epicenter location of the 1952 Kern County Earthquake. Two focal mechanisms show dominantly thrust motion and also show that strike angle is rotated counterclockwise, dip angle becomes shallower. There is more strike slip component at NE portion of the White Wolf fault.

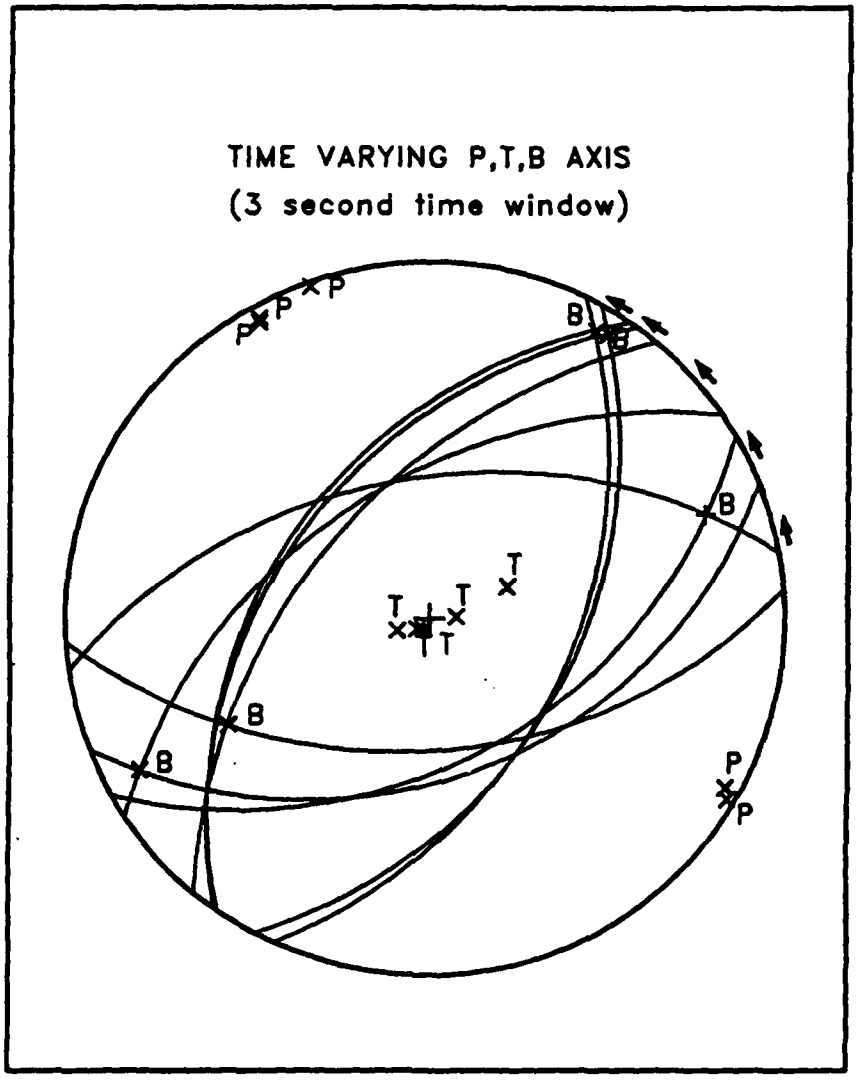

Figure 30. The evolving P, T, and B axes with 3 seconds time windows from zero to 15 seconds of seismic energy release. There are counterclockwise rotation in strike with time. All the P, T, and B axes from the waveform inversion are pretty well stabilized for this time interval.

constant) is much more consistent with the regional stress field as suggested by Zoback and Zoback (1980). This may be explained if in the area of the White Wolf fault the minimum principal horizontal stress and the vertical stress were approximately equal. Since these local stress domains (rotated T and B axes but consistent P axis) differ from the regional stress system, this indicates that different tectonic mechanisms, such as seismic thrust motion and aseismic uplift, operate around the Big Bend area.

In addition to those complex tectonic movement, the geometry of the Big Bend area, which is characterized by counterclockwise rotation from the NW-SE trend of the San Andreas fault such that the fault line is more E-W, implies the heterogeneity of the stress field of the region. Moreover, a probable weak, pre-existing E-W trending zone such as the White Wolf fault increases the possibility of E-W trending thrust motion rather than E-W trending strike-slip motion on the White Wolf fault, which makes change of slip direction and fault geometry on the multiple complex shear dislocation surfaces.

Comparing the P, T, and B axes between the first and the second subevents at that location, there is a greater strike-slip component at shallow depth (5 km) than for the first subevent (focal depth of 20 km), without much change of the nearly N-S direction of the P axis. This requires a relatively more horizontal and E-W direction of the T axis at a shallow depth, which is apparently more consistent with the regional tectonic stress field around the San Andreas fault. Even though it is a possible explanation for change of the direction of the P, T, and B axes, (the role of the local tectonic stress field is attenuated and aligned with the regional stress field of the San Andreas fault), P, T, and B directions of the second subevent could be also explained by sliding on the weak, pre-existing fault plane or "coincidence" to the regional stress field.

Both evidences of this study of 1952, Kern County earthquake, that is, anomalous thrust motion (vertical minimum principal axis) near the Big Bend area at depth and relatively more strike-slip motion (a relatively more horizontal and E-W direction of the minimum principal axis) far from the Big Bend area implies the local concentration of thrust motion and locally complicate the stress pattern near the Big Bend area. The initial focal depth of 20 km, which is about twice the usual depth of seismicity around the San Andreas fault system, could provide strong evidence that the thrust motion is the result of a local stress system dominant near the Big Bend. This local limitation of the thrust motion, or the local stress domain, implies that the tectonic boundary between thrust motion and typical strike-slip motion exists there, and that this boundary is not far from the Big Bend. This local stress domain could significantly constrain the boundary of aseismic tectonic uplift of the Southern California Transverse Ranges and the next seismic break.

In studying the resultant moment tensor functions, we found substantially and consistently high CLVD values or non-double-couple components both for five time windows of 2-s duration from 0 to 15 s and for those of the two-subevent assumption, as shown in Figure 31. Among the possible explanations for the high CLVD, as discussed in the previous section, inherent source characteristics such as tensile failure under high fluid pressure caused by magma injection, as suggested by Sipkin (1986), could be one possible explanation for all the time windows. However, for our study inadequate seismic waveform data could be the most probable explanation, since we are using seismic waveforms recorded on a variety of seismic instruments. Moreover, no one has suggested that the seismic origin of the Kern County earthquake was magma-related, which was proposed by Sipkin (1986) for a series of earthquakes at the Long Valley Caldera region and which is still arguable.

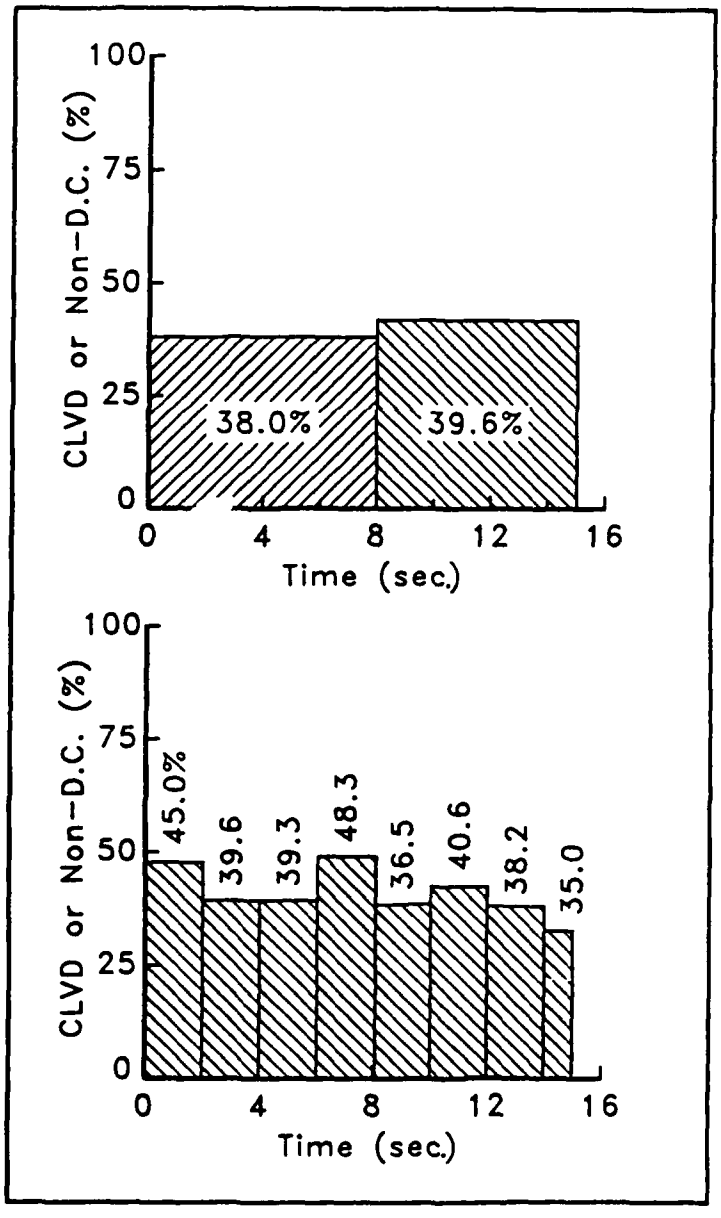

Figure 31. Histogram of percent CLVD for the 1952 Kern County Earthquake for different time windows of two subevents and of 2 seconds time windows. Histogram shows considerably high CLVD component for time windows of two subevents and two seconds.

There are several more reasons to have a sizable CLVD component. For example, intrinsic seismic source complexity or two overlapped asperities, which may not be represented by a simple double-couple point source or sources, are basic assumptions in the moment tensor inversion of teleseismic body waves. At first, Ishida and Kanamori (1980) suggested that the White Wolf fault has enough asperities to explain the seismicity and spectrum of small pre- and post-earthquakes of the Kern County earthquake. A synthetic example of the time dependent moment tensor inversion for a double event with overlap and simultaneous fault geometry change between two subevents also showed substantially high CLVD and, unexpectedly, an averaged single focal mechanism for the one-point-source assumption, even though two subevents have purely double-couple-dominated focal mechanisms. The experience with the same synthetic example also demonstrated that the two-point-source assumption using the same resultant moment tensor functions still gives a high CLVD component for both the first and the second point sources. The results of the same synthetic match the substantially and consistently high CLVD component observed for all the time windows of the Kern County earthquake. Moreover, in regard to the physics of actual fault planes, the relationship of two point sources resolved from the moment tensor inversion with a point-source assumption (upward propagation from 20 km, which is unusually deep compared with the depths of the rest of the seismicity to a 5-km focal depth) may possibly be represented by a greater overlap of fault planes or by many small, distributed fault planes for a significant geometrical interval with constant fault plane geometries rather than by two independently separated fault planes with abrupt changes in geometries at some boundary point. Finally, possible model evidence for overlapped asperities for the Kern County earthquake comes from the less-developed temporal consistency at the beginning of the second subevent' seismic energy release (Figure 28) derived from moment tensor functions with a Green's function for 5-km

focal depth. This is in contrast with a relatively clearer temporal consistency at the final stage of seismic energy release with the Green's function of the same focal depth. Considering just the point-source assumption for the moment tensor inversion of the teleseismic body waveforms, which is valid for the wavelength for seismic waveform data and distances greater than the dimension of faulting, the moment tensor inversion could map this kind of source complexity, such as overlapped asperities, with a different fault plane geometry into two apparent double-couple point sources with substantially and consistently high CLVD components. The boundary between the first and second subevent would be somewhere between overlapped asperities.

If we assume that the fault model with overlapped asperities and a simultaneously changing fault geometry more closely represents the White Wolf fault, it is possible that geodetic data modeling, which applies a static response to a seismic event rather than a dynamic response as done by Stein and Thatcher (1981) in their waveform modeling for the Kern County earthquake, may map overlapping asperities in combination with varying fault geometry as one independent fault plane which has intermediate dip and rake angle that lies within Stein and Thatcher's (1981) three evolving fault planes. Moreover, the P, T, and B axes of three evolving fault planes on the White Wolf fault plane as suggested by Stein and Thatcher (1981) do not differ significantly from those of our two-point double-couple source solution and Dunbar et al.'s interpretation (1980). Therefore, instead of attributing the high CLVD contribution simply to inadequate data and then stating that any double-couple source parameters obtained from these inversions must be unreliable, it is reasonable to consider a substantially and consistently high CLVD as an alternative explanation. For the 1952 Kern County earthquake, the substantially and consistently high CLVD component of the moment tensor can be attributed to source complexity rather than merely to inadequate data.

*U.S. GOVERNMENT PRINTING OFFICE 1990-760-009/00041

REFERENCES

Allen, C.R., G.R. Engen, T.C. Hanks, J.M. Nordquist, and W.R. Thatcher, 1971. Main shock and larger aftershocks of the San Fernando earthquake, February 9 through March 1, 1971, U.S. Geol. Sur. Prof. Pap., 733, 17-20.

Ambraseys, N.N. and C.P. Melville, 1983. Seismicity of Yemen, Nature, 303, 321-322.

Backus, G. and M.Mulcahy, 1976. Moment tensors and other phenomenological description of seismic sources- I. Continuous displacements, Geophys. J., 46,341-361.

Backus, G. and M.Mulcahy, 1976. Moment tensors and other phenomenological description of seismic sources- II. Discontinuous displacements, Geophys. J., 47, 301-329.

Baker, J.S. and C.A. Langston, 1981. Inversion of teleseismic body waves for the moment tensor of the 1978 Thessaloniki, Greece, earthquake, Bull. Seismol. Soc. Am., 71, 1423-1444.

Baker, J.S. and C.A. Langston, 1982. Moment tensor inversion of complex earthquakes, Geophys. J. R. astr. Soc., 68, 777-803.

Baker, J.S., 1984. A seismological analysis of the May 1980 Mammoth Lakes, California, Earthquakes, Ph.D. dissertation.

Benioff, H., 1955. Mechanism and strain chatracteristics of the White Wolf fault as indicated by aftershock sequence, Earthquakes in Kern County, California, during 1952, Division of Mines, State of California.

Buland, R. and F. Gilbert, 1976. Matched filtering for the seismic moment tensor, Geophys. Res. Papers 3,205-206.

Burdick, L.J., T.C. Wallace, and T. Lay,1984. Modeling near-field and teleseismic observations from the Amchitka test site, 89, 4373-4388.

Buwalda, J.P. and P. St. Amand, Geological effects of the Arvin-Tehachapi earthquake, Calif. Div. Mines Geol. Bull., 170(2), 131-142, 1954.

Cagniard, L., 1962. Reflection and refraction of progressive seismic waves, translated by E.A. Flinn and C.H. Dix, McGraw-Hill, New York.

Castle, R.O., Leveling surveys and the southern California uplift, Earthquake Inform. Bull., 10, 88-92, 1978.

Chapman, C.H., 1978. A new method for computing synthetic seismograms, Geophys. J. R. astr. Soc., 54,481-518.

Choy, G.L. and R. Kind, 1987. Rupture complexity of a moderate-sized (m_b 6.0) earthquake: broadband body-wave analysis of the north Yemen earthquake of 13 December 1982, Bull. Seismol. Soc. Am., 77, 28-46.

Crowell, J.C., 1954. Geology of the Ridge Basin area, Los Angeles and Ventura Counties, Calif. Div. of Mines Bull., 170, Map Sheet No 7.

deHoop, A.T., 1960. A modification of Cagniard's method for solving seismic pulse problems, Appl. Sci. Res., B8, 349-356.

Dunbar, W.S., D.M. Boore, and W. Thatcher, Pre-, Co-, and post-seismic strain changes associated with the 1952 M_L=7.2 Kern County, California, earthquake, Bull. Seismol. Soc. Am., 70, 1893-1905, 1980.

Geller, R.J., 1976. Body force equivalents for stress-drop seismic sources, Bull. Seismol. Soc. Am., 66, 1801-1804.

Gilbert, F., 1970. Excitation of the normal modes of the earth by a point source, Geophys. J., 22, 223-226.

Gilbert, F. and A.M. Dziewonski, 1975. An application of normal mode theory to the retrieval of structural parameters and source mechanisms from seismic spectra, Phil. Trans. Roy. Soc. London, Ser. A., 278, 187-269.

Hadley, D. and H. Kanamori, 1978. Recent seismicity in the San Fernando region and tectonics in the west-central Transverse Ranges, California, Bull. Seismol. Soc. Am., o8, 1449-1457.

Hanks, T.C., 1974. The faulting mechanism of the San Fernando earhtquake, J. Geophys. Res., 79, 1215-1229.

Heaton, T.H. and D.H. Helmberger, 1979. Generalized ray models if the San Fernando earthquake, Bull. Seismol. Soc. Am., 69, 1311-1341.

Heaton, T.H., 1982. The 1971 San Fernando earthquake: a double event?, Bull. Seismol. Soc. Am., 72, 2037-2062.

Helmberger, D.M., 1968. The crust-mantle transition the Bering sea, Bull. Seismol. Soc. Am., 58, 179-214.

Helmberger, D.M., 1974. Generalized ray theory for shear dislocations, Bull. Seismol. Soc. Am., 64, 45-64.

Helmberger, D.V. and S.D. Malone, 1975. Modeling local earthquake as shear dislocation in a layered half space, J. Geophys. Res., 35, 4881-4888.

Ishida, M., and H. Kanamori, Temporal variation in seismicity and spectrum of small earthquakes preceding the 1952 Kern County, California, earthquake, Bull. Seismol. Soc. Am., 70, 509-527, 1980.

Kanamori, H. and D.L. Anderson, 1975. Theoretical basis of some empirical relations in seismology, Bull. Seismol. Soc. Am., 65, 1073-1095.

Kanamori, H. and P.C. Jennings, 1978. Determination of local magnitude, ML, from strong motion accelerograms, Bull. Seismol. Soc. Am., 68, 471-485.

Kanamori, H. and C.R. Allen, 1986. Earthquake repeat time and average stress drop, Geophysical Monograph 37, AGU, 227-235.

Kim, J. and T.C. Wallace, 1986. A comparison of moment tensor inversion technique; time dependent and time independent elements, Eos Trans. AGU, 67, 1104.

Kim, J. and T.C. Wallace, 1988. Time dependent moment tensor inversion of the 1952 Kern County earthquake, Eos Trans. AGU, 69.

Lanczos, C., 1961. Linear differential operators, Van Nostrand, London, 564 pp.

Langston, C.A. and D.M. Helmberger, 1975. A procedure for modeling shallow dislocation sources, Geophys. J. R. astr. Soc., 42, 117-130.

Langston, C.A., 1978. The February 9, 1971 San Fernando earthquake: a study of source finiteness in teleseismic body waves, Bull. Seismol. Soc. Am., 68, 1-29.

Langston, C.A., 1981. Source inversion of seismic waveforms: the Koyna, India, earthquakes of 13 September 1967, Bull. Seismol. Soc. Am., 71, 1-24.

Langer, C.J., G.A. Bollinger, and H.M. Merghelani, 1987. Aftershocks of the 13 December 1982 North Yemen earthquake: conjugate normal faulting in an extensional setting, Bull. Seismol. Soc. Am., 77, 2038-2055.

Lay, T., T.C. Wallace, and D.M. Helmberger, 1984. The effects of tectonic release on short period P waves from NTS explosions, Bull. Seismol. Soc. Am., 74, 819-842.

McCann, M.W. and D.M. Boore, 1983. Variability in ground motions: root mean square acceleration and peak acceleration for the 1971 San Fernando, California, earthquake, Bull. Seismol. Soc. Am., 73, 615-632.

Mendiguren, J., 1976. Inversion of surface wave data in source mechanism studies, J. Geophys. Res., 82, 889-894.

Plafker, G., R. Agar, A.H. Asker, and M. Hanif, 1987. Surface effects and tectonic setting of the 13 December 1982 North Yemen, Bull. Seismol. Soc. Am., 77, 2038-2055.

Sipkin, S.A., 1982. Estimation of earthquake source parameters by the inversion of waveform data: synthetic waveforms, Phys. Earth planet. Int., 30, 242-259.

Sipkin, S.A., 1986. Interpretation of non-double-couple earthquake mechanisms derived from moment inversion, J. Geophys. Res., 91, 531-547.

Stein, R.S., and W. Thatcher, 1981. Seismic and aseismic deformation associated with the 1952 Kern County, California, earthquake and relation to the Quaternary history of the White Wolf fault, J. Geophys. Res., 86, 4913-4928.

Strelitz, R.A., 1978. Moment tensor inversion s and source models, Geophys. J., 52, 359-364.

Stump, B.W. and L.R.Johnson, 1977. The determination of source properties by the linear inversion of seismograms, Bull. Seismol. Soc. Am., 67, 1489-1502.

Stump, B.W., L.R.Johnson, 1984. Near-field source characterization of contained nuclear explosion in tuff, Bull. Seismol. Soc. Am., 74, 1-26.

Vidale, J.E.and D.V. Helmberger, 1988. Elastic Finite-difference modeling of the 1971 San Fernando, California earthquake, Bull. Seismol. Soc. Am., 78, 122-141.

Wallace, T.C., D.M. Helmberger, and G.R. Engen, 1983. Evidence of tectonic release from underground nuclear explosion in long-period P waves, Bull. Seismol. Soc. Am., 73, 593-613.

Wallace, T.C., D.M. Helmberger and G.R. Engen, 1985. Evidence of tectonic release from underground nuclear explosion in long-period S waves, Bull. Seismol. Soc. Am., 75, 157-174.

Wallace, T.C., 1985. Reexamination of the moment tensor solutions of the 1980 Mammoth Lakes earthquake, J. Geophys. Res., 90, 11171-11176.

Wiggins, R.A., 1972. The general linear inverse problem: Implication of surface waves and free oscillations for earth structure, Reviews of Geophysics and Space physics, 10, 251-285.

Yao, Z.X. and D.G. Harkrider, 1983. A generalized reflection-transmission coefficient matrix and discrete wavenumber method for synthetic seismograms, Bull. Seismol. Soc. Am., 73, 1685-1699.

Zoback, M.L., and M. Zoback, 1980. State of stress in the conterminous United States, J. Geophys. Res., 85, 6113-6156.

CONTRACTORS (United States)

Prof. Thomas Ahrens
Seismological Lab, 252-21
Division of Geological & Planetary Sciences
California Institute of Technology
Pasadena, CA 91125

Prof. Charles B. Archambeau
CIRES
University of Colorado
Boulder, CO 80309

Prof. Muawia Barazangi
Institute for the Study of the Continent
Cornell University
Ithaca, NY 14853

Dr. Douglas R. Baumgardt
ENSCO, Inc
5400 Port Royal Road
Springfield, VA 22151-2388

Prof. Jonathan Berger
IGPP, A-025
Scripps Institution of Oceanography
University of California, San Diego
La Jolla, CA 92093

Dr. Lawrence J. Burdick
Woodward-Clyde Consultants
566 El Dorado Street
Pasadena, CA 91109-3245

Dr. Karl Coyner
New England Research, Inc.
76 Olcott Drive
White River Junction, VT 05001

Prof. Vernon F. Cormier
Department of Geology & Geophysics
U-45, Room 207
The University of Connecticut
Storrs, CT 06268

Prof. Steven Day
Department of Geological Sciences
San Diego State University
San Diego, CA 92182

Dr. Zoltan A. Der
ENSCO, Inc.
5400 Port Royal Road
Springfield, VA 22151-2388

Prof. John Ferguson
Center for Lithospheric Studies
The University of Texas at Dallas
P.O. Box 830688
Richardson, TX 75083-0688

Prof. Stanley Flatte
Applied Sciences Building
University of California
Santa Cruz, CA 95064

Dr. Alexander Florence
SRI International
333 Ravenswood Avenue
Menlo Park, CA 94025-3493

Prof. Henry L. Gray
Vice Provost and Dean
Department of Statistical Sciences
Southern Methodist University
Dallas, TX 75275

Dr. Indra Gupta
Teledyne Geotech
314 Montgomery Street
Alexandria, VA 22314

Prof. David G. Harkrider
Seismological Laboratory
Division of Geological & Planetary Sciences
California Institute of Technology
Pasadena, CA 91125

Prof. Donald V. Helmberger
Seismological Laboratory
Division of Geological & Planetary Sciences
California Institute of Technology
Pasadena, CA 91125

Prof. Eugene Herrin
Institute for the Study of Earth and Man
GeophysicalLaboratory
Southern Methodist University
Dallas, TX 75275

Prof . Robert B. Herrmann
Department of Earth & Atmospheric Sciences
St. Louis University
St. Louis, MO 63156

Prof. Bryan Isacks
Cornell University
Department of Geological Sciences
SNEE Hall
Ithaca, NY 14850

Dr. Rong-Song Jih
Teledyne Geotech
314 Montgomery Street
Alexandria, VA 22314

Prof. Lane R. Johnson
Seismographic Station
University of California
Berkeley, CA 94720

Prof. Alan Kafka
Department of Geology & Geophysics
Boston College
Chestnut Hill, MA 02167

Prof. Fred K. Lamb
University of Illinois at Urbana-Champaign
Department of Physics
1110 West Green Street
Urbana, IL 61801

Prof. Charles A. Langston
Geosciences Department
403 Deike Building
The Pennsylvania State University
University Park, PA 16802

Prof. Thorne Lay
Department of Geological Sciences
1006 C.C. Little Building
University of Michigan
Ann Arbor, MI 48109-1063

Prof. Arthur Lerner-Lam
Lamont-Doherty Geological Observatory
of Columbia University
Palisades, NY 10964

Dr. Christopher Lynnes
Teledyne Geotech
314 Montgomery Street
Alexandria, VA 22314

Prof. Peter Malin
University of California at Santa Barbara
Institute for Crustal Studies
Santa Barbara, CA 93106

Dr. Randolph Martin, III
New England Research, Inc.
76 Olcott Drive
White River Junction, VT 05001

Dr. Gary McCartor
Mission Research Corporation
735 State Street
P.O. Drawer 719
Santa Barbara, CA 93102 (2 copies)

Prof. Thomas V. McEvilly
Seismographic Station
University of California
Berkeley, CA 94720

Dr. Keith L. McLaughlin
S-CUBED
A Division of Maxwell Laboratory
P.O. Box 1620
La Jolla, CA 92038-1620

Prof. William Menke
Lamont-Doherty Geological Observatory
of Columbia University
Palisades, NY 10964

Stephen Miller
SRI International
333 Ravenswood Avenue
Box AF 116
Menlo Park, CA 94025-3493

Prof. Bernard Minster
IGPP, A-025
Scripps Institute of Oceanography
University of California, San Diego
La Jolla, CA 92093

Prof. Brian J. Mitchell
Department of Earth & Atmospheric Sciences
St. Louis University
St. Louis, MO 63156

Mr. Jack Murphy
S-CUBED, A Division of Maxwell Laboratory
11800 Sunrise Valley Drive
Suite 1212
Reston, VA 22091 (2 copies)

Dr. Bao Nguyen
GL/LWH
Hanscom AFB, MA 01731-5000

Prof. John A. Orcutt
IGPP, A-025
Scripps Institute of Oceanography
University of California, San Diego
La Jolla, CA 92093

Prof. Keith Priestley
University of Nevada
Mackay School of Mines
Reno, NV 89557

Prof. Paul G. Richards
Lamont-Doherty Geological Observatory
of Columbia University
Palisades, NY 10964

Dr. Wilmer Rivers
Teledyne Geotech
314 Montgomery Street
Alexandria, VA 22314

Dr. Alan S. Ryall, Jr.
Center for Seismic Studies
1300 North 17th Street
Suite 1450
Arlington, VA 22209-2308

Prof. Charles G. Sammis
Center for Earth Sciences
University of Southern California
University Park
Los Angeles, CA 90089-0741

Prof. Christopher H. Scholz
Lamont-Doherty Geological Observatory
of Columbia University
Palisades, NY 10964

Prof. David G. Simpson
Lamont-Doherty Geological Observatory
of Columbia University
Palisades, NY 10964

Dr. Jeffrey Stevens
S-CUBED
A Division of Maxwell Laboratory
P.O. Box 1620
La Jolla, CA 92038-1620

Prof. Brian Stump
Institute for the Study of Earth & Man
Geophysical Laboratory
Southern Methodist University
Dallas, TX 75275

Prof. Jeremiah Sullivan
University of Illinois at Urbana-Champaign
Department of Physics
1110 West Green Street
Urbana, IL 61801

Prof. Clifford Thurber
University of Wisconsin-Madison
Department of Geology & Geophysics
1215 West Dayton Street
Madison, WS 53706

Prof. M. Nafi Toksoz
Earth Resources Lab
Massachusetts Institute of Technology
42 Carleton Street
Cambridge, MA 02142

Prof. John E. Vidale
University of California at Santa Cruz
Seismological Laboratory
Santa Cruz, CA 95064

Prof. Terry C. Wallace
Department of Geosciences
Building #77
University of Arizona
Tucson, AZ 85721

Dr. Raymond Willeman
GL/LWH
Hanscom AFB, MA 01731-5000

Dr. Lorraine Wolf
GL/LWH
Hanscom AFB, MA 01731-5000

Prof. Francis T. Wu
Department of Geological Sciences
State University of New York
at Binghamton
Vestal, NY 13901

Dr. Monem Abdel-Gawad
Rockwell International Science Center
1049 Camino Dos Rios
Thousand Oaks, CA 91360

Prof. Keiiti Aki
Center for Earth Sciences
University of Southern California
University Park
Los Angeles, CA 90089-0741

Prof. Shelton S. Alexander
Geosciences Department
403 Deike Building
The Pennsylvania State University
University Park, PA 16802

Dr. Ralph Archuleta
Department of Geological Sciences
University of California at Santa Barbara
Santa Barbara, CA 93102

Dr. Thomas C. Bache, Jr.
Science Applications Int'l Corp.
10210 Campus Point Drive
San Diego, CA 92121 (2 copies)

J. Barker
Department of Geological Sciences
State University of New York
at Binghamton
Vestal, NY 13901

Dr. T.J. Bennett
S-CUBED
A Division of Maxwell Laboratory
11800 Sunrise Valley Drive, Suite 1212
Reston, VA 22091

Mr. William J. Best
907 Westwood Drive
Vienna, VA 22180

Dr. N. Biswas
Geophysical Institute
University of Alaska
Fairbanks, AK 99701

Dr. G.A. Bollinger
Department of Geological Sciences
Virginia Polytechnical Institute
21044 Derring Hall
Blacksburg, VA 24061

Dr. Stephen Bratt
Science Applications Int'l Corp.
10210 Campus Point Drive
San Diego, CA 92121

Michael Browne
Teledyne Geotech
3401 Shiloh Road
Garland, TX 75041

Mr. Roy Burger
1221 Serry Road
Schenectady, NY 12309

Dr. Robert Burridge
Schlumberger-Doll Research Center
Old Quarry Road
Ridgefield, CT 06877

Dr. Jerry Carter
Rondout Associates
P.O. Box 224
Stone Ridge, NY 12484

Dr. W. Winston Chan
Teledyne Geotech
314 Montgomery Street
Alexandria, VA 22314-1581

Dr. Theodore Cherry
Science Horizons, Inc.
710 Encinitas Blvd., Suite 200
Encinitas, CA 92024 (2 copies)

Prof. Jon F. Claerbout
Department of Geophysics
Stanford University
Stanford, CA 94305

Prof. Robert W. Clayton
Seismological Laboratory
Division of Geological & Planetary Sciences
California Institute of Technology
Pasadena, CA 91125

Prof. F. A. Dahlen
Geological and Geophysical Sciences
Princeton University
Princeton, NJ 08544-0636

Prof. Anton W. Dainty
Earth Resources Lab
Massachusetts Institute of Technology
42 Carleton Street
Cambridge, MA 02142

Prof. Adam Dziewonski
Hoffman Laboratory
Harvard University
20 Oxford St
Cambridge, MA 02138

Prof. John Ebel
Department of Geology & Geophysics
Boston College
Chestnut Hill, MA 02167

Eric Fielding
SNEE Hall
INSTOC
Cornell University
Ithaca, NY 14853

Prof. Donald Forsyth
Department of Geological Sciences
Brown University
Providence, RI 02912

Dr. Anthony Gangi
Texas A&M University
Department of Geophysics
College Station, TX 77843

Dr. Freeman Gilbert
Inst. of Geophysics & Planetary Physics
University of California, San Diego
P.O. Box 109
La Jolla, CA 92037

Mr. Edward Giller
Pacific Sierra Research Corp.
1401 Wilson Boulevard
Arlington, VA 22209

Dr. Jeffrey W. Given
Sierra Geophysics
11255 Kirkland Way
Kirkland, WA 98033

Prof. Steven Grand
University of Texas at Austin
Department of Geological Sciences
Austin, TX 78713-7909

Prof. Roy Greenfield
Geosciences Department
403 Deike Building
The Pennsylvania State University
University Park, PA 16802

Dan N. Hagedorn
Battelle
Pacific Northwest Laboratories
Battelle Boulevard
Richland, WA 99352

Kevin Hutchenson
Department of Earth Sciences
St. Louis University
3507 Laclede
St. Louis, MO 63103

Prof. Thomas H. Jordan
Department of Earth, Atmospheric
and Planetary Sciences
Massachusetts Institute of Technology
Cambridge, MA 02139

Robert C. Kemerait
ENSCO, Inc.
445 Pineda Court
Melbourne, FL 32940

William Kikendall
Teledyne Geotech
3401 Shiloh Road
Garland, TX 75041

Prof. Leon Knopoff
University of California
Institute of Geophysics & Planetary Physics
Los Angeles, CA 90024

Prof. L. Timothy Long
School of Geophysical Sciences
Georgia Institute of Technology
Atlanta, GA 30332

Dr. George Mellman
Sierra Geophysics
11255 Kirkland Way
Kirkland, WA 98033

Prof. John Nabelek
College of Oceanography
Oregon State University
Corvallis, OR 97331

Prof. Geza Nagy
University of California, San Diego
Department of Ames, M.S. B-010
La Jolla, CA 92093

Prof. Amos Nur
Department of Geophysics
Stanford University
Stanford, CA 94305

Prof. Jack Oliver
Department of Geology
Cornell University
Ithaca, NY 14850

Prof. Robert Phinney
Geological & Geophysical Sciences
Princeton University
Princeton, NJ 08544-0636

Dr. Paul Pomeroy
Rondout Associates
P.O. Box 224
Stone Ridge, NY 12484

Dr. Jay Pulli
RADIX System, Inc.
2 Taft Court, Suite 203
Rockville, MD 20850

Dr. Norton Rimer
S-CUBED
A Division of Maxwell Laboratory
P.O. Box 1620
La Jolla, CA 92038-1620

Prof. Larry J. Ruff
Department of Geological Sciences
1006 C.C. Little Building
University of Michigan
Ann Arbor, MI 48109-1063

Dr. Richard Sailor
TASC Inc.
55 Walkers Brook Drive
Reading, MA 01867

Thomas J. Sereno, Jr.
Science Application Int'l Corp.
10210 Campus Point Drive
San Diego, CA 92121

John Sherwin
Teledyne Geotech
3401 Shiloh Road
Garland, TX 75041

Prof. Robert Smith
Department of Geophysics
University of Utah
1400 East 2nd South
Salt Lake City, UT 84112

Prof. S. W. Smith
Geophysics Program
University of Washington
Seattle, WA 98195

Dr. Stewart Smith
IRIS Inc.
1616 North Fort Myer Drive
Suite 1440
Arlington, VA 22209

Dr. George Sutton
Rondout Associates
P.O. Box 224
Stone Ridge, NY 12484

Prof. L. Sykes
Lamont-Doherty Geological Observatory
of Columbia University
Palisades, NY 1096[illegible]

Prof. Pradeep Talwani
Department of Geological Sciences
University of South Carolina
Columbia, SC 29208

Prof. Ta-liang Teng
Center for Earth Sciences
University of Southern California
University Park
Los Angeles, CA 90089-0741

Dr. R.B. Tittmann
Rockwell International Science Center
1049 Camino Dos Rios
P.O. Box 1085
Thousand Oaks, CA 91360

Dr. Gregory van der Vink
IRIS, Inc.
1616 North Fort Myer Drive
Suite 1440
Arlington, VA 22209

William R. Walter
Seismological Laboratory
University of Nevada
Reno, NV 89557

Dr. Gregory Wojcik
Weidlinger Associates
4410 El Camino Real
Suite 110
Los Altos, CA 94022

Prof. John H. Woodhouse
Hoffman Laboratory
Harvard University
20 Oxford Street
Cambridge, MA 02138

Dr. Gregory B. Young
ENSCO, Inc.
5400 Port Royal Road
Springfield, VA 22151-2388

Dr. Peter Basham
Earth Physics Branch
Geological Survey of Canada
1 Observatory Crescent
Ottawa, Ontario, CANADA K1A 0Y3

Dr. Eduard Berg
Institute of Geophysics
University of Hawaii
Honolulu, HI 96822

Dr. Michel Bouchon
I.R.I.G.M.-B.P. 68
38402 St. Martin D'Heres
Cedex, FRANCE

Dr. Hilmar Bungum
NTNF/NORSAR
P.O. Box 51
N-2007 Kjeller, NORWAY

Dr. Michel Campillo
Observatoire de Grenoble
I.R.I.G.M.-B.P. 53
38041 Grenoble, FRANCE

Dr. Kin Yip Chun
Geophysics Division
Physics Department
University of Toronto
Ontario, CANADA M5S 1A7

Dr. Alan Douglas
Ministry of Defense
Blacknest, Brimpton
Reading RG7-4RS, UNITED KINGDOM

Dr. Roger Hansen
NTNF/NORSAR
P.O. Box 51
N-2007 Kjeller, NORWAY

Dr. Manfred Henger
Federal Institute for Geosciences & Nat'l Res.
Postfach 510153
D-3000 Hanover 51, FRG

Ms. Eva Johannisson
Senior Research Officer
National Defense Research Inst.
P.O. Box 27322
S-102 54 Stockholm, SWEDEN

Dr. Fekadu Kebede
Seismological Section
Box 12019
S-750 Uppsala, SWEDEN

Dr. Tormod Kvaerna
NTNF/NORSAR
P.O. Box 51
N-2007 Kjeller, NORWAY

Dr. Peter Marshal
Procurement Executive
Ministry of Defense
Blacknest, Brimpton
Reading FG7-4RS, UNITED KINGDOM

Prof. Ari Ben-Menahem
Department of Applied Mathematics
Weizman Institute of Science
Rehovot, ISRAEL 951729

Dr. Robert North
Geophysics Division
Geological Survey of Canada
1 Observatory Crescent
Ottawa, Ontario, CANADA K1A 0Y3

Dr. Frode Ringdal
NTNF/NORSAR
P.O. Box 51
N-2007 Kjeller, NORWAY

Dr. Jorg Schlittenhardt
Federal Institute for Geosciences & Nat'l Res.
Postfach 510153
D-3000 Hannover 51, FEDERAL REPUBLIC OF GERMANY

Prof. Daniel Walker
University of Hawaii
Institute of Geophysics
Honolulu, HI 96822

Dr. Ramon Cabre, S.J.
Observatorio San Calixto
Casilla 5939
La Paz, Bolivia

Prof. Hans-Peter Harjes
Institute for Geophysik
Ruhr University/Bochum
P.O. Box 102148
4630 Bochum 1, FRG

Prof. Eystein Husebye
NTNF/NORSAR
P.O. Box 51
N-2007 Kjeller, NORWAY

Prof. Brian L.N. Kennett
Research School of Earth Sciences
Institute of Advanced Studies
G.P.O. Box 4
Canberra 2601, AUSTRALIA

Dr. Bernard Massinon
Societe Radiomana
27 rue Claude Bernard
75005 Paris, FRANCE (2 Copies)

Dr. Pierre Mecheler
Societe Radiomana
27 rue Claude Bernard
75005 Paris, FRANCE

Dr. Svein Mykkeltveit
NTNF/NORSAR
P.O. Box 51
N-2007 Kjeller, NORWAY

Dr. Ralph Alewine III
DARPA/NMRO
1400 Wilson Boulevard
Arlington, VA 22209-2308

Mr. James C. Battis
GL/LWH
Hanscom AFB, MA 01731-5000

Dr. Robert Blandford
DARPA/NMRO
1400 Wilson Boulevard
Arlington, VA 22209-2308

Eric Chael
Division 9241
Sandia Laboratory
Albuquerque, NM 87185

Dr. John J. Cipar
GL/LWH
Hanscom AFB, MA 01731-5000

Dr. H.B. Durham
Sandia National Laboratory
Albuquerque, NM 87185

Dr. Jack Evernden
USGS - Earthquake Studies
345 Middlefield Road
Menlo Park, CA 94025

Art Frankel
USGS
922 National Center
Reston, VA 22092

Dr. T. Hanks
USGS
Nat'l Earthquake Research Center
345 Middlefield Road
Menlo Park, CA 94025

Dr. James Hannon
Lawrence Livermore Nat'l Laboratory
P.O. Box 808
Livermore, CA 94550

Paul Johnson
ESS-4, Mail Stop J979
Los Alamos National Laboratory
Los Alamos, NM 87545

Janet Johnston
GL/LWH
Hanscom AFB, MA 01731-5000

Dr. Katharine Kadinsky-Cade
GL/LWH
Hanscom AFB, MA 01731-5000

Ms. Ann Kerr
IGPP, A-025
Scripps Institute of Oceanography
University of California, San Diego
La Jolla, CA 92093

Dr. Max Koontz
US Dept of Energy/DP 5
Forrestal Building
1000 Independence Avenue
Washington, DC 20585

Dr. W.H.K. Lee
Office of Earthquakes, Volcanoes,
& Engineering
345 Middlefield Road
Menlo Park, CA 94025

Dr. William Leith
U.S. Geological Survey
Mail Stop 928
Reston, VA 22092

Dr. Richard Lewis
Director, Earthquake Engineering & Geophysics
U.S. Army Corps of Engineers
Box 631
Vicksburg, MS 39180

James F. Lewkowicz
GL/LWH
Hanscom AFB, MA 01731-5000

Mr. Alfred Lieberman
ACDA/VI-OA'State Department Bldg
Room 5726
320 - 21st Street, NW
Washington, DC 20451

Stephen Mangino
GL/LWH
Hanscom AFB, MA 01731-5000

Dr. Robert Masse
Box 25046, Mail Stop 967
Denver Federal Center
Denver, CO 80225

Art McGarr
U.S. Geological Survey, MS-977
345 Middlefield Road
Menlo Park, CA 94025

Richard Morrow
ACDA/VI, Room 5741
320 21st Street N.W
Washington, DC 20451

Dr. Keith K. Nakanishi
Lawrence Livermore National Laboratory
P.O. Box 808, L-205
Livermore, CA 94550

Dr. Carl Newton
Los Alamos National Laboratory
P.O. Box 1663
Mail Stop C335, Group ESS-3
Los Alamos, NM 87545

Dr. Kenneth H. Olsen
Los Alamos Scientific Laboratory
P.O. Box 1663
Mail Stop C335, Group ESS-3
Los Alamos, NM 87545

Howard J. Patton
Lawrence Livermore National Laboratory
P.O. Box 808, L-205
Livermore, CA 94550

Mr. Chris Paine
Office of Senator Kennedy
SR 315
United States Senate
Washington, DC 20510

Colonel Jerry J. Perrizo
AFOSR/NP, Building 410
Bolling AFB
Washington, DC 20332-6448

Dr. Frank F. Pilotte
HQ AFTAC/TT
Patrick AFB, FL 32925-6001

Mr. Jack Rachlin
U.S. Geological Survey
Geology, Rm 3 C136
Mail Stop 928 National Center
Reston, VA 22092

Dr. Robert Reinke
WL/NTESG
Kirtland AFB, NM 87117-6008

Dr. Byron Ristvet
HQ DNA, Nevada Operations Office
Attn: NVCG
P.O. Box 98539
Las Vegas, NV 89193

Dr. George Rothe
HQ AFTAC/TGR
Patrick AFB, FL 32925-6001

Dr. Michael Shore
Defense Nuclear Agency/SPSS
6801 Telegraph Road
Alexandria, VA 22310

Donald L. Springer
Lawrence Livermore National Laboratory
P.O. Box 808, L-205
Livermore , CA 94550

Dr. Lawrence Turnbull
OSWR/NED
Central Intelligence Agency
Room 5G48
Washington, DC 20505

Dr. Thomas Weaver
Los Alamos National Laboratory
P.O. Box 1663, Mail Stop C335
Los Alamos, NM 87545

J.J. Zucca
Lawrence Livermore National Laboratory
Box 808
Livermore, CA 94550

GL/SULL
Research Library
Hanscom AFB , MA 01731-5000 (2 copies)

Secretary of the Air Force (SAFRD)

Washington, DC 20330

Office of the Secretary Defense
DDR & E
Washington, DC 20330

HQ DNA
Attn: Technical Library
Washington, DC 20305

DARPA/RMO/RETRIEVAL
1400 Wilson Boulevard
Arlington, VA 22209

DARPA/RMO/Security Office
1400 Wilson Boulevard
Arlington, VA 22209

Geophysics Laboratory
Attn: XO
Hanscom AFB, MA 01731-5000

Geophysics Laboratory
Attn: LW
Hanscom AFB, MA 01731-5000

DARPA/PM
1400 Wilson Boulevard
Arlington, VA 22209

Defense Technical Information Center
Cameron Station
Alexandria, VA 22314 (5 copies)

Defense Intelligence Agency
Directorate for Scientific &
Technical Intelligence
Washington, DC 20301

AFTAC/CA
(STINFO)
Patrick AFB, FL 32925-6001

TACTEC
Battelle Memorial Institute
505 King Avenue
Columbus, OH 43201 (Final Report Only)